Quantum Gravity Phenomenology and High-Energy Neutrinos

Dean Robert Morgan

Department of Applied Mathematics
University of Sheffield

Thesis submitted for the Degree of Doctor of Philosophy at the
University of Sheffield

· December 2005 ·

Abstract

In recent years, the field of quantum gravity phenomenology, which approaches the quantum gravity problem from an experimental point of view, has gained momentum. Typically, one searches for quantum gravity effects in particle systems that have high energies or which have travelled large distances. In this thesis, we consider how high-energy neutrino astronomy, which observe particles at both high energies and large path lengths, will be able to test for these effects.

We consider two possible modifications to standard physics which may arise as a consequence of quantum gravitational effects.The first of these is quantum decoherence, in which a pure quantum state evolves into a mixed quantum state. The second effect is the violation of Lorentz invariance resulting in modifications of the standard dispersion relation. Both of these effects potentially alter the form of the neutrino oscillation probability.

We consider how neutrino telescopes, such as ANTARES and IceCUBE, both under construction at the moment, will be able to test for these effects. We consider two different sources of neutrinos, both of which contribute to events seen within these detectors, namely atmospheric and astrophysical neutrinos. We find that, in many cases, these high energy neutrino experiments can test for quantum decoherence and Lorentz invariance violating effects with much greater precision than experimental data.

Contents

List of Figures

List of Tables

Acknowledgments

Many different people have helped me over the last three years, without whom I would not have completed this thesis. I am very grateful to my supervisor, Elizabeth Winstanley, without whose expertise and time I would not have reached the point I am at today. I am particularly grateful for Elizabeth's endless encouragement, having the project idea in the first place and for her patience, particularly in relation to the writing of this thesis. I would also like to thank Lee Thompson, for his support on ANTARES related issues and for his continuing interest in my work and the Linux HEP computing cluster in the Department of Physics and Astronomy and, in particular Paul Hodgson, for allowing me to run my code and for answering all my questions. I would also like to thank the University of Sheffield itself, for funding my research through a studentship and would also like to thank Phil Young, Stuart Thom and Erik Baxter for many interesting discussions, both work related and not.

Outside of Sheffield, I am particularly indebted to Dan Hooper, for the ideas, the collaboration that led to the work in chapter 8 and for many in depth questions. I am also indebted to Jurgen Brunner for his input on issues related to the ANTARES simulation software.

Last but not least, I would like to thank my family and friends, in particular, my wife, Sarah for supporting throughout my degree and PhD and for giving me that which I treasure most of all, our daughter, Emily.

Preface

The greater part of the contents of this thesis is the author's original work and has appeared in the following publications:

- **Chapters 4 and 5, sections 4.2 and 5.2**
  [200] Dean Morgan, Elizabeth Winstanley, Jurgen Brunner and Lee Thompson *Probing quantum decoherence in atmospheric neutrino oscillations with a neutrino telescope*
  Submitted to Astroparticle Physics. ArXiv:astro-ph/0412618.

- **Chapters 4 and 5, sections 4.2 and 5.2**
  [198] Dean Morgan and Elizabeth Winstanley *Probing quantum decoherence with atmospheric neutrino oscillations: simple model*
  ANTARES internal note:ANTARES-Phys/2003-007.

- **Chapters 4 and 5, sections 4.2 and 5.2**
  [197] Dean Morgan and Elizabeth Winstanley *Probing quantum decoherence with atmospheric neutrino oscillations: general model*
  ANTARES internal note:ANTARES-Phys/2004-001.

- **Chapters 4 and 5, sections 4.2 and 5.2**
  [196] Dean Morgan and Elizabeth Winstanley *Probing quantum decoherence with atmospheric neutrino oscillations: energy non-conserving models*
  ANTARES internal note:ANTARES-Phys/2004-003.

- **Chapters 6 and 7, sections 6.2 and 7.1**
  [199] Dean Morgan, Elizabeth Winstanley, Jurgen Brunner and Lee Thompson *Probing the violation of Lorentz invariance in atmospheric neutrino oscillations with a neutrino telescope*
  To appear.

- **Chapter 8, section 8.2**

  |160| Dan Hooper, Dean Morgan and Elizabeth Winstanley *Probing quantum decoherence with high-energy neutrinos*
  Physics Letters **B609** 206 (2005).

- **Chapter 8, sections 8.2 and 8.3**

  |159| Dan Hooper, Dean Morgan and Elizabeth Winstanley *Lorentz and CPT invariance violation in high-energy neutrinos*
  Physical Review **D72** 065009 (2005).

Chapters 1 and 2 contain review material. The analysis in section 3.2 is original. The analysis in chapter 4 is the author's, with the exception of section 4.1, with the entirety of chapter 5 being original. Chapters 6 and 7 are both original work with the exception of the review section 6.1. Finally, chapter 8 is entirely original with the exception of section 8.1.

Introduction

Perhaps the most pressing problem in modern day fundamental physics is that of quantum gravity; the unification of quantum field theory with general relativity. The traditional way of attacking the problem is from a purely theoretical direction and this approach has led to theories such as string theory and loop quantum gravity, to name just two.

In the last few years, however, an alternative approach of tackling this problem has emerged; this approach is known as *quantum gravity phenomenology*. Quantum gravity phenomenology tackles the problem from an experimental point of view, an approach that was considered impossible for many years.

Recently, many experimental systems have been used to look for possible quantum gravity effects, including cosmic rays and high energy photons. In this thesis, we consider high energy neutrinos.

The new field of neutrino astronomy promises to be a very exciting one as it opens up a whole new window through which to view the universe. Since neutrino telescopes typically observe high energy neutrinos that have travelled large distances, this makes them an ideal system in which to look for quantum gravity effects.

In chapter 1, we discuss the properties of neutrinos. We consider the sources of neutrinos which may be viewed through neutrino telescopes, presenting evidence as to why we might expect to observe neutrinos coming from these sources. The current status of neutrino telescopes is outlined and we describe one particular experiment, the ANTARES neutrino telescope, in detail. We finish the chapter by outlining the phenomenon of neutrino oscillations; presenting the mathematical formalism describing this effect and describing the current experimental status.

We then go on, in chapter 2, to describe the problem of quantum gravity; why, even though there is no direct experimental evidence for such a theory, we expect the problem to be solvable; and the current state of play.

In chapter 3, we present the methodology behind our simulations of atmospheric

neutrinos relevant to the ANTARES experiment. We show how we may produce spectra describing the number of events as a function of neutrino telescope observables and how we may simulate sensitivity contours, showing us the regions of parameter space which the ANTARES neutrino telescope will be able to probe.

In chapters 4 and 5 we consider the first effect which may arise due to a quantum gravity environment; the phenomenon of quantum decoherence. In chapter 4 we present the theory behind this phenomenon, describing how it may arise and how it could alter the probability that one atmospheric neutrino oscillates into another. We then use the simulations presented in chapter 3 to examine whether the ANTARES neutrino telescope observe for these novel effects.

In chapters 6 and 7 we consider a second possible quantum gravity effect; the violation of Lorentz invariance. We present the theory underlying this phenomenon in chapter 6 and describe how the atmospheric neutrino oscillation probability could be altered. Chapter 7 presents the results of simulations of atmospheric neutrinos for the ANTARES neutrino telescope when we include these effects.

Finally, in chapter 8, we show how both quantum decoherence and Lorentz invariance violating effects manifest themselves in neutrinos oscillations when the neutrinos originate in astrophysical objects. We show that by considering these sources, neutrino telescopes will be able to place the most stringent bounds to date on both quantum decoherence and Lorentz invariance violating model parameters.

The ultimate goal for many physicists is the construction of a unified quantum theory of gravity. In its broadest sense, this thesis represents a small step in that direction. When the neutrino telescopes described in chapter 1 have been completed, we face an exciting time in both astronomy and the field of quantum gravity.

Chapter 1

Neutrinos

Over the last ten years, there has been an explosion in research into neutrino physics. In this chapter, we present an overview of the neutrino physics which we shall later utilize in order to examine the possible effects of quantum gravity. We begin this chapter with a summary of the history of the neutrino and our current understanding of this elusive particle. We then describe the two sources of neutrinos for our quantum gravity work; namely atmospheric neutrinos and those from astrophysical sources. The final section of this chapter outlines a phenomenon we shall consider throughout this thesis: the phenomenon of neutrino oscillations.

1.1 Neutrinos: an overview

The existence of the neutrino was first postulated over seventy years ago by Pauli [78]. Since that time, it has played an important part in particle physics and is now the focus of a large body of research. The emergence of the phenomena of neutrino oscillations has opened the first window to physics beyond the standard model of particle physics. Neutrinos are also playing a central role in the fields of astrophysics and cosmology. In this section, we shall present an overview of the history of the neutrino and our current understanding of neutrino properties. For a comprehensive overview of neutrino physics, see, for example, reference [244].

1.1.1 The history of the neutrino

In the early twentieth century, radioactive beta decay seemed to violate the known laws of physics as it appeared to violate the conservation of momentum. Many so-

lutions were suggested, including modifications to the conservation of energy. However, in December 1930, Wolfgang Pauli suggested a radical alternative (see, for example [78]). Pauli suggested that, in addition to the known electron, a further particle, which is electrically neutral, is also involved in beta decay, thus conserving momentum. This particle, subsequently named the neutrino by Enrico Fermi, was first detected by Cowan and Reines in 1956 [85]. Since 1956, neutrinos have been detected from nuclear reactors [84], particle accelerators [166], the Sun [22,23], the Earth's atmosphere [131] and, in 1987, from a supernova [27,233].

In 1962, it was found that there were at least two types of neutrino [99]. The first was the electron neutrino postulated by Pauli and detected by Cowen and Reines. The second discovered was found to be a partner of the muon and subsequently named the muon neutrino. In 2001, the third expected neutrino, the tau neutrino was detected [203].

1.1.2 Neutrinos in the present

One of the most successful models in modern day physics is the standard model of particle physics which describes the 17 known elementary particles and their interactions. Three of these fundamental particles are the neutrinos, which are now known to be neutral partners of the massive leptons. Table 1.1 shows the standard model particles and their properties. The fermions, particles with non-integer spin, are separated into two groups, the quarks and leptons. The particles within these groups are further categorized into three families with increasing mass. The gauge bosons, particles with integer spin, mediate the particle interactions; with the photon mediating the electromagnetic interaction, W and Z bosons the weak force and the gluons the strong force. The final particle within the standard model is the Higgs boson which is responsible for generating the mass of particles. This is the only particle of the standard model not yet directly observed experimentally.

Over the last seventy years, much has been learned about the neutrino and we present an overview here (all values here are taken from the Particle Data Group [112] unless otherwise stated):

Number of families The number of families of neutrinos with a mass less than that of half of the Z mass is 3 ± 0.06. This very tight constraint was found by considering the Z resonance peak at LEP, CERN [137].

Family	Particle	Mass (MeV)	Charge (units of e)
Leptons	e	0.511	-1
	μ	105.7	-1
	τ	1780	-1
	ν_e	$< 3 \times 10^{-6}$	$< 2 \times 10^{-14}$
	ν_μ	< 0.19	$< 2 \times 10^{-14}$
	ν_τ	< 18.2	$< 2 \times 10^{-14}$
Quarks	u	1.5 - 4	$\frac{2}{3}$
	d	4 - 8	$-\frac{1}{3}$
	s	80 - 130	$-\frac{1}{3}$
	c	1150 - 1350	$\frac{2}{3}$
	b	4100 - 4400	$-\frac{1}{3}$
	t	$(1.692 - 1.794) \times 10^5$	$\frac{2}{3}$
Gauge bosons	γ	0	0
	W	80400	+1
	Z	91200	0
	g	0	0
Higgs boson	h	> 114400	0

Table 1.1: The particle content of the Standard Model of Particle Physics. The particles are categorized into fermions, comprising the leptons and quarks, the gauge bosons and the, as yet, undiscovered Higgs boson. The masses and charges are taken from [112].

Mass Until recently, the question of whether neutrinos had mass was open. With the detection of neutrino oscillations, as described in section 1.4, this indicates that, at least one of the neutrinos has mass. However, no direct measurement of neutrino mass has been possible to date. Direct mass searches are often performed by considering beta decay and these experiments have been able to place upper bounds on the neutrino masses of

$$m_e < 3\ eV, \qquad m_\mu < 0.19\ MeV, \qquad m_\tau < 18.2\ MeV.$$

Limits on neutrino masses have also been placed from cosmological considerations. Data from the WMAP collaboration [68], together with that from the Sloan Digital Sky Survey [242] and another 27 cosmic microwave background (CMB) experiments have been able to conclude $\sum m_\nu < 0.75\ eV$.

Neutrino Oscillations Although neutrino oscillations were first proposed over 50

years ago [208–210], direct proof of oscillations was only found in 1998 at the Super-Kamiokande experiment in Japan [131]. The study of neutrino oscillations makes up a large proportion of this thesis and, rather than give a brief description here, we shall introduce neutrino oscillations in detail in section 1.4.

Charge Limits on the charge of neutrinos come from astrophysical observations. By considering the amount of energy lost from the sun, and from red giant star clusters, by the escape of neutrinos created by electromagnetic processes, limits of 10^{-14} e (where e is the charge on the electron) for all neutrinos have been found.

Overall, given the ghost-like nature of the neutrino, large steps have been taken towards understanding these elusive particles. Much of this thesis relies on the phenomenon of neutrino oscillations and we shall present the theory behind this phenomenon, and the current experimental data, in section 1.4. In the next section, we shall concentrate on describing the possible sources of neutrinos in which we shall be interested and the mechanisms of neutrino production within these sources.

1.2 Sources of high energy neutrinos

In this section, we shall concentrate on two particular sources of high energy neutrinos. We shall explain how neutrinos may be produced in cosmic accelerators and also how they may be created within the Earth's atmosphere from the interaction of cosmic rays with atmospheric nuclei. Although the stages on which these neutrinos are created are fundamentally different, the two processes are intimately related since the cosmic rays which generate the atmospheric neutrino flux also originate in cosmic accelerators. These cosmic accelerators may take many forms including Active Galactic Nuclei (AGN) [54,100,201,212], Gamma-Ray Bursts (GRB) [101,145,193,236,237], microquasars [106,178], supernova remnants, star clusters and X-ray binaries. Figure 1.1 shows an image of an AGN.

Although neutrinos may be created in a variety of sources, there are, in general, two processes which result in the creation of high energy neutrinos:

- All three flavours of neutrino may be created from the decay or interactions of hadrons. For example, Fermi accelerated protons, or charged nuclei, may

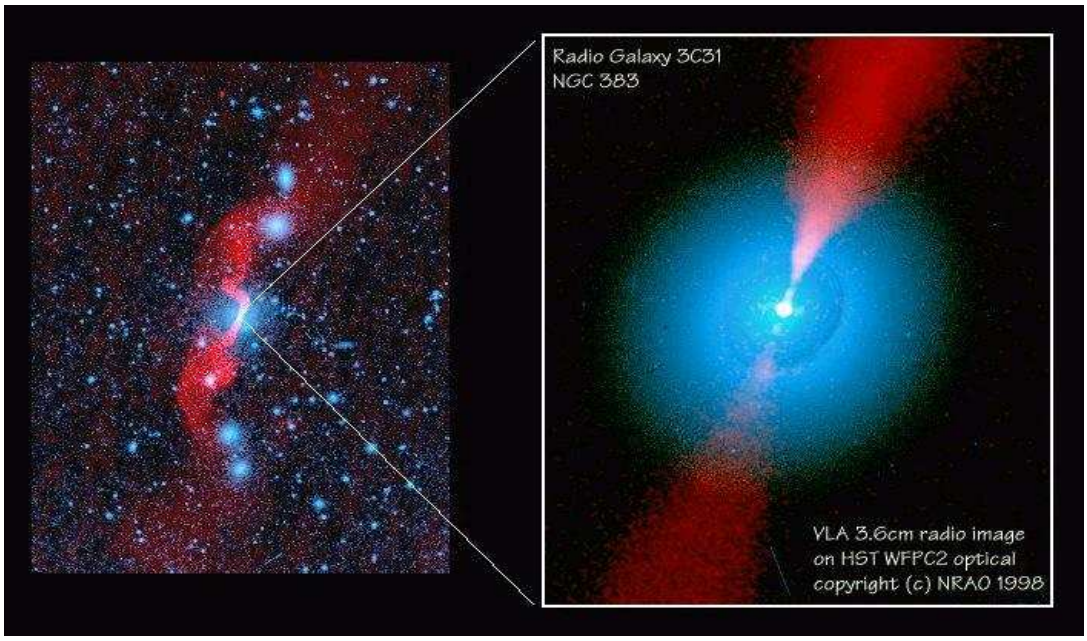

Figure 1.1: An image of active galaxy 3C31. The red parts of the figure were taken with a radio telescope with the blue regions observed optically (taken from [10]).

collide with other hadrons or photons generating charged and neutral pions. These pions then decay, generating muon and electron type neutrinos:

$$\begin{aligned} \pi^+ &\to \mu^+ \nu_\mu \to e^+ \nu_e \overline{\nu_\mu} \nu_\mu; \\ \pi^- &\to \mu^- \overline{\nu_\mu} \to e^- \overline{\nu_e} \nu_\mu \overline{\nu_\mu}. \end{aligned} \tag{1.1}$$

In an analogous way, tau neutrinos may be created due to the decay of D_s mesons formed by hadronic interactions. However, the tau neutrino flux at the source is negligible compared to that of the electron and muon neutrinos since the D_s mesons have a high production threshold and very small production cross section.

- A beam of pure anti-electron neutrinos, at the source, may be created by the disintegration of Fermi accelerated atomic nuclei by interactions with infrared photons around their source. These interactions can strip away atomic neutrons which decay to give anti-electron neutrinos:

$$n \to p^+ e^- \overline{\nu_e}. \tag{1.2}$$

We now examine in more detail the two sources of high energy neutrinos, beginning

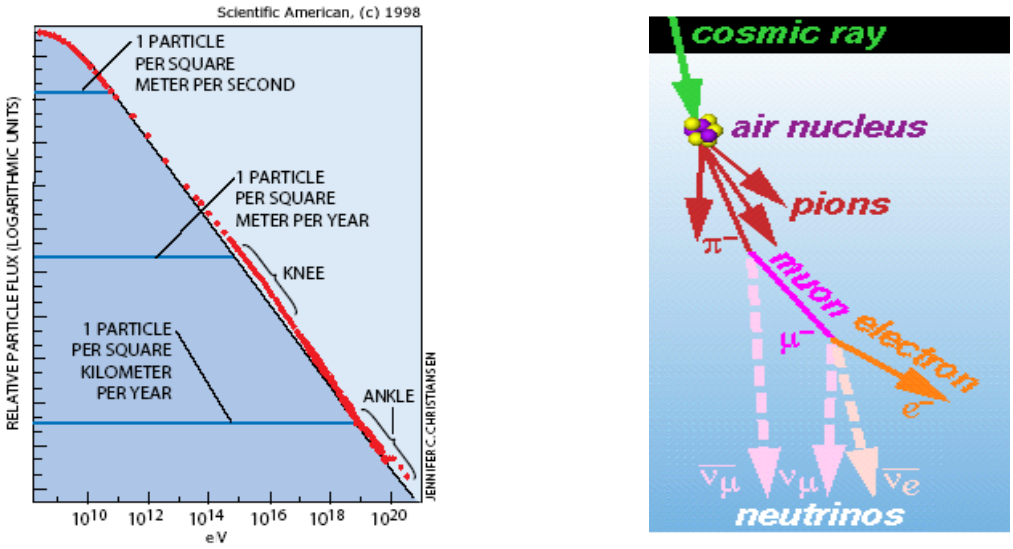

Figure 1.2: The left plot shows the measured cosmic ray spectrum as a function of energy from various cosmic ray experiments (modified from [97]). The right diagram shows how atmospheric neutrinos are generated by the interaction of cosmic rays with atomic nuclei in the Earth's atmosphere. This diagram is modified from that found at [4].

with those created in the Earth's atmosphere.

1.2.1 Cosmic rays and atmospheric neutrinos

It has been known for many years that there exists a flux of particles bombarding the Earth from space. This flux has been intensively studied and the cosmic ray spectrum is now very well known. The left plot of figure 1.2 shows the measured cosmic ray spectrum. At energies above 10 GeV, the spectrum can be split into three parts with each section being fitted by a power law. The flux between 10 GeV and 1 PeV is thought to contain galactic protons and the spectrum between these energies has a spectral index of around -2.7. At 1 PeV, the spectral index changes from approximately -2.7 to around -3 at point known as the knee. From 1 PeV to around 3 EeV, the flux is no longer dominated by galactic protons but galactic heavy nuclei instead. The flux then flattens at 3 EeV and regains a spectral index of -2.7. At this point, the flux is again dominated by protons. This proton domination at very high energies is thought to signal a change in the source of cosmic rays. At energies lower than the ankle, the flux is all galactic, however at energies above the ankle, the flux is considered to be extra-galactic since any galactic protons with these very large energies would no longer be contained within the galaxy by the galactic

magnetic field.

Recently, anisotropies in the cosmic ray flux at large energies have been detected [63, 70, 155]. These anisotropies, it has been argued, are evidence that some of the cosmic ray flux is due to galactic neutrons rather than protons. Here, the high energy neutrons would be very Lorentz boosted in order to remain quasi-stable and travel to the Earth without decaying. If this is the case, then we can expect neutrons with lower energies to be created in the same sources which decay by the process described above. Therefore, evidence from the cosmic ray flux hints that there may be beams of anti-electron neutrinos present within our galaxy [41].

A second interesting point of discussion which arises from the cosmic ray flux is the GZK effect [144, 243]. At very high energies, we would expect a cut-off in the cosmic ray flux as the protons would see the CMB as a sea of gamma ray photons and therefore interact with these photons to produce pions, resulting in the protons essentially being absorbed. However, there is inconclusive evidence to show that there is a flux of particles above this cut-off energy [229]. This may be a signature of new physics and we shall further discuss this possibility in chapter 6.

So, the Earth is constantly bombarded by cosmic rays, mainly protons but also some neutrons. These particles interact with atmospheric nuclei at heights of approximately 15-20 km, creating muons and muon neutrinos as we described above in (1.1). The diagram on the right of figure 1.2 shows a sketch of this process. The created muons are often of high enough energy that they are sufficiently Lorentz boosted that they may reach the surface of the earth. However, other muons will be created with smaller energies and subsequently decay in flight, producing both electron and muon type neutrinos. These neutrinos, together with those created in the first hadronic interaction, are termed *atmospheric neutrinos*. We would therefore expect the ratio of electron neutrinos to muon neutrinos to be approximately $1:2$. As we shall discuss in section 1.4, this expected ratio is not observed when the neutrino travel large distances.

1.2.2 Astrophysical neutrinos

The main signal for which neutrino telescopes are searching originate from astrophysical objects, such as AGN and GRB's. Because neutrinos interact weakly, this makes them ideal candidates with which to perform astronomy compared to traditional methods; photons, whilst created in copious amounts, are readily absorbed at

high energies by the CMB and cosmic infrared background (CIRB) whilst protons are deflected by magnetic fields making it impossible to determine their source. In these cosmic accelerators, both of the mechanisms discussed above in (1.1) and (1.2) may produce neutrinos.

The important thing to keep in mind when considering neutrinos from astrophysical sources are the ratios of flavours. Neutrinos produced in pion decay follow the ratio $\nu_e : \nu_\mu : \nu_\tau = 1/3 : 2/3 : 0$, since the created tau neutrino flux is so small. For neutrinos created from neutron decay, they follow the ratio $\nu_e : \nu_\mu : \nu_\tau = 1 : 0 : 0$. It is also interesting to note that neutrinos from pion decay produce both neutrinos and anti-neutrinos whilst only anti-neutrinos are created from neutron decay.

From a measurement point of view, point sources of neutrinos are much more useful than diffuse neutrino sources. With a point source, it is likely that the distance over which the neutrinos have travelled will be known. Also, sources which emit neutrinos for only a short period time are very useful in order to reduce the background by only considering events within a certain window of time. For this very reason, AGN and GRB's are likely to be the most useful sources. However, bright galactic sources would also be very useful.

To date, the only neutrinos observed from an astrophysical object came in 1987 from a supernova [27,233]. There are, however, tantalizing hints that bright sources of astrophysical neutrinos exist. We have already discussed the first; the presence of neutrons in the cosmic ray flux. The second comes from the neutrino telescope AMANDA-II [43]. The collaboration recently reported the detection of two neutrinos [8,148,216] which were coincident with TeV flares seen by the Whipple gamma-ray telescope [158] from the AGN 1ES 1959+650. Unfortunately, these events were not found within a blind analysis and so their statistical significance cannot be determined. However, the indirect evidence for neutrinos with astrophysical origins is mounting.

Whilst neutrinos created within cosmic accelerators are considered to be the main source of astrophysical neutrinos, more exotic processes may also be responsible for the creation of neutrinos. Processes such as annihilating or decaying dark matter or topological defects [59,69,139,224] and Hawking radiating black holes [83,149] may also be responsible for creating neutrinos. However, for the purpose of this thesis, we shall concentrate on the two standard mechanisms. For an overview of sources of neutrinos and also the detection methods discussed in the next section, see, for example, [147].

1.3 Neutrino telescopes

We have seen that neutrinos open a new window to the universe and will be able to tell us about astrophysical processes which are invisible at the moment. Throughout this thesis, we shall concentrate on neutrinos detected by neutrino telescopes. The numerical simulations in chapters 5 and 7 are applicable to the ANTARES [170] neutrino telescope. We would expect other neutrino telescopes to obtain very similar results. In this section, we briefly describe the general detection methods for neutrino telescopes. We shall also describe existing and planned experiments briefly, but present a slightly more in depth overview of the ANTARES experiment.

1.3.1 Detection methods

Neutrino telescopes consist of arrays of photomultiplier tubes (PMTs). The PMTs detect Cherenkov radiation which is emitted by charged particles, the product of neutrino interactions, travelling faster than light within the medium containing the experiment. Neutrino telescopes do not, therefore, detect neutrinos directly, rather, they detect the daughter particles created when a neutrino interacts with atomic nuclei around the detector. Figure 1.3 shows the interaction of a muon neutrino with an oxygen nucleus in ice and the emission of Cherenkov radiation from the charged muon.

The direction of neutrinos at the detector is isotropic, since neutrinos are able to travel through the Earth and so the detector sees neutrino from both above and below the horizon. This turns out to be very useful as the Earth will act as a shield to all particles originating from the opposite side of the Earth except neutrinos. Neutrino telescopes, therefore, point downwards. If an up going event occurs, we can be confident that it is a neutrino event and not an event from, say, a cosmic ray. In addition to using the Earth as a shield, the experiments are built as deep as possible in order to eliminate as much of the background from down-going events as possible.

1.3.2 High-energy neutrino detection

Once the high-energy neutrinos described in the last section have been created and propagate to earth, there are several ways in which they may be detected:

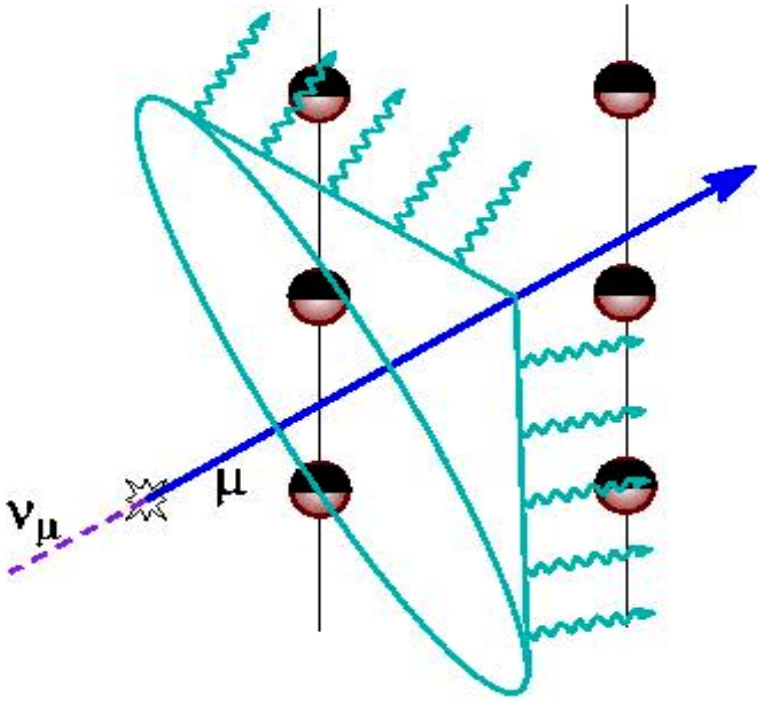

Figure 1.3: A schematic diagram of a neutrino interaction and the emission of Cherenkov radiation by the daughter muon (taken from [1]).

Shower events All high-energy neutrino interactions produce shower events. Neutral current interactions of neutrinos of all flavours generate hadronic showers which can be detected. In addition, charged current interactions of electron neutrinos generate observable electromagnetic showers. Since all flavours of neutrinos generate shower events, it is not possible to identify the flavour ratios of the neutrinos at the detector by considering shower events alone.

Muon neutrino events High-energy muon neutrinos may interact with the experimental medium to produce muons by charged current interactions. These muons generated in or around the detector are potentially observable and therefore present us with a way of distinguishing the flavour of a muon neutrino.

Tau neutrino events If tau neutrinos have an energy lower than $\sim 1\ PeV$, then their flavour cannot be identified. At these lower energies, only shower events are seen as a tau lepton generated will decay before it can be detected. The situation is much more promising, however, at higher energies, since the tau lepton travels a longer distance before decay, enabling its track to be identified. This leads to a class of events unique to tau neutrinos, namely "lollipop" and

"double bang" events. A double bang event is observed when the tau neutrino interacts via a charged current inside the detector. The tau neutrino generated in this event travels across the detector where its decay occurs within the detector volume. However, in a high-energy neutrino telescope, the showers must be separated by a distance of between 100 and 400 meters to be resolved. The second class of events useful for identifying tau neutrinos are lollipop events, in this case, the neutrino has a higher energy than that which creates a double bang event and so the tau lepton travels a greater distance. A lollipop event occurs when the first shower of a double bang event occurs outside the volume of the detector but the decay of the tau lepton happens inside the detector. Unfortunately, the converse, the case in which a shower is seen, followed by a leptonic track, does not indicate a tau neutrino as muons or tau leptons generated in ordinary hadronic or electromagnetic showers could mimic this event.

Therefore, we have three types of event which may be detected and from which we can infer the flavour ratios of the neutrinos. Figure 1.4 shows a schematic overview of these processes.

1.3.3 Neutrino telescopes

As we saw in the last section, to construct a high-energy neutrino telescope, we need a deep site with a transparent Cherenkov medium. There are two types of sites that occur naturally which lend themselves to the construction of a neutrino telescope; the deep sea and deep ice, for example, at the Antarctic. There have been various attempts to construct neutrino telescopes in these challenging environments:

AMANDA and IceCUBE The AMANDA - Antarctic Muon And Neutrino Detector Array - neutrino telescope is based in the Antarctic and so observes the northern sky. AMANDA uses ice at a depth of around 2 kilometers as the Cherenkov medium. Initially, the experiment was known as Amanda B10 [239] and consisted of 302 PMTs on 10 strings. The results for this generation of the AMANDA experiment can be found in [44]. The experiment was subsequently upgraded and at present has 19 lines which house a total of 677 PMTs. This current phase of the AMANDA experiment is often called AMANDA-II [43]. To date, the AMANDA neutrino telescope has only been able to detect atmospheric neutrinos. Figure 1.5 shows a map of this data.

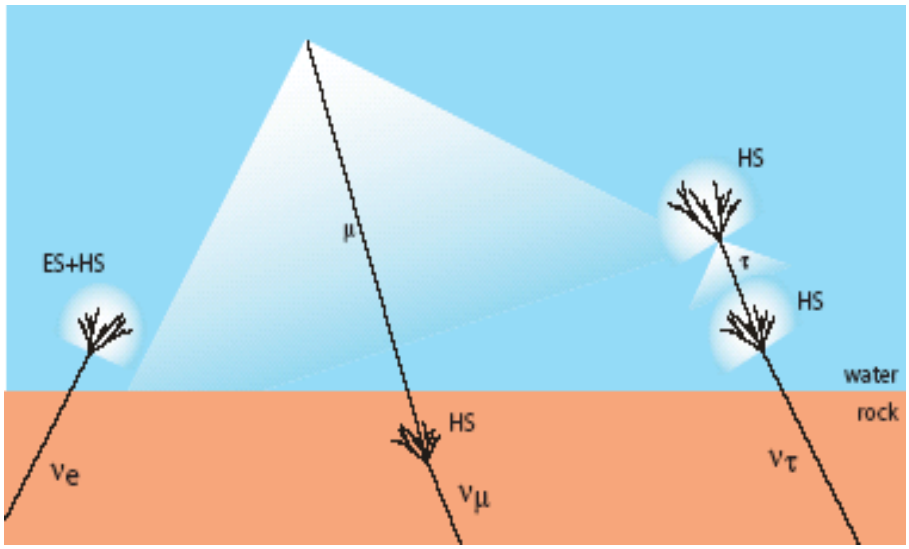

Figure 1.4: A schematic diagram showing the interactions of different flavours of neutrinos. The electron neutrino simply creates electromagnetic (ES) and hadronic showers (HS). A high-energy muon neutrino may be detected by the emitted Cherenkov light and so a track is observed. Tau neutrinos may be identified as double bang or lollipop events. A double bang event occurs when both the hadronic showers (HS) shown are contained within the detector, linked by the observed track of the tau lepton. A lollipop event occurs when the hadronic shower is seen with a leptonic track but the first shower occurs outside the detector. Diagram taken from [74].

There are plans to further upgrade this experiment so that the experiment volume measures one cubic kilometer. This experiment is known as IceCUBE [25, 138]. Because of the large volume of this experiment, it will be able to distinguish flavour ratios much better than the current generation of experiments. In chapter 8, where we consider neutrinos of astrophysical origin, we assume a detector with this volume. Figure 1.6 shows a schematic diagram of the detector.

Baikal The Baikal neutrino telescope [64], named after the lake in which it sits in Siberia, consists of 8 lines of 200 PMTs. The main disadvantages of this experiment are that it is only at a depth of around 1.3 km and that the optical properties of the lake are significantly worse than those in deep ice or the deep ocean.

Dumand The Dumand experiment [73] was the first attempt to construct a neutrino telescope in deep water. It was based in the ocean around Hawaii. Unfortu-

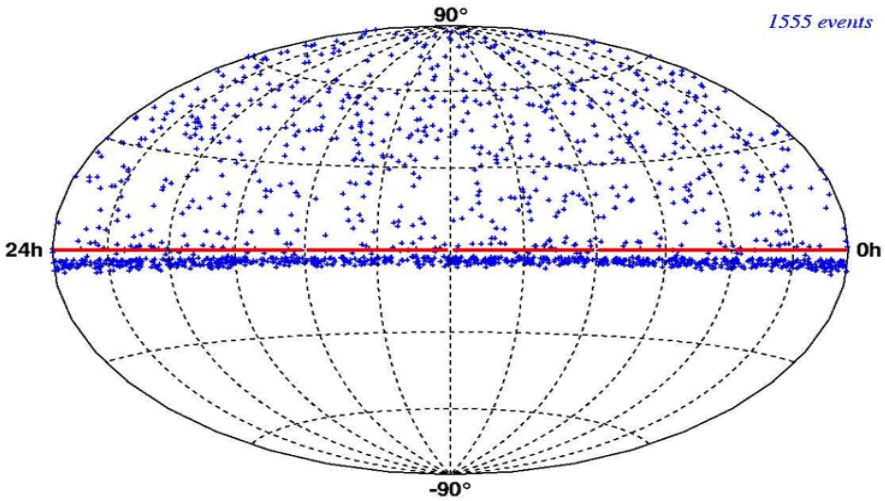

Figure 1.5: A sky map of atmospheric neutrino data from AMANDA. The thick band of events below the horizon (the red line) is from down-going atmospheric muon contamination (taken from [1]).

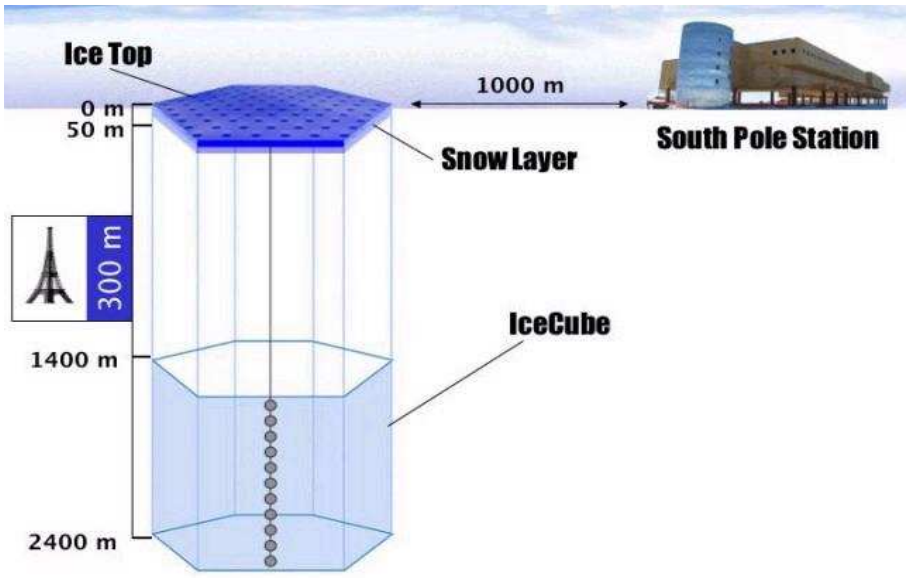

Figure 1.6: A diagram of the IceCUBE neutrino telescope (taken from [5]).

nately, the project was cancelled in 1996 before the experiment was completed.

Nestor The Nestor experiment [217], which is currently at the testing stage, is a Greek contribution to neutrino astronomy. The site lies in the Mediterranean sea at a depth of around 3.8 km. At present, the first stage of the detector is in place and has started to take data [19].

In addition to these traditional methods of construction of neutrino telescopes, others have been proposed. These include acoustic detection as in the case of the ACORNE experiment [14], the detection of horizontal air showers in cosmic ray experiments such as AUGER [72,86], EUSO [207] and OWL [227] and radio Cherenkov detection as in the case of the RICE [175] experiment.

1.3.4 The ANTARES experiment

A large proportion of this thesis is particularly relevant for the ANTARES neutrino experiment [170]. In chapter 3, we outline numerical simulations of ANTARES results and then show how this experiment will be able to probe for quantum gravity effects in atmospheric neutrinos in chapters 5 and 7. In this section, we shall, therefore, describe the ANTARES neutrino telescope in more detail than those experiments considered above.

The ANTARES site

The ANTARES site lies at a depth of around 2.4 km, approximately 40 km off the south coast of France, in the Mediterranean sea, as shown in figure 1.7. The black square towards the bottom of this figure is the ANTARES site and is connected to the shore station, the black square towards the top of the figure, by a cable.

The experiment

A schematic diagram of the experiment is shown in figure 1.8. The experiment consists of lines of PMTs which are anchored to the sea bed. Buoys on top of these lines keep them approximately vertical. The PMTs are grouped in threes around the string and look down towards the sea bed at an angle of 45°. Three PMTs make up one storey. Each of the lines houses 90 PMTs over 30 storeys, with a distance between the storeys of 12 m. Overall, each line is 348 m high. Each of the lines is

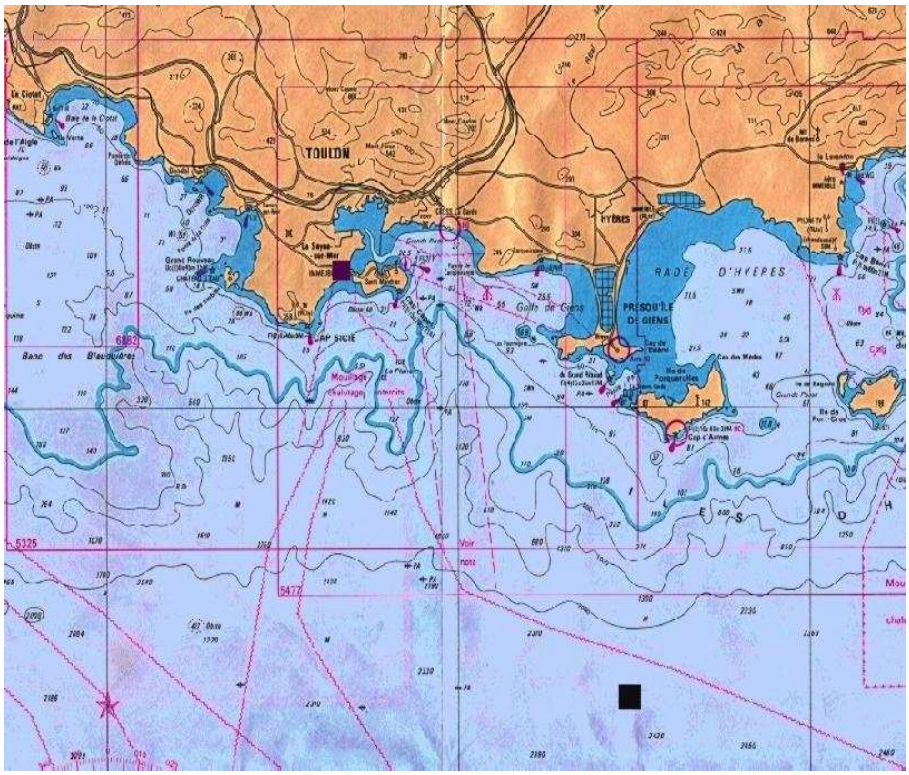

Figure 1.7: A map of the ANTARES site off the south coast of France. The black square towards the bottom of this figure is the ANTARES site with the shore station shown by the black square towards the top of the figure (taken from [2]).

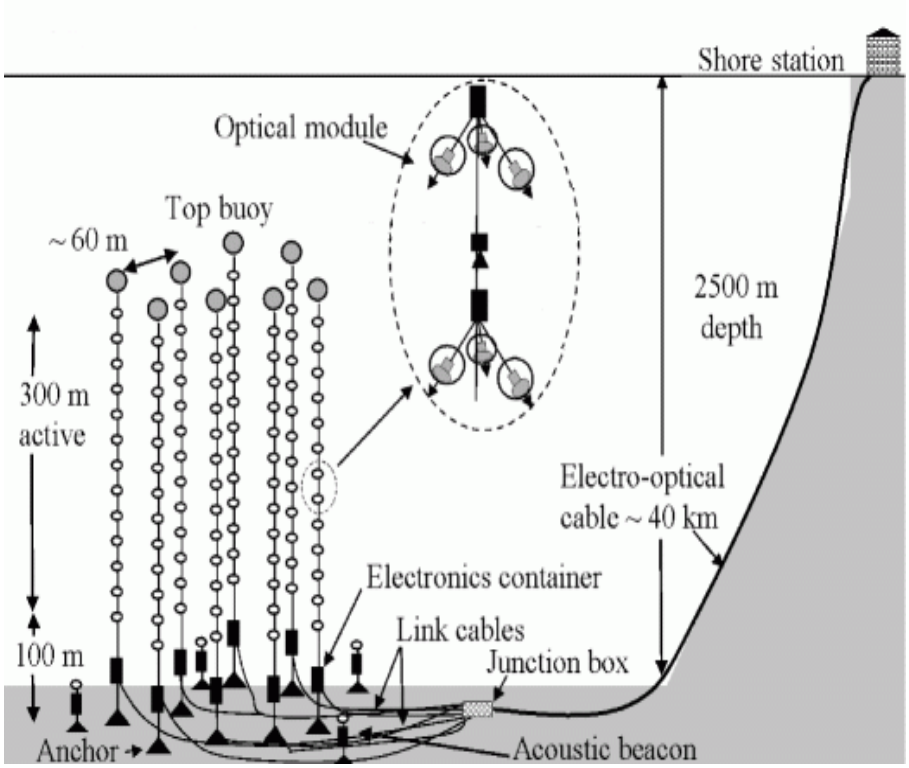

Figure 1.8: Schematic diagram of the ANTARES experiment (taken from [2]).

connected to a junction box which is connected to the cable to the shore station. Altogether, the experiment has an instrumented volume of 0.1 km.

Current status

The construction stage of the ANTARES experiment is under way. The electro-optical cable connecting the experiment to the shore station was laid in October 2001 and the junction box was connected to the cable at the end of 2002. A mini-instrumentation line comprising of various instruments to measure the environment at the site and a pre-production sector line consisting of PMTs were attached to the junction box in March 2003, both taking data for a number of months. In March 2005, the MILOM, the main instrumentation line, was deployed and connected to the junction box. The main sector lines are being constructed and the whole detector will be deployed by 2007.

Although the detector itself will not be finished until this time, the instrumentation already deployed is taking data. As an example, the seismic instrumentation detected an earthquake, originating in Japan on 30th August 2005, measuring 6.2 on the Richter scale. Figure 1.9 shows the ANTARES data compared to a dedicated earthquake detector on the French mainland.

1.4 Neutrino oscillations

In the previous sections, we introduced some of the basic properties of neutrinos and described how they may be created within the Earths atmosphere and astrophysical objects. One phenomenon we alluded to earlier was that of neutrino oscillations where one flavour of neutrino may change into another. A large part of this thesis will be concerned with examining how novel effects due to quantum gravity may alter the neutrino oscillation probability. Here, we present the standard neutrino oscillation case and discuss our present knowledge of the neutrino oscillation parameters.

1.4.1 Formalism

Vacuum oscillations

Normally, neutrinos are identified by their flavour (e, μ, τ) rather than their mass. Neutrinos which have definite flavour need not be states of definite mass, however. If

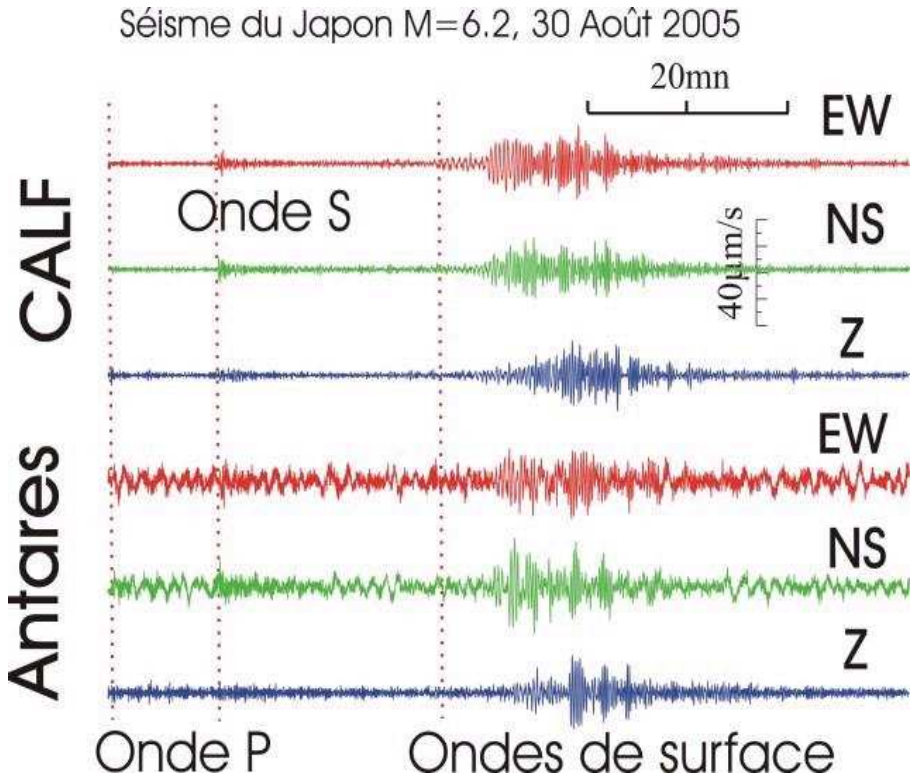

Figure 1.9: Plot showing the measurement of an earthquake which originated in Japan. The top three waves are those from an earthquake detector on the mainland whilst the bottom three plots are the results from the ANTARES seismic instrumentation (taken from [2]).

this is the case, we consider the flavour eigenstates, $|\nu_\alpha\rangle$, to be a linear combination of mass eigenstates, $|\nu_i\rangle$:

$$|\nu_\alpha\rangle = \sum_i U_{\alpha i}|\nu_i\rangle, \tag{1.3}$$

where $U_{\alpha i}$ are the components of the unitary leptonic mixing matrix. In the Schrödinger representation, the time evolution of the mass eigenstates has the form

$$i\frac{d}{dt}|\nu_i(t)\rangle = m_i|\nu_i(t)\rangle, \tag{1.4}$$

where t is the time in the mass frame and m_i are the mass eigenvalues. Using equation (1.4), the probability of oscillation from ν_α to ν_β can be calculated to be

$$\begin{aligned} P(\nu_\alpha \to \nu_\beta) &= \delta_{\alpha\beta} - 4\sum_{j>i} \Re(U^*_{\alpha j}U_{\beta j}U_{\alpha i}U^*_{\beta i})\sin^2[\Delta m^2_{ji}(L/4E)] \\ &\quad +2\sum_{j>i} \Im(U^*_{\alpha j}U_{\beta j}U_{\alpha i}U^*_{\beta i})\sin[\Delta m^2_{ji}(L/2E)]. \end{aligned} \tag{1.5}$$

where $\Delta m^2_{ji} \equiv m^2_j - m^2_i$, the quantity E is the energy of the neutrino and L is the path length. We have assumed that the neutrino is relativistic and set $c = \hbar = 1$. If we consider three flavours of Majorana neutrinos, then the 3×3 mixing matrix is given by $U = V \cdot M$ where

$$V = \begin{pmatrix} c_{12}c_{13} & s_{12}c_{13} & s_{13}e^{-i\delta_{CP}} \\ -s_{12}c_{23} - c_{12}s_{23}s_{13}e^{i\delta_{CP}} & c_{12}c_{23} - s_{12}s_{23}s_{13}e^{i\delta_{CP}} & s_{23}c_{13} \\ s_{12}s_{23} - c_{12}c_{23}s_{13}e^{i\delta_{CP}} & -c_{12}s_{23} - s_{12}c_{23}s_{13}e^{i\delta_{CP}} & c_{23}c_{13} \end{pmatrix},$$

$$M = \begin{pmatrix} e^{i\phi_1} & 0 & 0 \\ 0 & e^{i\phi_2} & 0 \\ 0 & 0 & 1 \end{pmatrix}. \tag{1.6}$$

Here, c_{ij} and s_{ij} represent the cosine and sine of the mixing angle θ_{ij} respectively, the quantity δ_{CP} is a CP violating phase and the phases in M are the Majorana phases. For Dirac neutrinos, the situation is similar but the Majorana phases may be absorbed into the phases of the mass eigenstates. In practice, since the mixing angle θ_{13} has been found to be small [142], systems involving just two neutrinos are often considered. Then, replacing c and $\hbar$, the vacuum oscillation probability reduces to

$$P(\nu_\alpha \to \nu_\beta) = \sin^2 2\theta \sin^2 \left[1.27\Delta m^2 \frac{L}{E}\right], \tag{1.7}$$

where Δm^2 is measured in eV^2, the distance the neutrino travels, L, is measured in kilometers and E is measured in GeV. By convention, θ_{12} and Δm^2_{21} are solar oscillation parameters, describing $\nu_e \to \nu_{\mu,\tau}$ with θ_{23} and Δm^2_{32} the atmospheric neutrino oscillation parameters, describing $\nu_\mu \to \nu_\tau$.

Oscillations in matter

The situation becomes somewhat more complicated if neutrinos are passing through dense matter, for example in the Sun. In this case, the Hamiltonian in the mass basis is no longer diagonal which results in the mixing angles taking on an energy dependence. For simplicity, we will consider a two neutrino system. Incorporating matter effects, the Hamiltonian in the mass basis is [244]

$$H^i_m = \frac{1}{2E} \begin{pmatrix} m_1^2 + A\cos^2\theta & A\sin\theta\cos\theta \\ A\sin\theta\cos\theta & m_2^2 + A\sin^2\theta \end{pmatrix}, \tag{1.8}$$

Parameter	Value in 2002	Value in 2005
$\Delta m^2_{\odot}$	$7.2 \times 10^{-5}\ eV^2$	$8.3 \times 10^{-5}\ eV^2$
Δm^2_{atm}	$2.6 \times 10^{-3}\ eV^2$	$2.3 \times 10^{-3}\ eV^2$
$\sin^2\theta_{\odot}$	0.38	0.27
$\sin^2\theta_{atm}$	0.50	0.50
$\sin^2\theta_{13}$	< 0.09	< 0.05

Table 1.2: Status of neutrino oscillation parameters from Super-Kamiokande (SK), K2K, KamLAND, (KL), CHOOZ and solar and atmospheric neutrino experiments. The second and third columns show the measured values of the parameters in 2002 [140] and 2005 [142] respectively.

where A, embodying the matter effects, is $A = 2\sqrt{2}EG_FN_e$ with G_F the Fermi constant and N_e the electron number density. The oscillation probability therefore becomes

$$P(\nu_\alpha \to \nu_\beta) = \sin^2 2\theta_m \sin^2 [\Omega L]\,, \tag{1.9}$$

where

$$\sin 2\theta_m = \frac{\Delta m^2}{4E}\frac{\sin 2\theta}{\Omega}, \tag{1.10}$$

with

$$\Omega = \frac{\Delta m^2}{4E}\sqrt{\left[\left(\frac{A}{\Delta m^2} - \cos 2\theta\right)^2 + \sin^2 2\theta\right]}. \tag{1.11}$$

Again, we have set $c = \hbar = 1$.

1.4.2 Where we stand - the status of neutrino oscillations

Solar neutrino oscillations

The first indirect evidence for neutrino oscillations came from neutrinos created in the Sun. The standard solar model [58] describes the complex nuclear processes occurring in the Sun and from this, predictions of the solar neutrino flux may be extracted. Early experiments measuring the solar neutrino flux, such as Chlorine [90] and Gallium [15, 150], were sensitive to electron neutrinos only and reported a neutrino flux significantly less than that predicted by the standard solar model. More recently, the SNO [22, 23] experiment, which is sensitive to all neutrino flavours, showed the total solar neutrino flux agrees well with the predictions of the standard solar model but with an appreciable suppression of the electron neutrino flux. This

suppression is definitive evidence of neutrino oscillations from $\nu_e \to \nu_{\mu,\tau}$. The KamLAND experiment [111], which detects electron anti-neutrinos from nuclear reactors, reported a significant suppression in event rates thus corroborating the SNO results. The KamLAND data fits the oscillation picture very well, as shown in figure 1.10. Using data from these experiments, a global analysis in 2005 found the solar neutrino oscillation parameters $\Delta m^2_{21} = \Delta m^2_{\odot}$ and $\sin^2\theta_{21} = \sin^2\theta_{\odot}$ with high precision. These values are shown in table 1.2 with the parameter space shown in figure 1.11, both are taken from [142].

Atmospheric neutrino oscillations

Whilst the first indirect evidence for neutrino oscillations came from solar neutrinos, the first direct evidence came from atmospheric neutrinos. The Kamiokande [156], IMB [71] and Soudan [32] experiments reported a significant deficit in the expected $\nu_\mu : \nu_e$ ratio [33, 62, 157], which suggested oscillations from ν_μ to ν_τ but was not conclusive. In 1998, this changed when the Super-Kamiokande collaboration showed the muon neutrino flux had a zenith angle dependence [130,131], shown in figure 1.12, which implied a dependence upon path length. This was the first direct evidence that neutrinos oscillate from one flavour to another since the probability of oscillation is a function of the distance a neutrino travels (see the previous section). A summary of the values of the atmospheric neutrino oscillation parameters in 2002 and the present is given in table 1.2. In chapters 5 and 7 we examine the parameter space for neutrino oscillations when we include possible quantum gravity effects. Figure 1.13 shows the allowed parameter space from the Super-Kamiokande experiment for standard neutrino oscillations [49].

Three neutrino oscillations

The standard analysis of solar and atmospheric neutrino flux is done within the two neutrino approximation. However, in order to place values on Δm^2_{31} and $\sin^2\theta_{31}$, the data must be analyzed taking all three neutrino flavours into account. Experiments such as CHOOZ [47] and SNO [22, 23] are sensitive to all three flavours of neutrinos and are able to place values on these parameters. Table 1.2 again shows the present state of play and the values as they were in 2002.

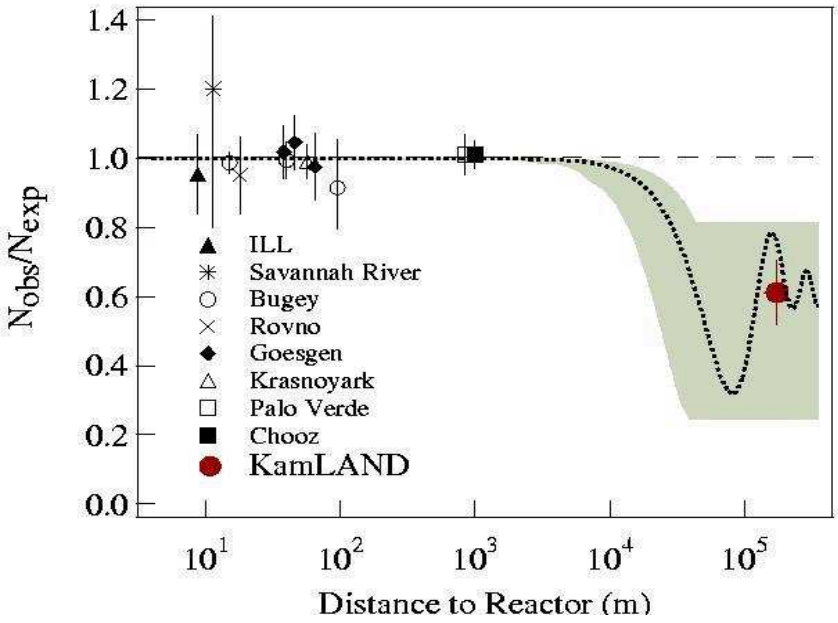

Figure 1.10: Comparison of KamLAND data and neutrino oscillations (taken from [111]).

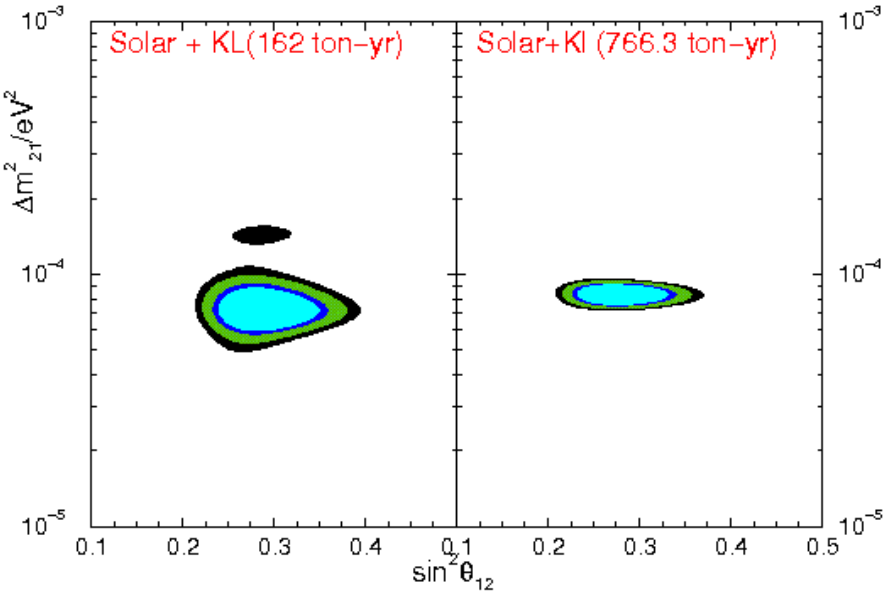

Figure 1.11: The solar neutrino oscillation parameter space. The frame on the left shows the global data plus data from KamLAND with 162 ton-years of data whilst the frame on the right shows the same plot but with KamLAND taking 766.3 ton-years of data (taken from [142]).

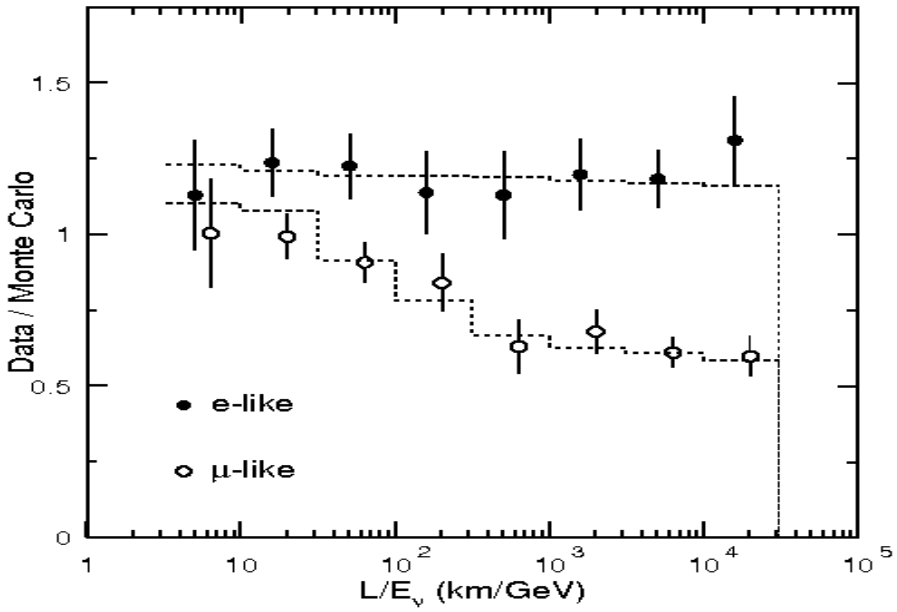

Figure 1.12: The first data from Super-Kamiokande showing a zenith angle dependence (taken from [130]).

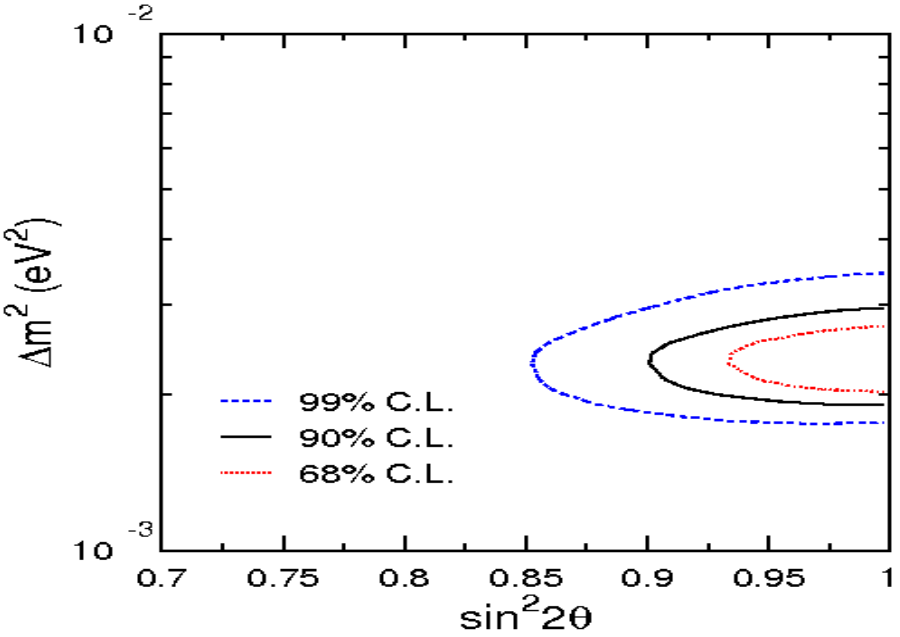

Figure 1.13: The region of allowed parameter space as found from the Super-Kamiokande experiment (taken from [49]).

The LSND result

It would seem from the discussion above that, give or take the precise values for the oscillation parameters, the neutrino oscillation situation is well understood. However, this is not entirely the case. The LSND experiment [53] produces a beam of neutrinos consisting of ν_e, ν_μ and $\overline{\nu}_\mu$ and then searches for the appearance of $\overline{\nu}_e$ that have oscillated from the muon anti-neutrinos. The outcome of this experiment cannot be reconciled with the solar and atmospheric neutrino oscillations as they found a mass difference which lies in the range $0.2 < \Delta m^2_{LSND} < 10\ eV^2$ [20]. If this result were corroborated by the miniBoone experiment [214], then it would provide indications of new physics, for in order to combine the LSND result with the atmospheric and solar oscillation results, one would have to invoke oscillations into sterile neutrinos or break CPT invariance. This latter possibility will be discussed in chapter 4.

Current and future neutrino experiments

In addition to those experiments already mentioned, there are a whole host of other experiments running or being planned, including:

K2K The K2K experiment [24] is a long baseline experiment. A beam of 12 GeV protons creates pions after interacting with an aluminium target at the High Energy Accelerator Research Organization (KEK) in Tsukuba city. The pions decay to muons and then muon neutrinos. The flux of neutrinos is measured at a near target in Tsukuba and also at the Super-Kamiokande detector, 250 km from the neutrino source to identify neutrinos of electron or tau flavours which have oscillated from the generated muon neutrinos.

T2K The T2K [163] experiment is somewhat similar to the K2K experiment and construction of the experiment is expected to be completed by 2009. In this case, a beam of 50 GeV protons will be created and used to generate an intense beam of muon neutrinos which travel to the Super-Kamiokande detector. The distance from source of the neutrinos to the far detector is 295 km.

MINOS The MINOS [225] experiment, due to start taking data imminently, is similar in design to the K2K and T2K experiments but the distance the neutrinos travel is much larger at 730 km. A beam of protons interact with a target of graphite or beryllium to produce pions. As in the K2K case, the MINOS

experiment has both a near and a far detector to quantify the appearance of neutrino flavours not in the original neutrino beam.

1.5 Summary

In this chapter, we have presented a brief overview of neutrino physics. We described the basic properties of the neutrino, including neutrino oscillations.

- We described how neutrinos were first postulated as a last resort to save the conservation of energy and momentum. We then described our present understanding of neutrinos and how they fit into the standard model of particle physics (section 1.1).

- We outlined the sources of neutrinos which will be important for our studies of quantum gravity. In particular, we are interested in neutrinos created in the Earth's atmosphere by the interactions of cosmic rays with atmospheric nuclei and those neutrinos created in astrophysical accelerators, such as GRBs (section 1.2).

- We described the processes by which neutrino telescopes detect neutrinos and outlined how, in principle, these experiments will be able to measure the flavour ratios of neutrinos via the combination of leptonic tracks, electromagnetic and hadronic showers. We then described the current status of various neutrino telescopes such as AMANDA and IceCUBE and described in more detail the ANTARES experiment (section 1.3).

- The phenomenon of neutrino oscillations was then considered. We outlined the formalism by which the probability of oscillation may be calculated and then described the current experimental situation (section 1.4).

The field of neutrino astronomy and astrophysics is a vast and very interesting one. However, in this thesis, we are interested in probing possible quantum gravity effects. Therefore, we have presented only an overview of the general processes which generate neutrinos in cosmic accelerators. We shall not concern ourselves with the details of these neutrino sources, rather, we shall simply be interested in the neutrinos generated. Of course, if a signal of quantum gravity were to be seen in a neutrino telescope, then we would have to be sure of the neutrino production process.

By considering the neutrinos generated in the Earth's atmosphere, we will show that neutrino telescopes will be able to place stringent bounds on quantum gravity effects in chapters 5 and 7. In chapter 8, we consider quantum gravity effects on neutrinos from astrophysical sources.

Chapter 2

Quantum gravity

At present, we have two supreme theories in fundamental physics. The first, general relativity, describes the gravitational interaction, whilst quantum theory, in the guise of quantum field theory, describes the strong, weak and electromagnetic interactions. In this chapter, we will begin with a brief overview of these two theories. We then move on to explain why a quantum theory of gravity is needed, why it is so difficult to develop and discuss the attempts that have been made to solve this problem. We finish this chapter by discussing the field of quantum gravity phenomenology.

Over the last thirty years, the subject of quantum gravity has grown immensely. There exists, therefore, a huge body of literature outlining many different approaches of quantum gravity. This chapter presents a short review but for more in depth overviews, see, for example, [52, 161, 168, 226].

2.1 Two successful theories

At the end of the nineteenth century, many physicists believed that they could describe the world around them and, with the exception of a few loose ends, all physical phenomena could be explained. However, at the beginning of the twentieth century, it soon became clear that this was not the case. In 1905, Einstein published papers on Brownian motion [115], the photo-electric effect [113] and the special theory of relativity [114]. The first of these theories provided evidence for the existence of atoms whilst the second showed that light was quantized. These two theories were, in essence, the birth of quantum mechanics. The special theory of relativity was subsequently generalized to describe gravity in the general theory of relativity [118].

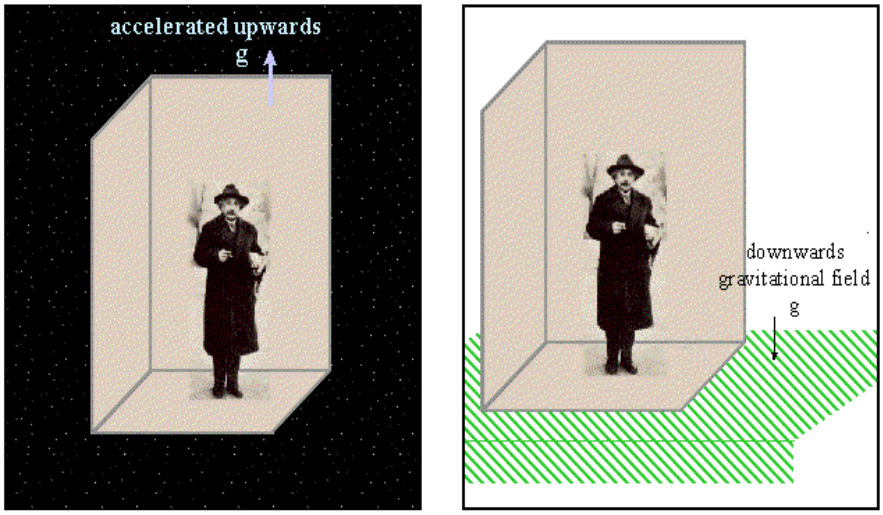

Figure 2.1: A diagrammatic illustration of the principle of equivalence. The situations shown in the left and right frames are experimentally indistinguishable (figure modified from [3]).

At present, both quantum mechanics and general relativity have been tested to great accuracy. In the following sections, we describe these two theories, their successes and their shortcomings.

2.1.1 General relativity

The theory of general relativity (GR) [118] is a classical theory which links gravity to geometry. Within GR, all observables are numbers or functions. The theory of GR is dependent upon two postulates:

- The speed of light is a constant in all reference frames.
- The equivalence principle. This assumes that freely falling frames can be assumed to be local inertial frames. An alternative way of stating this principle is that inertial mass and gravitational mass are identical. Figure 2.1 shows this principle diagrammatically.

Assuming these postulates are true leads to the Einstein field equations:

$$G_{\mu\nu} = \frac{8\pi G_N}{c^4} T_{\mu\nu}, \tag{2.1}$$

where $G_{\mu\nu}$ is the Einstein tensor and $T_{\mu\nu}$ is the stress-energy tensor. The classical Einstein tensor describes the geometry and curvature of space-time since it is made

up of the Riemann tensor, whilst the classical stress-energy tensor describes the matter and energy content of the space-time. So, the energy and matter content alters the geometry of the space-time and the geometry of the space-time affects the motion of matter. Essentially, matter tells space-time how to curve whilst space-time tells matter how to move. From a quantum gravity point of view, the key aspect of this theory of gravitation is the dynamical nature of space-time. It is not simply a stage upon which physical processes take place, rather, the space-time plays an integral role within these processes.

Experimental evidence

When GR was first published, it solved one long standing physical problem and predicted a new phenomena.

In the early twentieth century, the orbit of Mercury was puzzling. The perihelion, the point of closest approach of Mercury to the Sun, rotates around the Sun. Using Newtonian mechanics, the rotation of the perihelion had been calculated and, including perturbations from the other planets, and was found to differ from the measured value by 43" per century. Assuming a Schwarzschild metric [222], this value can be exactly accounted for using GR [117] and so provided the first experimental evidence for GR.

One of the first predictions Einstein made using GR was that light should be deflected by gravitational fields [116]. So, for example, light which passes close to the Sun will be deflected. This deflection could cause us to see multiple images of a single object which lies on the opposite side of the Sun. This prediction was observed in the solar eclipse of 1919 [110] and was the first GR phenomenon to be predicted before it was observed. The detection of this effect led to Einstein becoming an international celebrity. This effect is used in modern day astronomy and is termed gravitational lensing [215].

Since the early twentieth century, many other experiments testing general relativity have been performed and GR has passed with flying colours. However, one prediction of GR which has not yet been confirmed directly is the existence of gravitational waves [119], although they have been observed indirectly by considering in-spiralling binary pulsars [230]. It is expected that nearly all astrophysical objects emit gravitational radiation and the most violent ones, such coalescing black holes, would emit the most radiation. Many experiments, such as the VIRGO [16],

LIGO [167], TAMA [42] and AIGO [192] interferometers are looking for these waves but have not yet been successful. A new space based experiment, LISA [182], will be launched in 2015 and should have the required sensitivity to detect these waves if they exist. In addition to LISA, second generation interferometers, such as advanced LIGO [12], due to start taking data in 2013, are also being constructed. The detection of gravitational waves by ground or space based experiments will provide further experimental evidence that GR is the correct classical theory of gravity and open up a whole new area of astronomy.

The shortcomings of GR

The most obvious shortcoming of GR is that it is a purely classical theory, and so is readily applied to describing the gravitational interaction between planets, stars and the evolution of the universe itself, but is unable to describe how atoms fall. Of course atoms do fall under gravity and so the theory needs extending to include the quantum realm.

In addition, GR, to some extent, predicts its own downfall. When a large amount of matter collapses under its own gravity, a black hole may form, at the center of which lies a singularity. Here, classical physics, including GR, breaks down.

2.1.2 Quantum field theory

As the name suggests, quantum field theory (QFT) theory describes the remaining three interactions, the electromagnetic, the weak and the strong nuclear interactions, on quantum scales. These interactions are represented by the exchange of quanta, so, for example, the electromagnetic interaction between two electrons is mediated by a photon as shown in figure 2.2. Similarly, the weak interaction is mediated by the W and Z bosons with the strong interaction being mediated by gluons. The quantum field theories which describe these three interactions collectively form the standard model of particle physics. For an in depth overview of quantum field theory, see, for example, [146, 165, 186, 206, 238].

There are various ways to construct a quantum field theory, such as the path integral method [126] or the algebraic approach [55] but the one introduced in many text books in that of canonical quantization [146, 165, 186, 206, 238]. Utilizing this method, at least in flat space-times, one begins with a Lagrangian density from which an action may be defined. By varying this action, one is able to derive the

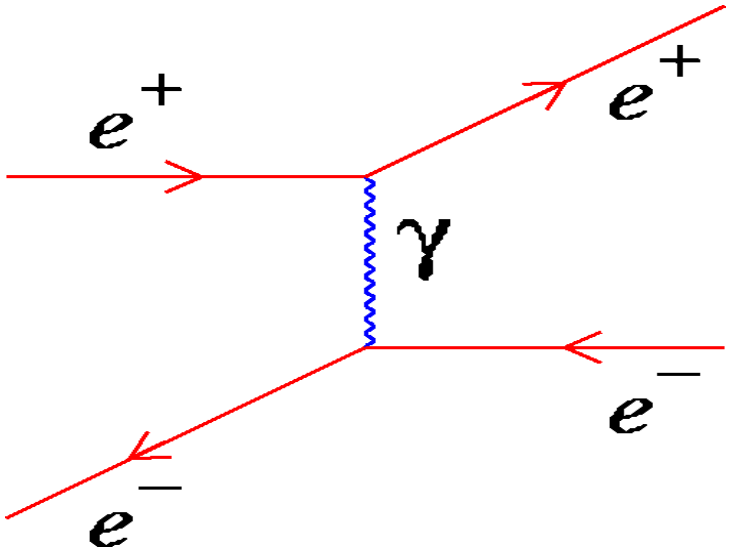

Figure 2.2: A feynman diagram showing electron-positron scattering. The force between the two particles is mediated by a photon (figure modified from [11]).

field equations. The solutions of these equations form a set of mode solutions which are defined to have positive frequency. By defining a scalar product with respect to these mode solutions and choosing an appropriate normalization, one obtains an orthonormal basis of solutions to the field equations. Expanding the solutions of the field equations and the corresponding canonical conjugate variable in terms of this orthonormal basis and, ensuring that the solutions satisfy relevant equal time commutation relations, promotes the measurable quantities to operators. This is one of the major differences between a classical theory and a QFT: in a classical theory, measurable quantities are represented by numbers or functions whilst those in a QFT are represented by operators. Once these operators have been defined, we are able to define a vacuum state from which particles may be created and subsequently destroyed.

In practice, QFTs often lead to infinities and physically meaningful results are only obtained after the process of renormalization [77, 93]. Renormalization is necessary as we, for example, do not measure the bare mass of an electron, rather we measure the bare mass plus all the possible internal interactions. By redefining these quantities, the theory becomes physically meaningful and predictive.

Experimental evidence

Unlike GR, which was formulated to include gravity into the relativity picture, QFT was formulated as a way to explain experimental results. However, as in every good

physical theory, it also leads to testable predictions. On particularly fine example of this is the anomalous magnetic moment of the electron, the famous $g-2$ experiment [94]. The magnetic moment of a charged lepton is given by $\boldsymbol{\mu} = g\mu_B \boldsymbol{s}$ where $s_z = \pm 1/2$. Using the Dirac equation, the quantity $g = 2$. However, using QFT, g is no longer exactly 2, there is an anomaly. The experimental measurement of this anomaly and the full QFT theoretical values are [95]:

$$\begin{aligned} a_{exp} &= 0.001159652209 \pm 31 \\ a_{th} &= 0.001159652411 + 166 \end{aligned} \tag{2.2}$$

where $2a = (g-2)$. There is an agreement between theory (at the three loop level) and experiment of 1 part in 10^8. Various other experiments have been performed, such as measuring the anomalous magnetic moment of the muon [95], which have verified the validity of quantum field theory.

Quantum field theory is the language of the standard model of particle physics, introduced in chapter 1. The success of the standard model is intimately related to the success of QFT.

2.2 A quantum theory of gravity?

We have seen above that we have two supreme theories which seem to describe nature to incredible accuracy. So, one could ask the question: why do we need a quantum theory of gravity? After all, we have no experimental indications for such a theory and we can describe the universe around us without such a theory. This may be the case, but there are some reasons to tackle this problem:

- From an aesthetic point of view, we would like to unify the force of gravity with the other three forces. After all, there is only one 'nature' and it seems strange that this entity would be described by two completely separate theories.

- Although the force of gravity is very weak compared to the other three forces in the world around us, there are regions of our universe where this is not the case, for example:

  - Black-holes are regions in which matter has collapsed to form objects so dense that not even light may escape. In these regions of space, gravity

is extremely strong and, if we want to know what quantum effects are taking place within the event horizon of a black hole, we need to be able to describe gravity on quantum scales.

- When the universe was very young, at times prior to the Planck time $\sim 10^{-43}$ seconds, space-time was folded up upon itself and so gravity was very strong. If we wish to know anything about the origin of the universe around us, we need to construct a quantum theory of gravity.

In both these cases, classically, a singularity is present - a region of space with infinite density. A complete theory of quantum gravity will be able to tell us if this is the case or if quantum effects inhibit the formation of true singularities.

What should quantum gravity tell us?

If we are to find a complete theory of quantum gravity, what form would we like it to take and what answers would we like it to provide? A full theory of quantum gravity must:

1. Describe nature at all scales;
2. Tell us if the postulates upon which quantum field theory and general relativity are built are true or whether they are in need of modification;
3. Describe what happens to the classical singularities which form in GR;
4. Describe the link between quantum theory, gravity and statistical mechanics. In particular, it must give us a derivation of the black hole temperature and entropy;
5. Describe the end state of black hole evaporation: do they totally disappear, leading to the loss of information; or does the evaporation lead to the leaking of information back into the universe; or do we end up with a black hole remnant which contains all the information trapped within it?
6. Give us predictions for the scattering of gravitons, the quanta of the gravitational interaction, with other quanta and themselves;
7. Describe how the classical theory of GR emerges from the full quantum theory.

In addition to answering these, and more, questions, we would expect a full theory of quantum gravity to:

- Be background independent in the same way as GR;
- Quantize space-time;
- Provide us with experimental tests with which to falsify the theory.

In the remainder of this chapter, we shall briefly review the current status of quantum gravity. We shall begin by considering what happens when we construct a quantum field theory on a curved space-time in order to highlight the difficulties of quantizing gravity.

2.2.1 QFT + GR

When we attempt to construct a quantum field theory on curved space-time, the initial generalization is usually straight-forward. However, there are important issues which need to be addressed. When we construct the mode solutions, how do we choose which coordinates to use, for example, time is observer dependent. Also, there is not always a time-like Killing vector, so how do we ensure the modes have positive frequency? Although we may perform renormalization, we find that there are still divergences in the vacuum expectation value of the stress-energy tensor. Finally, in QFT on flat space-times, we are only interested in differences of energy and the problem that the vacuum has infinite energy is resolved by normal ordering. When we move to curved space-times, since we are interested in the stress-energy tensor, absolute values of energy are important and this is infinite. The basic problems are, therefore, the definition of a suitable vacuum and the choice of the time coordinate. Although these issues are sizeable, there has been a large amount of progress in the construction of QFT on curved space-times.

Two key triumphs of this approach are due to Unruh [232] and Hawking [152]. The first of these, the Unruh effect [232], highlights the problem of which vacuum to choose. In this case, a stationary observer can define a vacuum (in Minkowski space, this is the same vacuum as in standard QFT) which, by definition is empty. However, an accelerating observer who considers the same vacuum will detect particles. So, a stationary observer and an accelerating observer disagree on the choice of vacuum. Experiments such as the ASTRA laser [9] are proposing to measure this

effect. Recently, however, there has been some controversy over whether this is a real effect which may be measured [128].

The second is the Hawking effect [152] which shows that, with respect to a stationary observer at infinity, black holes radiate thermally. This is a particulary important result as, in principle, it violates unitarity, since pure quantum states may evolve into mixed quantum states, a process we shall consider in chapter 4.

Although a large amount of progress has been made on constructing QFT's on curved space-times, these results remain semi-classical as we are applying quantum theories on fixed, classical backgrounds. A true quantum theory of gravity would describe quantum effects of space-time itself. There have been many attempts to unify quantum mechanics and general relativity but, so far, none have succeeded. These theories include twistor theory [204], non-commutative geometry [96], causal sets [108], quantum geometry [51] and condensed matter inspired models [177,234]. Here, however, we shall describe the two theories which, at the moment, are considered to be most promising, namely string theory and loop quantum gravity.

2.2.2 String theory

As the name suggests, string theory [161,195,221] considers extended objects, strings, to be fundamental rather than the point-like particles of the standard model. The theory was first constructed to explain the strong force but with the development of quantum chromodynamics, was discarded. However, the theory was resurrected when it was discovered that the theory naturally contained a massless, spin 2 particle: the graviton, and string theory as a theory of quantum gravity was born. In fact, string theory can be thought as a 'theory of everything' since, at least in principle, it has the potential to describe all four interactions on quantum scales.

At present, there are five different string theories which exist naturally in 10 or 26 dimensions and in order for the theories to be tachyon free, all the theories are supersymmetric [26]. The five theories may be classified by the form of the strings contained within them, since theories exist in which the strings are open or closed, so that they form loops. The five string theories [221] are known as type I, which contains both open and closed strings and type IIA, type IIB, heterotic $SO(32)$ and heterotic $E(8) \times E(8)$ which all contain closed strings only. There are some indications that these five theories are related and, in fact, are 10-dimensional representations of the final theory of quantum gravity, M-theory, which is 11 dimensional [240].

All the string theories above are examples of critical string theory as they are only mathematically consistent within critical number of dimensions, 10 or 26. Attempts to formulate string theory within just the four dimensions we observe led to theories known as non-critical string theories [102–104, 107, 123, 189]. The violation of CPT symmetry, which we shall discuss in chapter 4, is allowed within these theories.

In order for any of the critical string theories to describe the universe we observe, the extra dimensions must be hidden from our perception. There are two ways in which these extra dimensions are hidden, firstly, one may compactify these dimensions so they would only be observable on very small scales, of the order of the Planck length, secondly, one may force the extra dimensions to be large, so that the four space-time dimensions we see are embedded within this larger bulk [75, 176]. The standard model particles are confined to the four dimensional brane with gravitons allowed to propagate within the bulk. This leads to the quantum gravity scale being reduced from the Planck scale to energies of order $\sim$ TeV.

The successes of string theory

Some of the successes of string theory can be categorized as follows:

- Perhaps the main strength of string theory lies in the fact that it is a unified theory, in that it can describe all four of the fundamental interactions on a quantum scale. That we have a consistent theory that can do so is a great achievement.

- There are indications that string theory can describe the scattering of gravitons. The perturbation theory governing these interactions have been shown to be finite to the two loop level [105] and there are hints that the series is finite at all orders [46].

- Due to the relationship between the different types of string theories [136], the theory, in some cases, predicts a minimum length scale, hinting at the quantization of space-time. However, in other cases, this is not seen.

- String theory may be able to give us a description of quantum black holes. By considering near-extremal black holes, where the charge is approximately equal to the mass, the calculation of quantum numbers near these black holes agree exactly with semi-classical calculations [76].

- String theory may be able to provide an answer to the information loss paradox [154, 162, 185]. In all cases, the evolution of quantum states is shown to be unitary.

- Sting theory has provided predictions which may be tested experimentally. If large extra dimensions exist, then the scale at which quantum gravity effects become important may be $\sim TeV$, rather than the Planck scale. This leads to the predictions that black holes will be produced at the LHC [6] and their subsequent evaporation will produce an experimentally observable signature [109].

Open questions in string theory

Although great steps have been made in string theory towards finding a consistent theory which quantizes gravity, there still exist many open questions and issues:

- In string theory, the background is not dynamical. In fact, processes described by string theory, such as graviton propagation, take place on a fixed background in direct disagreement with the lessons we learned from GR.

- At present, there exist large numbers of string backgrounds and string theories and we have no indication which one will describe the universe we see around us. In addition, we have no way of knowing how to reduce the number of string backgrounds.

- String theory seems to be incompatible with a positive cosmological constant [241].

It seems, therefore, that there is much work to do, although some of the answers to the above concerns may be close. If an 11-dimensional M-theory is constructed which is consistent with the known string theories, then it may well be background independent. However, the issue of which string vacuum to choose and how to do this is more difficult. That some string theorists have begun to mention the anthropic principle [87] is perhaps worrying.

2.2.3 Loop quantum gravity

In contrast to string theory, loop quantum gravity [219] does not attempt to unify the four interactions, rather it is a program to quantize gravity. Due to this less

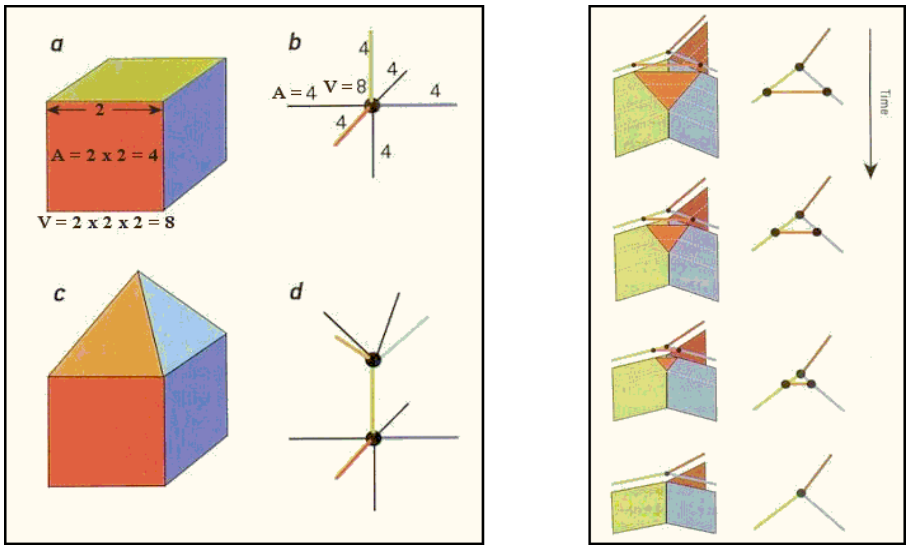

Figure 2.3: The left hand frame shows how volumes are represented in spin networks, the volume of the cube in figure (a) is represented by a point in figure (b) with the planes enclosing the volume represented by lines normal to the planes. The numbers represent the volume and areas in Planck units. Figure (d) shows the spin network for the volume in part (c). The right hand frame shows a spin foam, the evolution of a spin network in time (figures taken from [7]).

ambitious aim, loop quantum gravity is perhaps nearer completion than the string theory program. Loop quantum gravity relies on nothing more than GR and QFT. In addition, it is assumed that the theory will be background independent as in GR.

As we might expect, since it is based on GR, the theory is geometric. Loop quantum gravity has been constructed to describe space-time at the Planck scale and it has been found that space-time may be represented by a spin foam [57] with space being represented by a spin network [56]. A spin network simplifies the description of extended space by representing a volume with a node and the area which encloses the volume as a line perpendicular to the areas' face, as in the left frame of figure 2.3. The numbers in part (b) in the left hand frame of figure 2.3 represent the areas and volume of the cube in part (a) in units of the Planck length. By connecting many such volumes, we construct a spin network. The evolution in time of a spin network is known as a spin foam. These may again be represented diagrammatically, with the lines of the spin network becoming planes and the nodes representing the enclosed volume becoming lines. The right frame of figure 2.3 shows a spin foam where three volumes merge to become one. In this way, loop quantum gravity has made perhaps its largest achievement; it has quantized space-time and kept it a dynamical entity within the theory.

The successes of loop quantum gravity

Loop quantum gravity has made significant progress towards its goal of providing a quantum description of space-time. These achievements include:

- The fact that time and space are derived quantities rather than being defined.
- The quantization of space-time in terms of the Planck length. In actual fact, it turns out that the Planck length is less fundamental than areas and volumes [220]. Loop quantum gravity predicts that there is a fundamental limit to size of areas and volumes, processes cannot take place on smaller scales since smaller scales do not exist. Larger scales are built up from a number of these space-time quanta.
- A detailed quantum description of general black holes [50]. The entropy of black holes has been computed and found to agree with the semi-classical result and a derivation of Hawking radiation has also been performed [61,174]. In short, loop quantum gravity can reproduce and explain the thermodynamic properties of black holes.
- Predictions that may be tested experimentally, such as deviations from the usual dispersion relation, which result in the speed of light having an energy dependence, so higher energy photons travel faster than those with lower energy [29]. Similar modifications to dispersion relations are found for fermions [28,30].

It seems, therefore, that loop quantum gravity can claim to be a true quantum theory of gravity in that it can quantize and retain the dynamical nature of space-time. In addition, it provides concrete predictions which may be verified or ruled out by experiment.

Open questions in loop quantum gravity

Although the situation seems very promising for loop quantum gravity, there are still issues that need to be resolved before it can be accepted as a viable picture for the quantum nature of space-time [219]:

- It has yet to be shown that the low energy limit of loop quantum gravity is general relativity.

Questions	String theory	Loop quantum gravity
Theory describes nature at all scales	B	B
Postulates of QFT and GR need modifying?	A	A
Problem of classical singularities resolved?	B	B
Explains link between quantum theory, gravity and thermodynamics	B	A
Explains end product of black-holes	C	C
Gives predictions of graviton scattering	B	C
Emergence of GR in low-energy limit	A	B

Table 2.1: Summary of the current status of quantum gravity theories. A = solved, B = some results, C = work in progress.

- It remains to be seen if spin foam models of space-time have a suitable low energy limit.
- The inclusion of matter into loop quantum gravity is problematic.

Although this list of open questions is particularly short, the details are highly non-trivial. It may be some time, therefore, before a complete loop quantum gravity approach is formulated which may be applied to the universe.

2.2.4 Summary

There has been an impressive amount of progress in quantum gravity over the last twenty years and, though we are still some way from obtaining a consistent theory, many theorists are confident that it is close. The present status of string theory and loop quantum gravity, with respect to the questions posed in section 2.2, are shown in table 2.1.

It is the view of many that the final theory will have elements of both the theories above, for example, it may be that the final theory of quantum gravity will describe space-time in terms of quantum foam. However, one important aspect of these theories still eludes us; falsifiable predictions. For many years, experimental tests of quantum gravity were thought to be out of reach. However, this view has changed over the last five years. In the next section we describe why the original view was taken and how this was overturned.

Planck quantity	Constant content	Value
Energy	$\sqrt{\frac{\hbar c^5}{G}}$	$1.2 \times 10^{19}\ GeV$
Length	$\sqrt{\frac{\hbar G}{c^3}}$	$1.6 \times 10^{-35}\ m$
Time	$\sqrt{\frac{\hbar G}{c^5}}$	$5.4 \times 10^{-44}\ s$
Mass	$\sqrt{\frac{\hbar c}{G}}$	$2.2 \times 10^{-8}\ kg$
Temperature	$\sqrt{\frac{\hbar c^5}{Gk^2}}$	$1.4 \times 10^{32}\ K$

Table 2.2: Values of the Planck quantities and the combination of constants used to construct them, where c is the speed of light, $\hbar$ is Planck's constant, G is Newton's constant and k is Boltzmann's constant.

2.3 Quantum gravity phenomenology

For many years, the pursuit for a theory of quantum gravity was thought to be a solely theoretical one. This train of thought arose because the scales at which gravitational effects become important are far removed from those we see in experiments. We can estimate the relevant scales at which relativity, gravity and quantum physics merge by taking constants from each theory: namely the speed of light, c, from relativity; Newton's constant, G, from gravity; and Planck's constant, $\hbar$, from quantum theory; and combining them into quantities which have, for example, the dimensions of energy, length and time. The combinations of these constants and resulting values are shown in table 2.2. Consider the Planck energy, given by $E_p = \sqrt{\hbar c^5/G} \approx 1.2 \times 10^{19}\ GeV$, this an incredibly large energy which is out of reach of any current or planned terrestrial experiment. As a comparison, the LHC [125] which is currently being built at CERN will collide particles with a center of mass energy in the range of 1000 GeV. Since quantum gravity effects are expected to be suppressed by at least one order of the Planck energy, then it was considered that experimental tests of quantum gravity would not be possible.

Recently, however, this view has changed. By considering elements of the quantum gravity theories discussed in section 2.2, we can take these elements and examine the consequences they would have on experiments. Once again, there is a large body of literature on this subject, for an in depth overview of quantum gravity phenomenology, see, for example, [34, 36, 38–40]. To date, work on quantum gravity phenomenology has concentrated on two particular aspects of these theories.

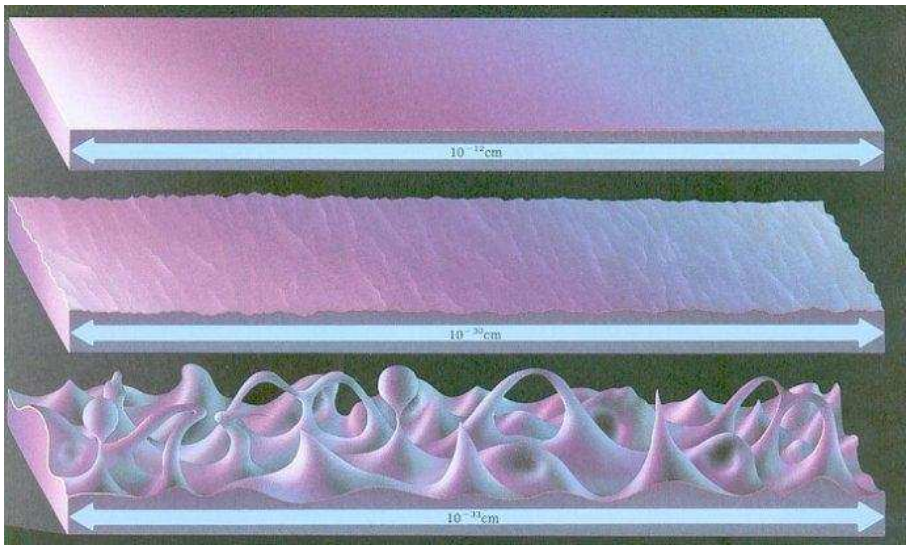

Figure 2.4: An artist's impression of space-time foam (taken from [7]).

2.3.1 Quantum decoherence

In 1974 [151, 152], Hawking showed that black-holes radiate thermally and, as we have seen above, to a certain extent, both string theory and loop quantum gravity have been able to reproduce this semi-classical result exactly. If we consider a pure quantum state which collapses to form a black-hole, then the pure state evolves into a mixed one since the final state is thermal. This evolution from pure to mixed states, known as quantum decoherence, is a process which is not allowed in standard quantum mechanics, as it violates CPT invariance, since unitarity is violated [228].

It has been suggested that space-time has a foamy nature due to quantum fluctuations, figure 2.4 shows an artist's impression of this space-time foam. If this is the case, then particles travelling through space will interact with quantum fluctuations of the gravitational field, in the form of quantum singularities. These virtual black-holes conserve mass, angular momentum, charge but violate quantum numbers such as lepton or baryon number. Through interactions with these black-holes, a particle may 'forget' its initial flavour. Therefore, a particle of one flavour at early times may be seen as a particle of different flavour at late times. This interaction may lead, for example, to proton decay, since one of the quarks in the proton may change into a lepton. Although these effects are expected to be very small, they may be cumulative and so particles travelling large distances may exhibit quantum gravity related phenomena. We shall describe this process in more detail in chapter 4 and examine how neutrinos will be able to used as probes to look for these effects in

chapters 5 and 8.

2.3.2 The violation of Lorentz invariance

Both string theory and loop quantum gravity suggest the existence of a fundamental length scale. Theoretically, this is expected to be the Planck length. If this is the case, then this would suggest modifications to Lorentz invariance [35, 173].

If a fundamental length scale does exist, it throws up an immediate question; in which reference frame is the length considered to be fundamental? If we were able to perform an experiment to measure this length in one reference frame and then considered a length in a different frame, we would naively expect the measurements to differ due to Lorentz contraction. There are three options with which to resolve this issue, the first is that the Lorentz transformations hold at the Planck scale and so quantum gravity has no preferred frame. The second option is that Lorentz transformations do not hold at the Planck scale, as in the case of the standard model extensions which extend the standard model of particle physics to include all operators that break CPT [91] and Lorentz invariance [92]. The third case of interest leads to the deformation of the Lorentz transformation, as in doubly special relativity [37]. In this case, the transformations contain the Planck length as an invariant in much the same way that the speed of light is invariant. In the final two cases, this leads to modifications of the standard dispersion relation, $E^2 = p^2 + m^2$. Deviations from the norm may then be probed for. In chapter 6 we describe the theory behind this in more detail and examine what neutrinos can tell us about the violation of Lorentz invariance in chapters 7 and 8.

2.4 Summary

In this chapter, we outlined the motivation for, and gave a brief status report on, the subject of quantum gravity:

- We began the chapter by describing the two cornerstones of modern physics: general relativity and quantum field theory. In both cases, we presented experimental evidence showing that the theories are able to describe nature to very high precision (section 2.1).

- We then asked the question 'why do we need a theory of quantum gravity?',

after all, we have not one shred of experimental evidence which indicates that we need the theory. We described situations in which the theory would be applicable and outlined the questions which it should address. We then described some of the problems encountered when attempting to quantize gravity and outlined the two leading approaches to quantum gravity, namely string theory and loop quantum gravity (section 2.2)..

- Finally, we described quantum gravity phenomenology. We considered why this approach was not taken before and described some of the considerations by which this reasoning was overturned. We focused on two particular modifications to standard physics, namely quantum decoherence and Lorentz invariance violation, since these are the phenomena we shall concentrate on in the remainder of this thesis (section 2.3).

At the present moment, we have no complete theory of quantum gravity and, although there are two theories leading the way, there exist many other approaches we haven not considered here. The question is, therefore, which theory, if any, is taking the correct approach? Perhaps the theoretical approach is simply too difficult without guidance from experiment. Therefore, quantum gravity phenomenology can provide an invaluable guide towards the construction of the final theory.

However, since no theory of quantum gravity has provided us with any concrete experimental predictions, this makes looking for quantum gravitational effects very difficult, after all, how do we even know what to look for! Therefore, in order to perform quantum gravity phenomenology, we must use our physical intuition in order to identify any possible new quantum gravitational effects.

This is precisely the methodology embraced within this thesis. We concentrate on two particular modifications of standard physics which may arise due to quantum gravity effects, namely the violation of CPT invariance in form of quantum decoherence and the violation of Lorentz invariance. We concentrate on the effects that quantum decoherence could have on atmospheric neutrinos in chapters 4 and 5 and consider the effects Lorentz violation could have on the same system of neutrinos in chapters 6 and 7. We consider the effects of both of these modifications on neutrinos which originate in astrophysical objects in chapter 8.

Chapter 3

Simulations of atmospheric neutrino oscillations and ANTARES

In this chapter, we present the numerical methods we use to place upper bounds on possible quantum gravity effects in chapters 5 and 7. We present a brief description of the *OSCFIT* neutrino oscillation software package and show how we modified the package to include quantum gravity effects. We present plots for the case of standard neutrino oscillations to outline the kind of output we expect from the software package and for comparison with our results in later chapters.

3.1 The *OSCFIT* package

In order to examine the effects quantum gravity may have on the atmospheric neutrino flux and to enable us to place bounds on the quantum gravity model parameters, we turn to numerical methods. Here, we outline the basic ideas behind these numerical methods and sketch an outline of the *OSCFIT* package.

3.1.1 Overview

The *OSCFIT* package [80–82] was originally written to show that the ANTARES detector would be able to measure the standard oscillation parameters from the detection of atmospheric neutrinos. The package reads in simulated 'data' and bins this data so we are able to extract spectra: number of events as a function of zenith

angle and neutrino energy. Once these simulated spectra have been constructed, they are then compared to theoretical expectations to construct both sensitivity and measurement contours. Due to the speculative nature of the quantum gravity effects we are considering in this thesis, we shall concentrate just on sensitivity contours which show the region of parameter space in which the model parameters are consistent with the data compared to the situation of no oscillations. In this section, we expand on these points and explain how we modified the package to include quantum gravity effects.

Event generation

Until the ANTARES detector is completed and taking data, the only thing we can do is simulate the type of events which will be seen. The *OSCFIT* package comes complete with a data file containing such events called *in/3dall.dat*. The events were generated assuming a spectrum of $\Phi \sim E_\nu^{-2}$ for interacting neutrinos. If we assume a different spectrum, the results presented here may be altered. The simulations were performed for neutrinos lying in the energy range $10\ GeV < E_\nu < 1\ TeV$. By measuring neutrinos in this energy range, we can be sure that the neutrinos are atmospheric in origin as we would expect neutrinos from astrophysical sources to be of much higher energies. Event weights are used to to adapt the Monte Carlo to a real atmospheric neutrino flux and we used the Bartol theoretical flux [133] although we do not anticipate the results of the simulations altering significantly if an alternative theoretical flux is used. The flux is also normalized, with the total normalization being left as a free parameter. Our sensitivity results, presented in chapters 5 and 7, are, therefore, independent of this normalization. The input file contains a total of 94411 events which corresponds to 25 years of data taking, meaning that error from Monte Carlo statistics can be safely ignored. All data in the file is assumed to have been 'detected' by the detector consisting of 14 strings and 1260 PMT's.

Spectra production

Once the 'data' file has been read, the data is then binned depending upon which observable we wish to examine (see below). By entering various values of the oscillation parameters in the code, we are able to produce plots of the spectra expected for those values of the parameters. These spectra are simply the number of events in each bin as a function of the observable. The oscillation parameters alter the number

of events in each bin and we are able to examine the expected number of events and the shape of the spectrum for particular values of the oscillation parameters.

Oscillation analysis

In order to construct sensitivity contours, we use a χ^2 analysis, where we consider an observable x which depends upon the oscillation parameters. We fit these parameters by minimizing a χ^2 which we construct by varying the oscillation parameters with

$$\chi^2 = \sum_i [x_i - r * P_i]^2 / \sigma_i^2. \tag{3.1}$$

Here, x, introduced above, is the measured number of events, affected by oscillations, contained within bin i, the quantity P is the number of events expected from Monte Carlo simulations (which is dependent upon the neutrino oscillation survival probability), with r a normalization and σ representing the errors of the measured values. In order to include quantum gravity effects into the *OSCFIT* package, we need to modify the χ^2 analysis. We present this modification in section 3.2.

The errors in the measured number of events are considered to be Gaussian. We may also add a systematic error if we wish, so

$$\sigma_i = \sqrt{x_i + \sigma_{sys}^2}. \tag{3.2}$$

Throughout this thesis, we shall assume no systematic errors, so $\sigma_{sys} = 0$.

'Real' data

The quantity x in equation (3.1) is supposed to represent real data. However, since the detector is not yet built, we must simulate this as well. To do this, we calculate the expected number of events per bin and then smear this number assuming a Gaussian distribution. The errors bars on the data points are then given by the equation (3.2) with $\sigma_{sys} = 0$.

Confidence levels

Throughout this thesis, we present sensitivity contours at the 90% and 99% confidence levels. For a more detailed explanation, see section 3.2. We obtain output as a function of $\sin^2 2\theta$, where θ is the neutrino mixing angle. However, the code simply

finds the point of best fit for a given parameter and this may may include unphysical values of $\sin^2 2\theta$, that is, we find values of $\sin^2 2\theta$ not contained in the region $[0, 1]$. All the plots we we present, however, do respect these physical bounds.

Observables

The oscillation probability depends upon the path length and the neutrino energy. In addition, an oscillation pattern has been observed in the atmospheric neutrino spectrum in the zenith angle distribution and the quantity E/L in the Super-Kamiokande [49], KamLAND [48] and K2K [31] experiments and so we consider two observables, the first being the zenith angle.

The path length, L is dependent upon the zenith angle:

$$L = \sqrt{R^2 - (R-h)^2 \sin^2 \vartheta} + (R-h)\cos\vartheta, \tag{3.3}$$

where $R = 6378\ km$ is the Earth's radius, with $h = 10 - 20\ km$, the height above the Earth's surface at which the neutrino is created, and ϑ is the zenith angle, where $\vartheta = 0$ corresponds to a neutrino travelling vertically upwards. As we pointed out in chapter 1, neutrino telescopes point downwards to minimize the background from cosmic rays, so if we limit the zenith angle to upward going neutrinos only and make the assumption $R >> h$, then equation (3.3) becomes

$$L \approx 2R\cos\vartheta. \tag{3.4}$$

So, up to a factor of $2R$, the path length is equivalent to the cosine of the zenith angle. When we come to present the spectra of events, we shall therefore show them as functions of the neutrino energy and the cosine of the zenith angle rather than the path length.

The second observable we consider is E/L. As we saw above, the path length is directly related to the zenith angle and so, rather than take E/L to be our observable, we shall take $E/\cos\vartheta$.

It is also possible to construct spectra with the neutrino energy, E, as the observable. However, ANTARES is much more sensitive to the zenith angle than the neutrino energy and so we do not consider this observable further.

directory	details		
src	4 main	*oscexc.f*	- produces sensitivity contours
	programs:	*oscfix.f*	- produce measurement contours
		oscfloat.f	
		oscthree.f	
	subroutines:	*initx.f*	- fills 'real' arrays
		readevents.f	- reads and processes 'data'
		stepx.f	- fills MC arrays for specific parameters
	functions	*delchi.f*	- provides $\Delta\chi^2$ for desired CL
		ibin.f	- finds bin for value of observable
inc		*ibin.inc*	- finds bin for value of observable
		xfit.inc	- stores data from *readevents.f*
in		*3dall.dat*	- data from Monte Carlo

Table 3.1: The file structure of the neutrino oscillation software package *OSCFIT*. Of the four main programs, *oscexc.f* produces sensitivity contours with the other three producing measurement contours.

3.1.2 Simulation methodology

Above, we presented some of the basics of the software package *OSCFIT*. Here, we outline the file structure of the package and describe the simulation methodology.

File structure

The *OSCFIT* package contains four files, *runexc, runfix, runthree* and *runfloat*, all of which compile and execute a program to create sensitivity and measurement contours. The first file generates sensitivity contours whilst the other three generate measurement contours for various normalizations, r (see equation (3.1)). Since we will only be interested in generating sensitivity contours, we shall only concern ourselves with the files called by *runexc*. The main file in *runexc* is *src/oscexc.f* and is located in a subdirectory along with utility files and functions. Table 3.1 shows the file structure in more detail.

Input/Output

In order to generate sensitivity contours, the program *src/oscexc.f* reads in Monte Carlo generated neutrino data which is located in *in/3dall.dat*. Here, each line refers to one event and contains both the 'real' and reconstructed neutrino energy and zenith angle. The data is read and processed by the subroutine *src/readevents.f*, and

stored in the common file *xfit.inc*. If we wish to change the observable, we do so in *src/readevents.f*. In addition to this necessary input, an optional random seed may also be included in order to calculate the fluctuations in the 'real' data to produce realistic data points. Further input parameters are located in the main file which include

- Confidence level.
- Number of years of data taking.
- Range of parameter space.

As output, the code writes a single ASCII file containing a list of parameters. For standard oscillations, we obtain a list of $(\log_{10}(\Delta m^2/eV^2)\ ;\ \sin^2 2\theta)$, the coordinates of a sensitivity contour. When we include quantum gravity effects with one extra parameter, we obtain a three rather than two dimension parameter space. In this case, to obtain sensitivity contours, we project the three dimensional sensitivity volume onto the coordinate planes and take the extremal points to define the sensitivity contour.

Simulation algorithm

Here, we describe the algorithm used within *src/oscexc.f* to generate the sensitivity contours. We shall describe the simple version for standard oscillations with no quantum gravity effects. In order to define the sensitivity contours, we define a region of parameter space in which we are interested for Δm^2 and divide it up into a number of discrete points. We define at the beginning of the code how many points into which to divide this range. A χ^2 minimization procedure, as we shall outline in section 3.2, is then used to calculate a value of $\sin^2 2\theta$ for each particular value of Δm^2. In more detail, the procedure is:

1. We begin by defining a range of points for the parameter Δm^2, in which we expect the parameter to lie, and also the density of points with which we scan this parameter. If the parameter does not lie within the range specified, then no meaningful results are obtained. When we include quantum gravity parameters, we also define ranges for these parameters. In addition, the confidence level, number of years of data taking and systematic error is also defined.

2. The subroutine *src/readevents.f* is then called and the Monte Carlo generated neutrino data is read, processed and stored.

3. We then loop over the number of parameter points:

   - We divide up the range Δm^2 into discrete points, dependent upon the number of parameter points defined.
   - The subroutine *src/chired.f* is then called, which first reads in the appropriate observable processed from *src/readevents.f* and decides the appropriate bin number. This event is then added to both the non-oscillation and oscillation distributions with a suitable event weighting. In this way, we may extract spectra for the relevant observable.
   - The quantity χ_0^2, which is found using a χ^2 minimization procedure (see section 3.2), is then calculated and returned to the main program.

4. A value for the parameter $\sin^2 2\theta$ is then found for this particular value of Δm^2 using the calculated value of χ_0^2.

5. The coordinates $(\log_{10}(\Delta m^2)\ ,\ \sin^2 2\theta)$ are then written to an ASCII file

For standard neutrino oscillations with 1200 points, the code takes around 30 seconds to run. When we include an additional parameter, the code takes around two and a half hours to run for 400 points on the Linux HEP cluster in the Department of Physics and Astronomy at the University of Sheffield.

3.2 Oscillation analysis

In the previous section, we described the structure of the neutrino oscillation package *OSCFIT* and gave an overview of the simulation algorithm. A critical step in the algorithm is the calculation of the quantity χ_0^2, which is found from the non-oscillation and oscillation distributions. Here, we show how we arrive at the expression for χ_0^2 in the code. In subsequent chapters we include quantum gravity effects which significantly alter the neutrino oscillation probability and this alters the expression for χ_0^2. Here, we shall present our calculation of χ_0^2 for the most general oscillation probability which includes these new physical effects.

In order to construct sensitivity contours, the *OSCFIT* package minimizes χ^2 differences and tests whether the condition

$$\chi^2 > \chi^2_{cont} = \chi^2_{min} + \Delta\chi^2, \tag{3.5}$$

is satisfied. The sensitivity contour is then constructed from all the points which satisfy this condition. The quantity P_i, in equation (3.1), is dependent upon the neutrino survival probability. As we shall see in chapters 4 and 6, the general form of the oscillation probability for two neutrinos takes the form

$$\begin{aligned} P[\nu_a \to \nu_b] &= \frac{1}{2}\left\{\cos^2 2\theta\,[1 - M_{33}(E,L)] + \sin^2 2\theta\,[1 - M_{11}(E,L)]\right. \\ &\quad \left. -\frac{1}{2}\sin 4\theta\,[M_{13}(E,L) + M_{31}(E,L)]\right\}, \end{aligned} \tag{3.6}$$

where θ is the mixing angle and the M's, which are functions of the neutrino energy, E, and path length, L, contain the standard oscillation and quantum gravity parameters. Therefore, we may write the quantity P_i in equation (3.1) as

$$\begin{aligned} P_i &= \sum_j \left[1 - \frac{1}{2}\left\{\cos^2 2\theta\,[1 - M_{33}(E_j,L_j)] + \sin^2 2\theta\,[1 - M_{11}(E_j,L_j)]\right.\right. \\ &\quad \left.\left. -\frac{1}{2}\sin 4\theta\,[M_{13}(E_j,L_j) + M_{31}(E_j,L_j)]\right\}\right] \omega_j(E,L), \end{aligned} \tag{3.7}$$

where we sum over j, the number of events in bin i, and the quantity $\omega_j(E,L)$ is the statistical weight of the event. Defining

$$\begin{aligned} e_i &= \sum_j \omega_j, \\ f_i &= \frac{1}{2}\sum_j [1 - M_{11}(E_j,L_j)]\,\omega_j(E,L), \\ g_i &= \frac{1}{2}\sum_j [M_{33}(E_j,L_j) - 1]\,\omega_j(E,L), \\ h_i &= \frac{1}{2}[M_{13}(E_j,L_j) + M_{31}(E_j,L_j)]\,\omega_j(E,L) \\ t &= \sin^2 2\theta, \end{aligned} \tag{3.8}$$

we may write equation (3.1) as

$$\chi^2 = \sum_i [x_i - re_i + rt(f_i + g_i) - rg_i - \sqrt{t(1-t)}h_i]^2/\sigma_i^2. \tag{3.9}$$

In the same way, we also express our data sample, x_i, in terms of oscillation and non-oscillation parts:

$$x_i = x_{0i} - s(z_i + y_i) + y_i + \sqrt{s(1-s)}q_i, \tag{3.10}$$

where the expressions for q, y and z are analogous to those in equation (3.8):

$$\begin{aligned} z_i &- \frac{1}{2}\sum_j [1 - M'_{11}(E_j, L_j)]\,\omega_j(E, L), \\ y_i &- \frac{1}{2}\sum_j [M'_{33}(E_j, L_j) - 1]\,\omega_j(E, L), \\ q_i &- \frac{1}{2}[M'_{13}(E_j, L_j) + M'_{31}(E_j, L_j)]\,\omega_j(E, L) \\ s &- \sin^2 2\theta'. \end{aligned} \tag{3.11}$$

but the primed quantities now contain the true oscillation and quantum gravity parameters and s is equivalent to t but has a dependence upon the true mixing angle, θ'. We are interested in finding average sensitivity contours, which means that the non-oscillation part of the input data is simply given by the statistical weight of the data, this means that $x_{oi} = e_i$ and, since we are dealing with simulations, the minimum of χ^2 is found when the 'real' parameters are equal to the fitted parameters, so we have $\chi^2_{min} = 0$. Hence, χ^2 for the non-oscillation hypothesis is

$$\chi^2_0 = \sum_i [e_i - s(z_i + y_i) + y_i + \sqrt{s(1-s)}q_i - re_i]^2/\sigma_i^2. \tag{3.12}$$

Expanding this expression and defining the quantity

$$[ab] = \sum_i \frac{a_i b_i}{\sigma_i}, \tag{3.13}$$

Confidence level %	$k=1$	$k=2$	$k=3$	$k=4$
70	1.07	2.41	3.67	4.88
90	2.71	4.61	6.25	7.78
95	3.84	5.99	7.81	9.49
99	6.63	9.21	11.34	13.28
99.9	10.83	13.82	16.27	18.47

Table 3.2: Table showing the values of $\Delta\chi^2$ for various confidence levels and number of parameters, k (taken from χ^2 statistical tables).

gives

$$\begin{aligned}\chi_0^2 \;=\; & 2rs[ey] + 2rs[ez] + 2s^2[yz] + r^2[ee] + [yy] - 2s[yy] + s^2[yy] + s^2[zz] \\ & -2r[ee] + 2[ey] + [ee] - 2r[ey] - 2s[yz] - 2s[ey] - 2s[ez] \\ & +\sqrt{s(1-s)}\,[2[eq] - 2s[qz] - 2s[qy] + 2[qy] - 2r[eq] \\ & +\sqrt{s(1-s)}[qq]\Big] . \end{aligned} \tag{3.14}$$

Minimizing this expressions with respect to r, which we consider to be a freely floating parameter, we find

$$r = 1 - \left(\frac{s[ey] + s[ez] - [ey] - \sqrt{s(1-s)}[eq]}{[ee]} \right) . \tag{3.15}$$

Substituting equation (3.15) into (3.14) with $\chi_0^2 = \Delta\chi^2$, since we are finding average sensitivity contours and $\chi^2_{min} = 0$, we find

$$As^2 + Bs + C\sqrt{s^3(1-s)} + D\sqrt{s(1-s)} + E = 0, \tag{3.16}$$

with

$$\begin{aligned} A \;&=\; [eq]^2 - [ey]^2 - [ez]^2 + [ee][yy] + [ee][zz] - [ee][qq] + 2[ee][yz] - 2[ey][ez], \\ B \;&=\; [ee][qq] - [eq]^2 + 2[ey]^2 + 2[ey][ez] - 2[ee][yz] - 2[ee][yy], \\ C \;&=\; 2[ey][eq] + 2[eq][ez] - 2[ee][qz] - 2[ee][qq], \\ D \;&=\; 2[ee][qy] - 2[eq][ey], \\ E \;&=\; [ee][yy] - [ey]^2 - [ee]\Delta\chi^2. \end{aligned} \tag{3.17}$$

All the quantities in the brackets, [..], can be calculated within the *OSCFIT* package

and the quantity $\Delta\chi^2$ is found from standard χ^2 statistical tables, for the appropriate confidence level. These values are shown in table 3.2. Therefore, in order to calculate $s = \sin^2 2\theta$, with θ the true mixing angle, for one set of oscillation and quantum gravity parameters, we must solve equation (3.16). For the most general case, we employ a simple root solver method: the bisector method [211]. However, more commonly, the quantities M_{13} and M_{31} in (3.7) are zero. In this case, we are able to find an analytic solution of (3.16):

$$s = \frac{A' \pm \sqrt{B'\Delta\chi^2 + C'}}{D'}, \tag{3.18}$$

where

$$\begin{aligned}
A' &= [yy][ee] + [yz][ee] - [ey]^2 - [ey][ez], \\
B' &= [zz][ee]^2 + [yy][ee]^2 + 2[yz][ee]^2 - 2[ey][ez][ee] - [ey]^2[ee] - [ez]^2[ee], \\
C' &= [zz][ee][ey]^2 - [zz][ee]^2[yy] + [yz]^2[ee]^2 - 2[ey][ez][yz][ee] + [ez]^2[yy][ee], \\
D' &= [zz][ee] + [yy][ee] + 2[yz][ee] - [ez]^2 - 2[ey][ez] - [ey]^2.
\end{aligned} \tag{3.19}$$

If we loop over the fitted oscillation and quantum gravity parameters, then s determines the sensitivity curve.

3.3 Standard oscillation results

In order to compare the results we obtain when we include quantum gravity effects in chapters 4 and 6, we present the results for standard oscillations here. Figure 3.1 shows the spectra for standard oscillations. The histograms on the left of figure 3.1 show the number of neutrino events. The black line shows the expected spectrum for no oscillations, with the coloured lines showing the expected spectra for neutrino oscillations for various values of Δm^2. The 'data' points are those obtained by smearing the 'data' as outlined above for $\Delta m^2 = 2.6 \times 10^{-3}\ eV^2$ [140]. The frames on the right of figure 3.1 show the ratio of the expected spectra compared to the no oscillation scenario. The top frames show the spectra as functions of $E/\cos\vartheta$ whilst the bottom frames show the spectra as functions of the zenith angle only. The top right frame shows a distinct oscillation minimum between 10 and 100 GeV. At high values of $\cos\vartheta$, the difference between the curves in the bottom right frame

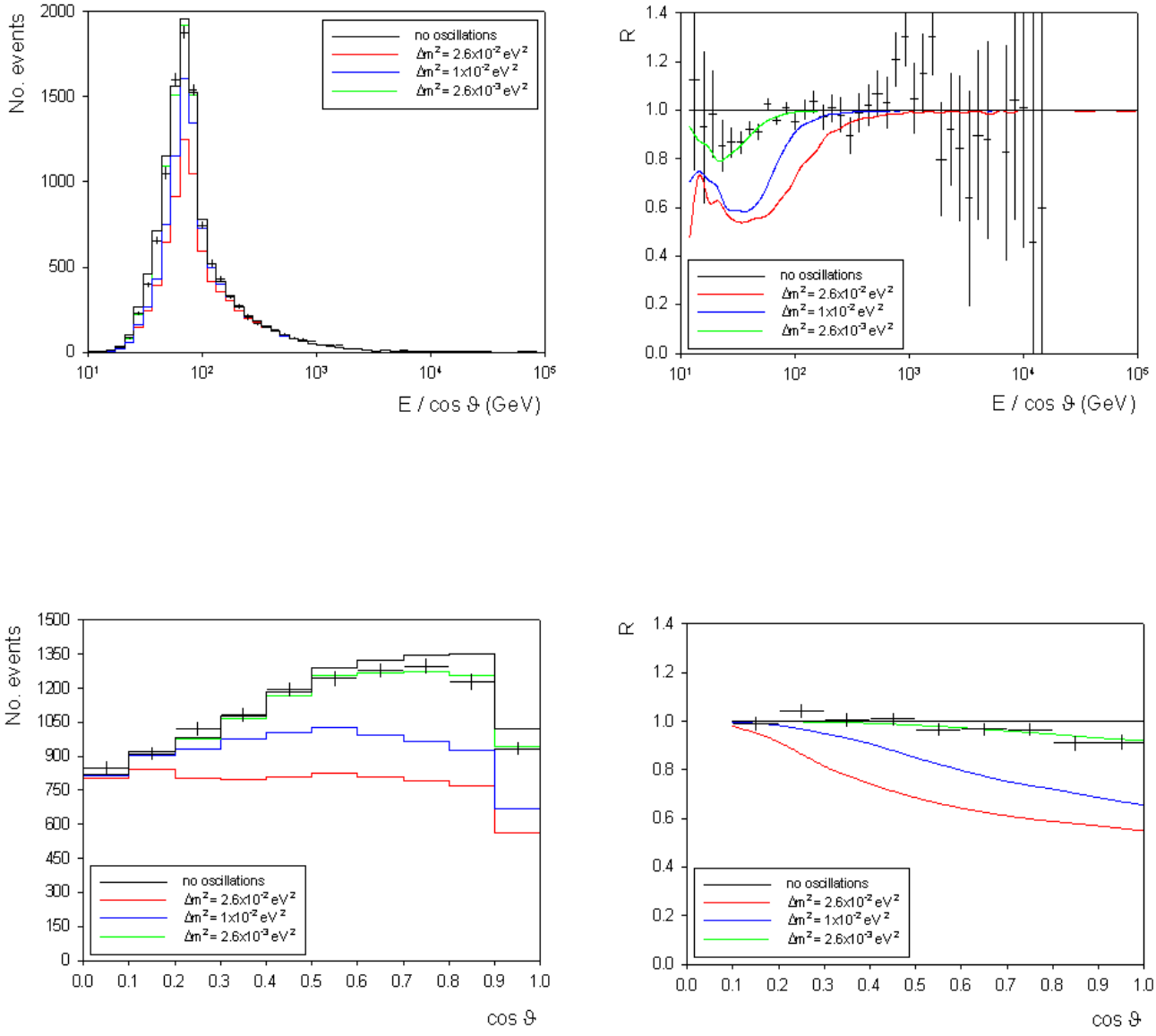

Figure 3.1: The spectra obtained for standard neutrino oscillations. The frames on the left show the number of events whilst those on the right show the ratio of the number of events expected when we include oscillations compared to the non-oscillation case. In all cases, the black lines show the non-oscillation spectra.

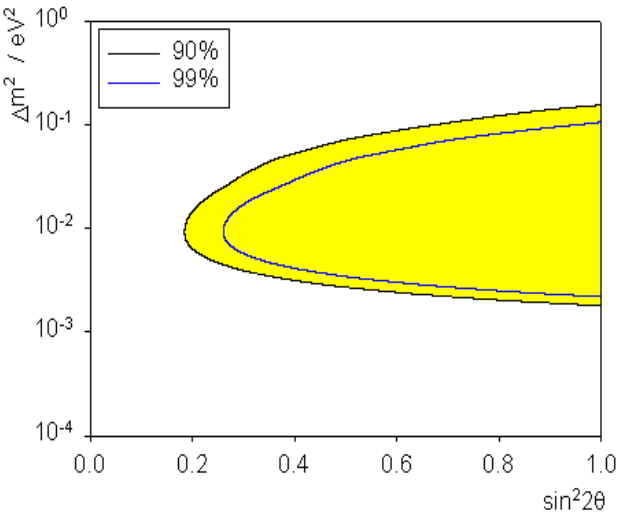

Figure 3.2: Sensitivity contours for standard oscillations at 90 and 99% confidence levels. The region compatible with the standard oscillations scenario lies within the contours, as highlighted in yellow, for the 90% confidence level.

is distinct and should enable us to measure Δm^2. The sensitivity region obtained from the *OSCFIT* package is shown in figure 3.2. The region which is compatible with neutrino oscillations at 90% confidence level lies inside the black contour, as highlighted in yellow, whilst the region compatible with neutrino oscillations at the 99% confidence level lies within the blue contour. Any points outside these regions are incompatible with the oscillation hypothesis.

3.4 Summary

In this chapter, we described in detail the *OSCFIT* software package which was originally written to study standard neutrino oscillations within atmospheric neutrinos.

- We began by giving an overview of the software package *OSCFIT*. We described the different types of output we are interested in, namely the spectra of events and sensitivity contours, and how they are generated. We also gave a detailed description of the file structure of the *OSCFIT* package and the basic algorithm for generating sensitivity contours (section 3.1).

- We showed how it is possible to modify the analysis utilized within the *OSCFIT* package to generate sensitivity contours for a more general oscillation probability than that for simply standard neutrino oscillations. We considered

a form of the oscillation probability which will be useful for us to examine quantum gravity effects within the system of atmospheric neutrinos (section 3.2).

- Finally, we showed an example of results generated from the *OSCFIT* package for the case of standard neutrino oscillations. We presented the spectra of events as functions of two different observables and showed how these spectra may be used to distinguish between the non-oscillation and oscillation scenarios. We also presented a plot showing the sensitivity contour for standard oscillations (section 3.3).

We shall utilize the methods and techniques described here when we examine how possible quantum gravity effects may manifest themselves within the atmospheric neutrino system. In chapter 5 we consider the case of quantum decoherence and the case of Lorentz invariance violation in chapter 7.

Chapter 4

Quantum decoherence - theory

In this chapter, we present the theory underlying the possible phenomenon of CPT invariance violation which arises due to quantum decoherence. We begin by describing the CPT theorem and how this theorem may be evaded. We then show how quantum decoherence effects may manifest themselves within the neutrino sector, at least for a two neutrino system, which we will use to place bounds on quantum decoherence parameters when we consider atmospheric neutrinos in the next chapter. We consider how these effects manifest themselves in a three neutrino system in chapter 8.

4.1 The CPT Theorem

The CPT theorem is a fundamental ingredient of quantum field theory in flat space-times [228]. The theorem ensures that the quantities appearing within these theories, such as the Hamiltonian and Lagrangian density, are invariant under the combined operations of charge conjugation (C), parity reflection (P), and time reversal (T). The CPT theorem holds in flat space-times provided the theory obeys [228]

- locality,
- unitarity,
- Lorentz invariance.

Deviation from any one of these requirements leads to CPT invariance violation (CPTV). It has been shown recently that CPTV also leads to the violation of Lorentz

invariance (LV) [143]. We shall consider the violation of Lorentz invariance in more detail in chapter 6.

4.1.1 Violations of CPT

The breaking of CPT symmetry, which we consider in this chapter, arises from the loss of unitarity leading to a phenomenon known as quantum decoherence. This loss of unitarity may arise due to the possible discrete nature of space-time or non-trivial topological effects. Therefore, we consider quantum decoherence as a phenomenon which violates the CPT theorem due to particles interacting with an environment with gravitational degrees of freedom. Since we, as observers, detect low energy degrees of freedom through scattering experiments, this may lead to an apparent loss of information from our point of view. In order to describe this non-unitary evolution, Hawking suggested a quantum gravitational modification to quantum mechanics [153], which is based on the density matrix formalism. Density matrices are used to describe the statistical state of a quantum system. For a mixed state, where the probability of the quantum system being in the state $|\Psi_j\rangle$, is p_j, the density matrix is given by

$$\rho = \sum_j p_j |\Psi_j\rangle\langle\Psi_j|. \tag{4.1}$$

This modification of quantum mechanics, suggested by Hawking, considers an initial quantum state which is described by a density matrix ρ_{in}. This state is then allowed to evolve into a final state ρ_{out}. These two density matrices are related:

$$\rho_{out} = \$\rho_{in} \tag{4.2}$$

with the operator $\$$ being the *super-scattering operator*. In standard quantum mechanics, this operator can be factorized as

$$\$ = \mathcal{S}\mathcal{S}^\dagger \tag{4.3}$$

where $\mathcal{S}$ is the usual S-matrix. In the case where the super-scattering operator is factorizable, this ensures pure states remain pure. However, in the case of quantum gravity, the super-scattering operator cannot be factorized, leading to the evolution of pure to mixed states.

To see why CPT is violated, at least in its strong form where we are unable to

define a CPT operator, by the non-factorizability of the super-scattering operator, we consider a proof due to Wald [235]. Suppose that a system is invariant under the CPT operator, Θ, and that equation (4.2) holds. By CPT invariance,

$$\rho_{in} = \Theta\rho'_{out} \tag{4.4}$$

for some out state, ρ'_{out}. Thus,

$$\rho_{out} = \$\Theta\rho'_{out}. \tag{4.5}$$

Acting on both sides with the CPT operator, Θ:

$$\Theta\rho_{out} = \Theta\$\Theta\rho'_{out}; \tag{4.6}$$

so, using

$$\Theta\rho_{out} = \rho'_{in}; \tag{4.7}$$

gives

$$\rho'_{in} = \Theta\$\Theta\rho'_{out}. \tag{4.8}$$

Since the Hilbert spaces of the primed and unprimed operators are the same, then equation (4.2) holds for both cases, thus

$$\rho'_{in} = \Theta\$\Theta\$\rho'_{in}; \tag{4.9}$$

which implies that there exists an inverse of the super-scattering operator, \$. However, this contradicts the proposal that the super-scattering operator is non-invertible and so the system is not CPT invariant. This is not the only possible situation, however. The CPT theorem may also be violated in its weak from by the existence of the super-scattering operator \$. In this case, although we may not be able to define a CPT operator, Θ, we may be able to define asymptotic in and out states.

The question remains, however, how does the existence of a quantum gravity environment lead to CPT violation and quantum decoherence? The topological nature of this environment may lead to the vacuum creation of quantum black-holes with event horizons having radii of order the Planck length, 10^{-35} m. This continuous creation and evaporation, through Hawking radiation, of these quantum singularities, results in space-time having a foamy nature. When particles pass by these

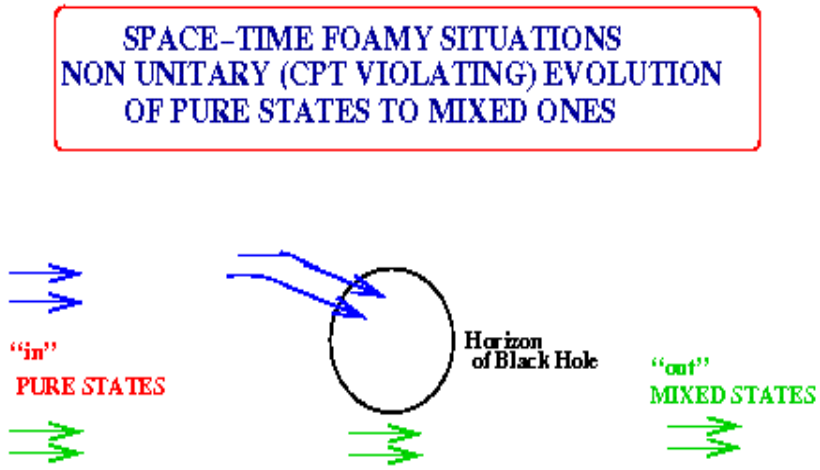

Figure 4.1: Schematic diagram of evolution from pure to mixed states (modified from [191]).

quantum black-holes, some of the particles' quantum numbers may be captured by these quantum singularities. With the evaporation of the black-holes, the captured information would be lost to the vacuum, inaccessible to low energy experiments. This loss of information results in initially pure quantum states evolving into mixed quantum states; a process forbidden within standard quantum mechanics. Figure 4.1 shows this process schematically. The pure state on the left of the figure travels through space and interacts with the environment. The environment absorbs some of the degrees of freedom, the blue arrows, resulting in the state being mixed on the right of figure 4.1.

Although, in principle, it is possible to use the super-scattering operator to examine the effects of quantum decoherence, we shall use an alternative; we shall, instead consider modifications to the time evolution of the density matrix. This method assumes only that pure states evolve into mixed states and so is independent of the source of quantum decoherence.

4.1.2 Modifications of quantum mechanics

Within standard quantum mechanics, the unitary evolution of the density matrix is governed by the equation

$$\dot{\rho} = -i[H, \rho]. \tag{4.10}$$

where ρ is the density matrix, the quantity H is the Hamiltonian of the system and the dot denotes differentiation with respect to time. If we allow pure states to evolve in to mixed states, then this equation may become [120]

$$\dot{\rho} = -i[H, \rho] + \delta\not{H}\rho. \tag{4.11}$$

In this case, the extra term $\delta\not{H}$ represents the most general linear operator which maps Hermitian matrices to Hermitian matrices. It may be that a full theory of quantum gravity predicts more complicated forms for this extra term, such as a polynomial in $\delta\not{H}$ or $e^{\delta\not{H}}$. Here, however, we consider the simplest modification of quantum mechanics. In order that this extension is physically meaningful, we impose various restrictions upon this extra term [120], namely

$$\mathrm{Tr}\rho = 1, \tag{4.12}$$

so that probability is conserved and

$$\mathrm{Tr}\rho^2 = 1, \tag{4.13}$$

so the entropy is always real.

From the discussion above, we now have an equation (4.11) which describes the time dependence of the density matrix when we allow pure states to evolve into mixed states. The obvious question to ask, therefore, is what form does the quantity $\delta\not{H}$ take? One particularly mathematically important form of this term is the Lindblad form [179], which ensures that the density matrix has complete positivity [141]. This ensures the density matrix is positive when coupled to a finite dimensional system. If complete positivity does not hold, then it may be that probabilities lose their physical meaning since they may not be positive definite in some regions of parameter space. However, in the case when complete positivity does hold, the term in (4.11) takes the form

$$\delta\not{H}\rho = \sum_j \left(\{\rho, D_j^\dagger D_j\} - 2 D_j D_j^\dagger \right) \tag{4.14}$$

where the operators D_j and $D_j^\dagger$ represent the system interacting with an environment and $\{...\}$ represents an anti-commutator. From a physical point of view, we may require that energy is conserved, on average, and that the von-Neumann entropy increases monotonically. In this case, we find that the D operators must be self-

adjoint and that they commute with the Hamiltonian. We therefore find

$$\delta \not{H} \rho = \sum_j [D_j, [D_j, \rho]]. \tag{4.15}$$

From a quantum gravity perspective, we would expect the operators, D, to be proportional to the inverse of the Planck mass and thus $\delta \not{H} \rho \propto M_p^{-2}$. In many of the models considered in this thesis, complete positivity [141] does not hold and so the extra term in equation (4.11) does not take the Lindblad form.

4.1.3 The theoretical status of quantum decoherence

We have seen that there is physical motivation for the violation of CPT and quantum decoherence. Here, we review the theoretical status of quantum decoherence.

Quantum decoherence in string theory

The evolution of mixed states into pure states, as described above, results in problems with defining an S matrix. Since string theory relies on the defining of S matrices, quantum decoherence is generally not expected within string theory. However, one class of string theories, namely non-critical string theories [102–104, 107, 123, 189], may allow decoherence. In this case, we find an analogous expression for the time evolution of the string matter density matrix as with equation (4.15) [191].

Quantum decoherence in loop quantum gravity

Whilst loop quantum gravity implies that space-time is discrete, there is no *a priori* reason to expect quantum decoherence. However, there have been proposals [134] suggesting that the discreteness of space-time may induce decoherence having the Lindblad form outlined above. However, it seems that there is still much work needed in order to clarify this.

Cosmological decoherence

In addition to quantum decoherence induced by space-time foam effects, it may be that decoherence arises from cosmological considerations. It is now established that the universe has entered a period of acceleration [205, 218] driven by some exotic dark energy. If this expansion continues, the universe will evolve into a de Sitter

universe, expanding at an exponential rate. This would imply the existence of a (future) cosmological horizon. This situation can be considered in the same way as that of the space-time foam except we, as the observers, now inhabit the space within the horizon instead of outside. The existence of this horizon would again lead to the inability to define S matrices, leading to decoherence. It has been argued in non-critical string theory, that this cosmological decoherence may be intimately linked with quantum gravity [190]. Considering a two level neutrino system, the cosmological decoherence parameter, γ_{cosmo}, is related to the cosmological constant, Λ, by [191]

$$\gamma_{cosmo} \sim \frac{\Lambda g_s^2 (\Delta m^2)^2}{E^2 M_s}, \tag{4.16}$$

where g_s is the weak string coupling, the quantity Δm^2 is the difference of the squares of the mass eigenstates, with E, the energy of the neutrino, and M_s the string mass scale.

4.2 Quantum decoherence in the atmospheric neutrino sector

In the last section, we saw how quantum decoherence, which may arise due to quantum gravity effects, alters the time evolution of quantum states. Here we consider how these effects manifest themselves within the atmospheric neutrino sector and so need only consider a system of two neutrinos, consisting of muon and tau flavours. We shall consider all three flavours of neutrinos when we examine quantum decoherence effects in astrophysical neutrinos in chapter 8. The mathematical outline presented here is not dissimilar to that applied to the neutral kaon system [120, 121] and ultra cold neutrons [66]. Throughout the following discussion we set c and $\hbar = 1$ and assume the neutrinos are travelling relativistically in order to identify t, the time, with L, the distance the neutrino travels.

In order to model the system of atmospheric neutrinos, we must implement equation (4.11). Whilst the equation looks non-relativistic, it can, in fact, be found from the dirac equation (see, for example, [98]) and so we are able to apply it to relativistic particles, such as neutrinos. To do this, we represent the quantities in equation (4.11) in a particular basis. We choose the basis which comprises the standard Pauli matrices. In terms of the Pauli matrices, the density matrix, Hamiltonian and $\delta\mathcal{H}$

may be written as

$$\rho = \frac{1}{2}\rho_\mu \sigma_\mu, \qquad H = \frac{1}{2}h_\nu \sigma_\nu, \qquad \delta\not{H} = \frac{1}{2}h'_k \sigma_k, \tag{4.17}$$

where the Greek indices run from 0 to 3 and a summation over repeated indices is understood. Using equation (4.11) we find

$$\dot{\rho}_\mu = (h_{\mu\nu} + h'_{\mu\nu})\rho_\nu, \tag{4.18}$$

where we have decomposed the time derivative of the density matrix in the same way as in (4.17):

$$\dot{\rho} = \frac{1}{2}\dot{\rho}_\mu \sigma_\mu. \tag{4.19}$$

Here, $\dot{\rho_\mu}$ is the time derivative of the quantities ρ_μ in (4.17). Standard neutrino oscillations are represented by h in equation (4.18) with the quantum decoherence effects being represented by h'. Using equations (4.12) and (4.13), we find the most general form of h' to be [120]

$$h' = -2\begin{pmatrix} 0 & 0 & 0 & 0 \\ 0 & a & b & d \\ 0 & b & \alpha & \beta \\ 0 & d & \beta & \delta \end{pmatrix} \tag{4.20}$$

where a, b, d, α, β and δ are real quantities parameterizing the quantum decoherence effects. Incorporating this matrix with that for standard neutrino oscillations, the time evolution of the density matrix becomes

$$\dot{\boldsymbol{\rho}} = -2\mathcal{H}\boldsymbol{\rho}. \tag{4.21}$$

where $\boldsymbol{\rho} = (\rho_0, \rho_1, \rho_2, \rho_3)^T$ and

$$\mathcal{H} = -2\begin{pmatrix} 0 & 0 & 0 & 0 \\ 0 & a & b-\omega & d \\ 0 & b+\omega & \alpha & \beta \\ 0 & d & \beta & \delta \end{pmatrix} \tag{4.22}$$

where $\omega = \frac{\Delta m^2}{4E}$ and Δm^2 is the difference in the square of the neutrino mass eigen-

states, with E being the neutrino energy. If we insist on conserving energy within the neutrino system, then $d = \beta = \delta = 0$.

Substituting (4.22) into (4.21), we find that the time evolution of the components of the density matrix obeys the following coupled differential equations:

$$\begin{aligned}
\dot{\rho}_0 &= 0; \\
\dot{\rho}_1 &= -2a\rho_1 - 2(b-\omega)\rho_2 - 2d\rho_3; \\
\dot{\rho}_2 &= -2(b+\omega)\rho_1 - 2\alpha\rho_2 - 2\beta\rho_3; \\
\dot{\rho}_3 &= -2d\rho_1 - 2\beta\rho_2 - 2\delta\rho_3.
\end{aligned} \tag{4.23}$$

In order to derive the neutrino oscillation probability, suppose that we, initially, have a muon neutrino and so at $t = 0$, the components of the density matrix take the values

$$\rho_0 = 1; \qquad \rho_1 = \sin 2\theta; \qquad \rho_2 = 0; \qquad \rho_3 = \cos 2\theta; \tag{4.24}$$

where θ is the neutrino mixing angle. We then integrate (4.23) with these initial conditions. The neutrino probability is found from

$$P[\nu_\mu \to \nu_\tau] = \mathrm{Tr}(\rho(t)\rho_\tau(0)), \tag{4.25}$$

with

$$\rho_\tau(0) = \begin{pmatrix} \sin^2\theta & -\frac{1}{2}\sin 2\theta \\ -\frac{1}{2}\sin 2\theta & \cos^2\theta \end{pmatrix}, \tag{4.26}$$

being the initial density matrix for a tau neutrino.

In general, the neutrino oscillation probability is given by [67]

$$\begin{aligned}
P[\nu_\mu \to \nu_\tau] = \frac{1}{2}\Big\{ &\cos^2 2\theta[1 - M_{33}(E,L)] + \sin^2 2\theta[1 - M_{11}(E,L)] \\
&- \frac{1}{2}\sin 4\theta[M_{13}(E,L) + M_{31}(E,L)]\Big\}
\end{aligned} \tag{4.27}$$

where the quantities $M_{11}(E,L)$, $M_{33}(E,L)$, $M_{13}(E,L)$ and $M_{31}(E,L)$ are functions of the neutrino energy, E and the path length, the distance the neutrino travels, L. The quantities M are defined as the elements of the matrix

$$M(E,L) = \exp[-2\tilde{\mathcal{H}}(E)L]. \tag{4.28}$$

where

$$\tilde{\mathcal{H}} = \begin{pmatrix} a & b-\omega & d \\ b+\omega & \alpha & \beta \\ d & \beta & \delta \end{pmatrix}. \tag{4.29}$$

In general, however, there exists no simple closed form solution to the differential equations in (4.23) and so in the next section, we shall consider a variety of special cases. In each case, we consider three possible forms of the quantum decoherence parameters which involve various dependences upon the neutrino energy (in models which have more than one quantum decoherence parameter, we assume that they have the same energy dependence):

1. The simplest model we consider is that when the quantum decoherence parameters have no dependence upon the neutrino energy. In this case, the quantum decoherence parameters have the form

$$\alpha = \frac{1}{2}\gamma_{\alpha}, \tag{4.30}$$

with similar expressions for the other quantum decoherence parameters.

2. We also consider the case in which the quantum decoherence parameters are inversely proportional to the neutrino energy:

$$\alpha = \frac{\mu_{\alpha}^2}{4E}. \tag{4.31}$$

This energy dependence has received the most attention in the literature to date [127,180] and results in the neutrino oscillation probabilities being Lorentz invariant. However, as we discuss in chapter 6, Lorentz symmetry may not hold at Planck scales.

3. The third model we consider is proportional to the square of the neutrino energy:

$$\alpha = \frac{1}{2}\kappa_{\alpha}E^2, \tag{4.32}$$

where κ_{α} is a constant. This model was suggested in [120] and also arises in some semi-classical considerations of quantum decoherence involving black-holes [124] and D-branes [122]. This energy dependence also arises due to discrete quantum gravity [134] and so, from a quantum gravity point of view,

this model is of most interest. From a dimensional point of view, the quantum decoherence parameter is proportional to the inverse of the Planck mass. This is somewhat unexpected as it corresponds to the existence of a non-renormalizable operator of dimension 5 [202]. From a natural point of view, we expect Newton's constant to appear in the action, therefore, we would expect parameters proportional to the inverse of the Planck mass squared.

It has also been suggested that quantum decoherence parameters may be proportional to [18, 188, 190, 191]

$$\frac{(\Delta m^2)^2}{E^2 M_p}, \tag{4.33}$$

but we have found that neutrino telescopes will have no appreciable sensitivity to quantum decoherence parameters which have this this energy dependence, as noted in [188].

4.2.1 Specific models of quantum decoherence

As we mentioned in the previous section, a simple closed solution of the differential equations in (4.23) does not exist in general. Therefore, we consider models which include quantum decoherence but in which we assume some parameters to be zero. In order to study different effects brought about as a consequence of quantum decoherence, we study different combinations of these parameters.

In the first class of models we consider, we set d and β to zero. This corresponds to the parameters $M_{13}(E, L)$ and $M_{31}(E, L)$ in (4.27) vanishing. The form of the quantities $M_{11}(E, L)$ and $M_{33}(E, L)$ are then found by solving the differential equations (4.23) directly. Solving the equations (4.23) with the assumption that the neutrino is initially a muon neutrino gives the components of the density matrix as

$$\begin{aligned}
\rho_0 &= 1; \\
\rho_1 &= e^{-(a+\alpha)L} \sin 2\theta \left[\cos(2\Omega L) + \frac{\alpha - a}{2\Omega} \sin(2\Omega L)\right]; \\
\rho_2 &= \frac{(\alpha - a)}{2(b - \omega)} e^{-(a+\alpha)L} \sin 2\theta \left[\cos(2\Omega L) + \frac{\alpha - a}{2\Omega} \sin(2\Omega L)\right] \\
&\quad + \frac{\Omega}{(b - \omega)} e^{-(a+\alpha)L} \sin 2\theta \left[\sin(2\Omega L) - \frac{\alpha - a}{2\Omega} \cos(2\Omega L)\right]; \\
\rho_3 &= e^{-2\delta L} \cos 2\theta;
\end{aligned} \tag{4.34}$$

where

$$\Omega = \left[\omega^2 - \frac{(\alpha - a)^2 + b^2}{4}\right]^{\frac{1}{2}}. \tag{4.35}$$

Using equations (4.25) and (4.26), we find the oscillation probability has the form (4.27) with

$$\begin{aligned} M_{11} &= \begin{cases} e^{-\Gamma_s}\cos\Gamma_1 & \text{if } a = \alpha; \\ e^{-\Gamma_s}\left(\cos\Gamma_2 + \frac{\Gamma_d}{\Gamma_2}\sin\Gamma_2\right) & \text{if } b = 0; \end{cases} \\ M_{33} &= e^{-2\delta L} \end{aligned} \tag{4.36}$$

where

$$\begin{aligned} \Gamma_s &= (\alpha + a)L; \\ \Gamma_d &= (\alpha - a)L; \\ \Gamma_1 &= 2\left[\left(\frac{\Delta m^2 L}{4E}\right)^2 - b^2L^2\right]^{\frac{1}{2}}; \\ \Gamma_2 &= 2\left[\left(\frac{\Delta m^2 L}{4E}\right)^2 - \frac{1}{4}(\alpha - a)^2L^2\right]^{\frac{1}{2}}. \end{aligned} \tag{4.37}$$

These equations contain two limits of interest. The first occurs when we set all the quantum decoherence parameters to zero, in this case, we recover the standard neutrino oscillation probability (1.7) when we replace c and $\hbar$. The second limit of interest occurs if we set the standard neutrino oscillation parameter, $\Delta m^2 = 0$. In this case, then atmospheric neutrino oscillations would be a purely quantum decoherence phenomena. Although it seems unlikely that this is the case given the widespread acceptance of the standard oscillation picture, analysis of existing data [127,180], found that this scenario was unfavoured but could not be completely ruled out. If we consider this scenario and set $\Delta m^2 = 0$ in (4.37), then it is clear that we must reduce the number of non-zero quantum decoherence parameters as we can only obtain a sensible oscillation probability if Γ_1 and Γ_2 are real. This requires $a = \alpha$ and $b = 0$. If we do not insist on these quantities being real, then the probability contains only damping terms and, given the success of the oscillation picture, we do not consider this possibility further in this thesis.

The second class of models we consider involves setting all the quantum deco-

herence parameters to zero except d and β. This violates energy conservation in the neutrino sector as the resulting form of $\delta\not{H}$ does not commute with the Hamiltonian. In this case, however, we cannot solve the differential equations (4.23) directly and we therefore utilize an alternative method.

The formal solution of equation (4.21) is

$$\rho(t) = e^{\mathcal{M}}\rho(0), \tag{4.38}$$

where $\mathcal{M} = -2\mathcal{H}$ and $\mathcal{H}$ is given by (4.29). If we find the eigenvalues of $\mathcal{M}$, call them λ_i, where $i = 1 \ldots 3$, then we may construct a diagonal matrix $\mathcal{M}'$ where

$$\mathcal{M}' = \mathrm{diag}(\lambda_1, \lambda_2, \lambda_3) = U^{-1}\mathcal{M}U, \tag{4.39}$$

where the matrix U is a transformation matrix which transforms from the non-diagonal basis to the diagonal basis. The columns of the matrix U consist of the corresponding eigenvectors of $\mathcal{M}$. Using the inverse transformation:

$$e^{\mathcal{M}t} = Ue^{\mathcal{M}'t}U^{-1}, \tag{4.40}$$

we find the components of the density matrix are given by

$$\rho_i(t) = e^{\lambda_j t}U_{ij}U^{-1}_{jk}\rho_k(0). \tag{4.41}$$

The oscillation probability is then found using (4.25), (4.26) and (4.41).

In the case at hand, we have

$$\mathcal{M} = -2\begin{pmatrix} 0 & -\omega & d \\ \omega & 0 & \beta \\ d & \beta & 0 \end{pmatrix}, \tag{4.42}$$

which has eigenvalues

$$\begin{aligned} \lambda_1 &= 0, \\ \lambda_2 &= 2i\Omega_{\beta d}, \\ \lambda_3 &= -2i\Omega_{\beta d}, \end{aligned} \tag{4.43}$$

where $\Omega_{\beta d} = \sqrt{\omega^2 - \beta^2 - d^2}$. The corresponding eigenvectors of $\mathcal{M}$ are

$$\begin{aligned}
\underline{\boldsymbol{v}}_1 &= \left(\frac{b}{\omega}, -\frac{d}{\omega}, 1\right)^T, \\
\underline{\boldsymbol{v}}_2 &= \left(\frac{\omega\beta - id\Omega_{\beta d}}{d^2+\beta^2}, \frac{-\omega d - i\beta\Omega_{\beta d}}{d^2+\beta^2}, 1\right)^T, \\
\underline{\boldsymbol{v}}_3 &= \left(\frac{\omega\beta + id\Omega_{\beta d}}{d^2+\beta^2}, \frac{-\omega d + i\beta\Omega_{\beta d}}{d^2+\beta^2}, 1\right)^T,
\end{aligned} \tag{4.44}$$

and so the matrix which diagonalizes $\mathcal{M}$ is

$$U = \begin{pmatrix} -\frac{\beta}{\omega} & \frac{-\omega\beta - id\Omega_{\beta d}}{d^2+\beta^2} & \frac{-\omega\beta + id\Omega_{\beta d}}{d^2+\beta^2} \\ \frac{d}{\omega} & \frac{\omega d - i\beta\Omega_{\beta d}}{d^2+\beta^2} & \frac{\omega d + i\beta\Omega_{\beta d}}{d^2+\beta^2} \\ 1 & 1 & 1 \end{pmatrix}, \tag{4.45}$$

having inverse

$$U^{-1} = \frac{1}{2\Omega_{\beta d}^2} \begin{pmatrix} 2\beta\omega & -2\omega d & 2\omega^2 \\ -\omega\beta + id\Omega_{\beta d} & \omega d + i\beta\Omega_{\beta d} & -(d^2+\beta^2) \\ -\omega\beta - id\Omega_{\beta d} & \omega d - i\beta\Omega_{\beta d} & -(d^2+\beta^2) \end{pmatrix}. \tag{4.46}$$

Using equations (4.41), (4.43)-(4.46), we find

$$\begin{aligned}
\rho_0 &= 1; \\
\rho_1 &= -\frac{\omega\beta}{\Omega_{\beta d}^2}\cos(2\theta) - \frac{\beta^2}{\Omega_{\beta d}^2}\sin(2\theta) + \frac{(\omega^2 - d^2)}{\Omega_{\beta d}^2}\sin(2\theta)\cos(2\Omega_{\beta d}t) \\
&\quad + \frac{\omega\beta}{\Omega_{\beta d}^2}\cos(2\theta)\cos(2\Omega_{\beta d}t) - \frac{d}{\Omega_{\beta d}}\cos(2\theta)\sin(2\Omega_{\beta d}t); \\
\rho_2 &= \frac{d\beta}{\Omega_{\beta d}^2}\sin(2\theta) + \frac{d\omega}{\Omega_{\beta d}^2}\cos(2\theta) - \frac{\beta d}{\Omega_{\beta d}^2}\sin(2\theta)\cos(2\Omega_{\beta d}t) \\
&\quad - \frac{\omega d}{\Omega_{\beta d}^2}\cos(2\theta)\cos(2\Omega_{\beta d}t) - \frac{\omega}{\Omega_{\beta d}}\sin(2\theta)\sin(2\Omega_{\beta d}t) \\
&\quad - \frac{\beta}{\Omega_{\beta d}}\cos(2\theta)\sin(2\Omega_{\beta d}t); \\
\rho_3 &= \frac{\omega^2}{\Omega_{\beta d}^2}\cos(2\theta) + \frac{\beta\omega}{\Omega_{\beta d}^2}\sin(2\theta) - \frac{\omega\beta}{\Omega_{\beta d}^2}\sin(2\theta)\cos(2\Omega_{\beta d}t) \\
&\quad - \frac{(d^2 + \beta^2)}{\Omega_{\beta d}}\cos(2\theta)\cos(2\Omega_{\beta d}t) - \frac{d}{\Omega_{\beta d}}\sin(2\theta)\sin(2\Omega_{\beta d}t). \qquad (4.47)
\end{aligned}$$

The oscillation probability therefore takes the general form of (4.27) with

$$\begin{aligned}
M_{11} &= \frac{(\omega^2 - d^2)}{\Omega_{\beta d}^2}\cos(2\Omega_{\beta d}L) - \frac{\beta^2}{\Omega_{\beta d}^2}; \\
M_{33} &= \frac{\omega^2}{\Omega_{\beta d}^2} - \frac{(d^2 + \beta^2)}{\Omega_{\beta d}^2}\cos(2\Omega_{\beta d}L); \\
M_{13} + M_{31} &= -\frac{2d}{\Omega_{\beta d}}\sin(2\Omega_{\beta d}L). \qquad (4.48)
\end{aligned}$$

This is the only model of quantum decoherence in which the quantities $M_{13}(E, L)$ and $M_{31}(E, L)$ are non-zero and, although both d and its square appear in this probability, since $\sin 4\theta \sim 0$ for atmospheric neutrinos, only d^2 can be measured directly with atmospheric neutrinos.

4.2.2 The physical content of quantum decoherence

In the last section, we showed how quantum decoherence effects, which may be a consequence of quantum gravity, could alter the atmospheric neutrino oscillation probability. Although we do not measure probabilities directly (we simply measure the number of neutrino events), examining the neutrino oscillation probability is useful as it can provide us with some physical insight into how these novel phenomena would affect the atmospheric neutrino system.

Standard neutrino oscillations

We begin by considering the oscillation probability for standard neutrino oscillations as a comparison. Restoring c and $\hbar$, the probability (1.7) becomes

$$P[\nu_\mu \to \nu_\tau] = \frac{1}{2}\left[1 - \cos\left(6.604 \times 10^{-3}\frac{L}{E}\right)\right]; \tag{4.49}$$

with the neutrino energy, E, measured in GeV and the path length, L, measured in km. Here, we have taken Δm^2 and $\sin^2 2\theta$ to have their best fit values [140]

$$\Delta m^2 = 2.6 \times 10^{-3}\ eV^2; \qquad \sin^2 2\theta = 1. \tag{4.50}$$

Figure 4.2 shows this probability as a function of path length for fixed energy with $E = 1\ GeV$ and $200\ GeV$ whilst figure 4.3 shows the probability as a function of the neutrino energy for $L = 10^4\ km$. Neutrino telescopes are sensitive to energies above $10\ GeV$ and so the plot in which we are particularly interested in has energies above this value. However, since atmospheric neutrino experiments have focused on energies lower than this, as the peak in the atmospheric neutrino spectrum is around $1\ GeV$, we have included lower values of the energy for comparison.

Quantum decoherence parameters with no dependence on the neutrino energy

Consider now the form of the neutrino oscillation probability when we include quantum decoherence effects. In order to illustrate these effects, we take values of the decoherence parameters from table 5.1 in chapter 5 except that we set $d = \beta = \delta = 0$ since these parameters have negligible effect on the neutrino probability.

We first consider the case when the quantum decoherence parameters have no

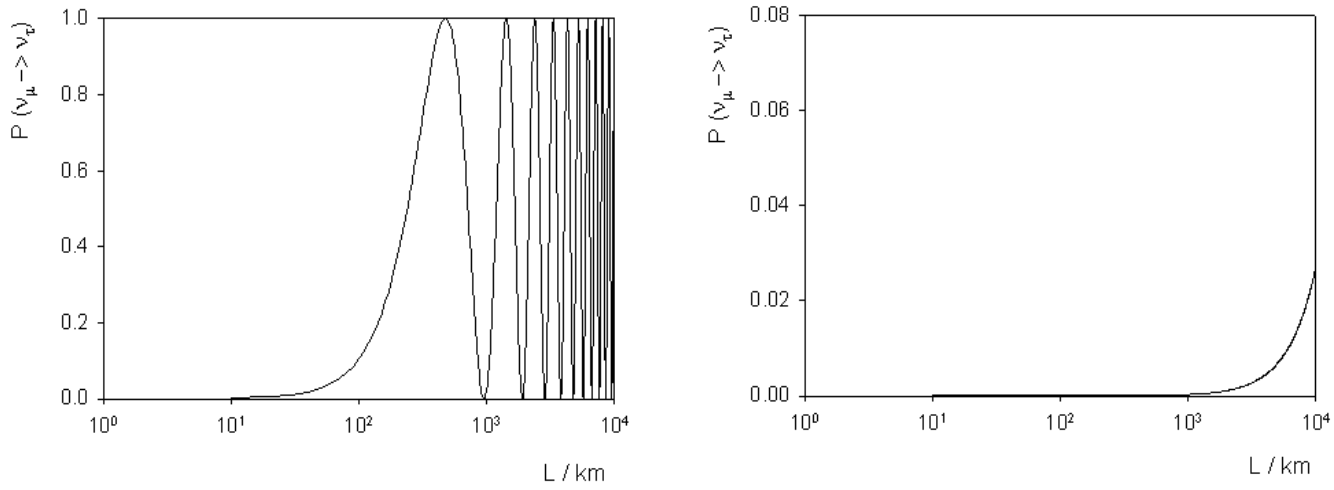

Figure 4.2: Standard atmospheric neutrino probability (4.49) as a function of the path length, L, for fixed values of the neutrino energy. The left frame fixes $E = 1\ GeV$ with the right frame having $E = 200\ GeV$.

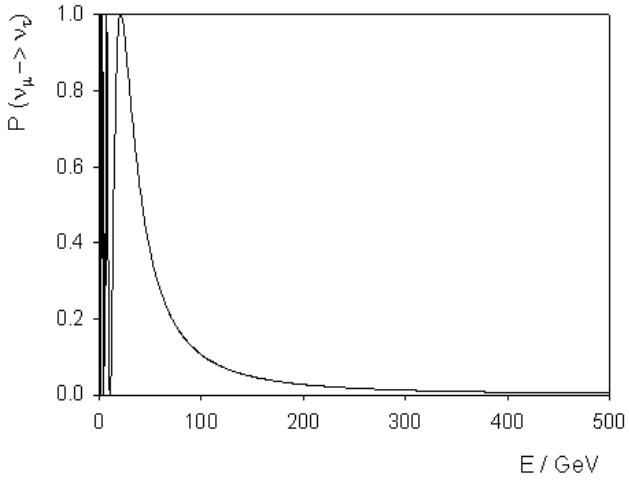

Figure 4.3: Standard atmospheric neutrino probability (4.49) as a function of the neutrino energy, E, for fixed path length, $L = 10^4\ km$.

dependence upon the neutrino energy. In this case, replacing the constants c and $\hbar$, the oscillation probability takes the form

$$P\left[\nu_\mu \rightarrow \nu_\tau\right] = \frac{1}{2}\left[1 - e^{-4.75\times10^{-4}L}\cos\left(2L\left\{\frac{1.09\times10^{-5}}{E^2} - 2.723\times10^{-12}\right\}^{\frac{1}{2}}\right)\right]. \quad (4.51)$$

Figure 4.4 shows the oscillation probability (4.51) in this case, when we fix the neutrino energy and should be compared with the plots in figure 4.2. Here, the effects of quantum decoherence can be clearly seen. At low energies, the oscillations are damped by quantum decoherence until the oscillation probability converges to one half at a path length which is of the same order as the diameter of the earth. At high energies, however, there is a marked difference in the oscillation probabilities. For the standard oscillation case, almost no oscillations take place over all the considered path lengths. However, quantum decoherence causes the probability to go to a half after the neutrinos have travelled large distances. This is a large difference from the standard case and would provide us with an excellent opportunity for observing such effects. Figure 4.5 shows the neutrino oscillation probability as a function of the neutrino energy for $L = 10^4\ km$. In the standard case, the probability very quickly tends to zero. The inclusion of quantum decoherence alters this significantly, since the damping factor in the probability causes the probability to tend towards a limiting value at large energies.

Quantum decoherence parameters inversely proportional to the neutrino energy

If we consider the case in which the decoherence parameters are inversely proportional to the neutrino energy, then the probability takes the form

$$P[\nu_\mu \rightarrow \nu_\tau] = \frac{1}{2}\left[1 - e^{-0.457\frac{L}{E}}\cos\left(6.604\times10^{-3}\frac{L}{E}\right)\right], \quad (4.52)$$

where we have set the quantum decoherence parameter $\mu_b^2 = 1\times10^{-3}\ eV^2$ in order to keep the argument of the cosine term real. We find the deviation from the standard case is particularly marked. This is due to the fact that the value we find for the quantum decoherence parameters, for this model, in the next chapter are fairly weak. Figures 4.6 and 4.7 show the oscillation probability, again as function of the path

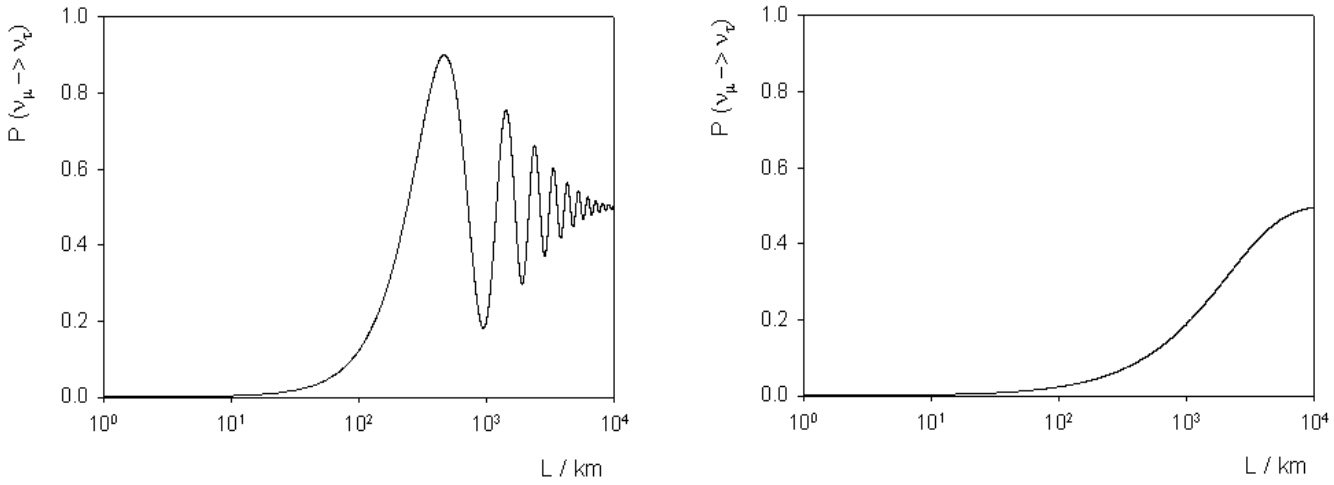

Figure 4.4: Atmospheric neutrino probability (4.51) including quantum decoherence parameters with no energy dependence, as a function of the path length, L, for fixed values of the neutrino energy. The left frame fixes $E = 1\ GeV$ with the right frame having $E = 200\ GeV$. Note the different scale on the right plot compared to that in figure 4.2.

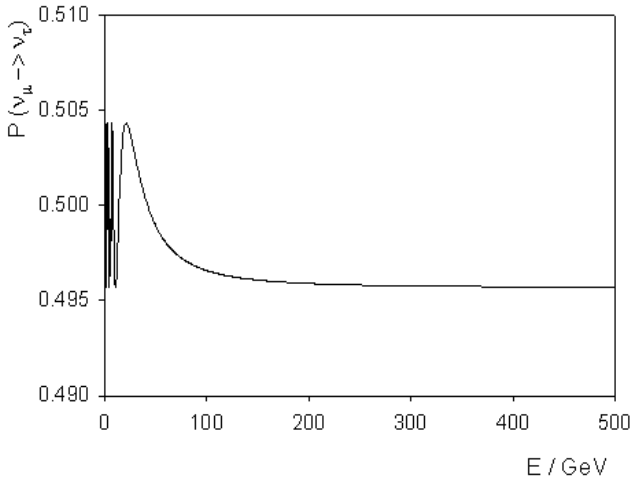

Figure 4.5: Atmospheric neutrino probability (4.51) including quantum decoherence parameters with no energy dependence as a function of the neutrino energy, E, for fixed path length, $L = 10^4\ km$. Note the different scale compared with figure 4.3.

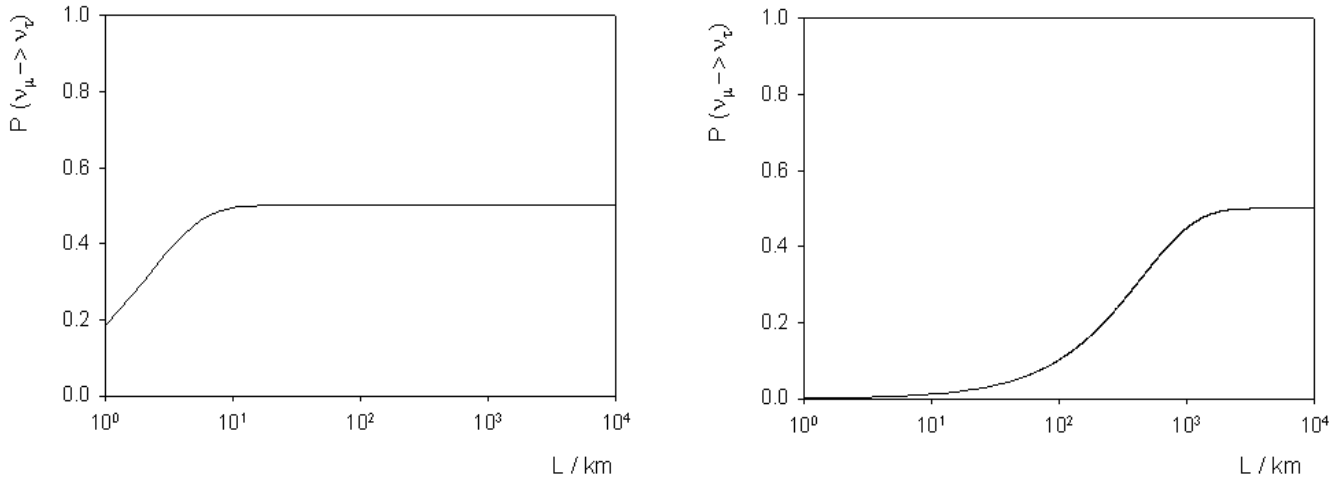

Figure 4.6: Atmospheric neutrino probability (4.52) including quantum decoherence parameters inversely proportional to the neutrino energy as a function of the path length, L, for fixed values of the neutrino energy. The left frame fixes $E = 1\ GeV$ with the right frame having $E = 200\ GeV$.

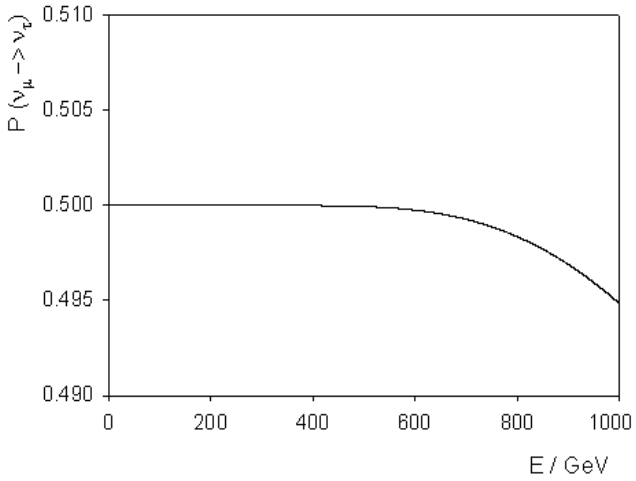

Figure 4.7: Atmospheric neutrino probability (4.52) including quantum decoherence parameters inversely proportional to the neutrino energy as a function of the neutrino energy, E, for fixed path length, $L = 10^4\ km$.

length and neutrino energy respectively. In figure 4.6, the first obvious feature is that, even at low energies, the oscillation signature is completely damped out. At low energies, the probability, as a function of path length, simply rises up to a half. At higher energies, the probability has the same form as that in the case when the quantum decoherence parameters have no dependence upon the neutrino energy, but the threshold at which the effects become important occurs at smaller path lengths. If we consider the probability as a function of energy as in figure 4.7, then we see this is completely different to that of the standard oscillation case. Here, the probability starts off at a limiting value and then at very high energies begins to drop off. Note we have extended the energy range to emphasise the falling probability. Overall, this shows the drastic effects that could occur if quantum decoherence effects were large. That oscillation minima have been observed in experimental data tells us that, for this model, if quantum decoherence effects occur then the parameters must be much smaller than those we have chosen here.

Quantum decoherence parameters proportional to the neutrino energy squared

If we now consider the case in which the quantum decoherence parameters are proportional to the neutrino energy squared, then, replacing c and $\hbar$, the oscillation probability takes the form

$$P[\nu_\mu \rightarrow \nu_\tau] = \frac{1}{2}\left[1 - e^{-2.024\times10^{-11}E^2L}\cos\left(2L\left\{\frac{1.09\times10^{-5}}{E^2} - 2.831\times10^{-32}E^4\right\}^{\frac{1}{2}}\right)\right]. \quad (4.53)$$

In fact, the bounds we find for this model in the next chapter turn out to be very strong and so, as we would expect, figures 4.8 and 4.9 show only small modifications to the standard oscillation picture rather than drastic modifications. Figure 4.8 shows the oscillation probability as a function of the path length for low ($E \sim 1\ GeV$) and high energy ($E \sim 200\ GeV$) neutrinos. In the low energy case on the left of figure 4.8, we note that this model is indistinguishable from the case of standard neutrino oscillations. It is not until we consider higher energy neutrinos that we see a marked difference in the two models. This is bourne out when we consider the plot shown in figure 4.9, which shows the neutrino oscillation probability as a function of the neutrino energy. At low energies, the probability mirrors that for standard

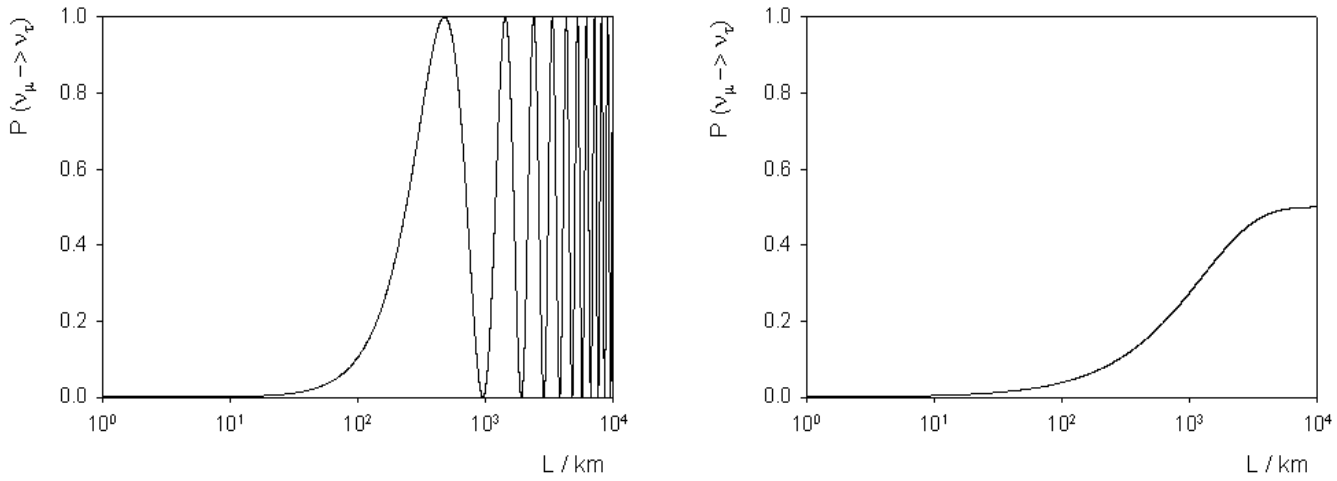

Figure 4.8: Atmospheric neutrino probability (4.53) including quantum decoherence parameters proportional to the neutrino energy squared as a function of the path length, L, for fixed values of the neutrino energy. The left frame fixes $E = 1\ GeV$ with the right frame having $E = 200\ GeV$.

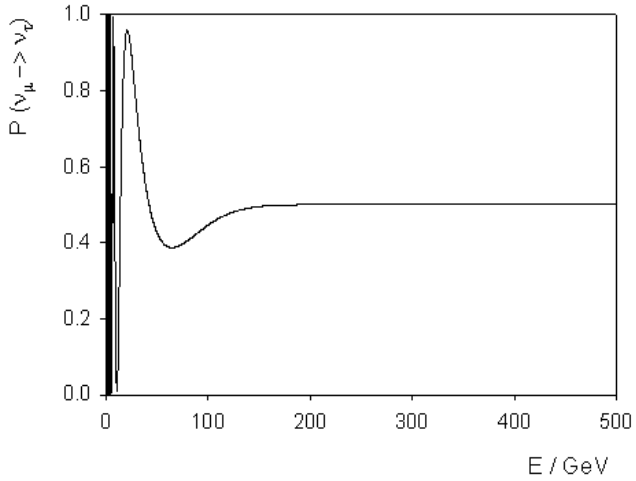

Figure 4.9: Atmospheric neutrino probability (4.53) including quantum decoherence parameters proportional to the neutrino energy squared as a function of the neutrino energy, E, for fixed path length, $L = 10^4\ km$.

oscillations but, rather than tending towards zero at higher energies, the probability instead tends towards a limiting value. Therefore, for this model, experiments which detect high energy neutrinos have a much greater advantage in detecting quantum decoherence than those which see only low energy neutrinos.

Quantum decoherence and the LSND anomaly

As we saw in chapter 1, the LSND result cannot be reconciled with the remainder of the neutrino oscillation data. One way to resolve this situation is to break CPT invariance and allow quantum decoherence in the anti-neutrino sector but not the neutrino sector [60]. If this is the case, then the oscillation probability for anti-neutrinos is modified as discussed above, whilst the probability of oscillation for neutrinos remains that shown in equation (1.7). Since quantum decoherence parameters appear along side the standard oscillation parameter, Δm^2, in the oscillation probability, this could lead to anti-neutrinos having a different effective mass difference from neutrinos. It is therefore possible to reconcile the LSND results with other existing oscillation data. Unfortunately, however, the model considered by the authors in [60] fails to fit the spectral distortions observed in the KamLAND experiment [48]. Having said that, the authors of reference [60] chose only one set of quantum decoherence parameters and so there is still much scope for further investigation.

4.3 Summary

In this section, we have shown how the CPT theorem may be evaded when we consider space-times which are not flat. We showed that one particular phenomena, namely quantum decoherence, the evolution of pure to mixed quantum states, which violates CPT, may modify quantum mechanics and thus the oscillation probability of a two neutrino system.

- We began by describing the CPT theorem and the three conditions upon which it depends, namely, unitarity, locality and Lorentz invariance. Violation of any one of these would cause CPT to be violated. We then outlined the motivation for quantum decoherence, a phenomenon which violates the CPT theorem as the time evolution of quantum states is no longer unitary. Furthermore, we

saw that we are able to model this phenomenon and examined how it modifies quantum mechanics (section 4.1).

- Using the model outlined in section 4.1, we then showed how quantum decoherence may be included into the phenomena of neutrino oscillations and saw that the probability which describes how one neutrino oscillates into another is altered. We parameterized quantum decoherence effects and considered three forms of the quantum decoherence parameters which depended upon the neutrino energy. We consider parameters which are proportional to

  - no power of the neutrino energy;
  - the inverse of the neutrino energy;
  - the square of the neutrino energy.

  We then showed how these effects would alter the oscillation probability and, whilst we do not measure probabilities, we were able to get a handle on the physical content of these models (section 4.2).

Whilst the CPT theorem may be evaded by violating unitarity, locality or Lorentz invariance, we have only considered the case when unitarity no longer holds. In subsequent chapters, (chapters 6 and 7), we shall concern ourselves with the violation of Lorentz invariance.

In the next chapter, we take the formalism presented here and use the *OSCFIT* software package described in chapter 3 to examine how ANTARES will be able to look for quantum decoherence phenomena in atmospheric neutrinos.

Chapter 5

Quantum decoherence - simulations

In this chapter, we describe the results of simulations, using the *OSCFIT* package described in chapter 3, of atmospheric neutrinos and show how neutrino telescopes will be able to place upper bounds upon model parameters. We begin by describing the models considered and show how the expected spectra of events is modified in the presence of quantum decoherence effects. We then present the results of our analysis and sensitivity regions for each model. We finish by presenting the upper bounds on the model parameters from our simulations and a discussion of how they compare with existing bounds.

5.1 Quantum decoherence models

In the last chapter, we showed how quantum decoherence effects modify the probability that one type of neutrino will oscillate into another, for a two neutrino system. For practical reasons, as we described in chapter 3, it is only possible to include a maximum of two parameters in addition to the parameter $\sin^2 2\theta$ and so we begin by presenting the models which include quantum decoherence effects which we shall consider in the remainder of this chapter.

5.1.1 Specific quantum decoherence models

Before we present the specific neutrino oscillation probabilities, we remind the reader that, for each model, the quantum decoherence parameters may have one of three

energy dependences:

- The parameters may be independent of the neutrino energy;
- The parameters may be inversely proportional to the neutrino energy;
- The parameters may be proportional to the square of the neutrino energy.

Below, we present nine models which contain a variety of combinations of the quantum decoherence parameters and so, along with the three different energy dependences, we have a total of twenty seven models to present. Before we present our results for all these models, we describe the form of the probabilities considered. In all cases, $c = \hbar = 1$.

Model QD1

The first model we consider is the simplest extension to the standard neutrino oscillation picture which includes quantum decoherence effects. In this case, we consider the decoherence parameters $a = \alpha$ in equation (4.20) to be non-zero and all the other quantum decoherence parameters to vanish. From equations (4.27), (4.36) and (4.37),the oscillation probability takes the form

$$P[\nu_\mu \to \nu_\tau] = \frac{1}{2}\sin^2 2\theta \left[1 - e^{-2\alpha L}\cos\left(\frac{\Delta m^2}{2E}L\right)\right]. \tag{5.1}$$

As will be the case in all the models presented here, if we set $\alpha = 0$, then we recover the standard neutrino oscillation probability (1.7). In some of the models we consider, it will be possible to set $\Delta m^2 = 0$ and consider the case where atmospheric neutrino oscillations arise purely from quantum decoherence effects. This is one particular model in which that is allowed and in this case, the probability reduces to

$$P[\nu_\mu \to \nu_\tau] = \frac{1}{2}\sin^2 2\theta \left[1 - e^{-2\alpha L}\right]. \tag{5.2}$$

It is worth noting that model **QD1** is the only model we consider which obeys the condition of complete positivity [141].

Model QD2

The second model we consider is a generalization of model **QD1**. In this case, we again consider the parameters a and α, with all other quantum decoherence

parameters zero, but we consider a and α to be independent. This leads to an oscillation probability of the form:

$$P\left[\nu_\mu \to \nu_\tau\right] = \frac{1}{2}\sin^2(2\theta)\left\{1 - e^{-\Gamma_s}\left[\cos\Gamma_2 + \frac{\Gamma_d}{\Gamma_2}\sin\Gamma_2\right]\right\}, \tag{5.3}$$

where

$$\begin{aligned} \Gamma_s &= (\alpha + a)\,L; \\ \Gamma_d &= (\alpha - a)\,L; \\ \Gamma_2 &= 2\left[\left(\frac{\Delta m^2 L}{4E}\right)^2 - \frac{1}{4}(\alpha - a)^2 L^2\right]^{\frac{1}{2}}. \end{aligned} \tag{5.4}$$

In this case, oscillations cannot be accounted for by quantum decoherence effects alone since setting $\Delta m^2 = 0$ renders Γ_2 imaginary and hence we lose the oscillatory nature. In this case, the probability takes on a damping term rather than the standard oscillation term. Therefore, in our simulations, we only consider quantum decoherence modifications to the standard neutrino oscillation scenario.

Model QD3

In our third model, we consider only a non-zero b in (4.20) and set all other quantum decoherence parameters to zero. The probability then becomes

$$P\left[\nu_\mu \to \nu_\tau\right] = \frac{1}{2}\sin^2(2\theta)\left[1 - \cos\Gamma_3\right], \tag{5.5}$$

where

$$\Gamma_3 = 2\left[\left(\frac{\Delta m^2 L}{4E}\right)^2 - b^2 L^2\right]^{\frac{1}{2}}. \tag{5.6}$$

As with the previous model, we cannot account for oscillations solely by quantum decoherence and we must include a non-zero Δm^2 in this probability. In the literature, it is often assumed that the parameter b will be much smaller than a or α, which would rule this model out. However, we include it here in order to examine the effect that this parameter can have on the neutrino system.

Model QD4

The fourth model we consider is, in effect, a combination of models **QD1** and **QD3**. We set $a = \alpha$ and b to be non-zero and have all other quantum decoherence parameters vanishing. We find the oscillation probability in this case to be

$$P\left[\nu_\mu \to \nu_\tau\right] = \frac{1}{2}\sin^2(2\theta)\left[1 - e^{-2\alpha L}\cos\Gamma_4\right], \tag{5.7}$$

where

$$\Gamma_4 = 2\left[\left(\frac{\Delta m^2 L}{4E}\right)^2 - b^2L^2\right]^{\frac{1}{2}}. \tag{5.8}$$

Once again, oscillations arising from quantum decoherence effects alone are prohibited and so we must have $\Delta m^2 \neq 0$. Whilst it would be more illustrative to combine models **QD2** and **QD3**, so $a \neq \alpha$, in practice, this is not practical due to the excessive running time of the simulations (see chapter 3).

Model QD5

The fifth model we consider is somewhat different to the ones already discussed as we now introduce the quantum decoherence parameter, δ, as the non-vanishing parameter with all other quantum decoherence parameters zero. In this case, energy is not conserved within the neutrino system. The oscillation probability in this case is

$$P\left[\nu_\mu \to \nu_\tau\right] = \frac{1}{2}\left\{\cos^2(2\theta)\left[1 - e^{-2\delta L}\right] + \sin^2(2\theta)\left[1 - \cos\left(\frac{\Delta m^2 L}{2E}\right)\right]\right\}. \tag{5.9}$$

The key feature of this model, and those that follow, is the presence of terms which multiply the $\cos^2 2\theta$ term, signifying the non-conservation of energy within the neutrino sector. In this case, we are not prohibited from setting $\Delta m^2 = 0$ and so we may consider the case of oscillations induced by quantum decoherence only. Setting $\Delta m^2 = 0$ in (5.9) reduces the oscillation probability to

$$P\left[\nu_\mu \to \nu_\tau\right] = \frac{1}{2}\cos^2(2\theta)\left[1 - e^{-2\delta L}\right]. \tag{5.10}$$

The form of this equation is similar to that in (5.2) but the here we have the cosine of the mixing angle in contrast to the sine of the mixing angle in (5.2).

Model QD6

This model combines the previous model with model **QD1**. Combining these models leads to an oscillation probability:

$$P\left[\nu_\mu \to \nu_\tau\right] = \frac{1}{2}\left\{\cos^2(2\theta)\left[1 - e^{-2\delta L}\right] + \sin^2(2\theta)\left[1 - e^{-2\alpha L}\cos\left(\frac{\Delta m^2 L}{2E}\right)\right]\right\}, \tag{5.11}$$

and, for this model, we may consider the case of quantum decoherence oscillations only. Setting $\Delta m^2 = 0$ leads to the oscillation probability given by

$$P\left[\nu_\mu \to \nu_\tau\right] = \frac{1}{2}\left\{\cos^2(2\theta)\left[1 - e^{-2\delta L}\right] + \sin^2(2\theta)\left[1 - e^{-2\alpha L}\right]\right\}. \tag{5.12}$$

This model differs slightly from most considered in that the model may preserve complete positivity provided $\delta < 2\alpha$ [67].

Model QD7

This is the final model which arises from equations (4.27), (4.36) and (4.37). Here, we consider the case where $a = \alpha = 0$ with b and δ being non-zero. The oscillation probability is therefore

$$P\left[\nu_\mu \to \nu_\tau\right] = \frac{1}{2}\left\{\cos^2(2\theta)\left[1 - e^{-2\delta L}\right] + \sin^2(2\theta)\left[1 - \cos\Gamma_7\right]\right\}, \tag{5.13}$$

where

$$\Gamma_7 = 2\left[\left(\frac{\Delta m^2 L}{2E}\right)^2 - b^2 L^2\right]^{\frac{1}{2}}. \tag{5.14}$$

In this case, we observe that we may not set $\Delta m^2 = 0$ and preserve an oscillatory nature within the probability, and so we only consider quantum decoherence effects as modifications to the standard oscillation picture. Once again, we find that complete positivity may not be satisfied with this model.

Model QD8

The final two models we consider within this thesis are special cases of equation (4.27) when the quantities $M_{11}(E,L)$, $M_{33}(E,L)$, $M_{13}(E,L)$ and $M_{31}(E,L)$ are given by equation (4.48). In this model, we consider all quantum decoherence parameters to

be zero apart from β. In this case, the oscillation probability takes the form

$$P[\nu_\mu \to \nu_\tau] = \frac{1}{2}\left\{\cos^2 2\theta\left[1 - \frac{\omega^2}{\Omega_\beta^2} + \frac{\beta^2}{\Omega_\beta^2}\cos(2\Omega_\beta L)\right] + \sin^2 2\theta\left[1 + \frac{\beta^2}{\Omega_\beta^2} - \frac{\omega^2}{\Omega_\beta^2}\cos(2\Omega_\beta L)\right]\right\}, \quad (5.15)$$

where $\Omega_\beta = \sqrt{\omega^2 - \beta^2}$ and $\omega = \frac{\Delta m^2}{4E}$ as before. We are unable to examine the case of oscillations which arise from purely quantum decoherence effects in this model as the argument of the cosine terms would become imaginary. Complete positivity is not satisfied in this model.

Model QD9

Our final model which includes quantum decoherence effects in the atmospheric neutrino system sets all quantum decoherence parameters to zero except d in (4.20). In this case, we find the oscillation probability has the form

$$P[\nu_\mu \to \nu_\tau] = \frac{1}{2}\left\{\cos^2 2\theta\left[1 - \frac{\omega^2}{\Omega_d^2} + \frac{d^2}{\Omega_d^2}\cos(2\Omega_d L)\right] + \sin^2 2\theta\left[1 + \frac{d^2}{\Omega_d^2}\cos(2\Omega_d L) - \frac{\omega^2}{\Omega_d^2}\cos(2\Omega_d L)\right] + \sin 4\theta\left[\frac{d}{\Omega_d}\sin(2\Omega_d L)\right]\right\}, \quad (5.16)$$

where $\Omega_d = \sqrt{\omega^2 - d^2}$. This is the only model in which the oscillation probability contains a term proportional to $\sin 4\theta$. Again, we are unable to set $\Delta m^2 = 0$ and have the probability retain an oscillatory nature. In a similar manner to the previous model, this case does not satisfy complete positivity.

5.1.2 Review of literature

Various models have been considered to date in the literature [67, 88, 169, 181, 183]. However, the only work we know of which involves analysis of experimental data is in [127, 180]. The models which have received the most attention are those in which the parameters a, α and b are non-zero with d, β and δ zero [67, 88, 183] and also models with α, β and δ non-zero with $a = b = d = 0$ [67, 88, 169, 181]. The authors

of reference [67] consider a very general model with all six quantum decoherence parameters non-zero but then specialize their models with $d = \beta = 0$ and also $\delta = 0$. They also impose the further constraint of complete positivity [141]. Secondly, they consider a general model with all parameters non-zero, and perform a second order perturbation approximation. All the models we have presented above are special cases of those considered in [67].

Liu and collaborators [181] considered a model with $a = b = d = 0$ and found that the oscillation probability can only be calculated numerically. In our models, we have a and α non-zero or both parameters zero. Therefore, the probabilities we presented in the previous section do not correspond to theirs.

The authors of [88] consider the same model as [181] but also set $\beta = 0$. Again, this does not tally with any of the models we have considered here. They also consider how the standard oscillation probability is altered by leading order corrections when a, b and α are non-zero with the other parameters vanishing.

Ma and collaborators [183] worked with an analytical oscillation probability having a, b and α non-zero. This model tallies with various combinations of parameters in models **QD2**-**QD5**.

Finally, the authors of reference [169] consider a model in which α and δ are the only non-zero quantum decoherence parameters.

5.2 ANTARES sensitivity to quantum decoherence in atmospheric neutrinos

In the previous section, we introduced nine models of quantum decoherence, each with three different types of energy dependence. In this section, we present the upper bounds we have been able to place on the quantum decoherence parameters and also the forms of the parameter space which ANTARES will be able to probe using atmospheric neutrinos. Before, we do this, however, we shall consider the spectra, the number of events expected in each case, as a function of path length and energy.

5.2.1 Spectra

The spectra of events, the shape of the graph of the number of events as a function of energy and path length, is important in neutrino physics. The Super-Kamiokande experiment has reported an oscillatory signature in the E/L spectrum of events [49] with similar spectral results found in the KamLAND [48] and K2K [31] experiments. In addition to their use in our sensitivity analysis, the spectra also provide us with an alternative method of searching for quantum decoherence effects by observing modifications to the shape of the spectra. All of the spectra we present here utilize the probability of model **QD1**, so we may outline the types of effects we would see in the spectra were quantum decoherence effects present. We only consider the oscillation probability from model **QD1** since we expect the parameters b and β to be smaller than those in this model and the remaining parameters are multiplied by small functions of the mixing angle. Therefore, we do not consider the shape of the spectra presented here to be dramatically altered by the inclusion of more quantum decoherence parameters.

Spectra for quantum decoherence parameters with no dependence on the neutrino energy

Figures 5.1 and 5.2 show the spectra when the quantum decoherence parameters have no dependence upon the neutrino energy. We plot the expected number of events for quantum decoherence effects only and standard oscillations plus decoherence respectively. Here, E is the neutrino energy and ϑ is the zenith angle. We begin by examining the spectra for quantum decoherence effects only in figure 5.1. The left frames of figure 5.1 show the number of events whilst the right frames show the ratio of the number of events compared to no oscillations. In each graph, the black line represents MC simulation of standard oscillations without decoherence whilst the coloured line represents MC simulation of quantum decoherence only. The data points correspond to three years of data taking assuming standard oscillations only. The first thing to notice is that for larger values of the decoherence parameter, we expect a suppression in the number of observed events when we compare this to the spectra for standard oscillations in figure 3.1. If, however, we consider the case when the quantum decoherence parameter takes small values, then the difference between standard oscillations and quantum decoherence is not so obvious. If we consider the frames on the right of figure 5.1, then we note that there are features which would

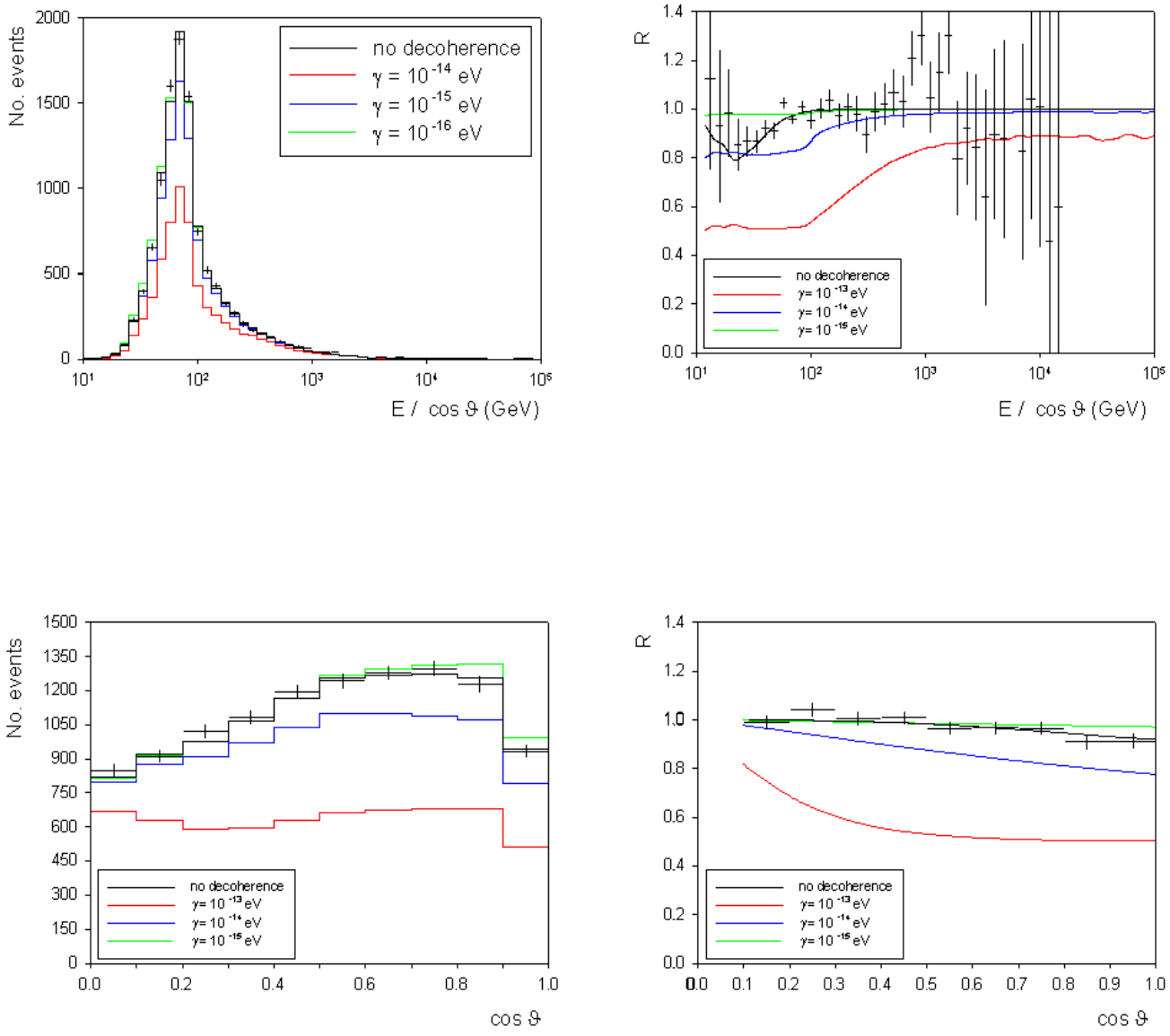

Figure 5.1: Spectrum of events when the quantum decoherence parameters have no dependence on the neutrino energy. The black line represents the MC simulation of standard oscillations with the coloured lines showing the spectra for oscillations from quantum decoherence.

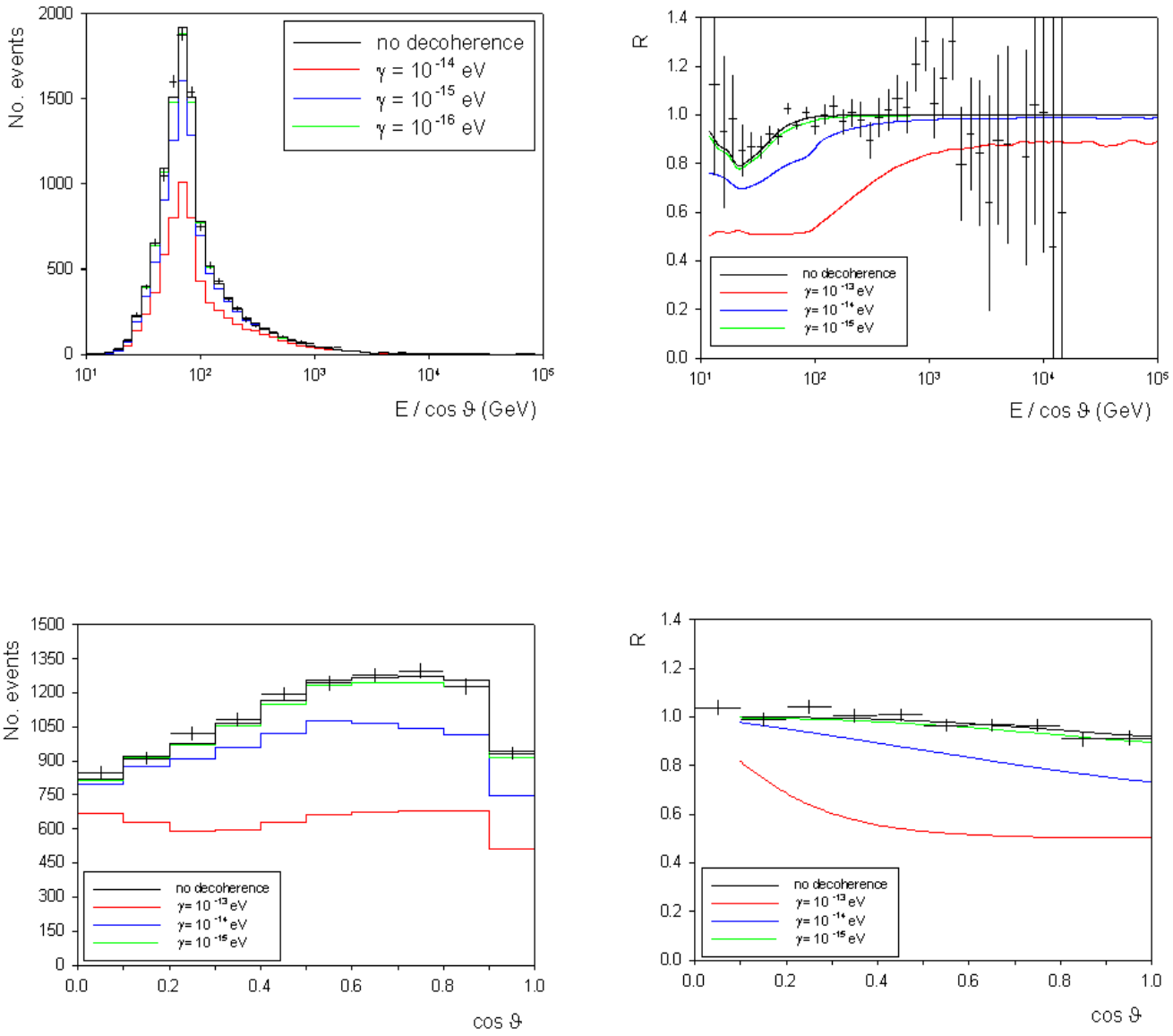

Figure 5.2: As figure 5.1 but the coloured lines show the spectra for standard oscillations plus decoherence.

allow us to distinguish between the two scenarios. In the top right frame, the curves are much flatter for decoherence than for standard oscillations in which we see an oscillation minimum. At higher energies, the difference is not so marked, particularly for small values of the decoherence parameters. It is also easy to distinguish between quantum decoherence effects and standard oscillations when we consider the plot in the bottom right of figure 5.1. For large values of the decoherence parameter, the difference is easily seen. However, in this case, we are able to distinguish between the two scenarios, even for small values of the quantum decoherence parameters, at high values of $\cos\vartheta$.

Secondly, we consider the case of standard oscillations plus quantum decoherence. Figure 5.2 shows the spectra and the ratio of number of events compared to no oscillations. Again, we see that large values of the decoherence parameters leads to a significant suppression of the number of events. When we consider the ratio of events as a function of $E/\cos\vartheta$, again, it easy to distinguish the two cases for large values of the quantum decoherence parameters, particularly at low energies. The situation is more tricky for smaller values of the decoherence parameters as we still see an oscillation minimum at low energies and, at high energies, the curves are indistinguishable. Considering the ratio of events as a function of the zenith angle only, we see, again, that the two scenarios are easily distinguishable for large values of the decoherence parameters. At higher values of $\cos\vartheta$, the situation again becomes more difficult, especially for small values of the decoherence parameters.

Spectra for quantum decoherence parameters inversely proportional to the neutrino energy

We now consider the spectra when the decoherence parameters are inversely proportional to the neutrino energy. Figure 5.3 shows the spectra and the ratios of the number of events to those expected if there were no oscillations, for the case when oscillations occur due to decoherence effects alone ($\Delta m^2 = 0$). For large values of the decoherence parameters, we see in the left hand frames that, as in the previous case, the number of events would be significantly suppressed. The difference in the two scenarios is seen in the plots on the right. In the top right plot, we see that the curves initially rise and then fall, which is in complete contrast to the curve for standard oscillations (the solid curve). At higher energies, these curves start to oscillate. When we consider the ratio of events as a function of the zenith angle, it

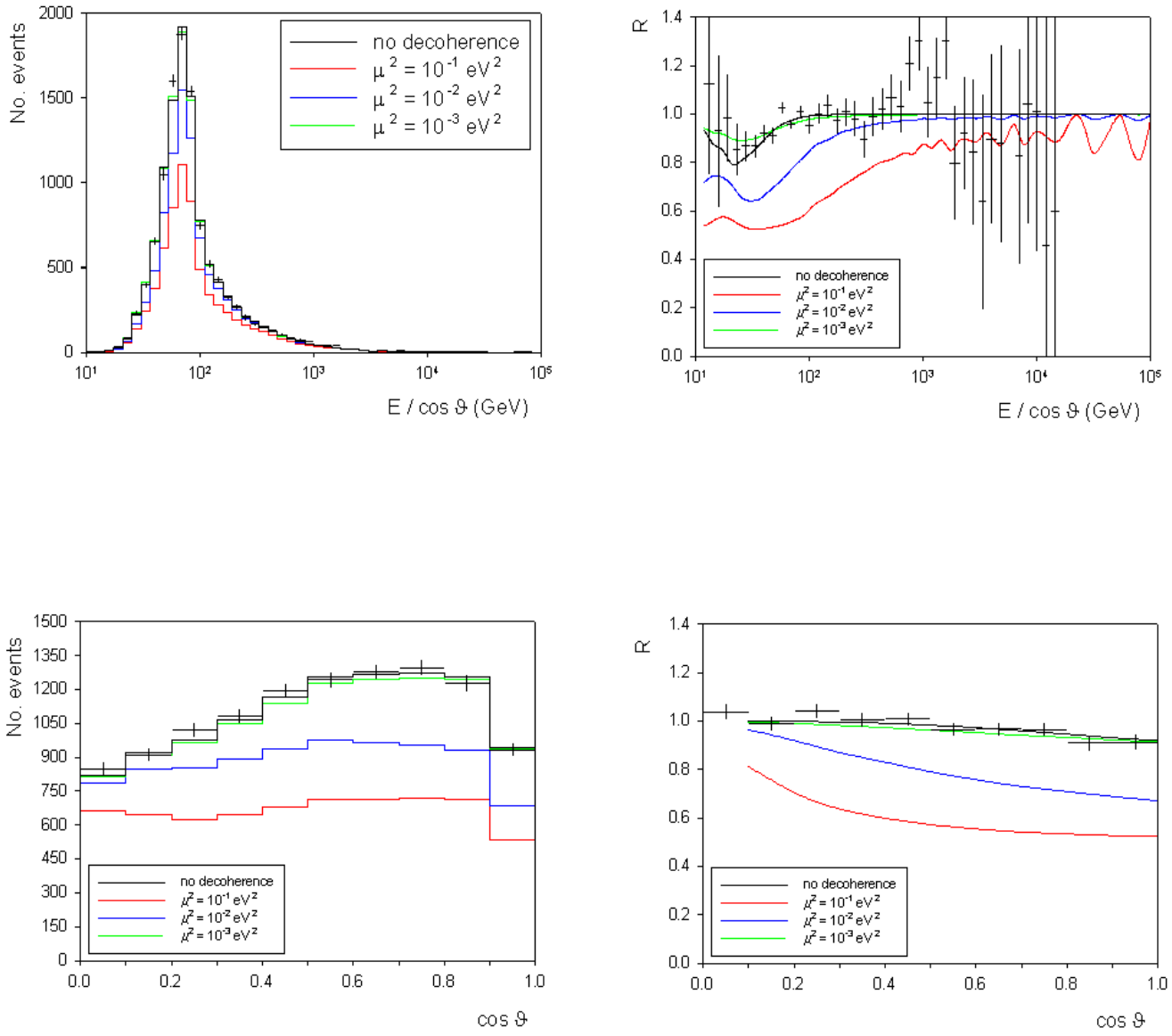

Figure 5.3: Spectrum of events when the quantum decoherence parameters are inversely proportional to the neutrino energy. The black line represents the MC simulation of standard oscillations with the coloured lines showing the spectra for oscillations from quantum decoherence.

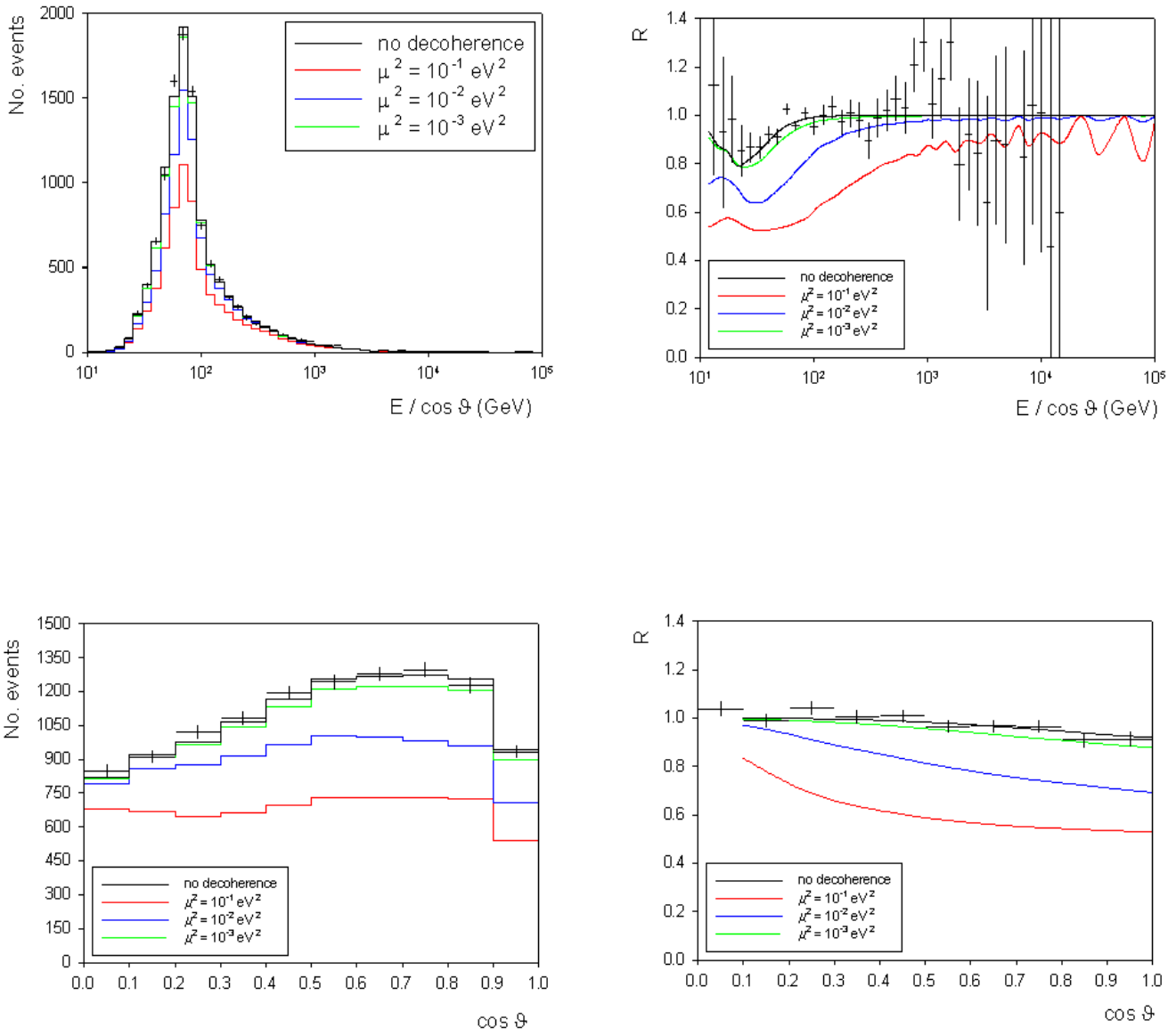

Figure 5.4: As figure 5.3 but the coloured lines show the spectra for standard oscillations plus decoherence.

should be simple to rule out the larger values of the decoherence parameters for this model.

Figure 5.4 shows the spectra we expect when quantum decoherence modifies standard neutrino oscillations. Again, the left hand plots show that decoherence effects would suppress the number of events observed. In this case, however, looking at the shape of the ratio curves in the top right plot, we see that although the curves rise for large values of the decoherence parameters, they also exhibit an oscillation minima and so distinguishing these effects from standard oscillations would be difficult. If we consider small values of the parameter, then the two curves are essentially indistinguishable. At higher energy, curves which arise from the larger values of the decoherence parameters oscillate but, to rule these values out, would take many years of data taking to reduce the size of the error bars on the data points.

Spectra for quantum decoherence parameters proportional to the neutrino energy squared

Figure 5.5 shows the spectra when the decoherence parameters are proportional to the neutrino energy squared for quantum decoherence effects only. We find the same general features for this energy dependence as for the other two. For large values of the decoherence parameters, there is a large suppression in the number of expected events. If we consider the ratio of events as a function of $E/\cos\vartheta$ (the top right plot), then, for all values of the quantum decoherence parameters, we see that there is no longer an oscillation minimum, in fact for some values of the quantum decoherence parameter, we see an increase in this ratio. Similarly, when the ratio is a function of just the zenith angle, we see that, even though the shape of the curve is the same as that for standard oscillations, the number of events is reduced to such a level, we should be able to rule out these values of the decoherence parameters.

The spectra obtained from our simulations when we consider standard neutrino oscillations modified by quantum decoherence effects is shown in figure 5.6. Again, for large values of the decoherence parameters, we would expect a significant suppression in the number of observed events. This is reflected in the curves showing the ratio of the number of events on the right hand side of this figure. The top right plot shows the ratio of events as a function of $E/\cos\vartheta$. For the largest value of the decoherence parameter, the curve at low energies is very flat and no oscillation minimum is seen. For smaller values of the parameter, the curves take on the same shape as the

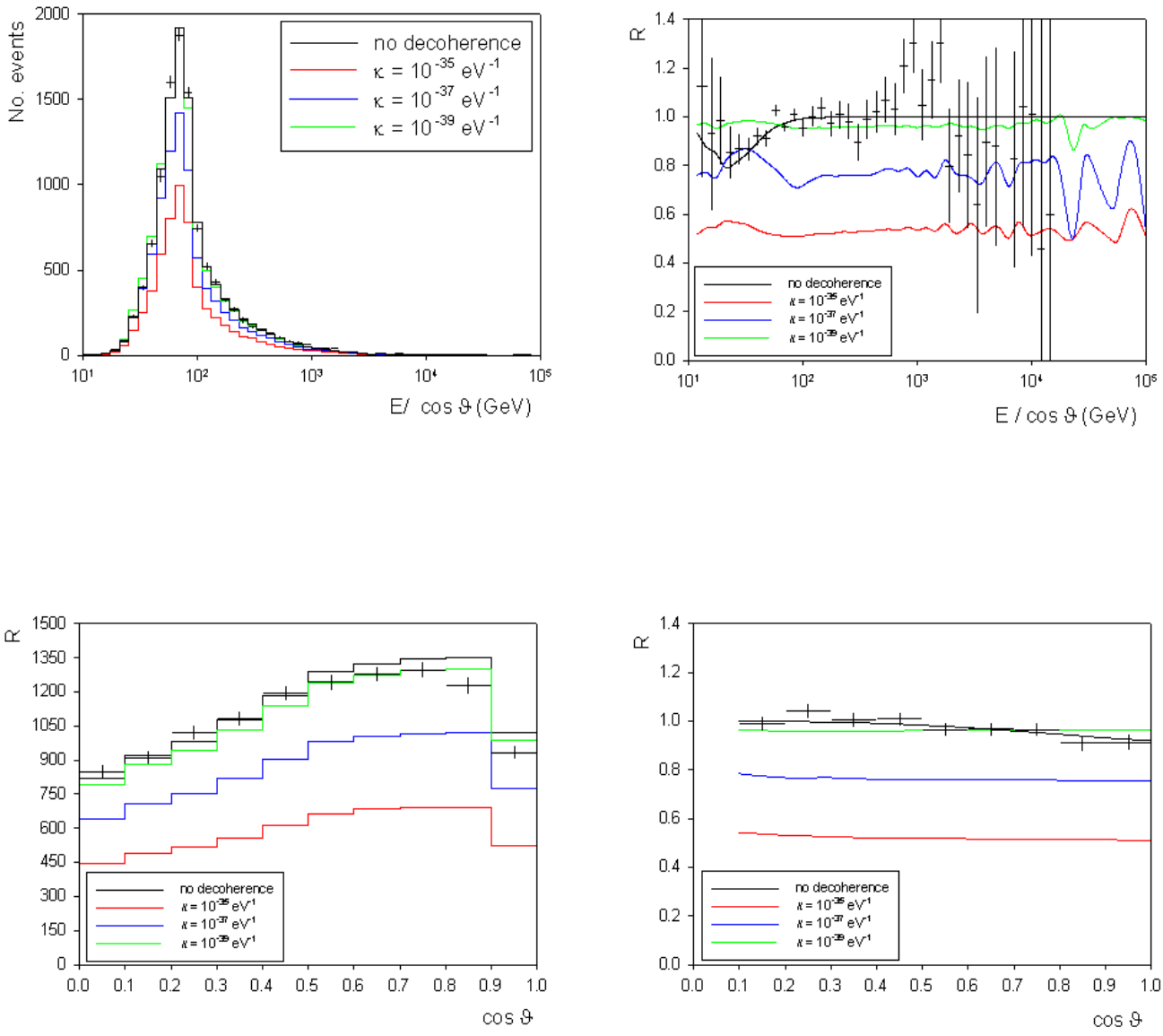

Figure 5.5: Spectrum of events when the quantum decoherence parameters are proportional to the neutrino energy squared. The black line represents the MC simulation of standard oscillations with the coloured lines showing the spectra for oscillations from quantum decoherence.

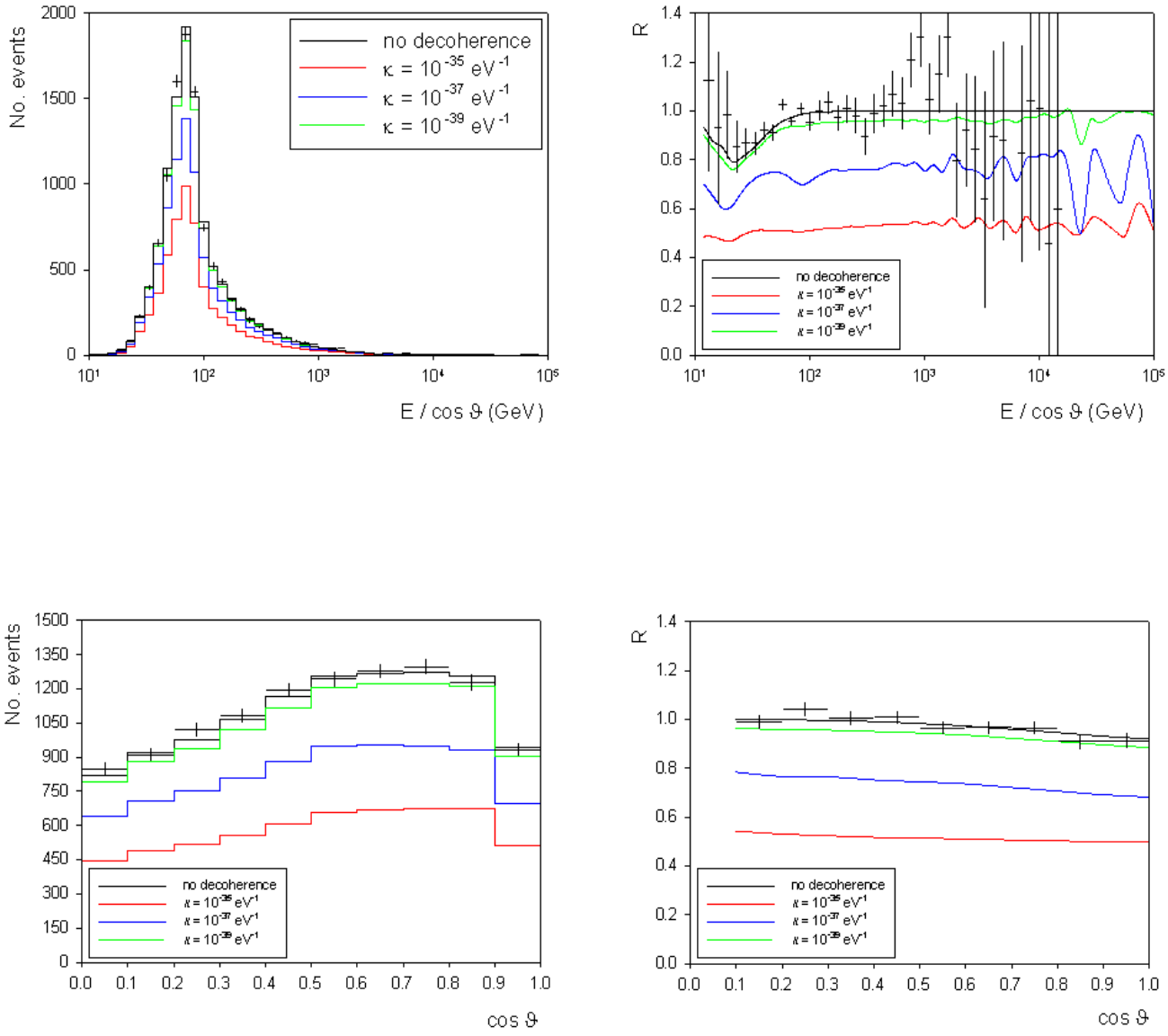

Figure 5.6: As figure 5.3 but the coloured lines show the spectra for standard oscillations plus decoherence.

standard neutrino oscillation case. At high energies, even the curve corresponding to the smallest value of the decoherence parameter considered here oscillates. However, it would take many years of data to be able to observe these oscillations. The bottom right plot shows the ratio of the number of events as a function of the zenith angle. Again, there is a distinct difference between the curves relating to the suppression of the number of events. The shape of the curves is the same in both scenarios, however.

The main thing to notice about this model is the value of the parameters we have chosen to illustrate the effects. The values we have chosen are significantly smaller than the current experimental bounds (see section 5.3), therefore, neutrino telescopes, such as ANTARES and IceCUBE, will be able to significantly improve the bounds on the quantum decoherence parameters for this model, the model which has the only theoretical link with quantum gravity.

We are now in a position to examine the sensitivity regions for the quantum decoherence parameters from our numerical simulations. Whilst we are interested in the regions of parameter space that ANTARES can probe, we are particularly interested in the upper bounds we can place on the quantum decoherence model parameters. We discuss each model in turn.

5.2.2 Model QD1

This model involves two non-zero quantum decoherence parameters, a and α, but we set $a = \alpha$. The oscillation probability is therefore given by (5.17).

Decoherence parameters with no dependence on the neutrino energy

Replacing the constants, c and $\hbar$ in model **QD1**, when the quantum decoherence parameters have no dependence upon the neutrino energy, gives the oscillation probability as

$$P[\nu_\mu \to \nu_\tau] = \frac{1}{2}\sin^2(2\theta)\left[1 - e^{-5\times10^9\gamma_\alpha L}\cos\left(\frac{2.54\Delta m^2}{E}L\right)\right], \qquad (5.17)$$

where α is measured in eV; the mass squared difference, Δm^2, is measured in eV^2; the energy, E, is measured in GeV; and the path length, L, is measured in km. In the cases discussed below, for all energy dependences and models, Δm^2, E and L

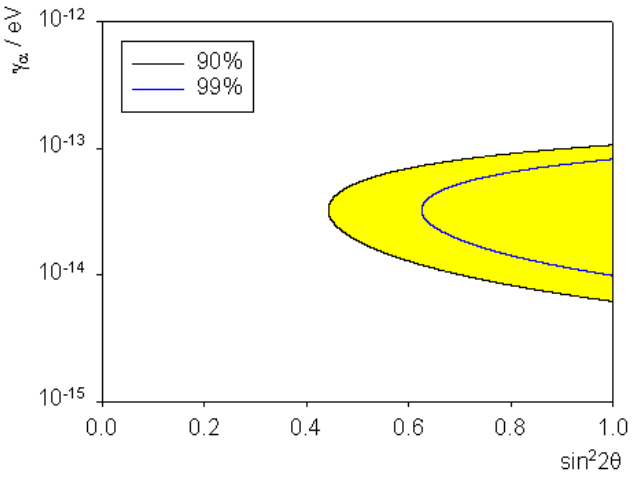

Figure 5.7: Sensitivity contours for model **QD1** at 90 and 99 percent confidence level for quantum decoherence effects only with the parameter γ_α, with no dependence on the neutrino energy. In this case, there are no existing bounds from data for comparison.

will be measured in these units unless stated otherwise. To arrive at this probability, we set $a = \alpha = \frac{\gamma_\alpha}{2}$.

As we mentioned above, for this model, there are two cases of interest. Firstly, if we set $\gamma_\alpha = 0$, then we retain the standard oscillation probability (1.7) and hence the sensitivity curve is that shown in figure 3.2.

The second limit of interest occurs when we set $\Delta m^2 = 0$ and so oscillations are purely a result of quantum decoherence effects. Restoring c and $\hbar$, the probability (5.2) becomes

$$P[\nu_\mu \to \nu_\tau] = \frac{1}{2}\sin^2(2\theta)\left[1 - e^{-5\times10^9\gamma_\alpha L}\right]. \tag{5.18}$$

Figure 5.7 shows the sensitivity region in this case. For this model, there are no bounds from the literature to which we may compare our results. The region in which the parameters are consistent with the data lies inside the curves and is highlighted in yellow at the 90% confidence level. We see that we are able to place an upper bound on this parameter of around $10^{-13}\ eV$.

If we now consider the more general case, with the oscillation probability taking the form (5.17), then, since we have three parameters, we obtain a three dimensional parameter space. This is shown in figure 5.8 with the sensitivity region lying above the surface. In order to make the comparison with existing results easier, we project this volume onto the relevant coordinate planes to obtain three plots of sensitivity contours. These contours are shown in figure 5.9. Again, the regions

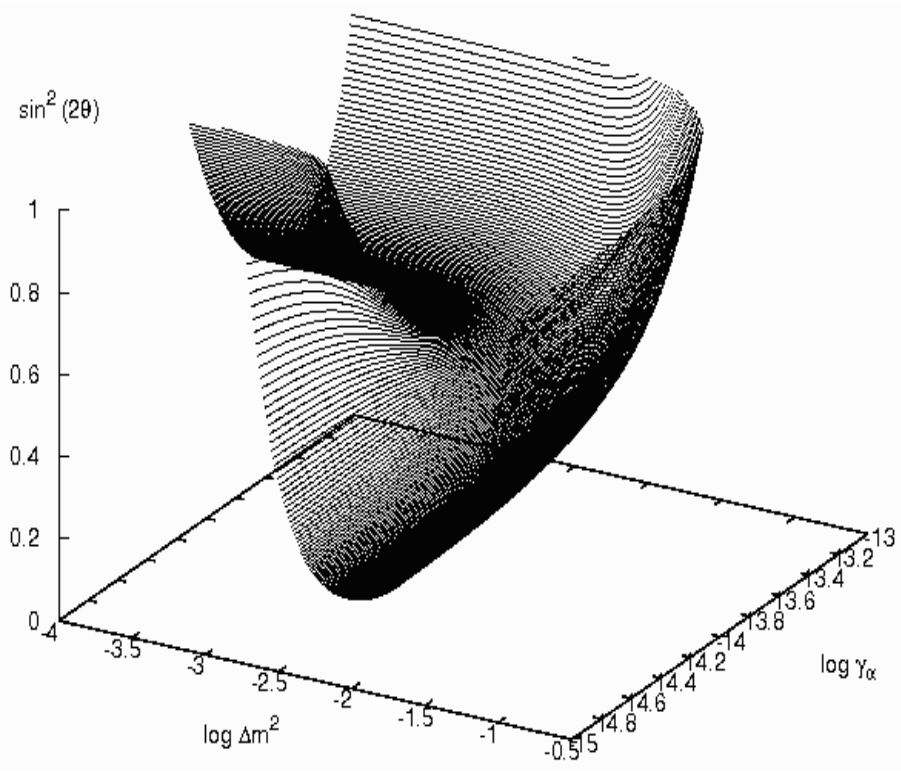

Figure 5.8: Sensitivity volume for model **QD1** at 90 percent confidence level including standard oscillations plus quantum decoherence effects with no dependence on the neutrino energy..

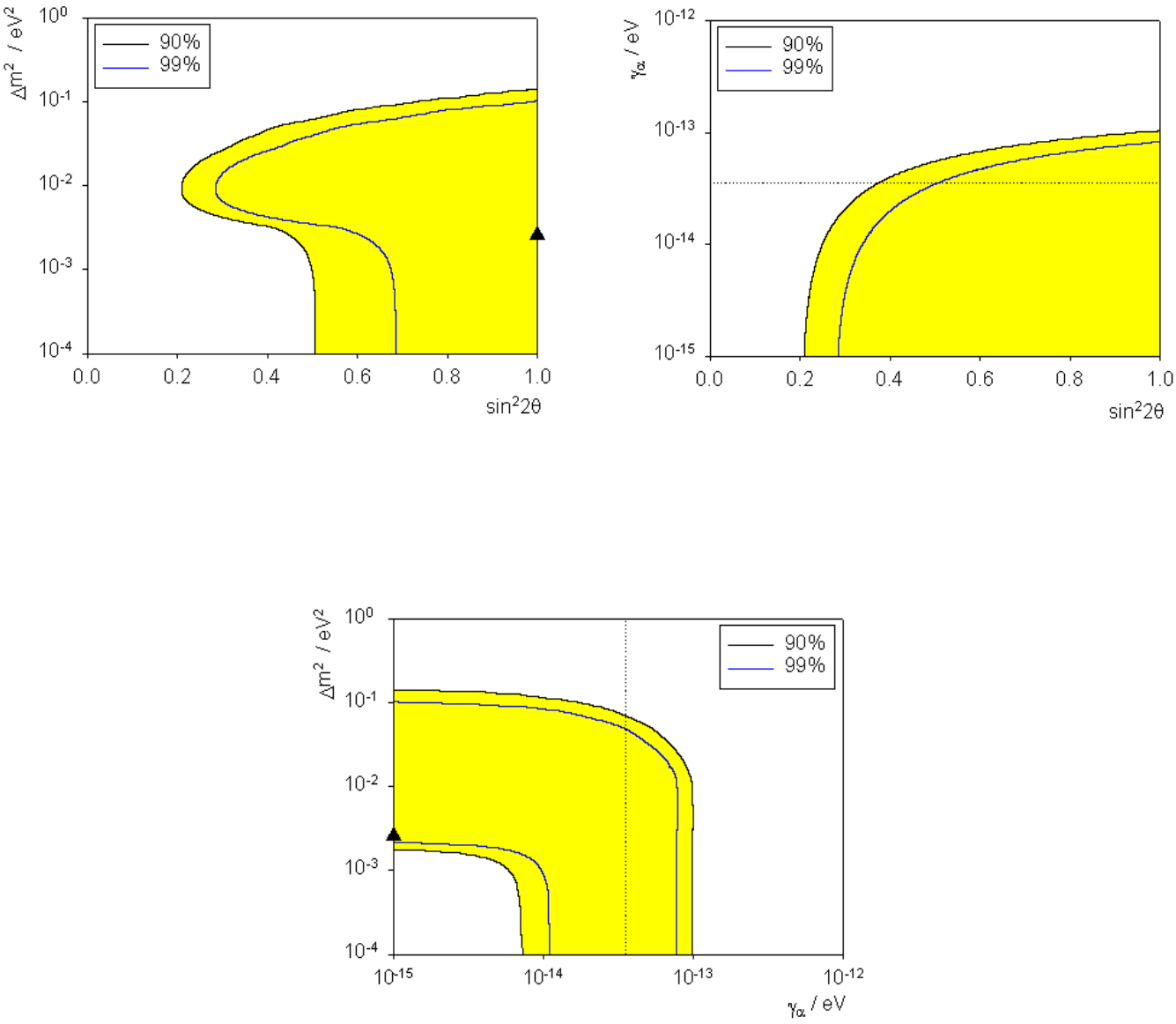

Figure 5.9: Sensitivity contours for model **QD1** at 90 and 99 percent confidence level including standard oscillations and quantum decoherence effects with no dependence on the neutrino energy. The triangle denotes the experimental point of best fit for Δm^2 and $\sin^2 2\theta$ [127], and the line denotes the current upper bound on γ_α from [180].

which are statistically allowed are shown in yellow at the 90% confidence level. The top left frame shows two standard oscillation parameters plotted against each other with the triangle denoting the point of best fit from the Super-Kamiokande data [127]. We note that this value lies within our sensitivity region. In addition, when $\sin^2 2\theta = 1$, the value $\Delta m^2 = 0$ is also allowed in this model and so backs up the first result presented above, that we cannot rule out neutrino oscillations which occur as a result of quantum decoherence alone. The top right frame shows the quantum decoherence parameter, γ_α, as a function of the mixing angle, θ, with the allowed region, highlighted in yellow, lying inside the contours. The line here shows the current upper bound. We note that our simulations are entirely consistent with the results presented in reference [180]. The third frame shows Δm^2 against γ_α with the yellow region identifying the area of parameter space allowed statistically.

Decoherence parameters inversely proportional to the neutrino energy

In this case, we set $a = \alpha = \frac{\mu_\alpha^2}{4E}$. The oscillation probability is

$$P[\nu_\mu \to \nu_\tau] = \frac{1}{2}\sin^2(2\theta)\left[1 - e^{-\frac{2.54\mu_\alpha^2}{E}L}\cos\left(\frac{2.54\Delta m^2}{E}L\right)\right], \tag{5.19}$$

where μ_α^2 is measured in eV^2. Again, we are able to model the situation in which neutrino oscillations arise from quantum decoherence effects only. The oscillation probability in this case is

$$P[\nu_\mu \to \nu_\tau] = \frac{1}{2}\sin^2(2\theta)\left[1 - e^{-\frac{2.54\mu_\alpha^2}{E}L}\right]. \tag{5.20}$$

The sensitivity contours for this case are shown in figure 5.10. Here, the allowed values of the parameter lie inside the contours and the sensitivity region at the 90% confidence level is highlighted in yellow. The circle denotes the current point of best fit for the parameter μ_α^2 [127] and we are able to place a weak bound of around $10^{-1}\ eV^2$ on the quantum decoherence parameter.

When we include a non-zero Δm^2, the probability is that in equation (5.19). The resulting sensitivity surface in the three dimensional parameter space is shown in figure 5.11, with the corresponding sensitivity contours in figure 5.12. The surface within the parameter space is very similar to that in the case when the quantum decoherence parameters have no dependence upon the neutrino energy and

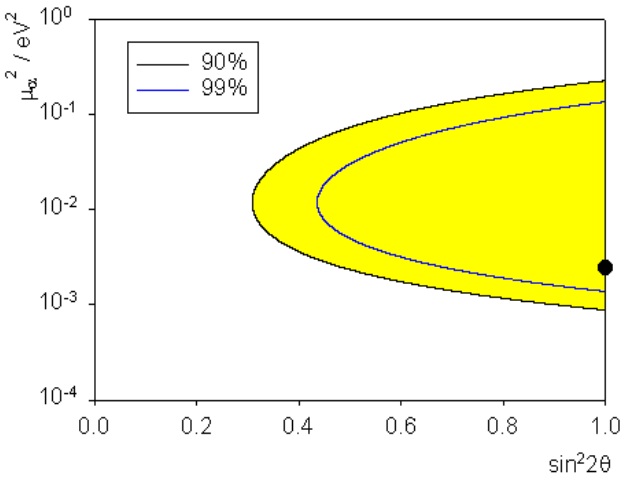

Figure 5.10: Sensitivity contours for model **QD1** at 90 and 99 percent confidence level for quantum decoherence effects only where the parameter μ_α^2 is inversely proportional to the neutrino energy. The circle denotes the experimental point of best fit from [127].

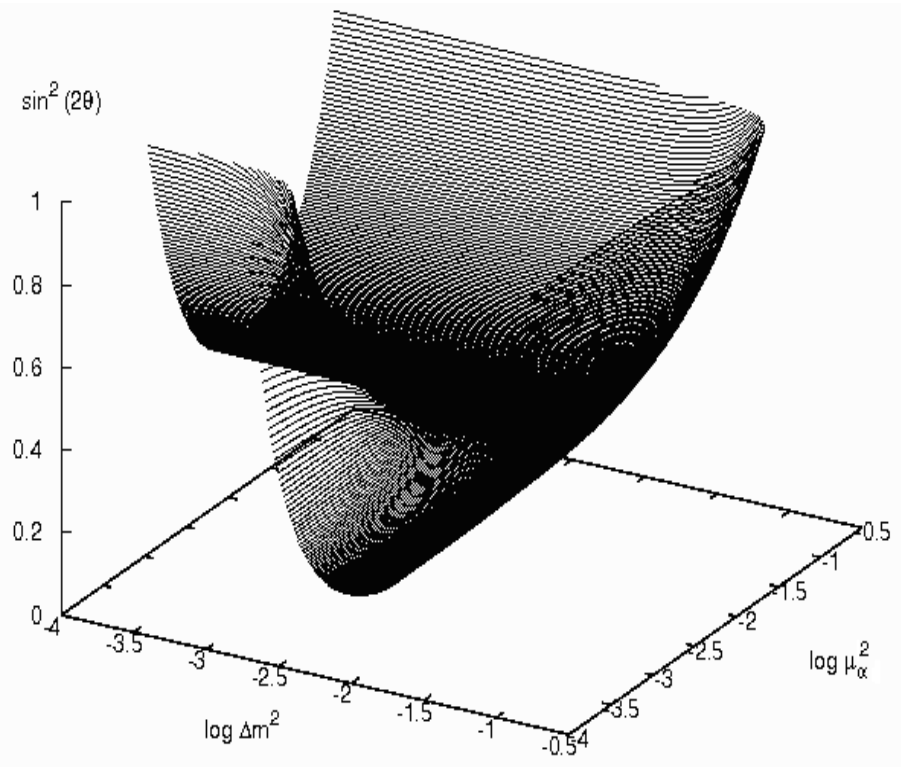

Figure 5.11: Sensitivity volume for model **QD1** at 90 percent confidence level including standard oscillations plus quantum decoherence effects inversely proportional to the neutrino energy.

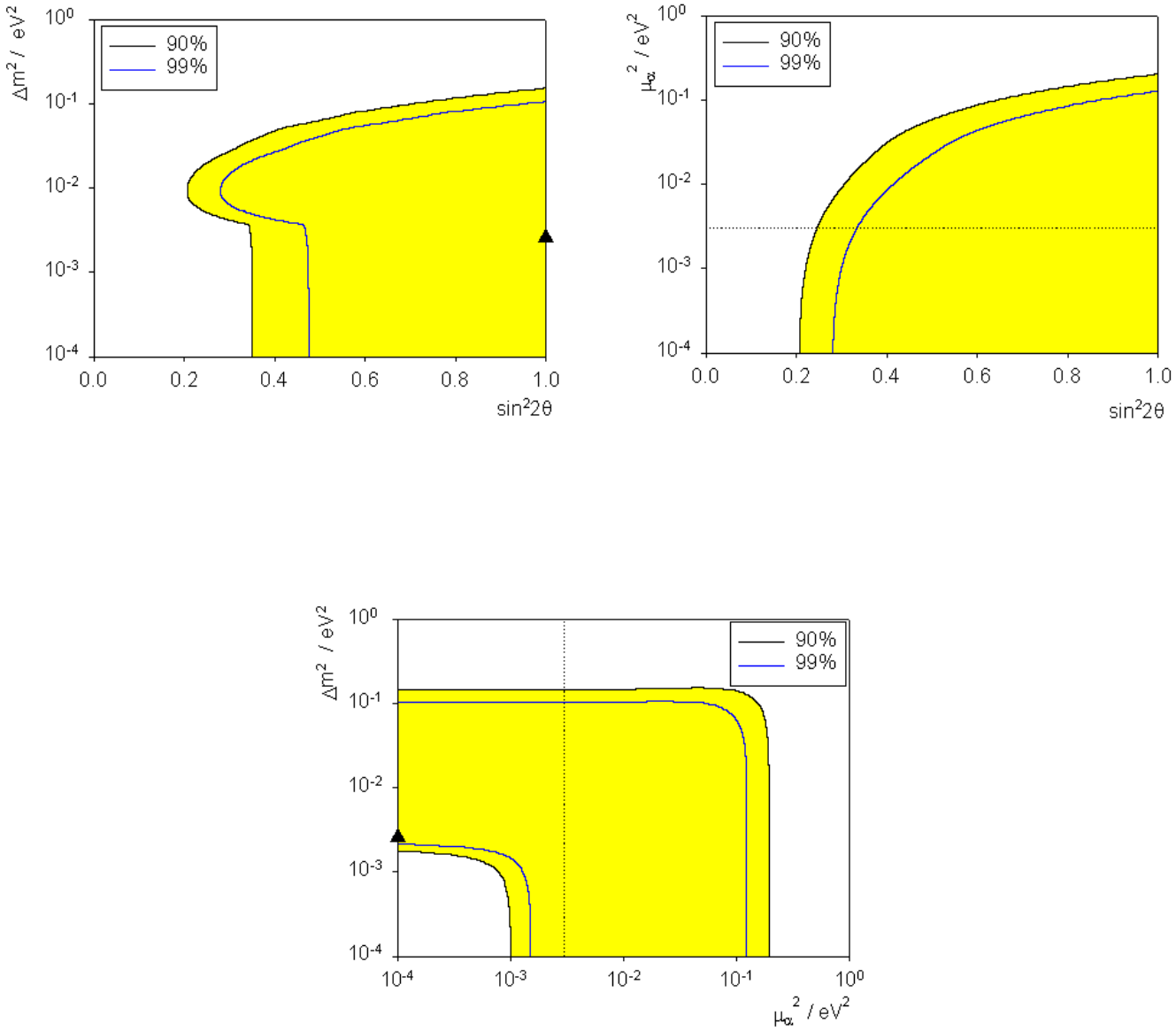

Figure 5.12: Sensitivity contours for model **QD1** at 90 and 99 percent confidence level including standard oscillations and quantum decoherence effects inversely proportional to the neutrino energy. The triangle denotes the experimental point of best fit for Δm^2 and $\sin^2 2\theta$ [127], and the line denotes the current upper bound on γ_α from [180].

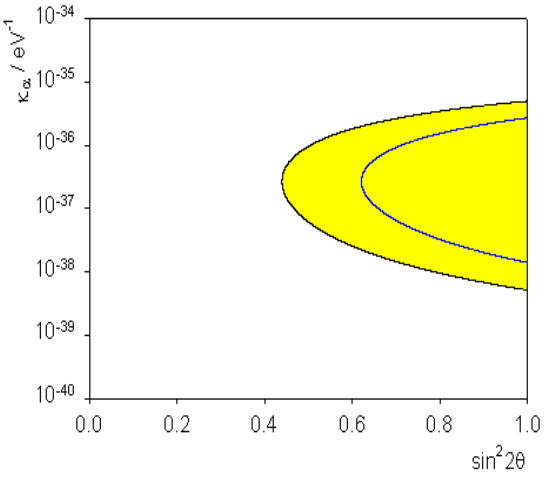

Figure 5.13: Sensitivity contours for model **QD1** at 90 and 99 percent confidence level for quantum decoherence effects only with the parameter κ_α proportional to the neutrino energy squared.

therefore, the sensitivity contours are also similar. The first plot in figure 5.12 shows Δm^2 against $\sin^2 2\theta$ with the sensitivity region lying to the right of the contours, highlighted in yellow at the 90% confidence level. The triangle, which is included within this region, denotes the current experimental point of best fit. The top right frame shows the quantum decoherence parameter as a function of the mixing angle. Again, the region of interest lies within the contours and the broken line shows the current upper bound. From our simulations, we are able to place a weak bound of $\mu_\alpha^2 \lesssim 10^{-1}\ eV^2$.

Decoherence parameters proportional to the neutrino energy squared

We now set $a = \alpha = \frac{\kappa_\alpha E^2}{2}$, so the oscillation probability takes the form

$$P[\nu_\mu \to \nu_\tau] = \frac{1}{2}\sin^2(2\theta)\left[1 - e^{-5.06\times10^{27}\kappa_\alpha E^2 L}\cos\left(\frac{2.54\Delta m^2}{E}L\right)\right]. \qquad (5.21)$$

We are again able to consider the case when $\Delta m^2 = 0$. In this case the oscillation probability takes the form

$$P[\nu_\mu \to \nu_\tau] = \frac{1}{2}\sin^2(2\theta)\left[1 - e^{-5.06\times10^{27}\kappa_\alpha E^2 L}\right]. \qquad (5.22)$$

The sensitivity contour for the simplified probability (5.22) is presented in figure 5.13. Here, the allowed region lies inside the contours, highlighted in yellow at the 90%

confidence level. We are able to place a very stringent bound on κ_α of approximately $10^{-35}\ eV^{-1}$.

When we include a non-zero Δm^2, we obtain the sensitivity surface and contours in figures 5.14 and 5.15 respectively. Again, the sensitivity surface in the three dimensional parameter space has a very similar shape to the previous models but here, the surface is split into two distinct parts. From figure 5.15, we see that the experimental point of best fit for Δm^2 lies within our sensitivity region and that we are able to place an upper bound on the quantum decoherence parameter of $\kappa_\alpha \lesssim 10^{-35}\ eV^{-1}$.

Summary of Model QD1

This is the simplest model which extends neutrino oscillations to include quantum decoherence effects and contains two quantum decoherence parameters which we assume to be equal, $a = \alpha$. In all cases, we are able to find sensitivity regions for neutrino oscillations which occur due to quantum decoherence effects only. We are also able to construct three dimensional sensitivity surfaces in the more general case when quantum decoherence effects modify standard oscillations.

5.2.3 Model QD2

This model generalizes the model **QD1** since we have two non-zero quantum decoherence parameters, a and α but, in this case, we leave them independent. In the limit $a = \alpha$, we regain Model **QD1**. Since we are able to only simulate two parameters in addition to $\sin^2 2\theta$, we fix $\Delta m^2 = 2.6 \times 10^{-3}\ eV^2$ [140]. In this model, we cannot consider the case of quantum decoherence effects and no standard oscillations as the quantity Γ_2 in equation (5.4) becomes imaginary.

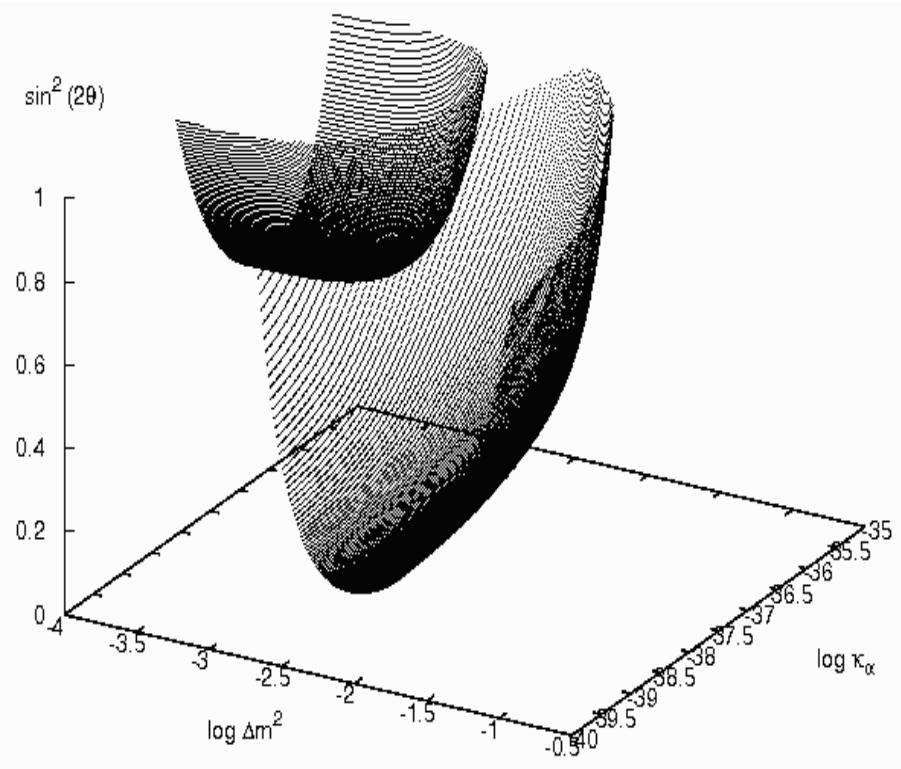

Figure 5.14: Sensitivity volume for model **QD1** at 90 percent confidence level including standard oscillations plus quantum decoherence effects proportional to the neutrino energy squared.

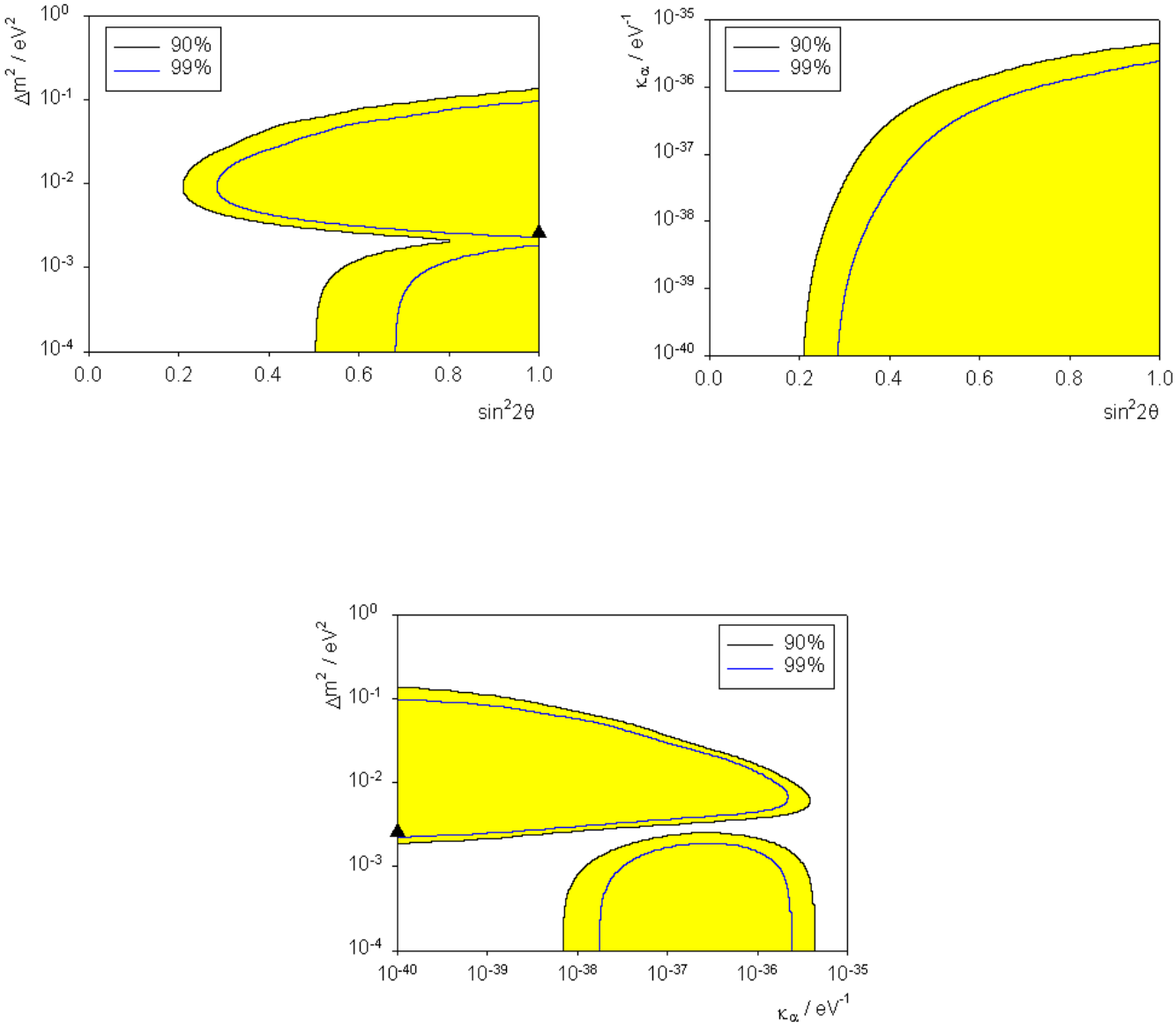

Figure 5.15: Sensitivity contours for model **QD1** at 90 and 99 percent confidence level including standard oscillations and quantum decoherence effects proportional to the neutrino energy squared.

Decoherence parameters with no dependence on the neutrino energy

Here, we set $a = \frac{\gamma_a}{2}$ and $\alpha = \frac{\gamma_\alpha}{2}$. The oscillation probability therefore takes the form (5.3) with

$$\begin{aligned} \Gamma_s &= 2.5 \times 10^9 (\gamma_\alpha + \gamma_a) L; \\ \Gamma_d &= 2.5 \times 10^9 (\gamma_\alpha - \gamma_a) L; \\ \Gamma_2 &= 2 \left[\left(1.27 \frac{\Delta m^2 L}{E} \right)^2 - \frac{1}{4} [2.5 \times 10^9 (\gamma_\alpha - \gamma_a) L]^2 \right]^{\frac{1}{2}}. \end{aligned}$$

Here, γ_a and γ_α are measured in eV.

The sensitivity surface in the three dimensional parameter space is shown in figure 5.16 with the resulting sensitivity contours shown in figure 5.17. The surface in figure 5.16 is somewhat unexpected as it collapses to a line at high values of the quantum decoherence parameters. This line is the cause of the spike in the lower plot in figure 5.17. For smaller values of these parameters, we obtain a genuine surface, above which lies the sensitivity volume. The sensitivity contours for γ_α and γ_a are very similar, as we might expect, and we are able to place an upper bound of approximately 10^{-13} eV on both these parameters, the relevant sensitivity regions lying to the right of the contours with the 90% confidence level region being highlighted in yellow. For both quantum decoherence parameters, zero is an allowed value at $\sin^2 2\theta = 1$ indicating the possibility of neutrino oscillations arising with no quantum decoherence effects. The lower plot of figure 5.17 shows the two quantum decoherence parameters plotted against each other and we are unable to distinguish between the 90 and 99% confidence levels.

Decoherence parameters inversely proportional to the neutrino energy

Here, we set $\alpha = \frac{\mu_\alpha^2}{4E}$ and $a = \frac{\mu_a^2}{4E}$ and so the oscillation probability (5.3) contains the quantities

$$\begin{aligned} \Gamma_s &= 1.27 (\mu_\alpha^2 + \mu_a^2) \frac{L}{E}; \\ \Gamma_d &= 1.27 (\mu_\alpha^2 - \mu_a^2) \frac{L}{E}; \\ \Gamma_2 &= \frac{2.54 L}{E} \left[(\Delta m^2)^2 - \frac{1}{4} (\mu_\alpha^2 - \mu_a^2)^2 \right]^{\frac{1}{2}}. \end{aligned}$$

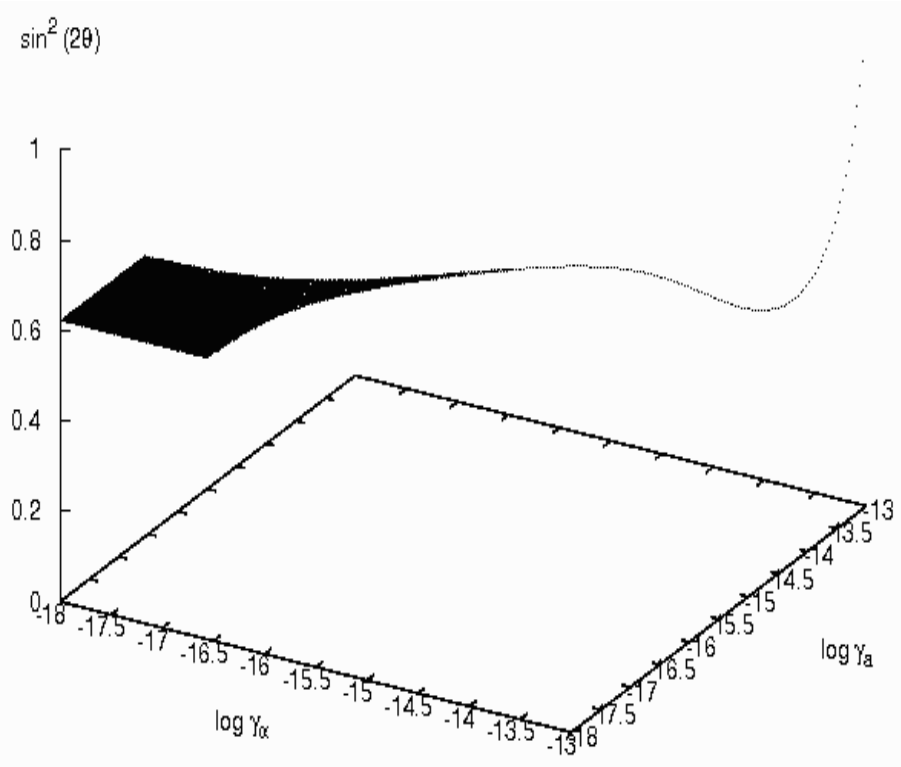

Figure 5.16: Sensitivity volume for model **QD2** at 90 percent confidence level for standard oscillations plus quantum decoherence effects with no dependence on the neutrino energy.

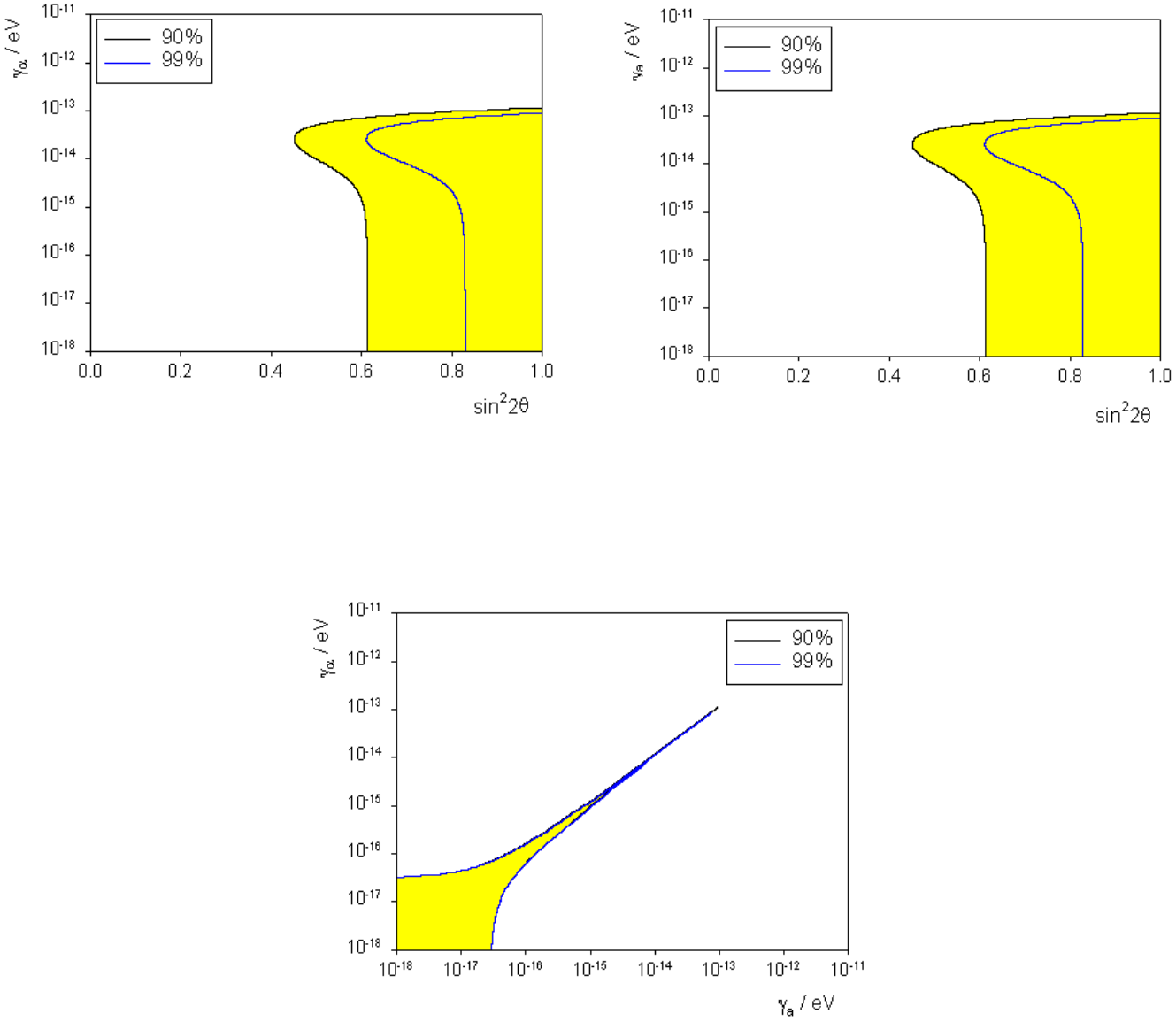

Figure 5.17: Sensitivity contours for model **QD2** at 90 and 99 percent confidence level including standard oscillations and quantum decoherence effects with no dependence on the neutrino energy.

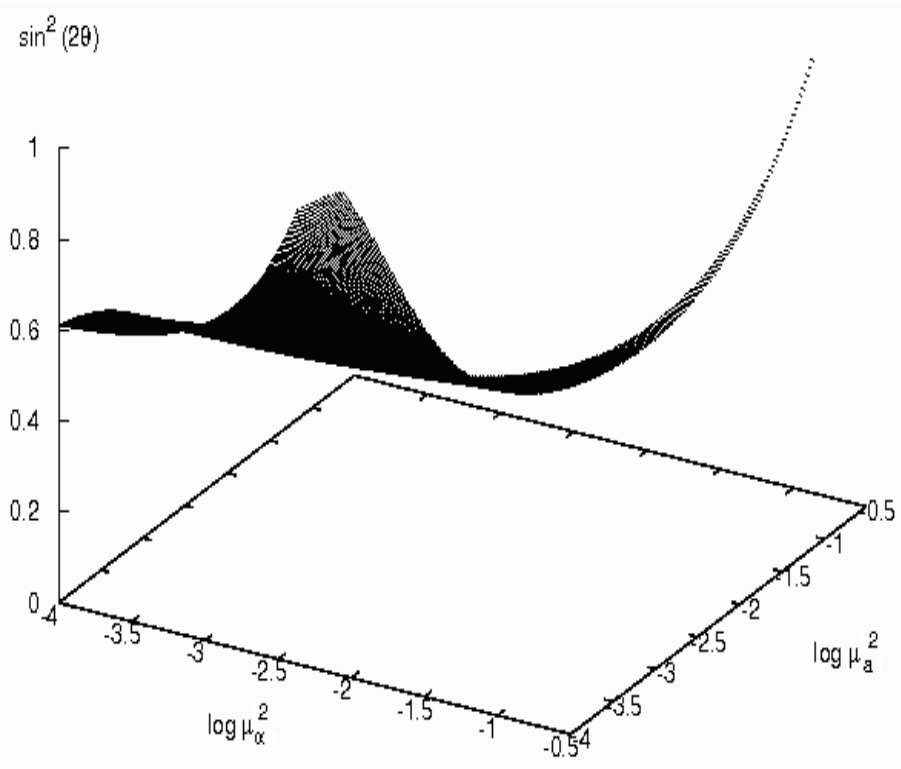

Figure 5.18: Sensitivity volume for model **QD2** at 90 percent confidence level for standard oscillations plus quantum decoherence effects inversely proportional to the neutrino energy.

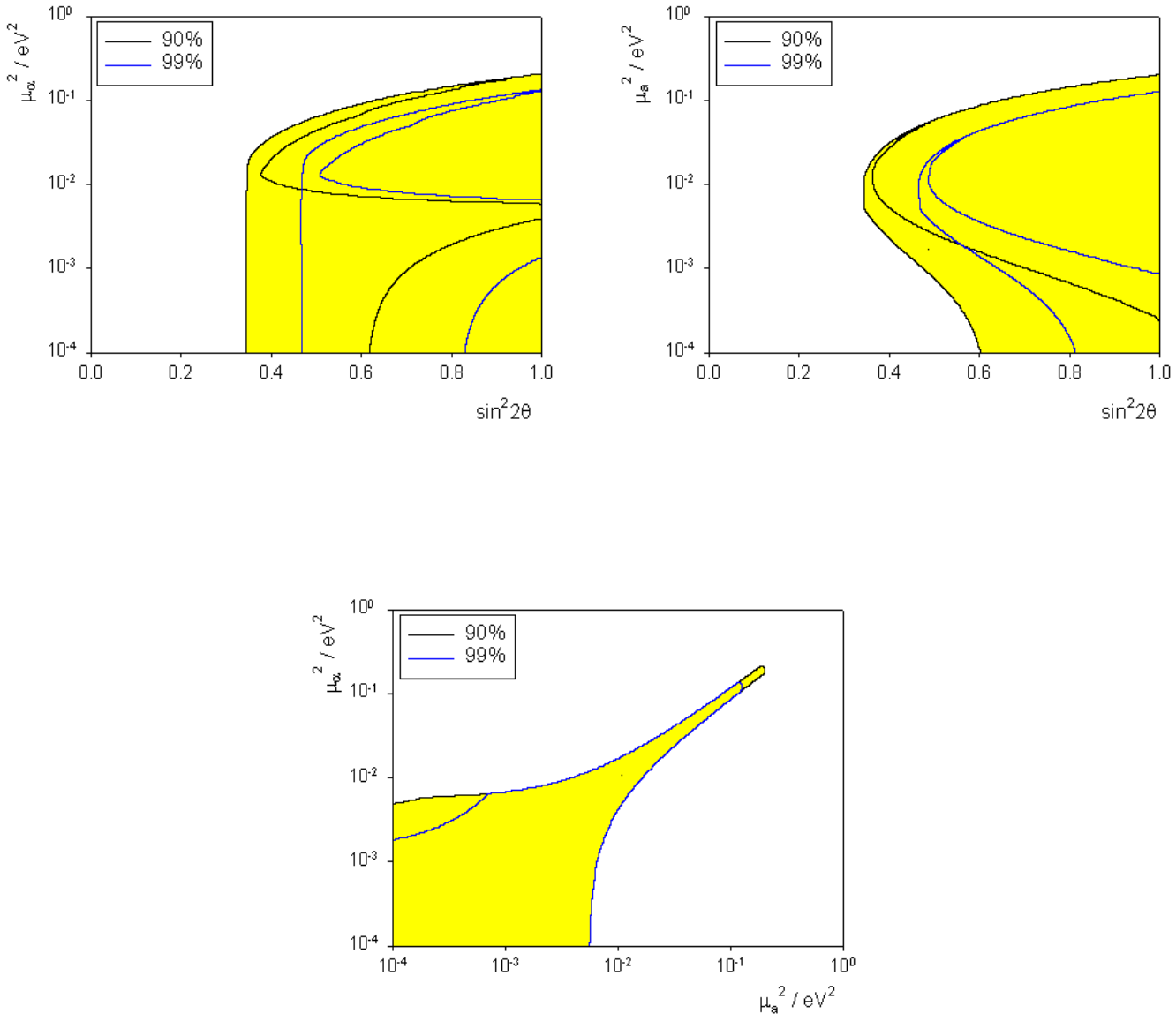

Figure 5.19: Sensitivity contours for model **QD2** at 90 and 99 percent confidence level including standard oscillations and quantum decoherence effects inversely proportional to the neutrino energy.

The sensitivity surface is shown in figure 5.18 with the corresponding sensitivity contours in figure 5.19. The surface shown in figure 5.18 shares some of the characteristics of that shown in figure 5.16 such as an almost collapsing spike at high values of the decoherence parameters. For smaller values of these parameters, however, the surface is not flat as in the previous case. Interpreting the sensitivity contours is, therefore, not trivial. The sensitivity volume lies above the surface shown in figure 5.19 and includes the region containing $\sin^2 2\theta = 1$. The sensitivity regions in figure 5.19 are shown, at the 90% confidence level, in yellow for clarity. In both the upper plots of this figure, the region lies inside the outer contours and contains zero corresponding to no quantum decoherence effects. It is interesting to note that the figures are not as symmetric as in the first case of this model we considered. From figure 5.19, we are able to place a weak upper bound on both decoherence parameters of 0.5 eV^2. The lower frame of figure 5.19 shows the two quantum decoherence parameters plotted against each other with the sensitivity region being contained within the spike. We are only just able to distinguish between the two confidence levels.

Decoherence parameters proportional to the neutrino energy squared

In this case, we set $a = \frac{\kappa_a E^2}{2}$ and $\alpha = \frac{\kappa_\alpha E^2}{2}$. The oscillation probability (5.3) now contains

$$\begin{aligned} \Gamma_s &= 2.53 \times 10^{27}(\kappa_\alpha + \kappa_a)E^2 L; \\ \Gamma_d &= 2.53 \times 10^{27}(\kappa_\alpha - \kappa_a)E^2 L; \\ \Gamma_2 &= 2\left[\left(1.27\frac{\Delta m^2 L}{E}\right)^2 - \frac{1}{4}\left[2.53 \times 10^{27}(\kappa_\alpha - \kappa_a)E^2 L\right]^2\right]^{\frac{1}{2}}; \end{aligned}$$

where κ_α and κ_a are measured in eV^{-1}.

The sensitivity surface and sensitivity contours are shown in figures 5.20 and 5.21 respectively. The sensitivity surface shown in figure 5.20 is very similar to that in figure 5.16 with the collapse of the surface to a line and the sensitivity region lying above the surface at small values of the quantum decoherence parameters. The contours for both κ_a and κ_α plotted against the mixing angle in figure 5.21 enable us to place upper bonds on these parameters of approximately 10^{-38} eV^{-1}, the sensitivity regions lying to the right of the contours. This upper bound is more

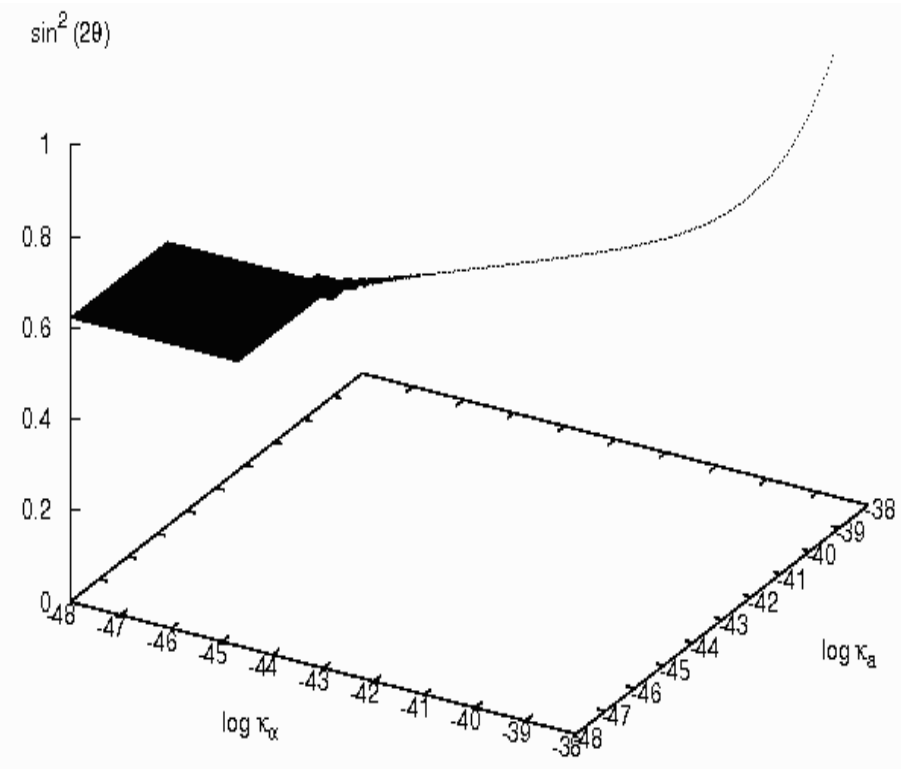

Figure 5.20: Sensitivity volume for model **QD2** at 90 percent confidence level for standard oscillations plus quantum decoherence effects proportional to the neutrino energy squared.

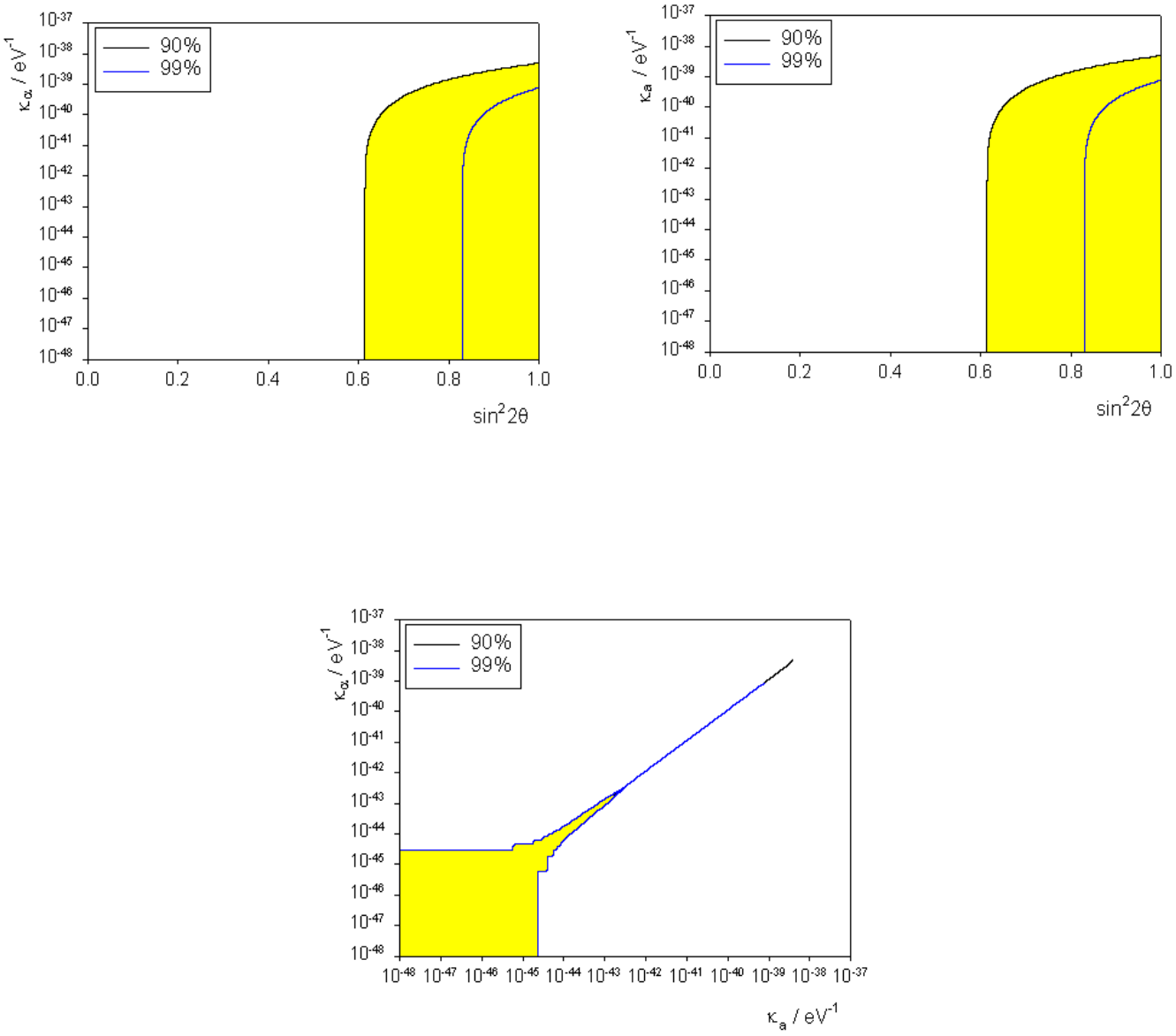

Figure 5.21: Sensitivity contours for model **QD2** at 90 and 99 percent confidence level including standard oscillations and quantum decoherence effects proportional to the neutrino energy squared.

stringent than that in model **QD1**, perhaps due to the collapse of the surface. The lower frame of figure 5.21 shows κ_a against κ_α. Here, we the sensitivity region lies inside the spike and we are unable to tell the difference between the two confidence levels.

Summary of Model QD2

This model is a generalization of the first model we considered as it contains two quantum decoherence parameters, a and α which, in this model, we consider to be independent. In all three cases, the surfaces which bound the sensitivity volume collapse down to a spike near $a = \alpha$ for larger values of these parameters. We also note that there is a symmetry between these two parameters in the first and third cases we considered but found that this symmetry was broken when we considered the parameters to be inversely proportional to the neutrino energy.

5.2.4 Model QD3

This model contains just one quantum decoherence parameter, b, and so we do not fix Δm^2. Since b lies in the argument of the cosine term in the oscillation probability (5.5) we are not able to set $\Delta m^2 = 0$ to examine oscillations which arise as a consequence of quantum decoherence alone, as otherwise, this argument would become imaginary. The general oscillation probability is given in equations (5.5) and (5.6).

Decoherence parameters with no dependence on the neutrino energy

Setting $b = \frac{\gamma_b}{2}$ and replacing the constants c and $\hbar$, the oscillation probability is that in equation (5.5) with

$$\Gamma_3 = 2\left[\left(1.27\frac{\Delta m^2 L}{E}\right)^2 - \left(2.5\times 10^9 \gamma_b L\right)^2\right]^{\frac{1}{2}}. \tag{5.23}$$

Figures 5.22 and 5.23 show the sensitivity volume and contours, respectively, in this case. The sensitivity region in figure 5.22 lies above the surface and it is simple to relate this surface to the contours shown in figure 5.23. The first plot in figure 5.23 shows Δm^2 as a function of the mixing angle, θ, with the sensitivity region lying inside the contours (highlighted in yellow at the 90% confidence level). The triangle

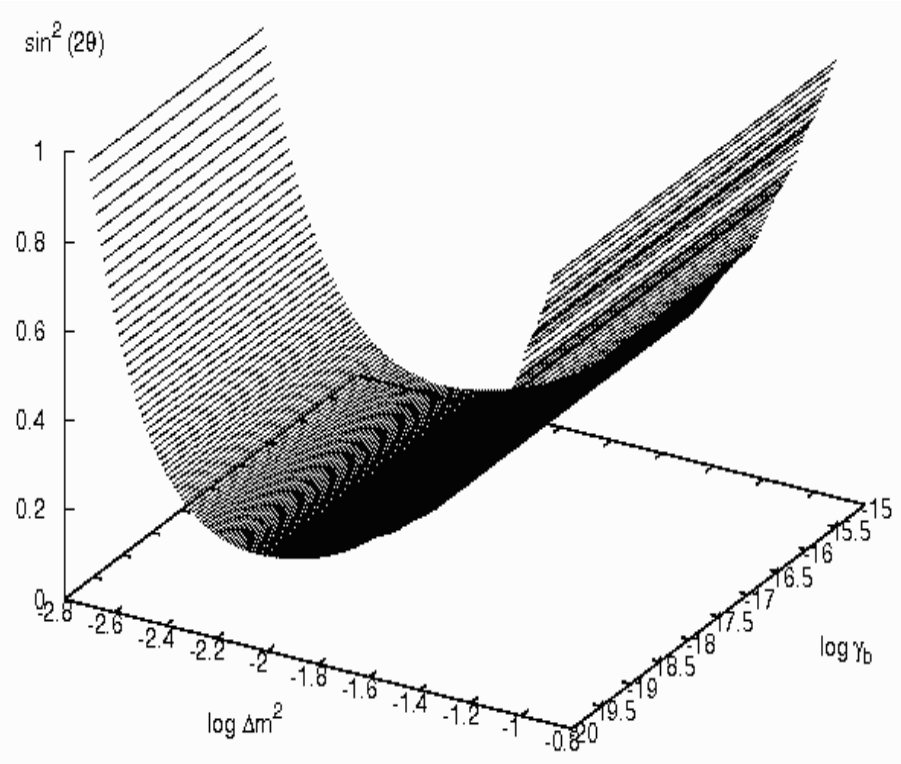

Figure 5.22: Sensitivity volume for model **QD3** at 90 percent confidence level for standard oscillations plus quantum decoherence effects with no dependence on the neutrino energy.

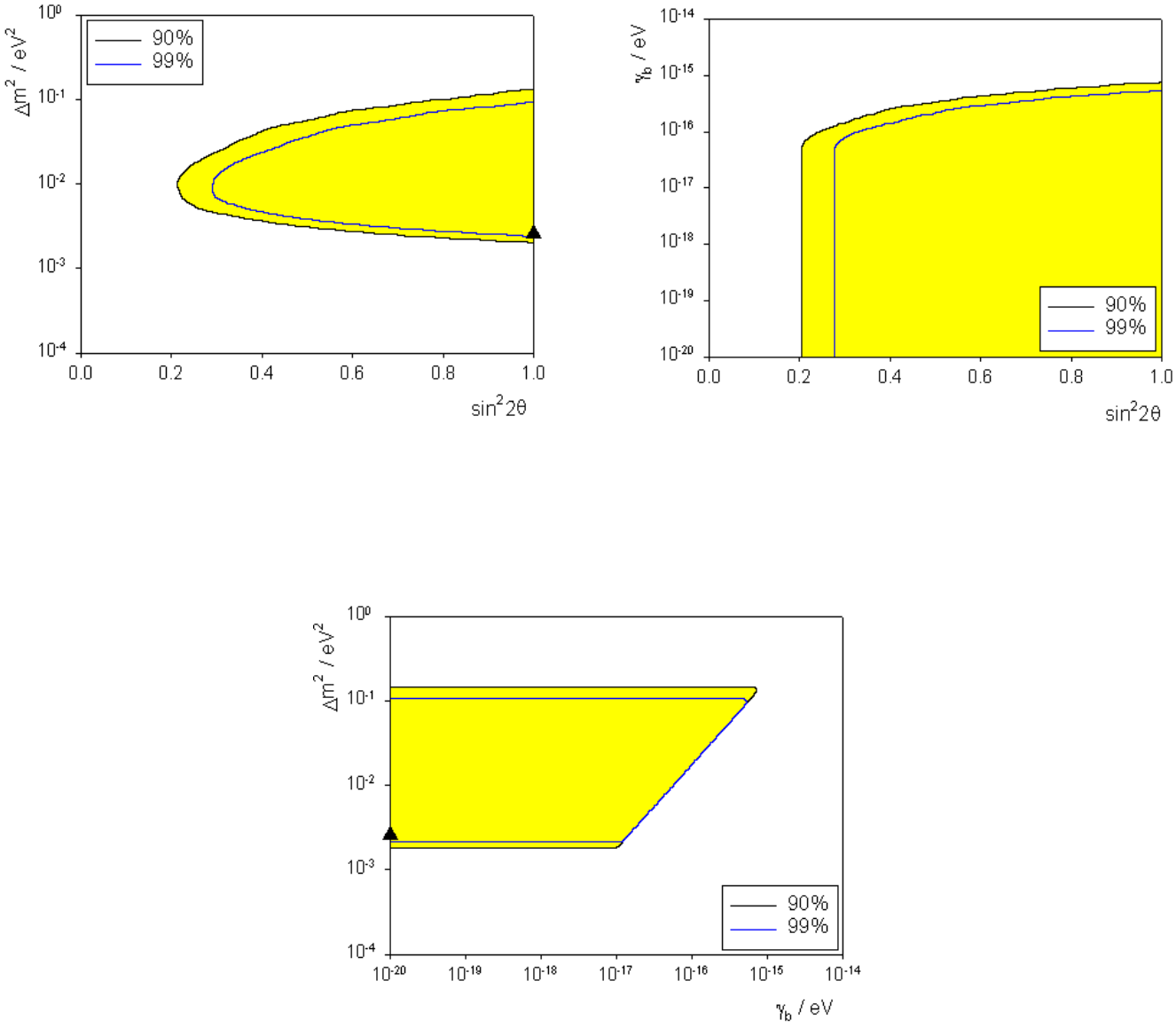

Figure 5.23: Sensitivity contours for model **QD3** at 90 and 99 percent confidence level including standard oscillations and quantum decoherence effects with no dependence on the neutrino energy.

denotes the point of best fit from Super-Kamiokande and K2K data. The top right frame of figure 5.23 shows γ_b against $\sin^2 2\theta$, the sensitivity region again lying to the right of the contours. We are able to place an upper bound on this parameter of 10^{-15} eV. The lower plot of figure 5.23 shows Δm^2 against γ_b.

Decoherence parameters inversely proportional to the neutrino energy

The oscillation probability takes the form in (5.5) where

$$\Gamma_3 = \frac{2.54L}{E}\left[\left(\Delta m^2\right)^2 - \left(\mu_b^2\right)^2\right]^{\frac{1}{2}}, \tag{5.24}$$

and we have replaced c and $\hbar$, and set $b = \frac{\mu_b^2}{4E}$, so μ_b^2 is measured in eV^2.

Figure 5.24 shows the sensitivity volume for this case. We note that it is almost the same as that in figure 5.22 except at high values of the decoherence parameter where the surface turns over. The corresponding sensitivity contours are shown in figure 5.25. The turning over of the surface leads to different contours from those in the first case. The first frame in figure 5.25 shows Δm^2 against $\sin^2 2\theta$ with the triangle denoting the experimental point of best fit. The contour is fairly complicated but the sensitivity region, at the 90% confidence limit, is highlighted in yellow for clarity. The point of best fit from experiment lies within this region. The second frame of figure 5.25 shows μ_b^2 as a function of $\sin^2 2\theta$ with the sensitivity region lying to the right of the contours. From this plot, we are able to place a very weak upper bound of 1 eV^2 on this parameter and we note that $\mu_b^2 = 0$ is also an allowed point implying that this model is compatible with standard neutrino oscillations. The lower frame of figure 5.25 shows the relationship between Δm^2 and μ_b^2 with the sensitivity region lying within the contours, as highlighted in yellow (at least for the 90% confidence limit).

Decoherence parameters proportional to the neutrino energy squared

For this energy dependence, we set $b = \frac{\kappa_b E^2}{2}$, so, replacing c and $\hbar$, the oscillation probability is that in (5.5) with

$$\Gamma_3 = 2\left[\left(1.27\frac{\Delta m^2 L}{E}\right)^2 - \left[2.53\times 10^{27}\kappa_b E^2 L\right]^2\right]^{\frac{1}{2}}, \tag{5.25}$$

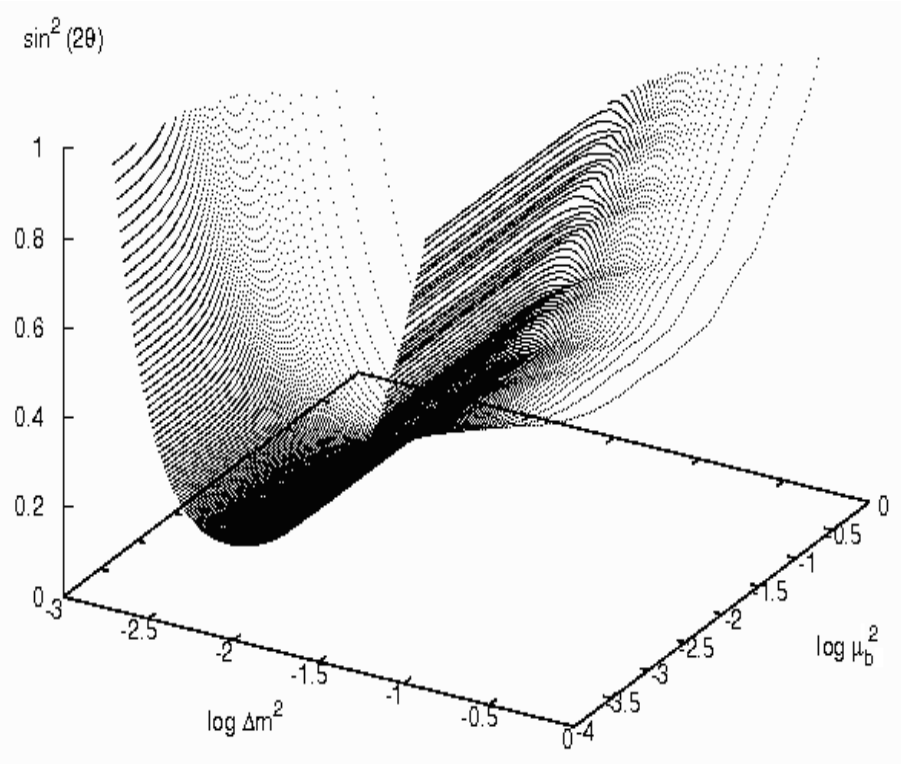

Figure 5.24: Sensitivity volume for model **QD3** at 90 percent confidence level for standard oscillations plus quantum decoherence effects inversely proportional to the neutrino energy.

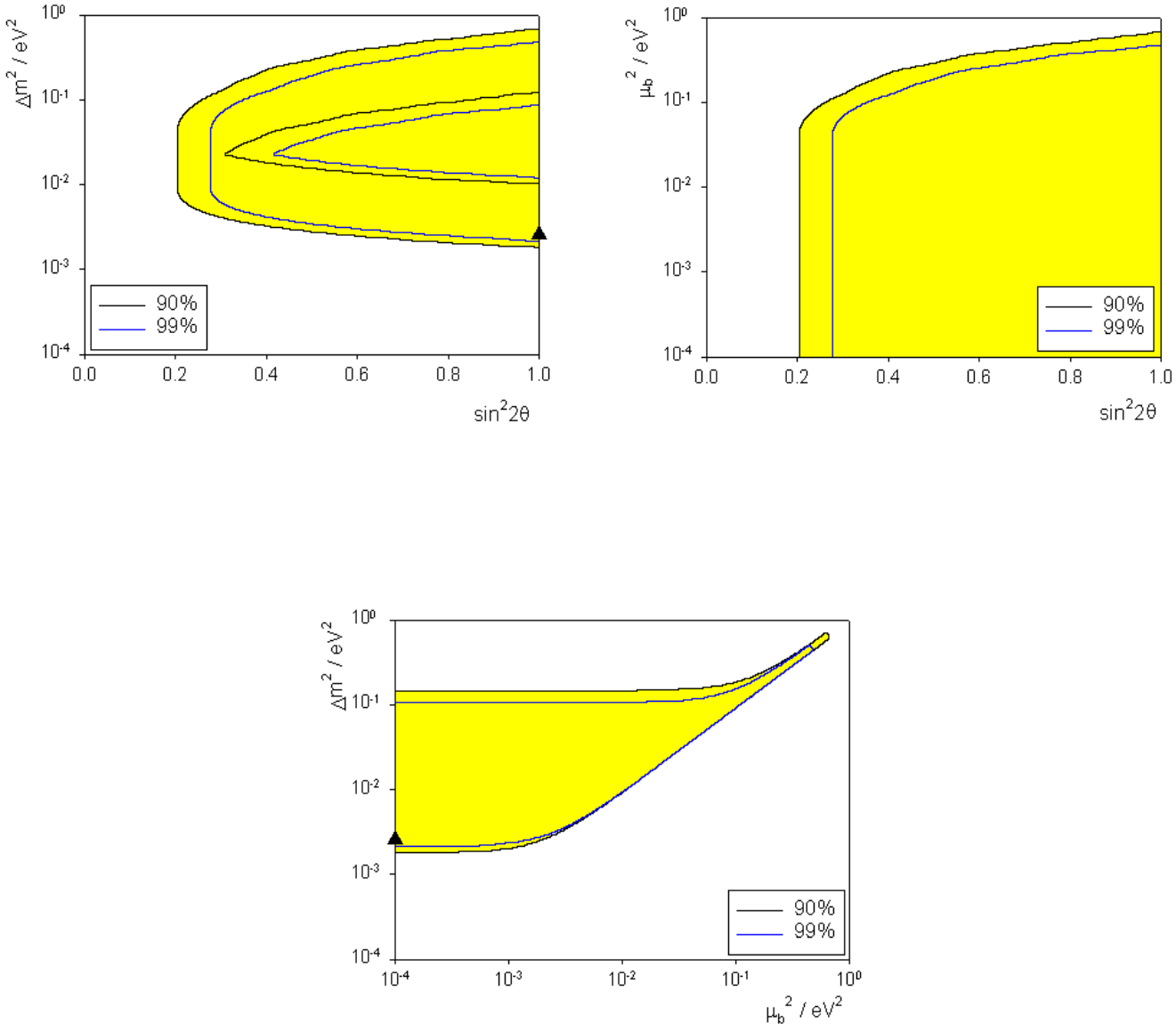

Figure 5.25: Sensitivity contours for model **QD3** at 90 and 99 percent confidence level including standard oscillations and quantum decoherence effects inversely proportional to the neutrino energy.

and κ_b is measured in eV^{-1}.

The sensitivity volume for this model is shown in figure 5.26 with the corresponding sensitivity contours shown in figure 5.27. The surface in figure 5.26 is qualitatively the same as that in the case when the decoherence parameters had no dependence upon the neutrino energy, resulting in very similar sensitivity contours. The first frame in figure 5.27 shows Δm^2 as a function of the mixing angle with the sensitivity region, highlighted in yellow, lying inside the contours. We note that the experimental point of best fit for Δm^2, denoted by the triangle, lies within this region. The top right frame of the same figure shows κ_b against $\sin^2 2\theta$ where the sensitivity region lies beneath the curve, including the value zero for this parameter. We are able to place an upper bound on the parameter κ_b of $10^{-43}\ eV^{-1}$. The lower frame of figure 5.27 plots Δm^2 against κ_b with the sensitivity region lying inside the curve.

Summary of Model QD3

This model contains one quantum decoherence parameter, b. Since we had just one extra parameter, we were able to let Δm^2 vary and, in each case, our simulated sensitivity regions included the experimental point of best fit. We were able to place upper bounds on the quantum decoherence parameters contained within this model and found they were significantly smaller than in the previous two models in the cases when the decoherence parameters had no dependence on the neutrino energy or were proportional to the square of the neutrino energy.

5.2.5 Model QD4

This model combines models **QD1** and **QD3** discussed above. We now have three non-zero decoherence parameters, $a = \alpha$ and b and, therefore, we fix Δm^2 to have the value $\Delta m^2 = 2.6 \times 10^{-3}\ eV^2$. The general form of the oscillation probability for this model is given by equations (5.7) and (5.8).

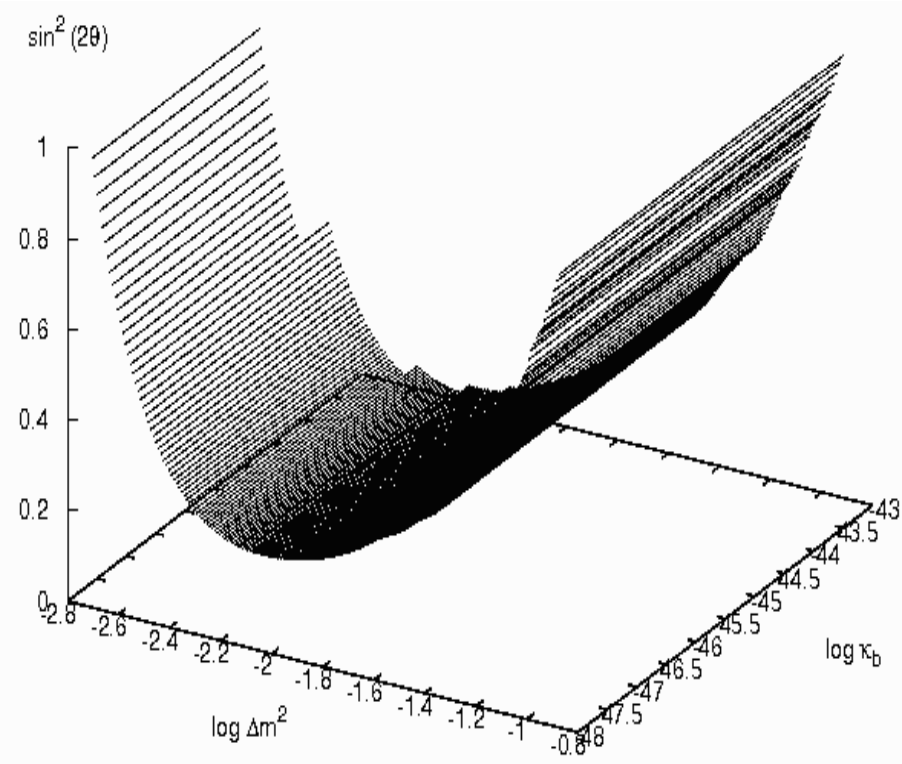

Figure 5.26: Sensitivity volume for model **QD3** at 90 percent confidence level for standard oscillations plus quantum decoherence effects proportional to the neutrino energy squared.

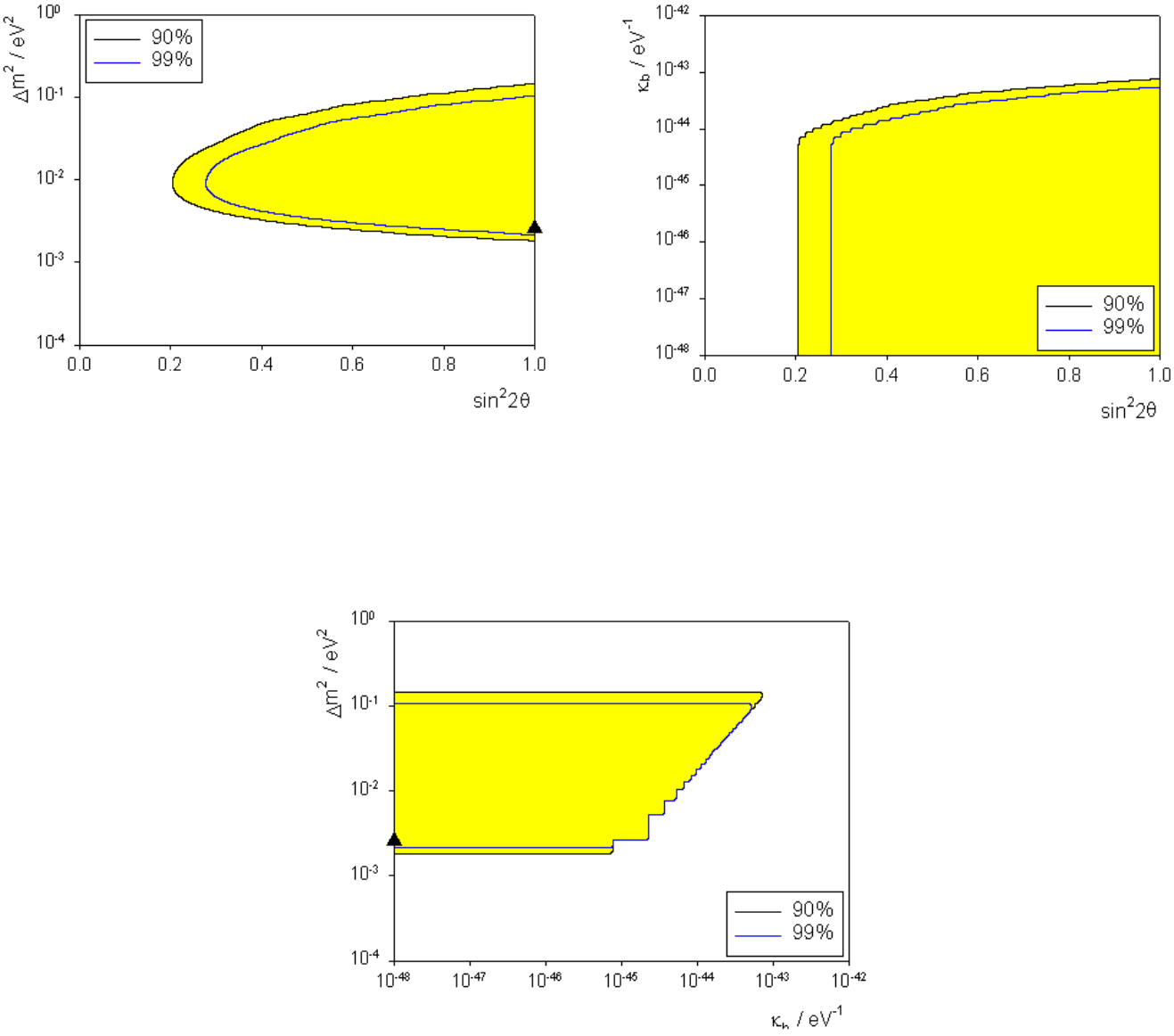

Figure 5.27: Sensitivity contours for model **QD3** at 90 and 99 percent confidence level including standard oscillations and quantum decoherence effects proportional to the neutrino energy squared.

Decoherence parameters with no dependence on the neutrino energy

For this energy dependence, we set $a = \alpha = \frac{\gamma_\alpha}{2}$ and $b = \frac{\gamma_b}{2}$. The oscillation probability, therefore, has the form in equation (5.7) with

$$\Gamma_4 = 2\left[\left(1.27\frac{\Delta m^2 L}{E}\right)^2 - [2.5\times 10^9 \gamma_b L]^2\right]^{\frac{1}{2}}; \tag{5.26}$$

and $2\alpha \rightarrow 5\times 10^9\gamma_\alpha$. Here, we have replaced c and $\hbar$ and both quantum decoherence parameters are measured in eV.

The sensitivity volume and contours are shown in figures 5.28 and 5.29 respectively. The sensitivity volume lies above the surface in figure 5.28, which corresponds to the regions on the right of the contours in the top two frames of figure 5.29 and to the left of the lower figure. From the first frame of figure 5.29, which shows γ_α against $\sin^2 2\theta$, we are able to place an upper bound on the quantum decoherence parameter of $10^{-12}\ eV$. The top right frame show γ_b as a function of $\sin^2 2\theta$ and we see that there is a sharp cut-off in this parameter enabling us to place a bound of $\gamma_b < 10^{-16}\ eV$ on γ_b. The bottom plot shows the relationship between the two decoherence parameters, γ_α and γ_b. Here, the two confidence levels are barely distinguishable.

Decoherence parameters inversely proportional to the neutrino energy

For this energy dependence, we set $a = \alpha = \frac{\mu_\alpha^2}{4E}$ and $b = \frac{\mu_b^2}{4E}$. Replacing the constants, c and $\hbar$, the oscillation probability takes the form of (5.7) where

$$\Gamma_4 = \frac{2.54L}{E}\left[\left(\Delta m^2\right)^2 - \left(\mu_b^2\right)^2\right]^{\frac{1}{2}}; \tag{5.27}$$

and $2\alpha \rightarrow 2.54\frac{\mu_\alpha^2}{E}$. Here, both quantum decoherence parameters are measured in eV^2.

The sensitivity volume for this model is shown in figure 5.30 with the corresponding sensitivity contours in figure 5.31. The sensitivity region in figure 5.30 lies above the surface shown. Examining figure 5.30, it is clear how the projection of the volume onto the $\mu_\alpha^2 - \sin^2 2\theta$ plane, shown in the top left frame of figure 5.31, arises. For each confidence level, we have two curves, which correspond to the front and back edges of the surface. The sensitivity region, therefore, lies inside these curves.

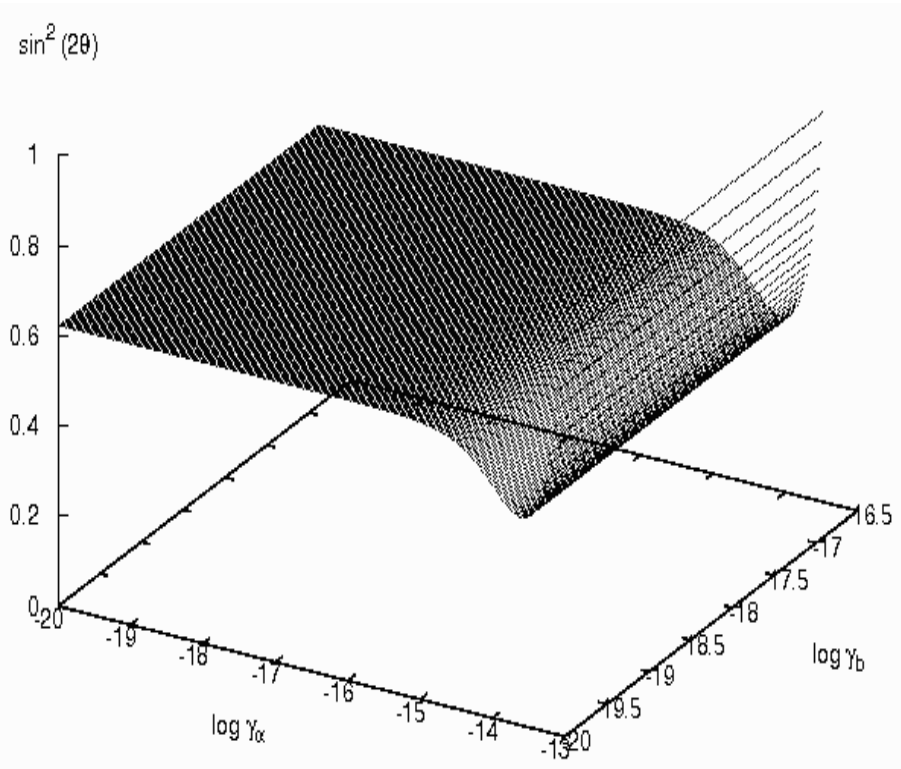

Figure 5.28: Sensitivity volume for model **QD4** at 90 percent confidence level for standard oscillations plus quantum decoherence effects with no dependence on the neutrino energy.

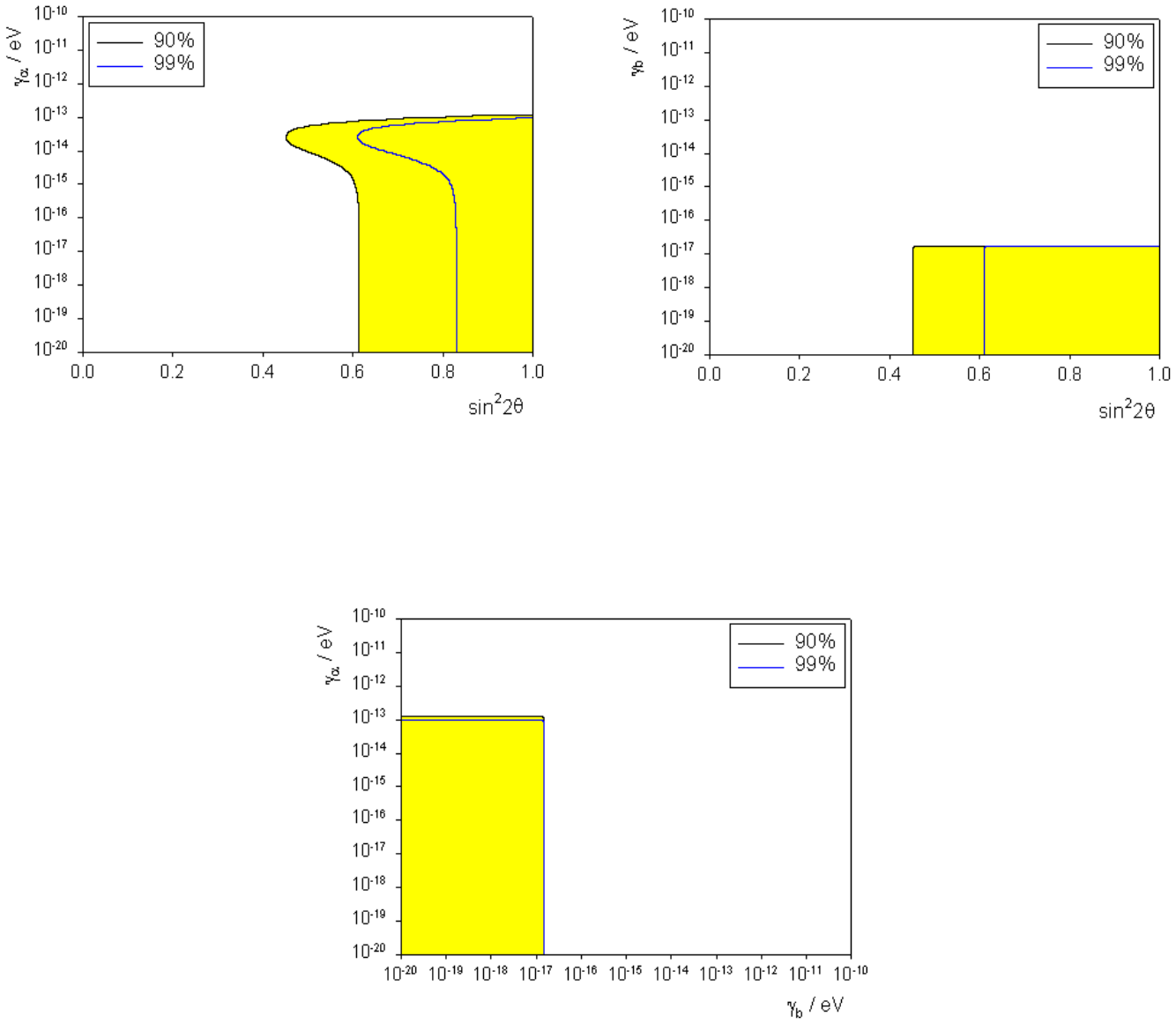

Figure 5.29: Sensitivity contours for model **QD4** at 90 and 99 percent confidence level including standard oscillations and quantum decoherence effects with no dependence on the neutrino energy.

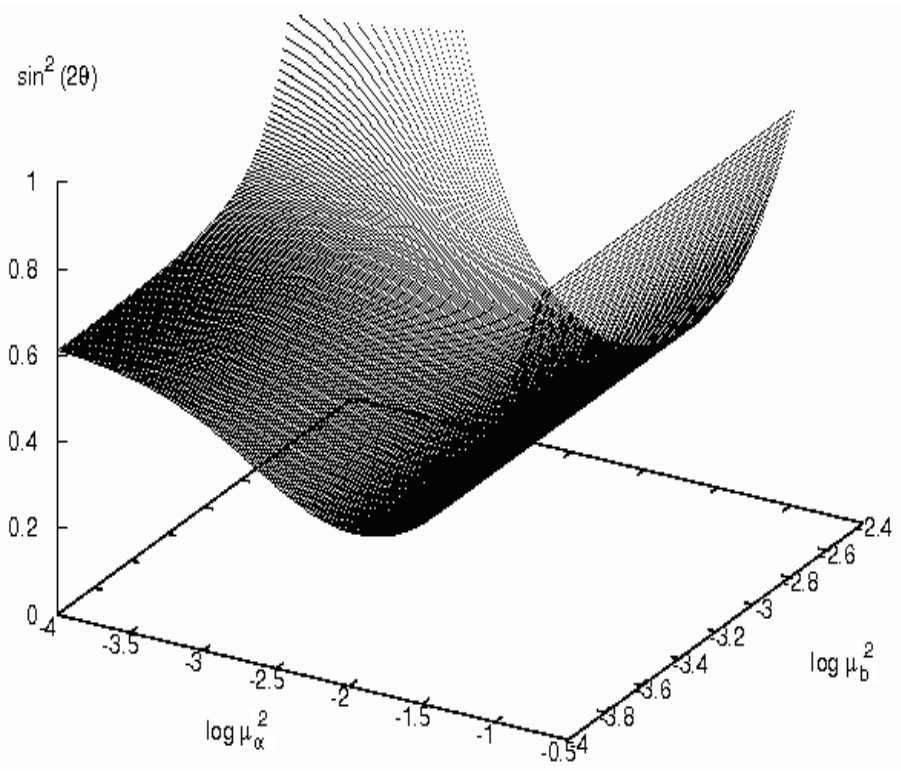

Figure 5.30: Sensitivity volume for model **QD4** at 90 percent confidence level for standard oscillations plus quantum decoherence effects inversely proportional to the neutrino energy.

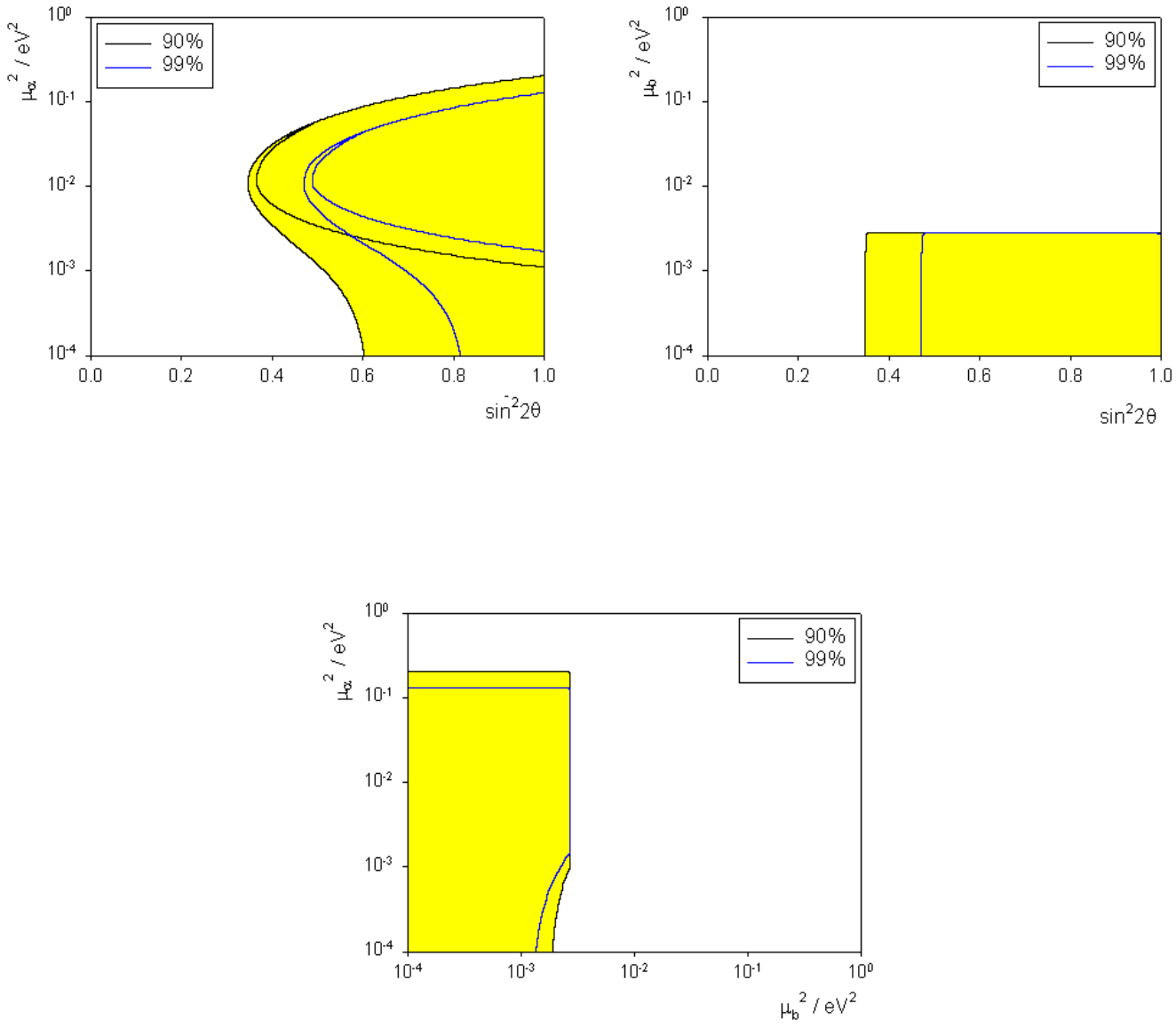

Figure 5.31: Sensitivity contours for model **QD4** at 90 and 99 percent confidence level including standard oscillations and quantum decoherence effects inversely proportional to the neutrino energy.

highlighted in yellow at the 90% confidence level. We are able to place a weak bound of 1 eV^2 on μ_α^2. The top right frame in figure 5.31 shows the projection of the surface onto the $\mu_b^2 - \sin^2 2\theta$ plane. Again, we note that there is a sharp cutoff in the quantum decoherence parameter corresponding to the value at which Γ_4 in (5.27) becomes imaginary. The upper bound for γ_b is therefore of the order 10^{-2} eV^2. The lower frame of figure 5.31 shows the relationship between the two quantum decoherence parameters with the sensitivity region lying inside the contours.

Decoherence parameters proportional to the neutrino energy squared

In this case, we set $a = \alpha = \frac{\kappa_\alpha E^2}{2}$ with $b = \frac{\kappa_b E^2}{2}$. The oscillation probability (5.7) takes the form

$$P[\nu_\mu \to \nu_\tau] = \frac{1}{2}\sin^2(2\theta)\left[1 - e^{-5.06\times 10^{27}\kappa_\alpha E^2 L}\cos\Gamma_4\right]; \tag{5.28}$$

where (cf. (5.8)):

$$\Gamma_4 = 2\left[\left(1.27\frac{\Delta m^2 L}{E}\right)^2 - [2.53\times 10^{27}\kappa_b E^2 L]^2\right]^{\frac{1}{2}}; \tag{5.29}$$

and κ_b and κ_α are measured in eV^{-1} and we have replaced the constants c and $\hbar$.

Figures 5.32 and 5.33 show the sensitivity volume and contours respectively for this energy dependence. The surface shown in figure 5.32 is qualitatively the same as that in the case in which the quantum decoherence parameters have no energy dependence. The resulting sensitivity contours are therefore similar. The first frame of figure 5.33 shows κ_α as a function of the mixing angle, θ, with the sensitivity region lying to the right of the contours. We can place an upper bound of 10^{-38} eV^{-1} on κ_α. The top right frame of the same figure shows the quantum decoherence parameter κ_b against $\sin^2 2\theta$. Again, there is a sharp cut-off in the parameter involving b and we find an upper bound of $\kappa_b < 10^{-45}$ eV^{-1}. The bottom frame shows the relationship between the two quantum decoherence parameters, where the relevant region lies inside the contours and includes the point at which both parameters vanish.

Summary for Model QD4

This model involves three quantum decoherence parameters, $a = \alpha$ and b. The surfaces which bound the sensitivity regions, broadly speaking, are the similar for each

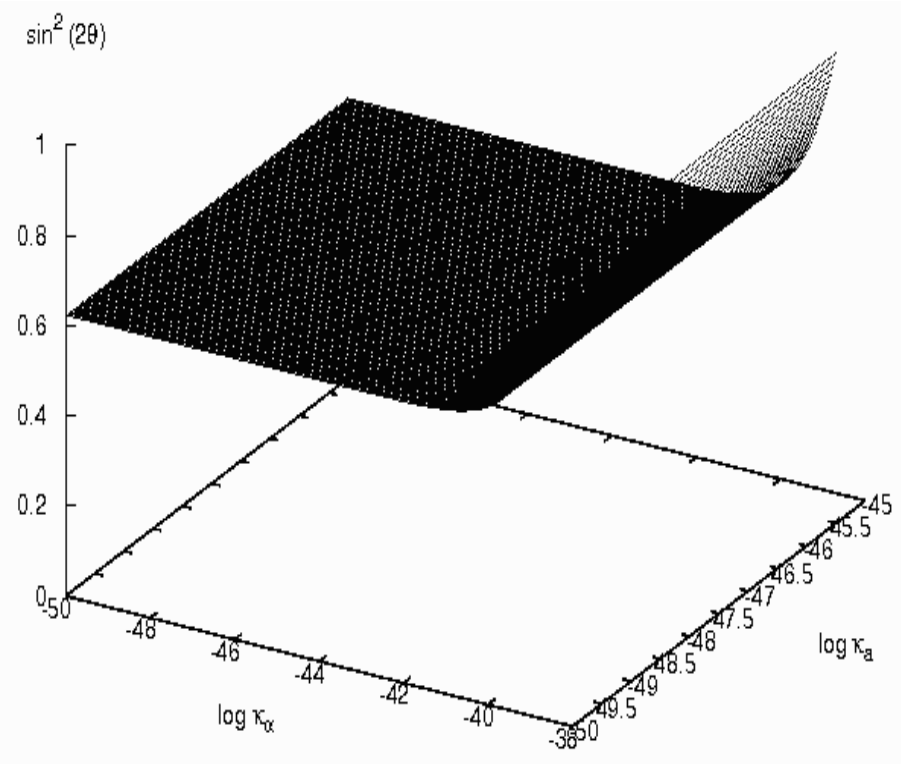

Figure 5.32: Sensitivity volume for model **QD4** at 90 percent confidence level for standard oscillations plus quantum decoherence effects proportional to the neutrino energy squared.

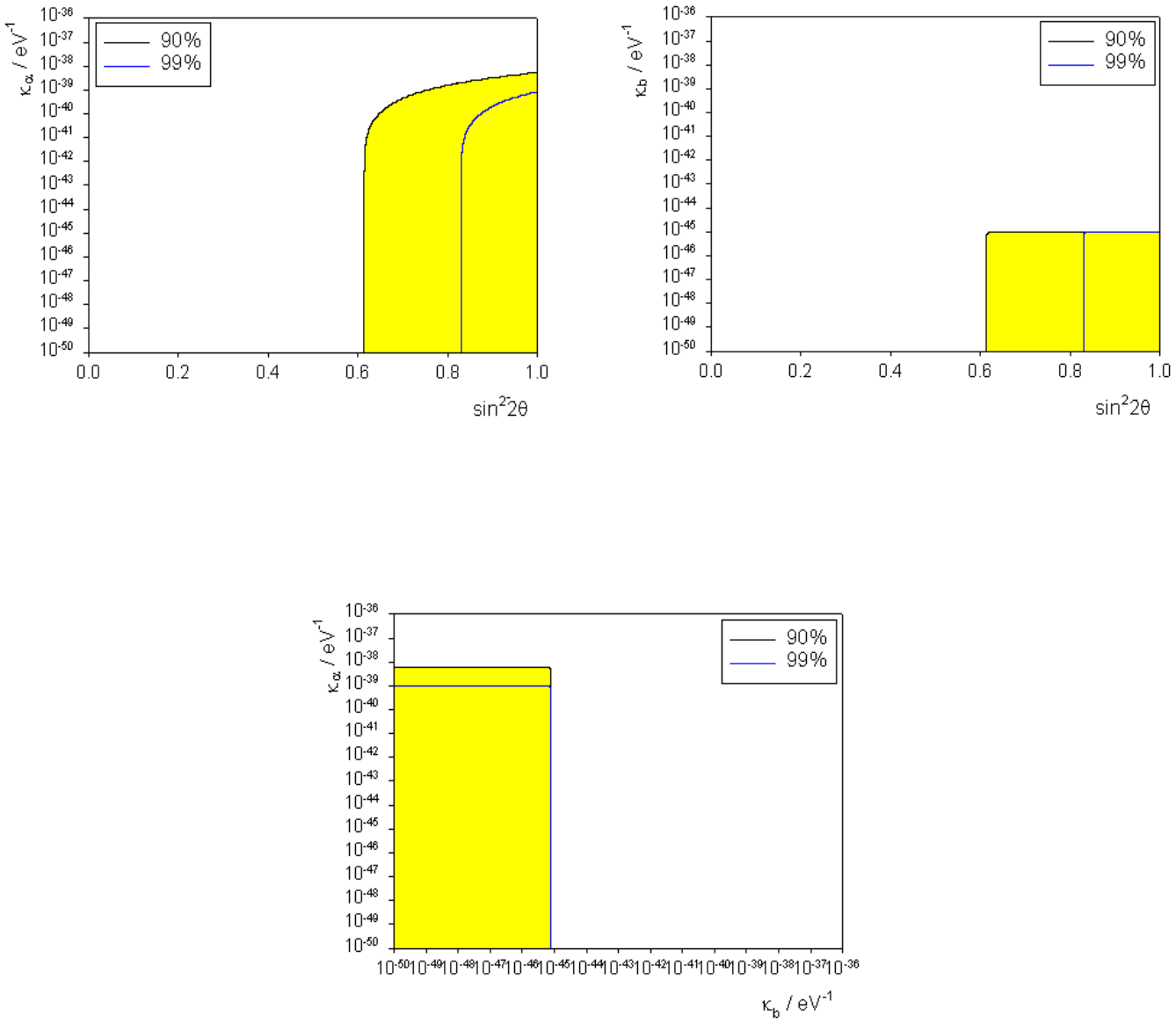

Figure 5.33: Sensitivity contours for model **QD4** at 90 and 99 percent confidence level including standard oscillations and quantum decoherence effects proportional to the neutrino energy squared.

dependence on the parameters of the neutrino energy. The main difference occurs in the surface where the quantum decoherence parameters are inversely proportional to the neutrino energy. In all three cases, we are able to place upper bounds on the quantum decoherence parameters and find that the bound on the b parameter is much smaller than that on the $a = \alpha$ parameter in each case.

5.2.6 Model QD5

This model differs from those we have considered so far as it introduces the quantum decoherence parameter δ, which allows for the non-conservation of energy within the neutrino sector. In this model, we consider all quantum decoherence parameters to be zero, except δ, which enables us to leave Δm^2 as a free parameter.

Decoherence parameters with no dependence on the neutrino energy

We first consider the case when the quantum decoherence parameters have no dependence upon the neutrino energy and so set $\delta = \frac{\gamma_\delta}{2}$. Restoring the constants c and $\hbar$, the oscillation probability (5.9) takes the form

$$P[\nu_\mu \to \nu_\tau] = \frac{1}{2}\left\{\cos^2(2\theta)\left[1 - e^{-5\times10^9\gamma_\delta L}\right] + \sin^2(2\theta)\left[1 - \cos\left(\frac{2.54\Delta m^2}{E}L\right)\right]\right\}; \tag{5.30}$$

where γ_δ is measured in eV.

In this model, we are able to consider the case when $\Delta m^2 = 0$. The oscillation probability in (5.10) therefore takes the form

$$P[\nu_\mu \to \nu_\tau] = \frac{1}{2}\cos^2(2\theta)\left[1 - e^{-5\times10^9\gamma_\delta L}\right]. \tag{5.31}$$

The resulting sensitivity contour is shown in figure 5.34. The sensitivity region lies within the contours, as highlighted in yellow, and the parameter γ_δ covers the region $10^{-13} - 10^{-14}\ eV$ at small values of $\sin^2 2\theta$. However, experimental results from the Super-Kamiokande [49] and K2K [31] experiments indicate that $\sin^2 2\theta \approx 1$. It seems, therefore, that we can rule out this model.

We now consider the case when Δm^2 is non-zero. Figure 5.35 shows the sensitivity volume in this case with the sensitivity contours presented in figure 5.36. The surface shown in figure 5.35 in this case is very complicated and difficult to interpret. The sensitivity volume lies above the parabolic surface which goes from the front to the

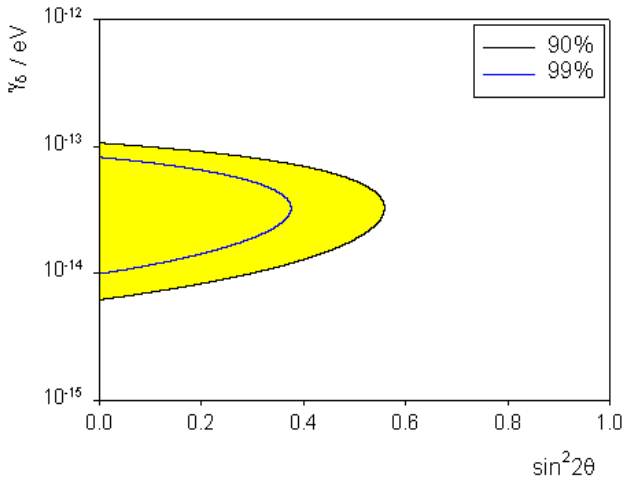

Figure 5.34: Sensitivity contours for model **QD5** at 90 and 99 percent confidence level for quantum decoherence effects only for the parameter γ_δ with no dependence on the neutrino energy.

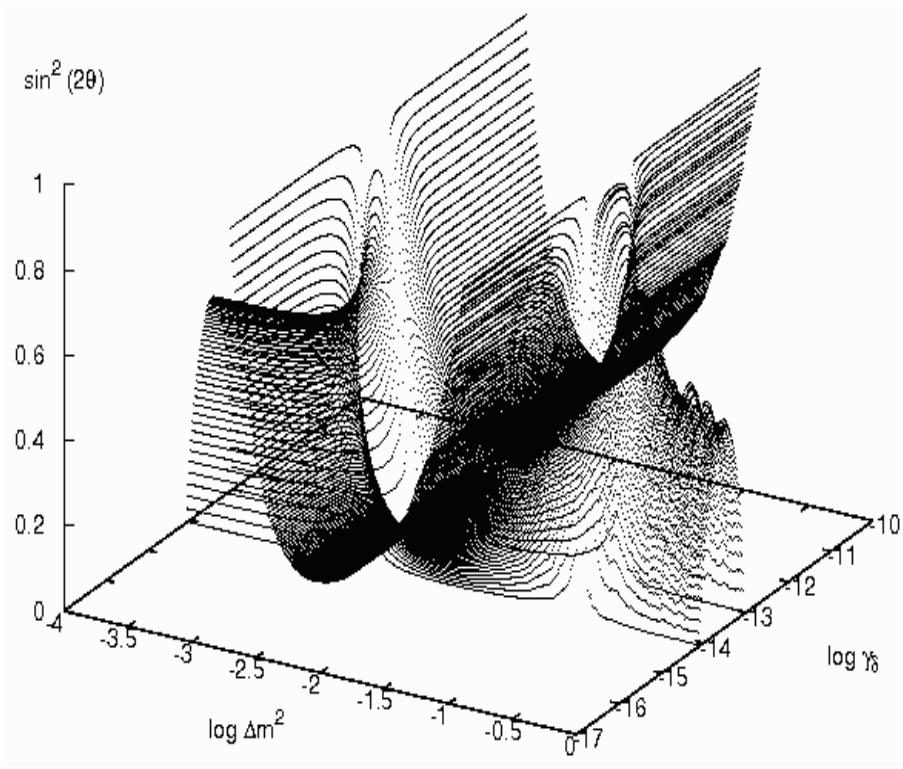

Figure 5.35: Sensitivity volume for model **QD5** at 90 percent confidence level for standard oscillations plus quantum decoherence effects with no dependence on the neutrino energy.

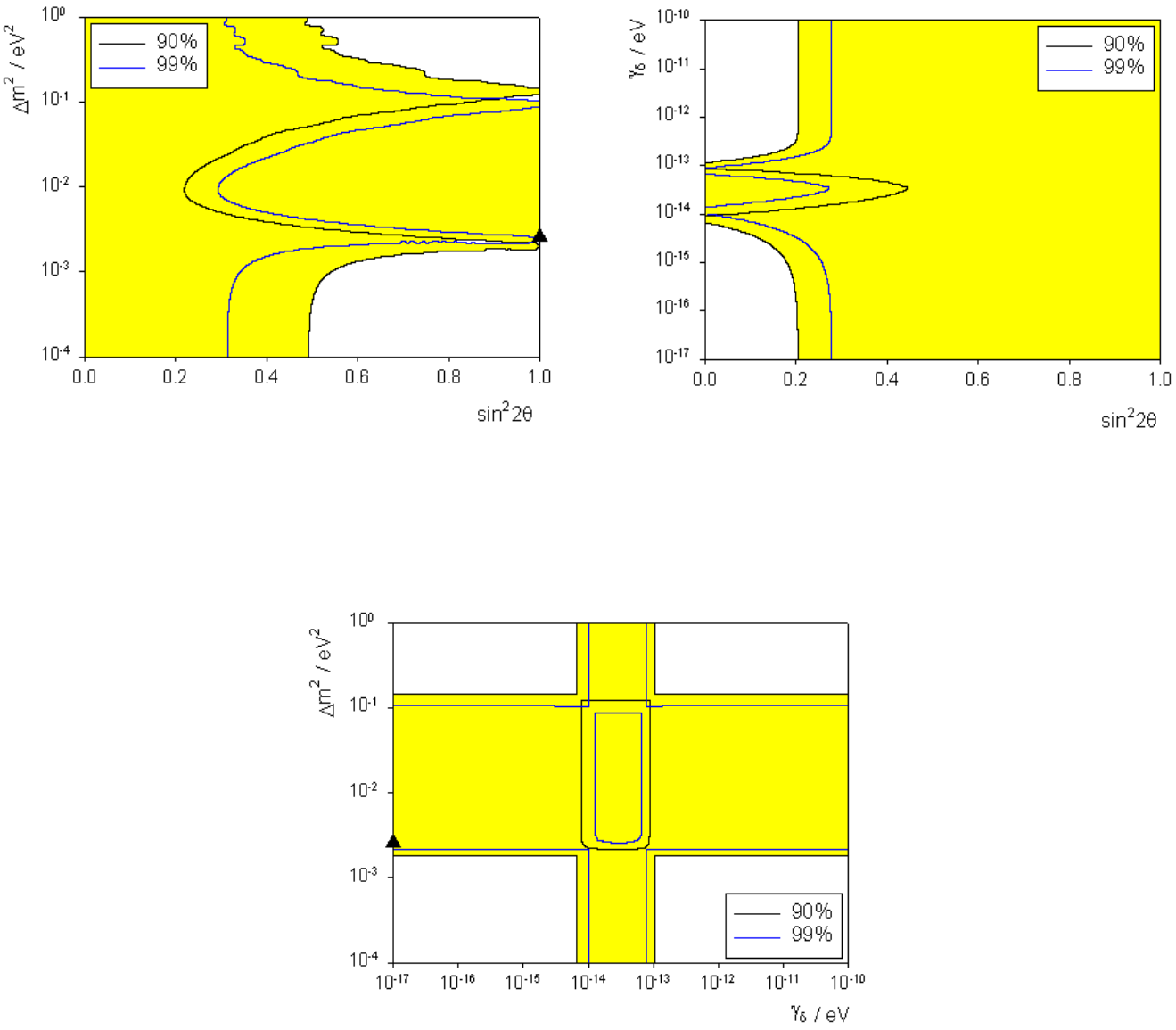

Figure 5.36: Sensitivity contours for model **QD5** at 90 and 99 percent confidence level including standard oscillations and quantum decoherence effects with no dependence on the neutrino energy.

back of the diagram (centered around $\Delta m^2 = 10^{-2}\ eV^2$ roughly) and also below the parabolic surface which runs across the plot, parallel to the Δm^2 axis. The lower part of this diagram corresponds to the sensitivity contours seen when we set $\Delta m^2 = 0$ as above. The sensitivity regions after we have projected the surface onto the coordinate planes are highlighted in yellow at the 90% confidence level, in figure 5.36. We note that the experimental point of best fit for Δm^2 is included in the sensitivity region in the top left frame but that we are unable to place an upper bound on γ_δ since all values of this parameter are allowed for $\sin^2 2\theta$ in the top right frame. The lower frame shows the relationship between Δm^2 and γ_δ.

Decoherence parameters inversely proportional to the neutrino energy

Setting $\delta = \frac{\mu_\delta^2}{4E}$ and restoring c and $\hbar$, the oscillation probability (5.9) takes the form

$$P[\nu_\mu \to \nu_\tau] = \frac{1}{2}\left\{\cos^2(2\theta)\left[1 - e^{-2.54\frac{\mu_\delta^2 L}{E}}\right] + \sin^2(2\theta)\left[1 - \cos\left(\frac{2.54\Delta m^2}{E}L\right)\right]\right\}, \tag{5.32}$$

where μ_δ^2 is measured in eV^2.

Letting $\Delta m^2 = 0$, the oscillation probability (5.10) which describes oscillations as a purely quantum decoherence effect is

$$P[\nu_\mu \to \nu_\tau] = \frac{1}{2}\cos^2(2\theta)\left[1 - e^{-2.54\frac{\mu_\delta^2 L}{E}}\right]. \tag{5.33}$$

The sensitivity contour in this case is shown in figure 5.37. As with the previous energy dependence, the sensitivity region lies within the contours at small values of the mixing angle, in contrast to experimental data.

In the case when we have a non-zero Δm^2, the sensitivity volume is shown in figure 5.38. The resulting sensitivity regions and contours are shown in figure 5.39.

Since the sensitivity volume is qualitatively similar to that in figure 5.35, then the sensitivity contours are also similar to those in which the quantum decoherence parameters have no energy dependence. We again note that the experimental point of best fit for Δm^2, as denoted by the triangle, lies within our sensitivity region and that we are not able to place an upper bound on μ_δ^2 at $\sin^2 2\theta = 1$.

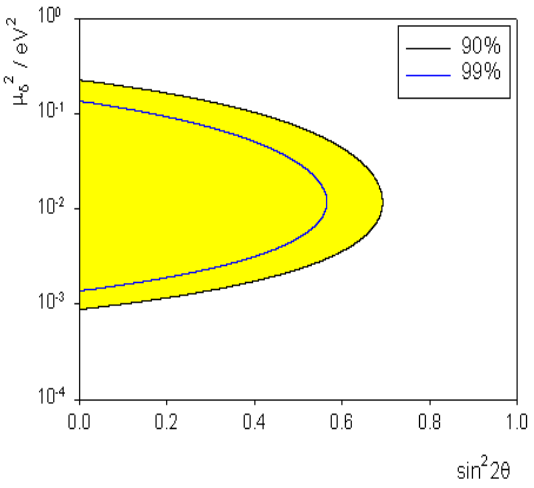

Figure 5.37: Sensitivity contours for model **QD5** at 90 and 99 percent confidence level for quantum decoherence effects only for the parameter μ_δ^2, which is inversely proportional to the neutrino energy.

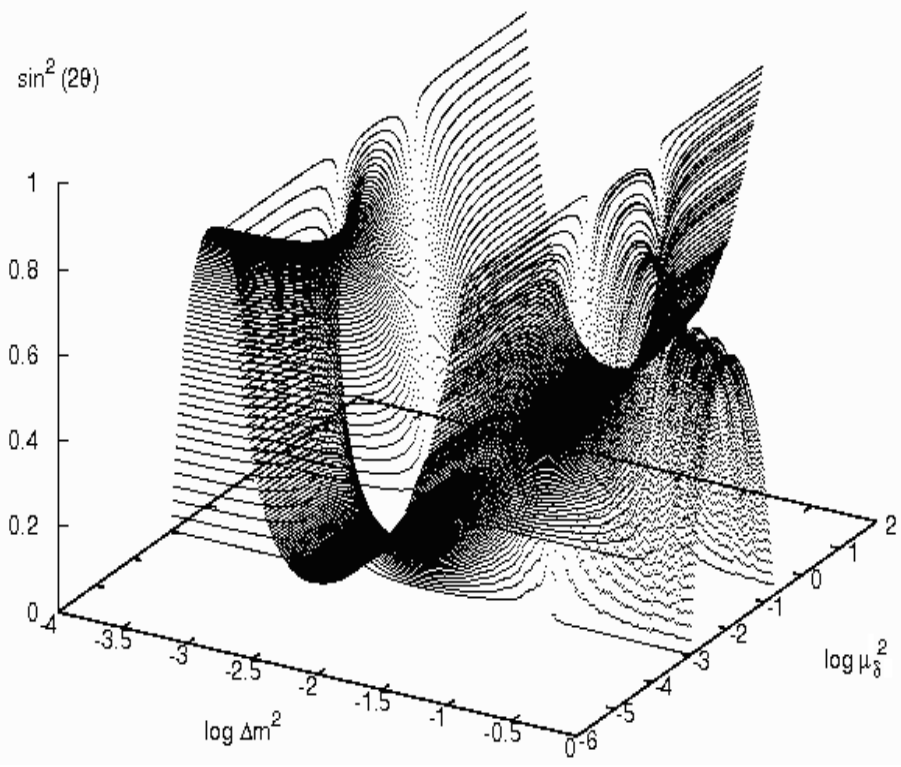

Figure 5.38: Sensitivity volume for model **QD5** at 90 percent confidence level for standard oscillations plus quantum decoherence effects inversely proportional to the neutrino energy.

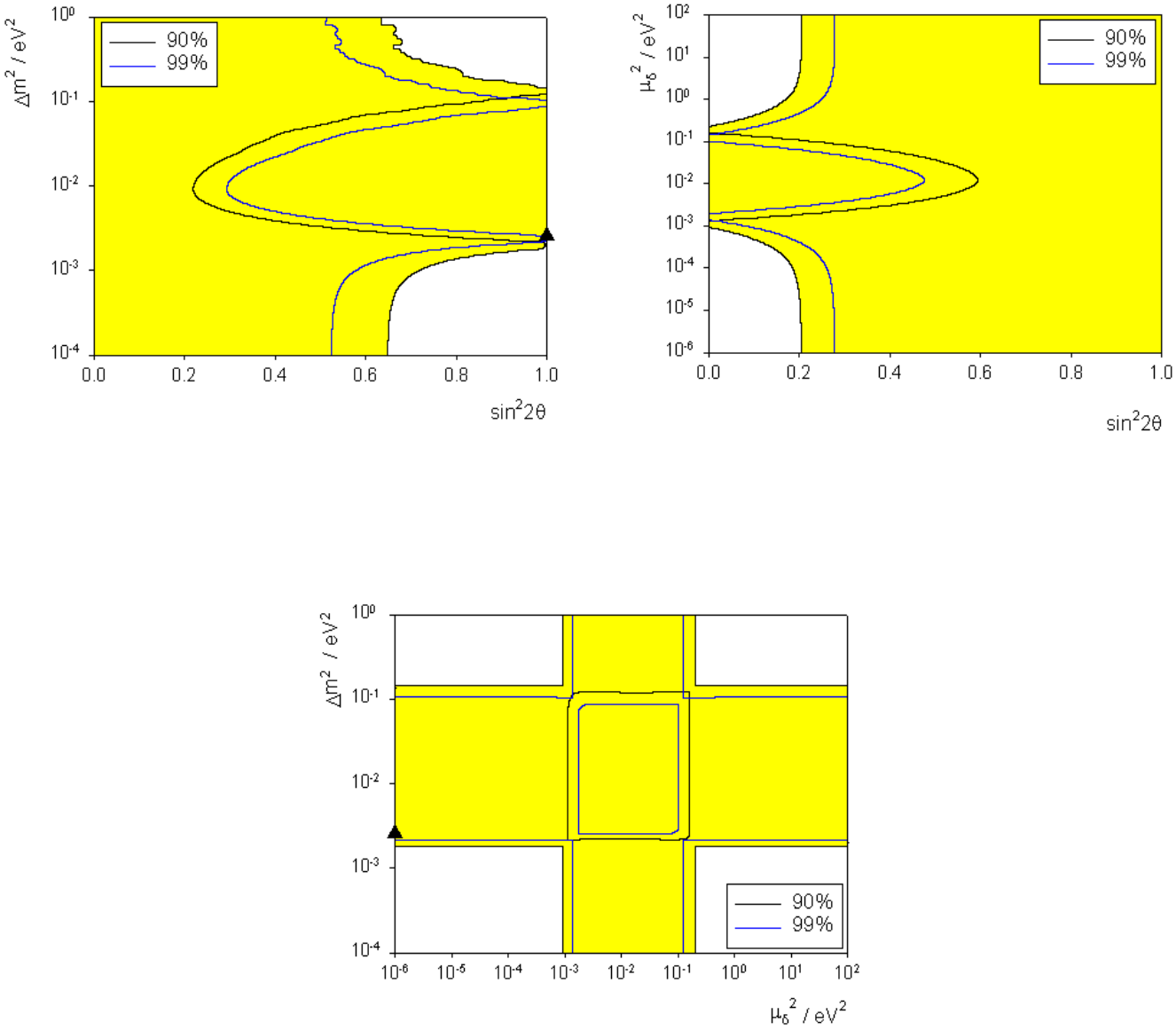

Figure 5.39: Sensitivity contours for model **QD5** at 90 and 99 percent confidence level including standard oscillations and quantum decoherence effects inversely proportional to the neutrino energy.

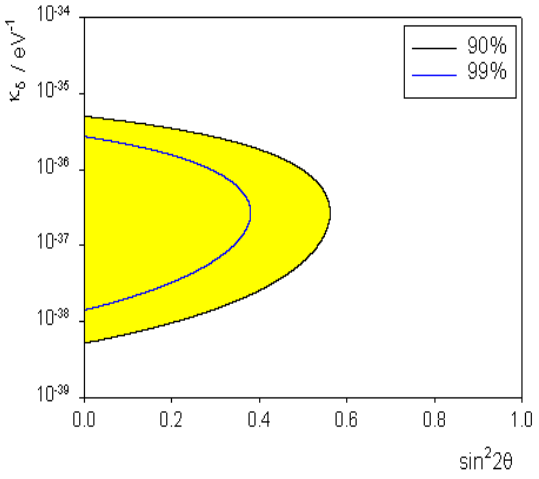

Figure 5.40: Sensitivity contours for model **QD5** at 90 and 99 percent confidence level for quantum decoherence effects only for the parameter κ_δ, proportional to the neutrino energy squared.

Decoherence parameters proportional to the neutrino energy squared

Restoring the constants c and $\hbar$, and setting $\delta = \frac{\kappa E^2}{2}$, the oscillation probability (5.9) has the form

$$P[\nu_\mu \to \nu_\tau] \qquad \frac{1}{2}\left\{\cos^2(2\theta)\left[1 - e^{-5.06\times10^{27}\kappa_\delta E^2 L}\right] + \sin^2(2\theta)\left[1 - \cos\left(\frac{2.54\Delta m^2}{E}L\right)\right]\right\}, \tag{5.34}$$

where κ_δ is measured in eV^{-1}.

Setting $\Delta m^2 = 0$, so oscillations are entirely due to quantum decoherence effects, leads the probability (5.10) to take the form

$$P[\nu_\mu \to \nu_\tau] = \frac{1}{2}\cos^2(2\theta)\left[1 - e^{-5.06\times10^{27}\kappa_\delta E^2 L}\right]. \tag{5.35}$$

The sensitivity contours for this model are shown in figure 5.40. As in the previous two subsections, the sensitivity regions lie inside the contours and so is not compatible with the current experimental data.

The sensitivity volume when we allow Δm^2 to take non-zero values is shown in figure 5.41, with the sensitivity regions shown in figure 5.42. For this energy dependence, the surface bounding the three dimensional sensitivity volume is very complicated. It has many similar features to the previous two surfaces for this model.

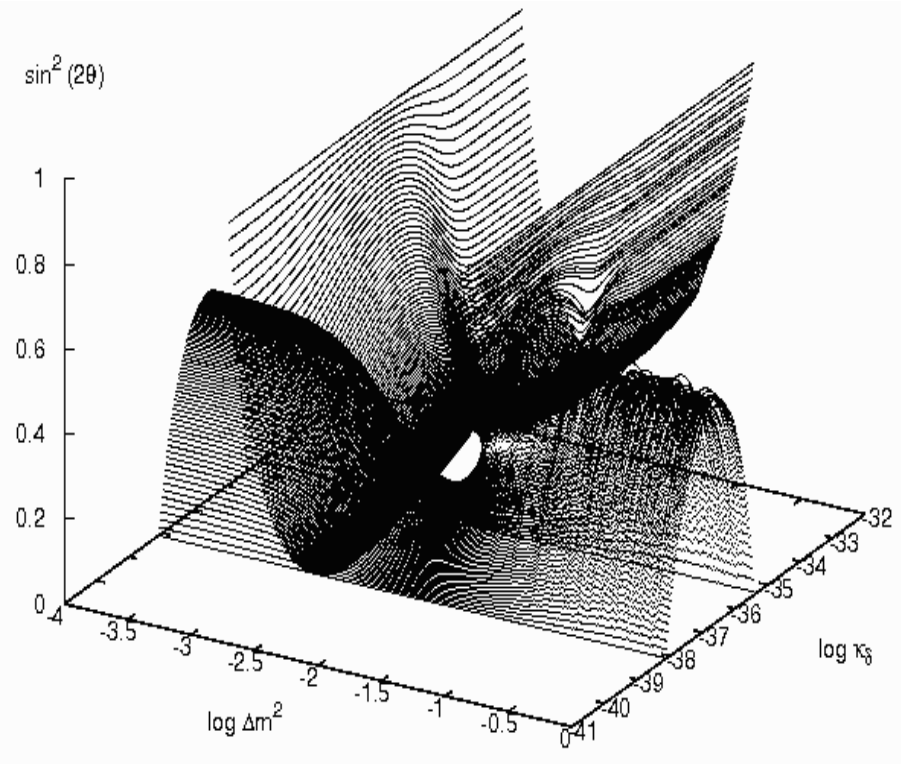

Figure 5.41: Sensitivity volume for model **QD5** at 90 percent confidence level for standard oscillations plus quantum decoherence effects proportional to the neutrino energy squared.

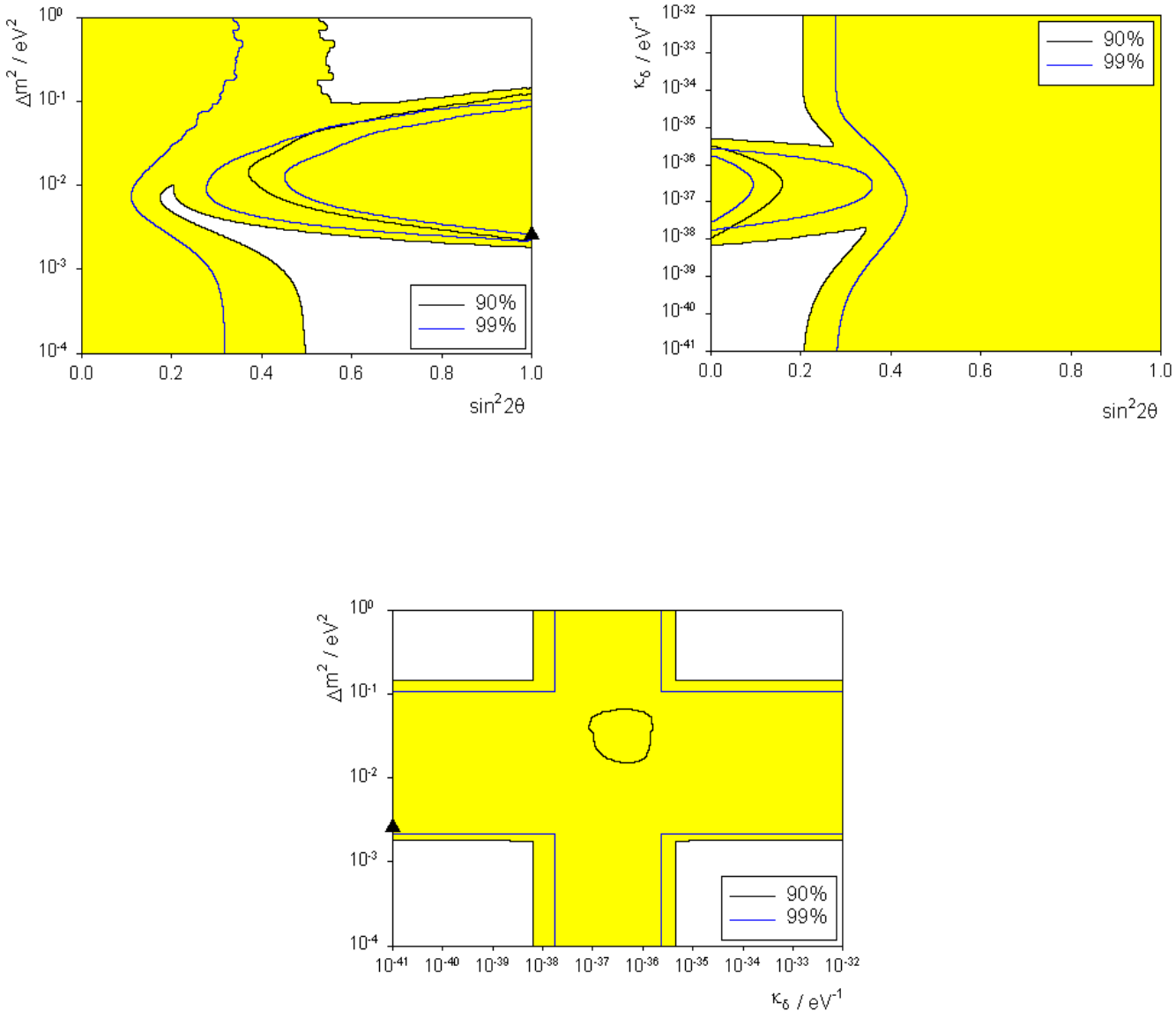

Figure 5.42: Sensitivity contours for model **QD5** at 90 and 99 percent confidence level including standard oscillations and quantum decoherence effects proportional to the neutrino energy squared.

however, this surface folds back on itself in a way that the surfaces in figures 5.35 and 5.38 did not. The sensitivity contours, correspondingly, are more complicated than those in figures 5.36 and 5.39, and are highlighted in yellow for clarity at the 90% confidence level. The experimental point of best fit for Δm^2 is contained within the region of interest in the top left frame of figure 5.42. As expected from our previous discussions, we are not able to place an upper bound on the quantum decoherence parameter, κ_δ.

Summary of Model QD5

The model discussed in this section contains a single decoherence parameter, δ, which multiplies the $\cos^2 2\theta$ term in the oscillation probability (5.9). Considering that the current experimental data favours $\cos^2 2\theta \approx 0$, then, as we have shown, it is likely that precise measurements of this parameter will not be possible with atmospheric neutrinos.

We considered the case where neutrino oscillations arise due purely to quantum decoherence effects but found that the sensitivity regions covered only small values of $\sin^2 2\theta$ and so will be able to be ruled out.

When $\Delta m^2 \neq 0$, we found that the three dimensional parameter space is bounded by a very complicated surface and that, as we mentioned above, we are unable to say anything meaningful about the quantum decoherence parameter in this model.

5.2.7 Model QD6

This model combines the previous model with model **QD1**, so we have three quantum decoherence parameters, $a = \alpha$ and δ. Since we have effectively have two quantum decoherence parameters, we fix Δm^2. We consider both the cases where $\Delta m^2 = 0$ and $\Delta m^2 = 2.6 \times 10^{-3}\ eV^2$.

Decoherence parameters with no dependence on the neutrino energy

Here, we set $a = \alpha = \frac{\gamma_\alpha}{2}$ and $\delta = \frac{\gamma_\delta}{2}$ where γ_α and γ_δ are measured in eV. The oscillation probability (5.11), with c and $\hbar$ restored, is

$$P[\nu_\mu \to \nu_\tau] = \frac{1}{2}\left\{\cos^2(2\theta)\left[1 - e^{-5\times10^9\gamma_\delta L}\right] + \sin^2(2\theta)\left[1 - e^{-5\times10^9\gamma_\alpha L}\cos\left(\frac{2.54\Delta m^2}{E}L\right)\right]\right\}. \quad (5.36)$$

Firstly, we take the limit in which Δm^2 is equal to zero. In this case, the neutrinos oscillate purely due to quantum decoherence effects and the probability (5.12) has the form

$$P[\nu_\mu \to \nu_\tau] = \frac{1}{2}\left\{\cos^2(2\theta)\left[1 - e^{-5\times 10^9 \gamma_\delta L}\right] + \sin^2(2\theta)\left[1 - e^{-5\times 10^9 \gamma_\alpha L}\right]\right\}. \quad (5.37)$$

The sensitivity volume is shown in figure 5.43 with the corresponding sensitivity contours shown in figure 5.44. The surface is very similar to that of figure 5.35. The sensitivity contours are similar to those in figure 5.36 with the role of Δm^2 being played by γ_α in this case. We are able to place an upper bound on γ_α of around $10^{-13}\ eV$ but, as in the previous case, we are unable to do the same for γ_δ.

Setting $\Delta m^2 = 2.6 \times 10^{-3}\ eV^2$, we find the sensitivity volume shown in figure 5.45 and sensitivity regions in figure 5.46. The sensitivity regions are marked in yellow for clarity. For values of $\sin^2(2\theta)$ close to 1, all values of γ_δ are included in the sensitivity region, as in the case with no standard oscillations. However, the range of values of γ_α in the sensitivity region is now much larger than in the absence of standard oscillations, and includes the value zero.

Decoherence parameters inversely proportional to the neutrino energy

Here, we set $\alpha = a = \frac{\mu_\alpha^2}{4E}$ and $\delta = \frac{\mu_\delta^2}{4E}$. The oscillation probability (5.11), with c and $\hbar$ restored, now has the form

$$\begin{aligned} P[\nu_\mu \to \nu_\tau] \quad - \quad & \frac{1}{2}\left\{\cos^2(2\theta)\left[1 - e^{-2.54\frac{\mu_\delta^2 L}{E}}\right]\right. \\ & \left. + \sin^2(2\theta)\left[1 - e^{-2.54\frac{\mu_\alpha^2 L}{E}}\cos\left(\frac{2.54\Delta m^2}{E}L\right)\right]\right\}; \end{aligned} \quad (5.38)$$

where μ_δ^2 and μ_α^2 are measured in eV^2.

Setting $\Delta m^2 = 0$, the neutrinos oscillate entirely due to quantum decoherence effects and the oscillation probability (5.12) takes the form

$$P[\nu_\mu \to \nu_\tau] = \frac{1}{2}\left\{\cos^2(2\theta)\left[1 - e^{-2.54\frac{\mu_\delta^2 L}{E}}\right] + \sin^2(2\theta)\left[1 - e^{-2.54\frac{\mu_\alpha^2 L}{E}}\right]\right\}. \quad (5.39)$$

The sensitivity volume and regions are shown in figures 5.47 and 5.48 respectively and are very similar to those in the last subsection (see also figure 5.36). If we now reset $\Delta m^2 = 2.6 \times 10^{-3}\ eV^2$, then we obtain the sensitivity volume in figure

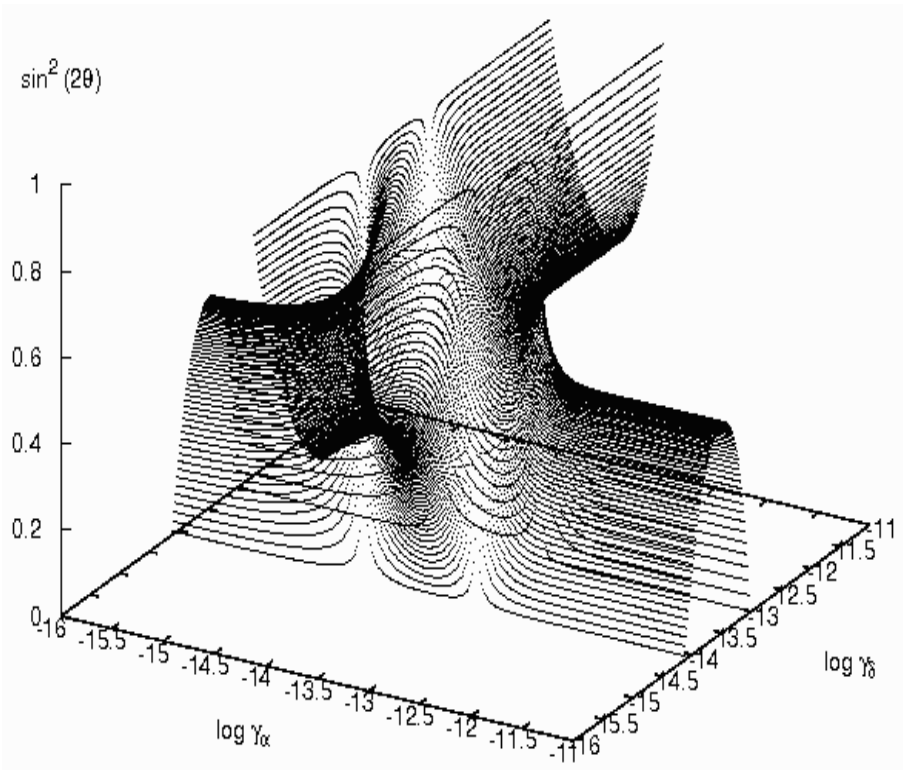

Figure 5.43: Sensitivity volume for model **QD6** at 90 percent confidence level for quantum decoherence effects only with no dependence on the neutrino energy.

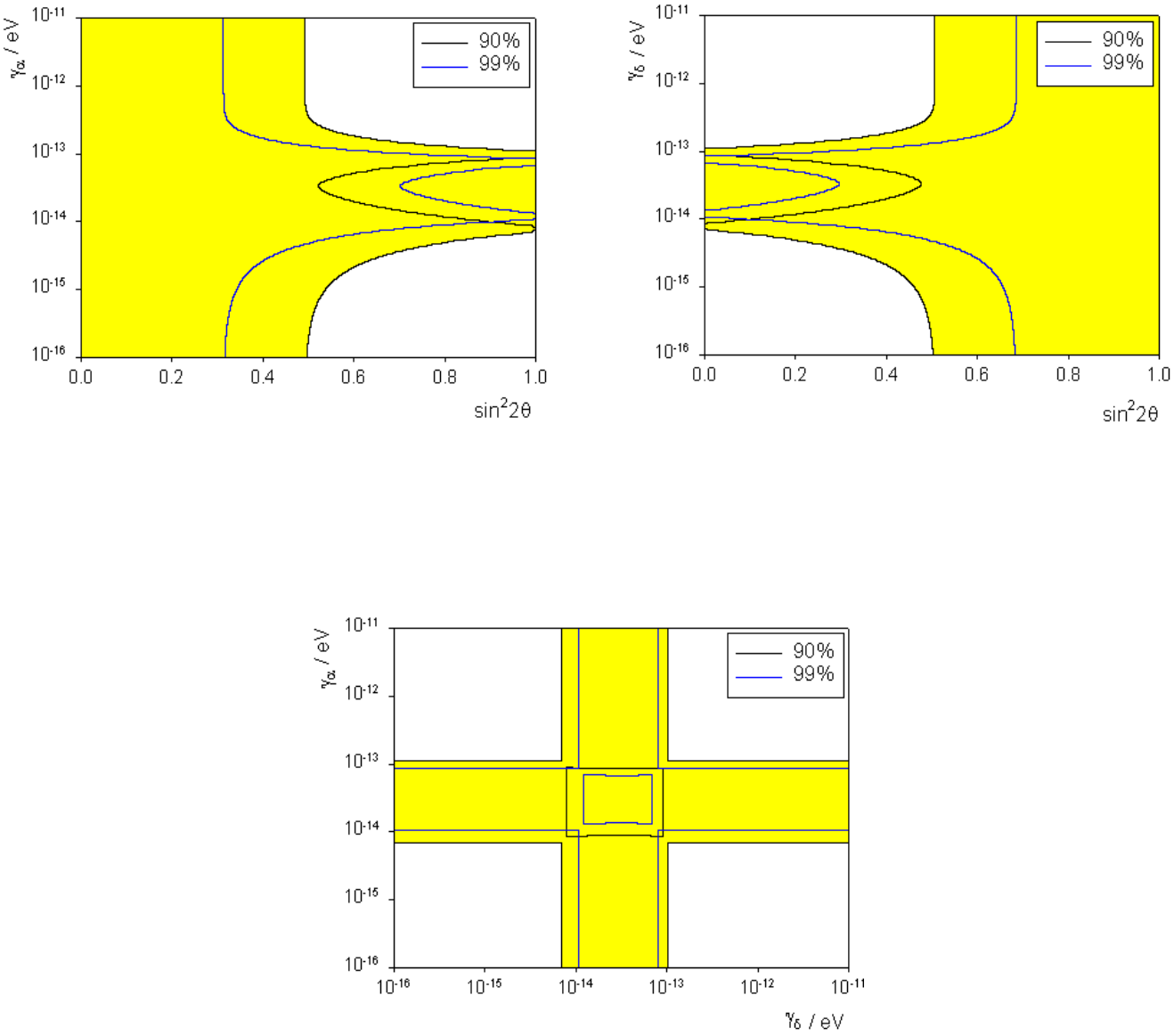

Figure 5.44: Sensitivity contours for model **QD6** at 90 and 99 percent confidence level including quantum decoherence effects only with no dependence on the neutrino energy.

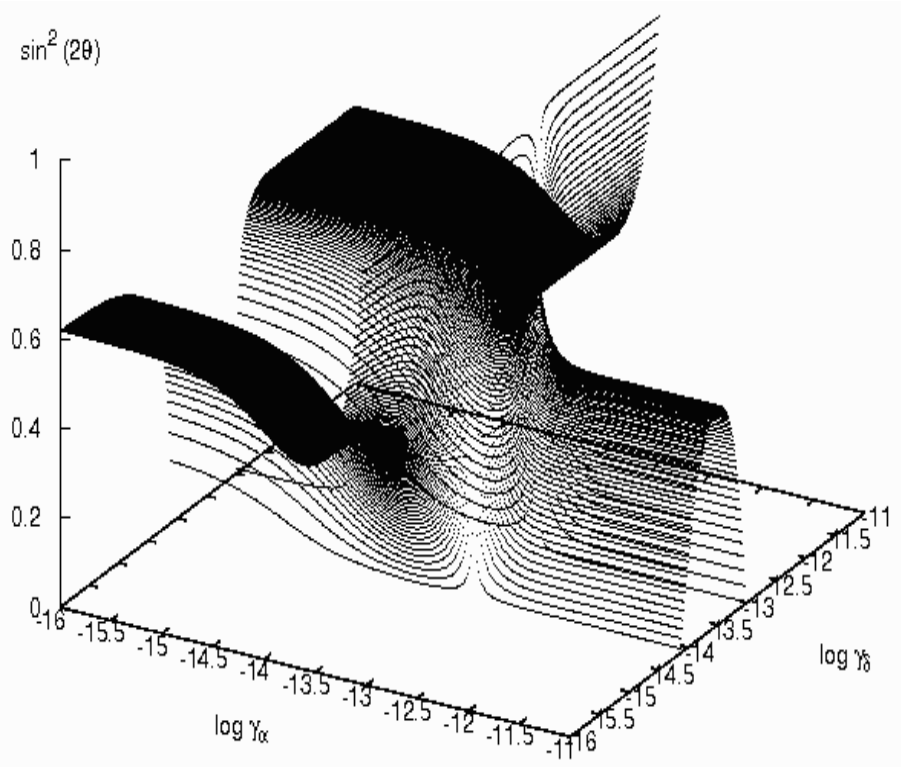

Figure 5.45: Sensitivity volume for model **QD6** at 90 percent confidence level for standard oscillations and quantum decoherence effects with no dependence on the neutrino energy.

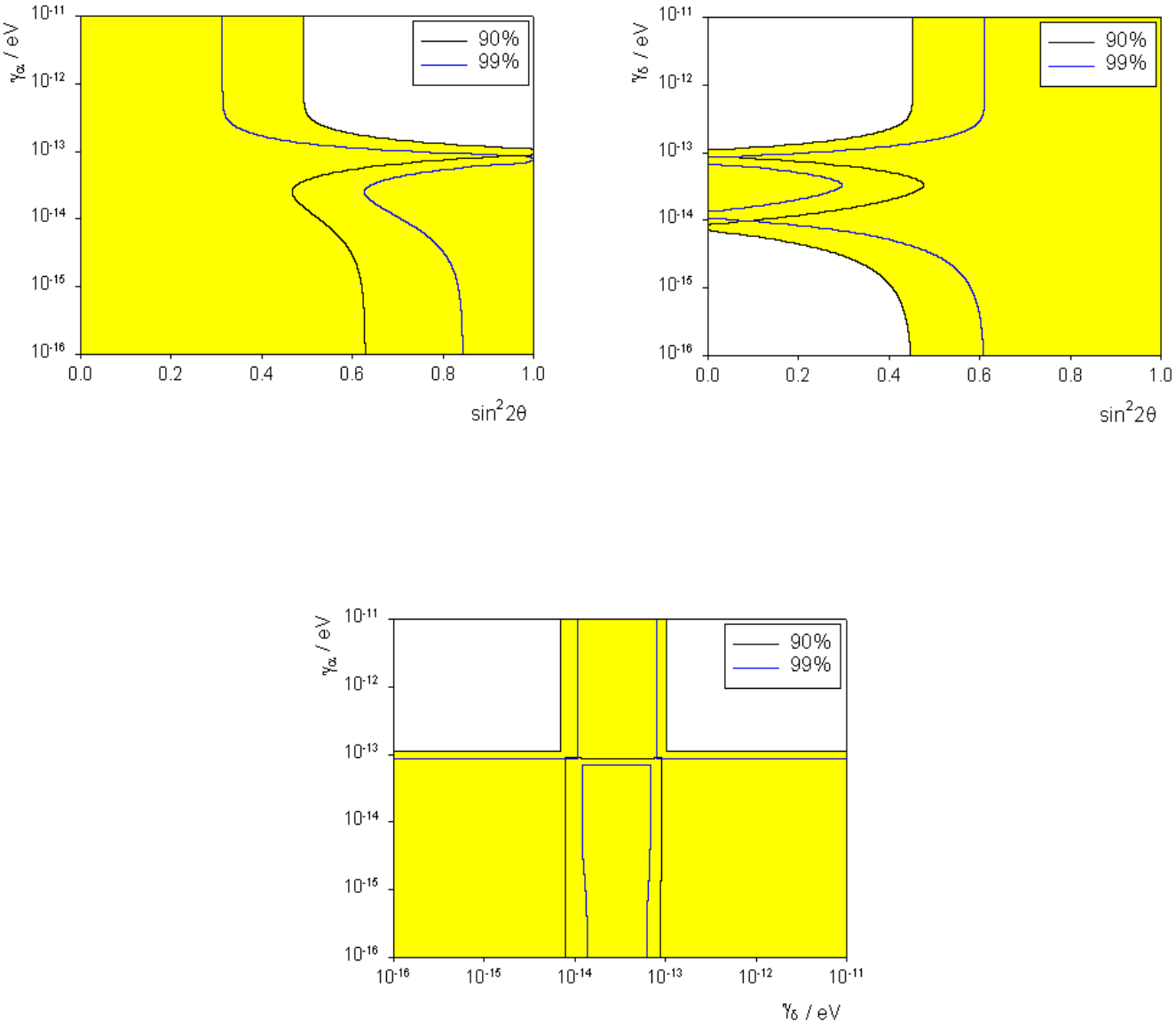

Figure 5.46: Sensitivity contours for model **QD6** at 90 and 99 percent confidence level including standard oscillations and quantum decoherence effects with no dependence on the neutrino energy.

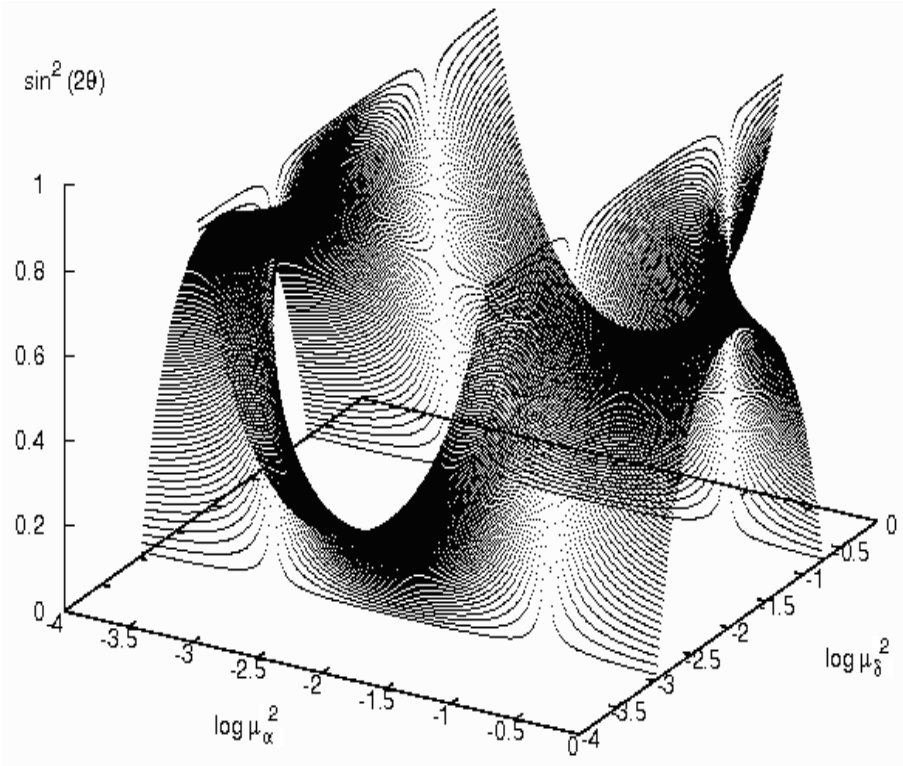

Figure 5.47: Sensitivity volume for model **QD6** at 90 percent confidence level for quantum decoherence effects only, inversely proportional to the neutrino energy.

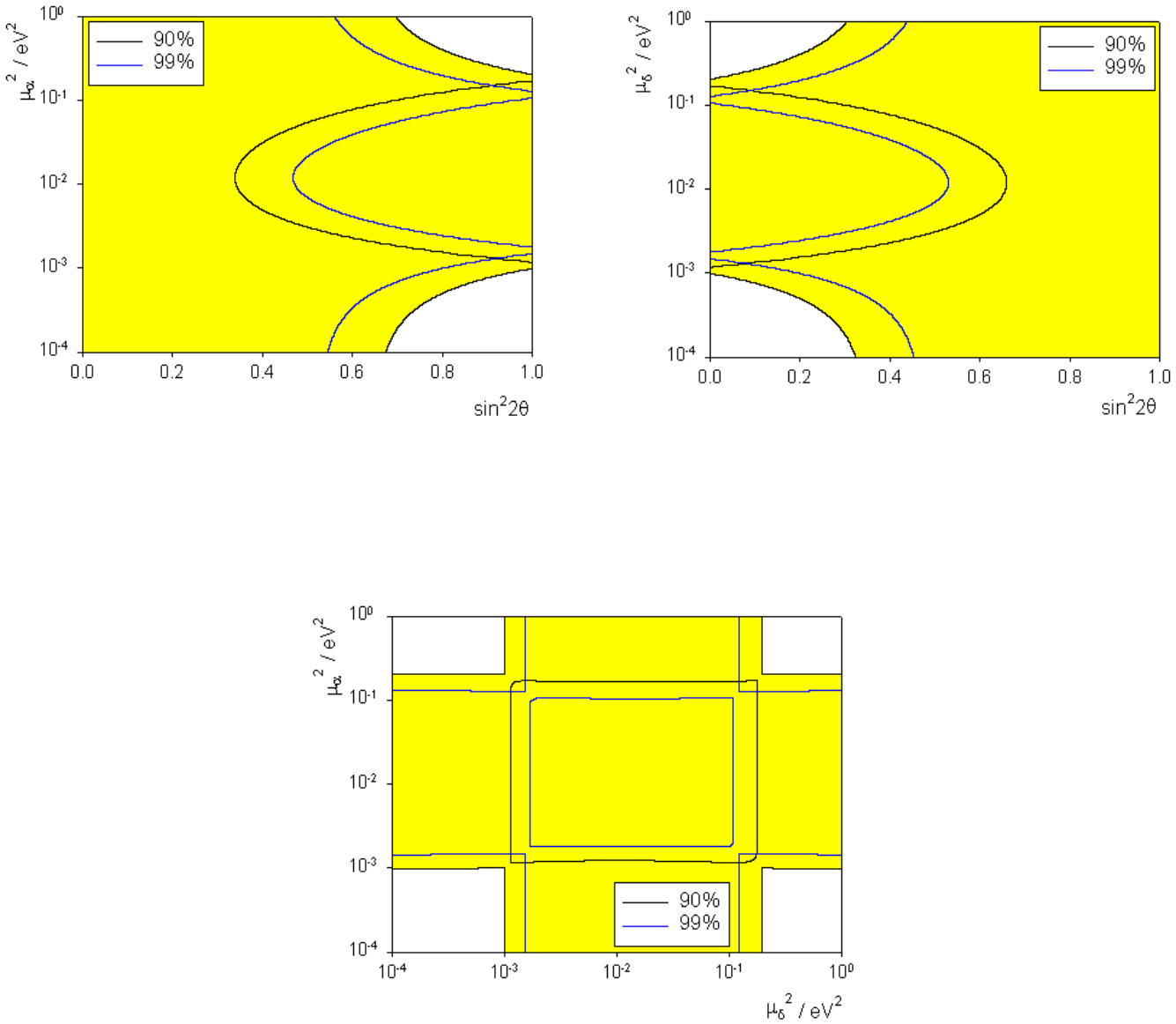

Figure 5.48: Sensitivity contours for model **QD6** at 90 and 99 percent confidence level including quantum decoherence effects only, inversely proportional to the neutrino energy.

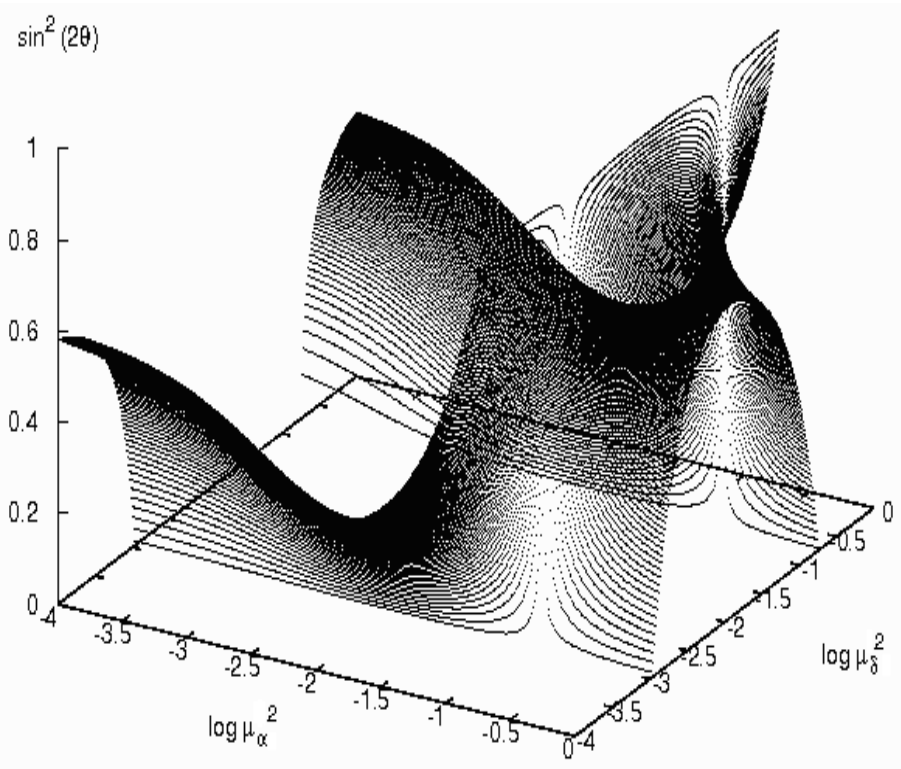

Figure 5.49: Sensitivity volume for model **QD6** at 90 percent confidence level for standard oscillations plus quantum decoherence effects inversely proportional to the neutrino energy.

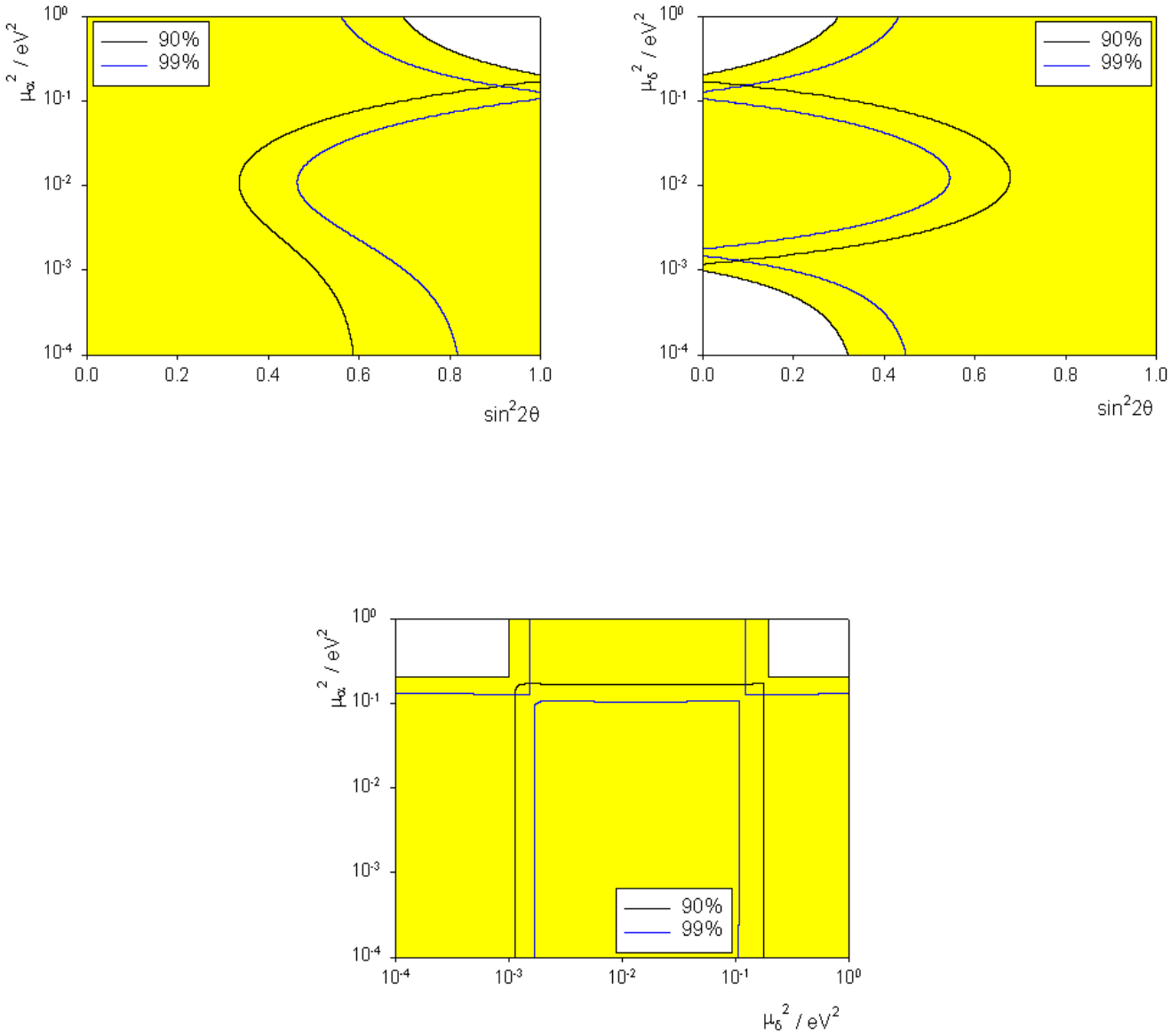

Figure 5.50: Sensitivity contours for model **QD6** at 90 and 99 percent confidence level including standard oscillations and quantum decoherence effects inversely proportional to the neutrino energy.

5.49 and sensitivity regions shown in figure 5.50. Again, the sensitivity regions are similar to those in the last subsection with all values of the parameter μ_δ^2 included at $\sin^2(2\theta) = 1$, and a large range of values of μ_α^2, including zero.

Decoherence parameters proportional to the neutrino energy squared

In this case, we set $\alpha = a = \frac{\kappa_\alpha E^2}{4}$ and $\delta = \frac{\kappa_\delta E^2}{4}$. The oscillation probability (5.11), with c and $\hbar$ restored, has the form

$$\begin{aligned} P[\nu_\mu \to \nu_\tau] \quad - \quad & \frac{1}{2}\cos^2(2\theta)\left[1 - e^{-5.06\times10^{27}\kappa_\delta E^2 L}\right] \\ & + \frac{1}{2}\sin^2(2\theta)\left[1 - e^{-5.06\times10^{27}\kappa_\alpha E^2 L}\cos\left(\frac{2.54\Delta m^2}{E}L\right)\right]; \end{aligned} \quad (5.40)$$

where κ_δ and κ_α are measured in eV^{-1}.

Allowing neutrinos to oscillate due to quantum decoherence effects only by setting $\Delta m^2 = 0$ means the probability (5.12) has the form

$$P[\nu_\mu \to \nu_\tau] = \frac{1}{2}\left\{\cos^2(2\theta)\left[1 - e^{-5.06\times10^{27}\kappa_\delta E^2 L}\right] + \sin^2(2\theta)\left[1 - e^{-5.06\times10^{27}\kappa_\alpha E^2 L}\right]\right\}. \quad (5.41)$$

The sensitivity volume and contours are shown in figures 5.51 and 5.52 respectively and are qualitatively the same as those in the previous subsections related to this model.

When we set $\Delta m^2 = 2.6 \times 10^{-3}\ eV^2$, then the situation is somewhat different to those above. The sensitivity volume in this case is shown in figure 5.53 and the resulting sensitivity regions presented in figure 5.54. The surface in figure 5.53 has two distinct parts with the sensitivity volumes lying above the top surface and below the bottom surface. This leads to the sensitivity regions in the top two frames of figure 5.54. The left hand regions of the top two frames correspond to the lower volume and are not relevant for $\sin^2 2\theta$ close to unity. As in previous sections, we find that all values of κ_δ are contained in the region for $\sin^2 2\theta \approx 1$ and the region for κ_α includes zero, up to an upper bound of $10^{-38}\ eV^{-1}$.

Summary for Model QD6

This model contains three quantum decoherence parameters, firstly δ which multiplies the $\cos^2 2\theta$ term in the oscillation probability (5.11), and $a = \alpha$. Since this

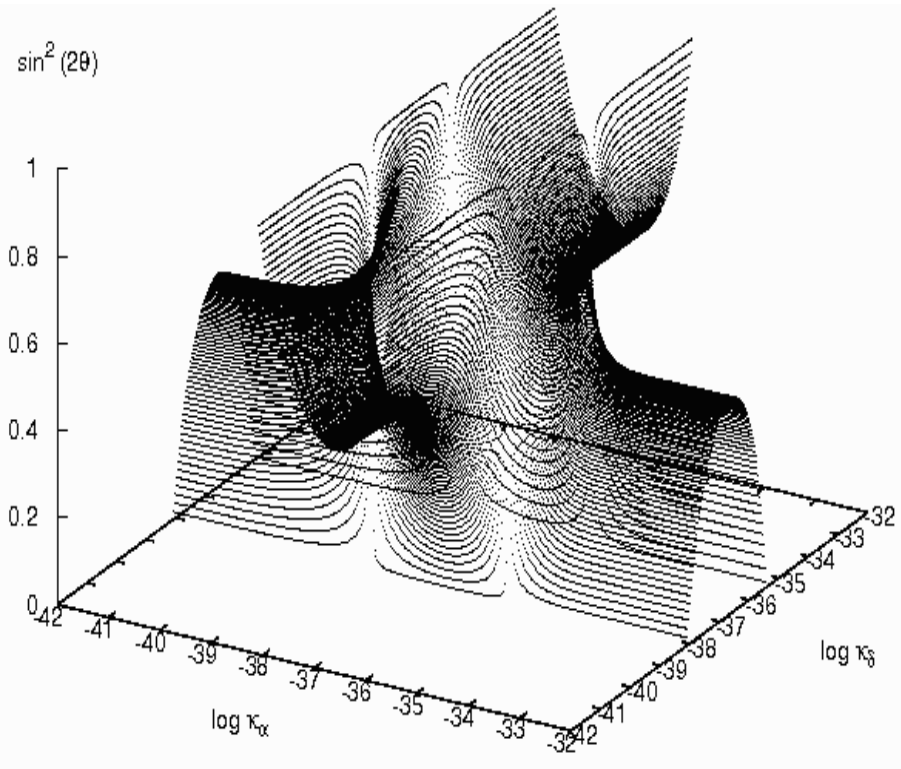

Figure 5.51: Sensitivity volume for model **QD6** at 90 percent confidence level for quantum decoherence effects only proportional to the neutrino energy squared.

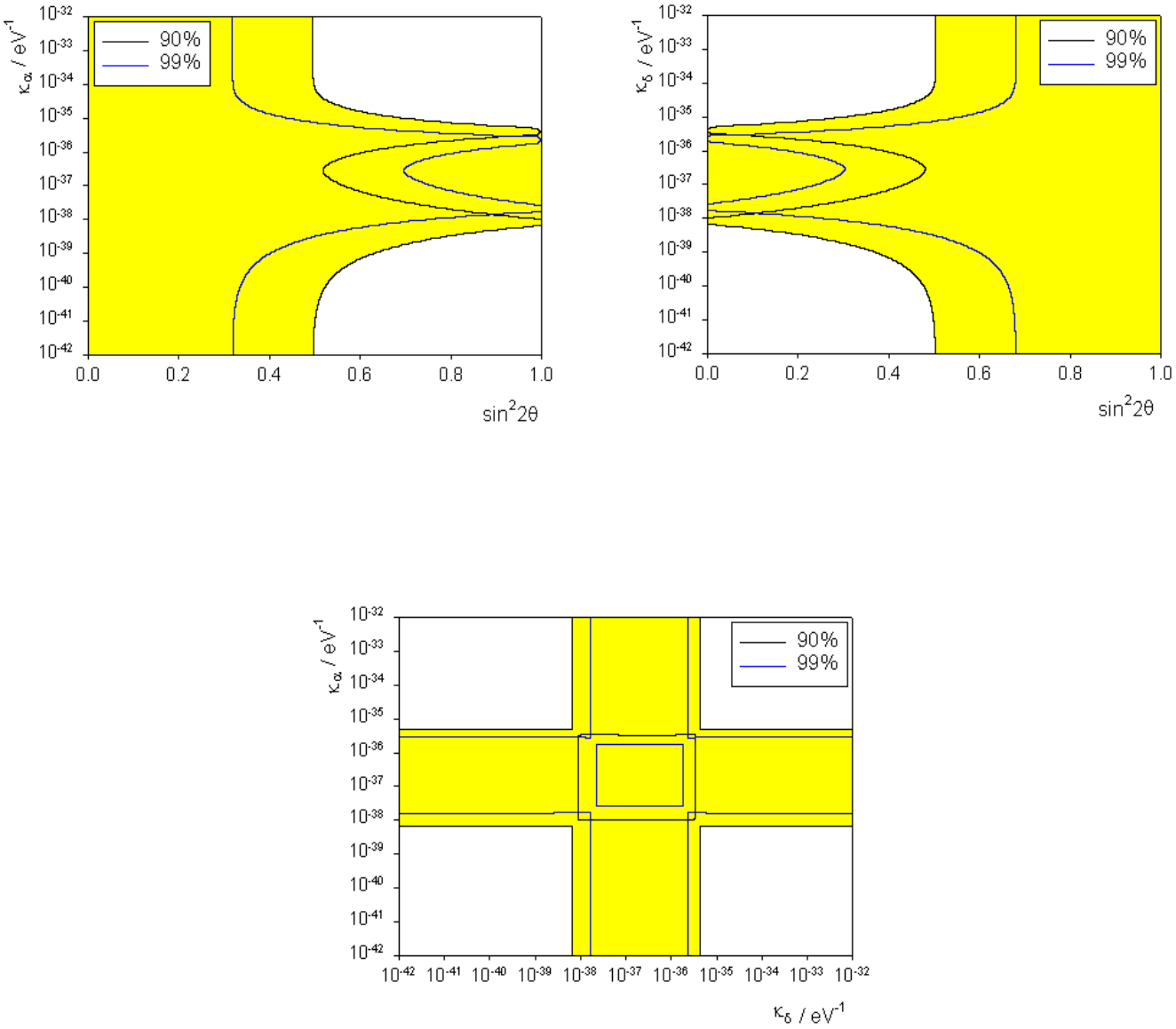

Figure 5.52: Sensitivity contours for model **QD6** at 90 and 99 percent confidence level including quantum decoherence effects only proportional to the neutrino energy squared.

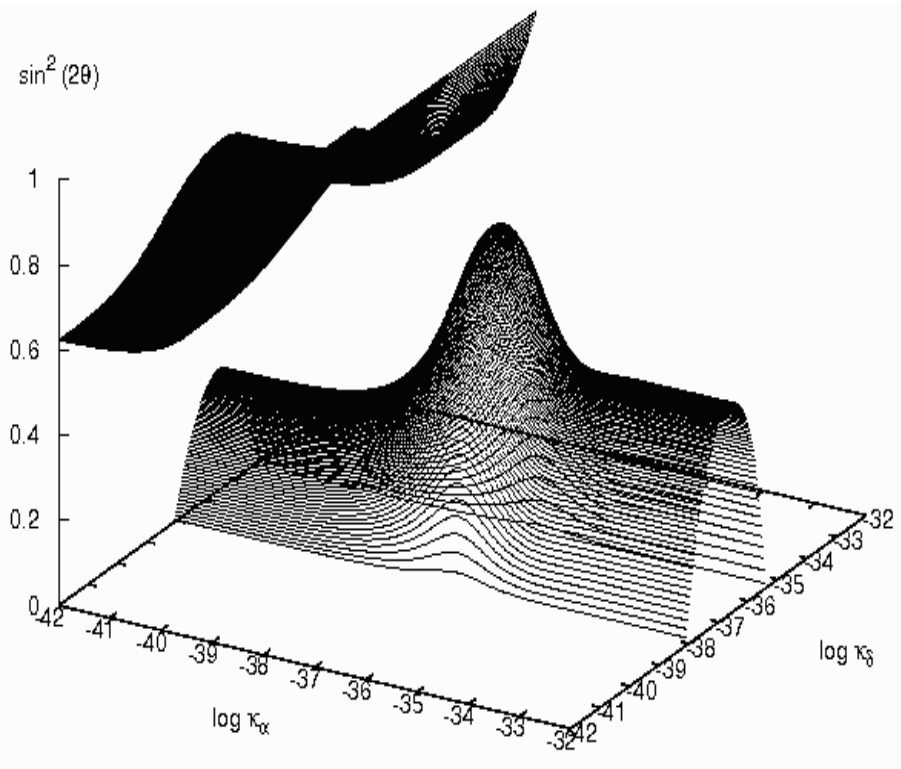

Figure 5.53: Sensitivity volume for model **QD6** at 90 percent confidence level for standard oscillations plus quantum decoherence effects proportional to the neutrino energy squared.

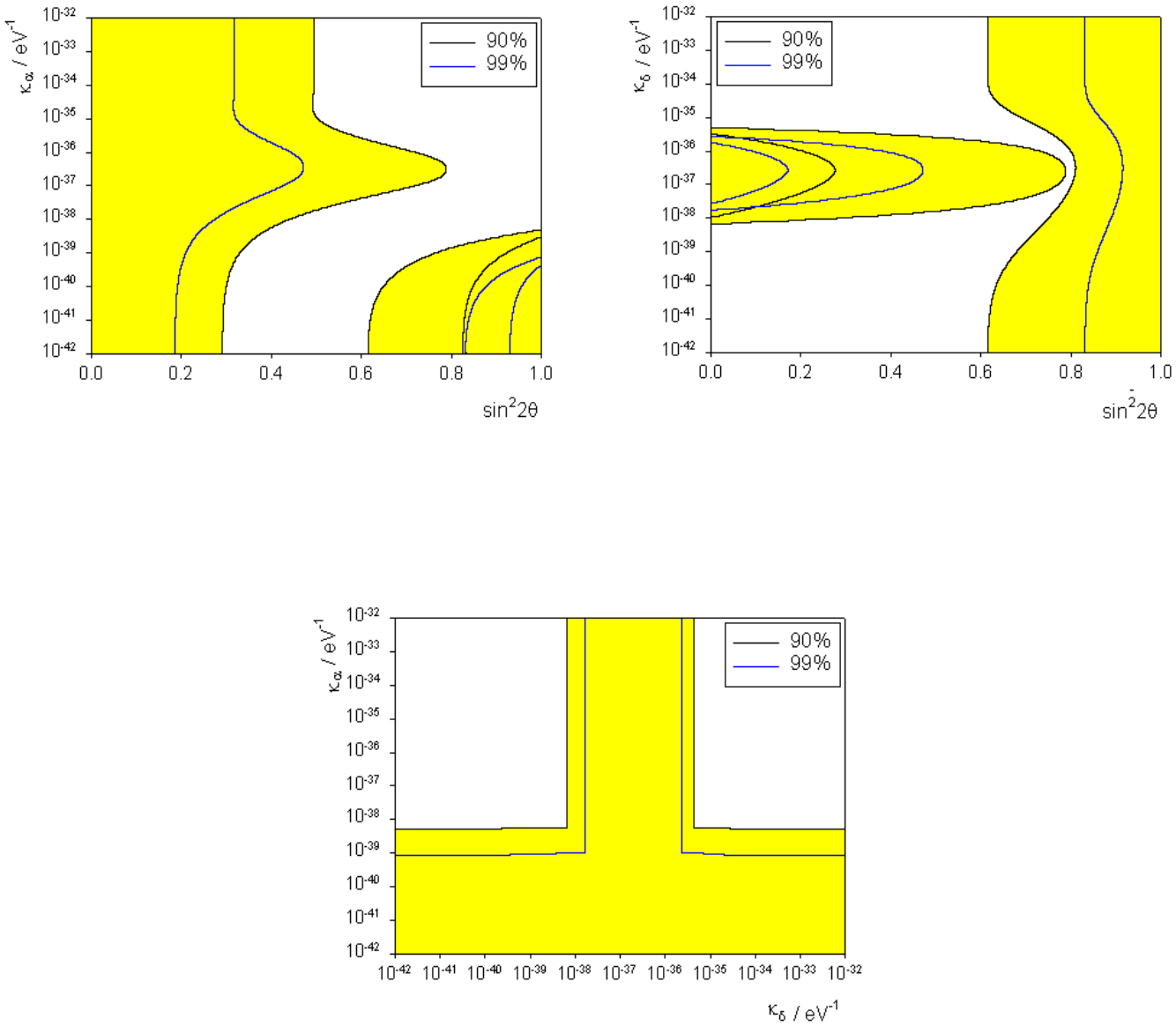

Figure 5.54: Sensitivity contours for model **QD6** at 90 and 99 percent confidence level including standard oscillations and quantum decoherence effects proportional to the neutrino energy squared.

model contains parameters in addition to δ, then this model cannot be ruled out at present.

5.2.8 Model QD7

This model incorporates the quantum decoherence parameter, b, with the energy non-conservation parameter, δ. Since we have two quantum decoherence parameters, we fix $\Delta m^2 = 2.6 \times 10^{-3}\ eV^2$. Unlike the last model, we cannot set this parameter to zero and examine oscillations which arise solely due to quantum decoherence effects, as the oscillation probability (5.13) loses its oscillation characteristics.

Decoherence parameters with no dependence on the neutrino energy

We begin by setting $b = \frac{\gamma_b}{2}$ and $\delta = \frac{\gamma_\delta}{2}$. Replacing c and $\hbar$, the oscillation probability has the form in equation (5.13) with

$$\Gamma_7 = 2\left[\left(1.27\frac{\Delta m^2 L}{E}\right)^2 - [2.5 \times 10^9 \gamma_b L]^2\right]^{\frac{1}{2}}, \tag{5.42}$$

and $2\delta \to 5 \times 10^9 \gamma_\delta$. Here, γ_δ and γ_b are measured in eV.

Figure 5.55 shows the sensitivity volume with the sensitivity regions shown in figure 5.56. The sensitivity regions are very much as we would expect from our discussions above. All values of γ_δ are contained in the sensitivity region for $\sin^2 2\theta$ close to unity. We also note that there is a cut-off in the parameter γ_b, with all values of this parameter contained in the sensitivity region below this point, including zero.

Decoherence parameters inversely proportional to the neutrino energy

In this case, we set $b = \frac{\mu_b^2}{4E}$ and $\delta = \frac{\mu_\delta^2}{4E}$. So, replacing c and $\hbar$, the oscillation probability takes the form (5.13) with $2\delta = 2.54\frac{\mu_\delta^2}{E}$ and (5.14) taking the form

$$\Gamma_7 = \frac{2.54L}{E}\left[\left(\Delta m^2\right)^2 - \left(\mu_b^2\right)^2\right]^{\frac{1}{2}}, \tag{5.43}$$

and μ_δ^2 and μ_b^2 are measured in eV^2.

Figure 5.57 shows the sensitivity volume for this model. In figure 5.58, we plot the sensitivity regions, highlighting the 90% confidence level sensitivity contours in yellow. As in the previous subsection, all values of μ_δ^2 are contained in the

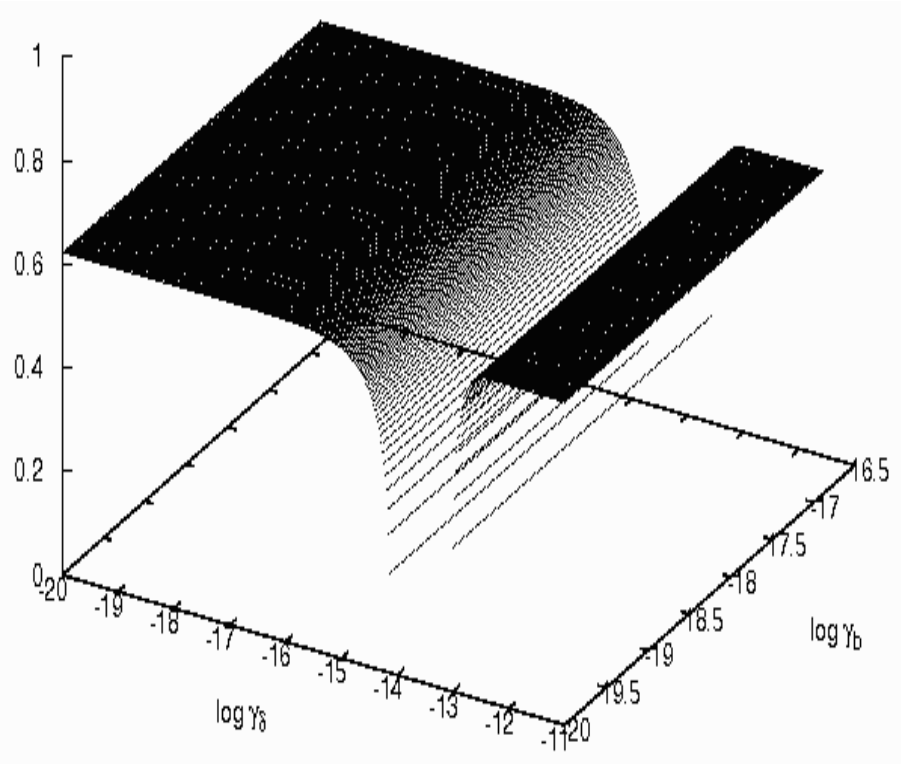

Figure 5.55: Sensitivity volume for model **QD7** at 90 percent confidence level for standard oscillations and quantum decoherence effects with no dependence on the neutrino energy.

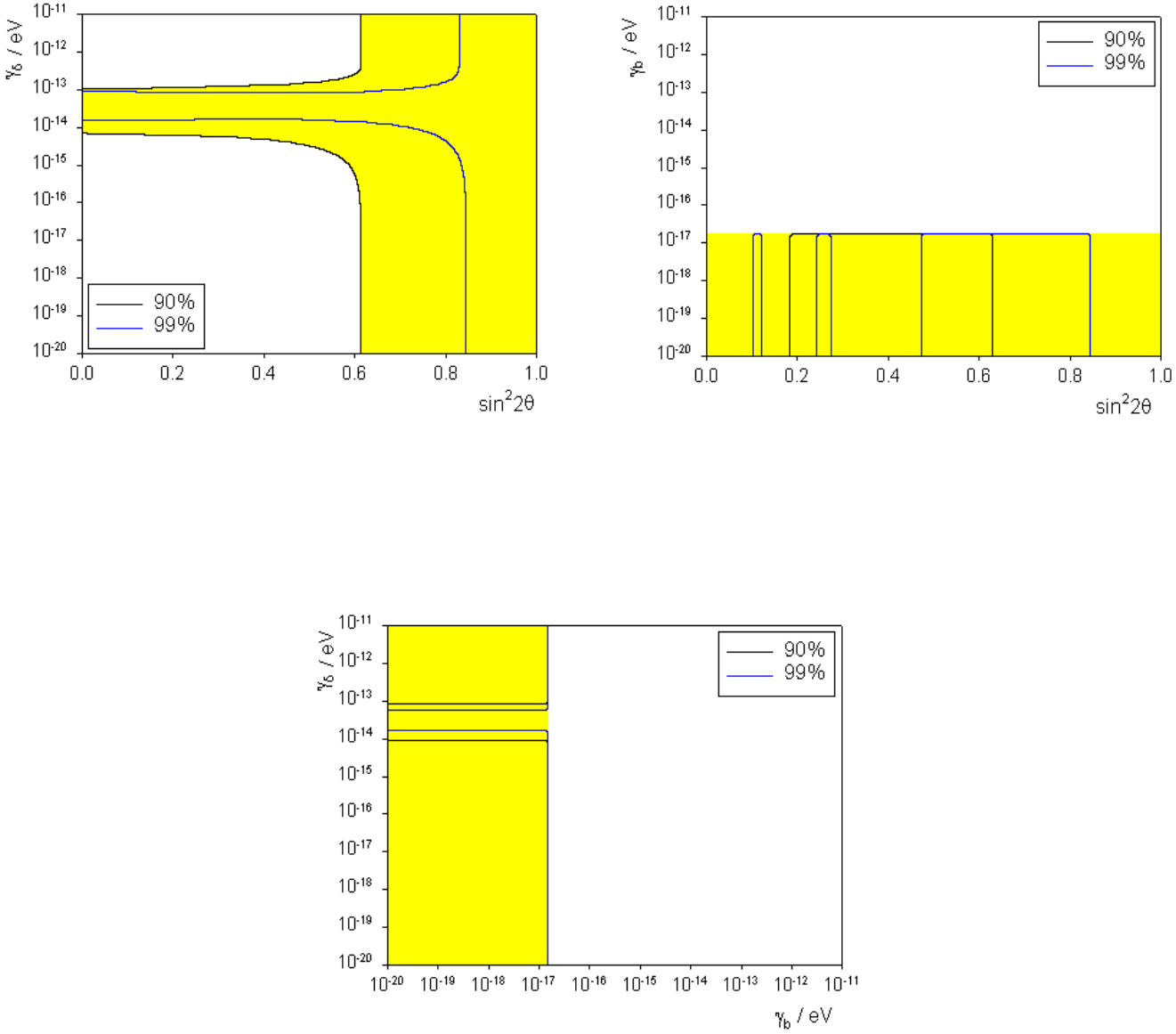

Figure 5.56: Sensitivity contours for model **QD7** at 90 and 99 percent confidence level including standard oscillations and quantum decoherence effects with no dependence on the neutrino energy.

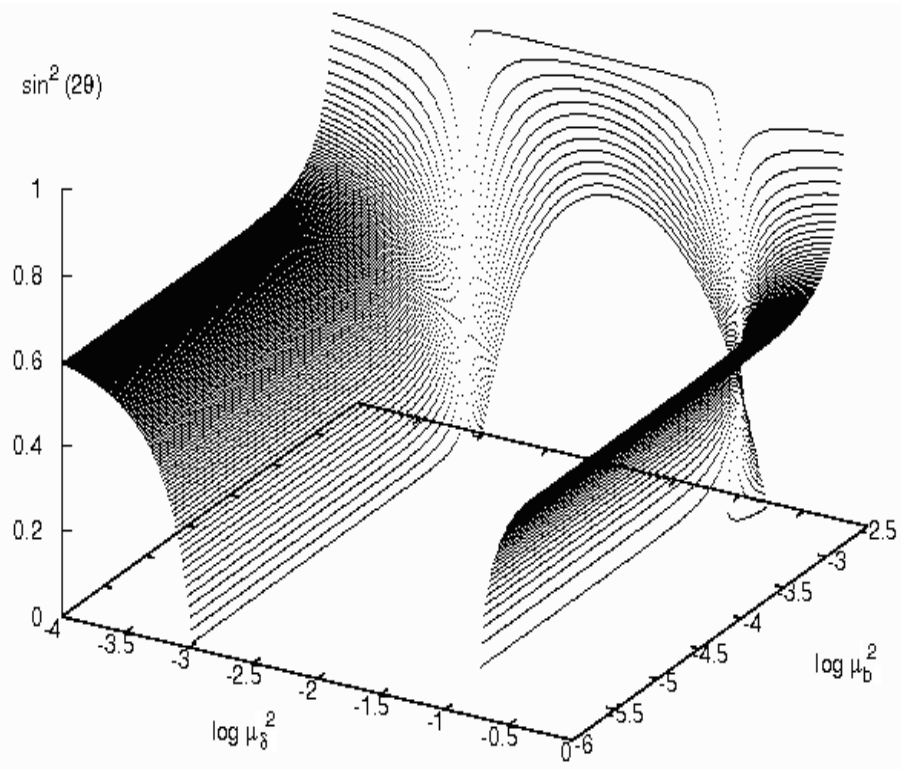

Figure 5.57: Sensitivity volume for model **QD7** at 90 percent confidence level for standard oscillations plus quantum decoherence effects inversely proportional to the neutrino energy.

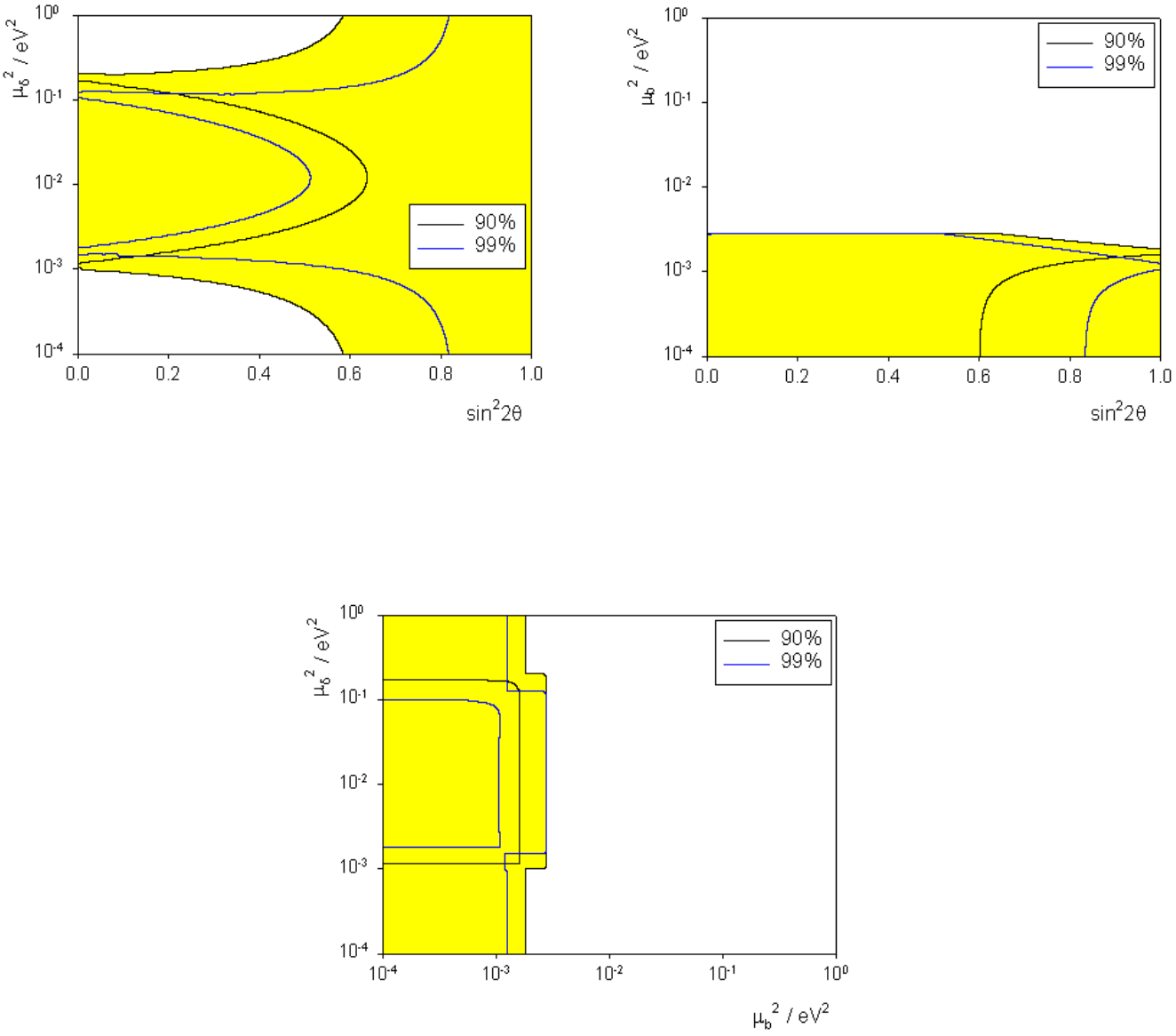

Figure 5.58: Sensitivity contours for model **QD7** at 90 and 99 percent confidence level including standard oscillations and quantum decoherence effects inversely proportional to the neutrino energy.

sensitivity region when $\sin^2 2\theta$ is close to unity and there is a cut-off in the parameter μ_b^2 due to Γ_7 (5.43) becoming imaginary.

Decoherence parameters proportional to the neutrino energy squared

Here, we set $b = \frac{\kappa_b E^2}{2}$ and $\delta = \frac{\kappa_\delta E^2}{2}$, which, on replacing c and $\hbar$, gives the oscillation probability (5.13) with $2\delta = 5 \times 10^{27} \kappa_\delta E^2$ and (5.14) given by

$$\Gamma_7 = 2\left[\left(1.27\frac{\Delta m^2 L}{E}\right)^2 - [2.53 \times 10^{27}\kappa_b E^2 L]^2\right]^{\frac{1}{2}}. \tag{5.44}$$

Here, κ_b and κ_δ are measured in eV^{-1}.

Figure 5.59 shows the boundary of the sensitivity volume in this case. The sensitivity regions are shown in figure 5.60. In this case, the sensitivity volume is split into two distinct parts with the sensitivity volume lying above the top surface; and below and inside the lower surface. The sensitivity regions in figure 5.60 are as expected, all values of κ_δ are contained within the sensitivity regions close to $\sin^2 2\theta = 1$ and there is a sharp cut-off in the parameter κ_b.

Summary of Model QD7

This model contains two quantum decoherence parameters, b and δ, and combines the properties of models **QD3** and **QD5**. The results are as we might have expected. Although the sensitivity regions have different shapes, dependent upon the energy dependence of the parameters, they share the same properties; all values of the parameter δ are contained in the sensitivity regions close to $\sin^2 2\theta = 1$; and we observe a cut-off in the parameter b.

5.2.9 Model QD8

Our penultimate model has one quantum decoherence parameter, β, which allows the non-conservation of energy in the neutrino system. Since we only have one extra parameter, we keep Δm^2 free also.

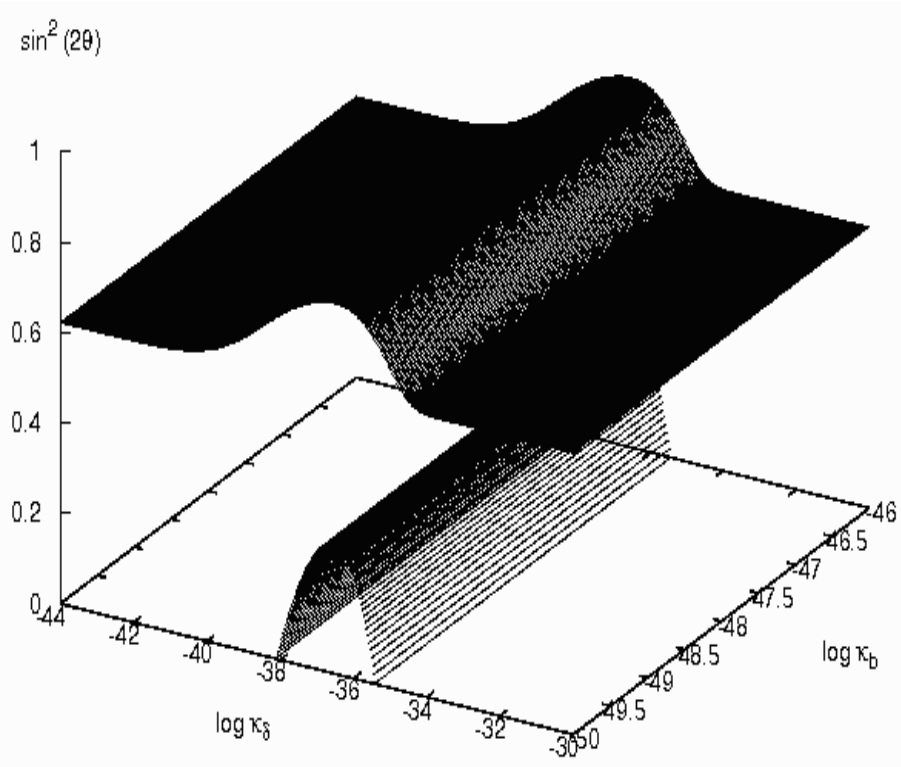

Figure 5.59: Sensitivity volume for model **QD7** at 90 percent confidence level for standard oscillations plus quantum decoherence effects proportional to the neutrino energy squared.

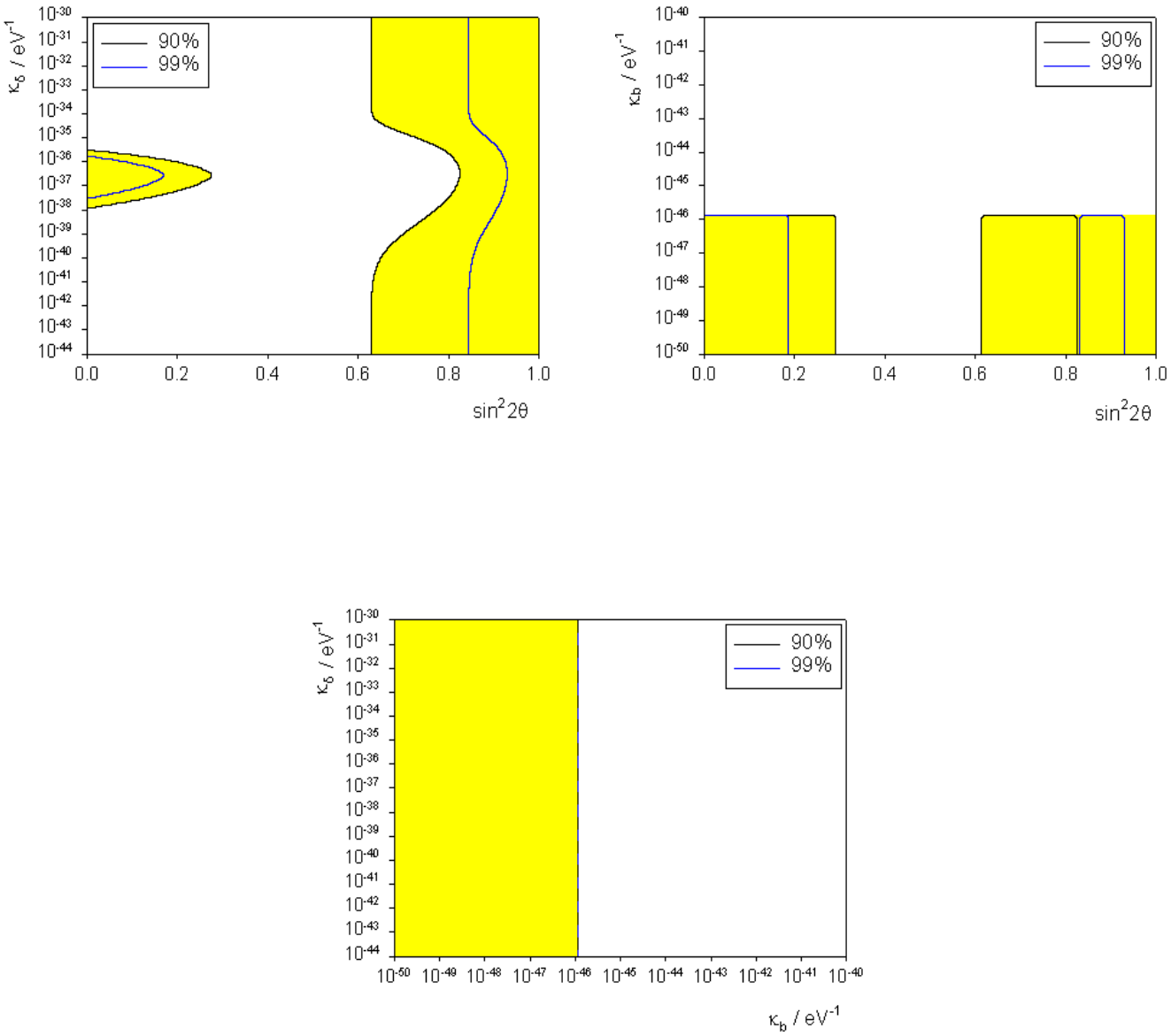

Figure 5.60: Sensitivity contours for model **QD7** at 90 and 99 percent confidence level including standard oscillations and quantum decoherence effects proportional to the neutrino energy squared.

Decoherence parameters with no dependence on the neutrino energy

In this case, we set $\beta = \frac{\gamma_\beta}{2}$ and so the oscillation probability (5.15) contains the quantities

$$\omega = 1.27\Delta m^2 \frac{L}{E}, \qquad \beta = 2.5 \times 10^9 \gamma_\beta L, \tag{5.45}$$

where we have replaced the constants c and $\hbar$.

The sensitivity volume is shown in figure 5.61, with the sensitivity contours shown in figure 5.62. The top left frame of figure 5.62 shows Δm^2 as a function of the mixing angle, θ. The triangle, which denotes the experimental point of best fit, clearly lies within this region. The second frame of this figure shows the quantum decoherence parameter, γ_β, against $\sin^2 2\theta$, with the sensitivity region lying inside the contours as highlighted in yellow (at least for the 90% confidence level). This region contains zero and we are able to place a bound on this parameter of $\gamma_\beta < 10^{-15}\ eV$. The lower plot shows the relationship between Δm^2 and γ_β.

Decoherence parameters inversely proportional to the neutrino energy

In this case, we set $\beta = \frac{\mu_\beta^2}{4E}$. Replacing the constants c and $\hbar$, the oscillation probability is given by (5.15) with

$$\omega = 1.27\Delta m^2 \frac{L}{E}, \qquad \beta = 1.27\mu_\beta^2 \frac{L}{E}, \tag{5.46}$$

where μ_β^2 is measured in eV^2.

The three dimensional sensitivity volume is shown in figure 5.63 with the sensitivity contours shown in figure 5.64. In contrast to the surface in the last subsection, the surface bounding the sensitivity volume in figure 5.63 is rather complicated, making interpretation of the sensitivity regions in figure 5.64 non-trivial. For clarity, the 90% confidence level is highlighted. The sensitivity volume lies above the surface in figure 5.63, including the value $\sin^2 2\theta = 1$. For very small values of the quantum decoherence parameter, the volume has the same shape as the surface in the last subsection, leading to the inclusion of the top right hand corner of the first frame in figure 5.64. However, at high values of μ_β^2, the surface turns over and all values of Δm^2 and μ_β^2 are included. For this reason, we are unable to place an upper bound on μ_β^2.

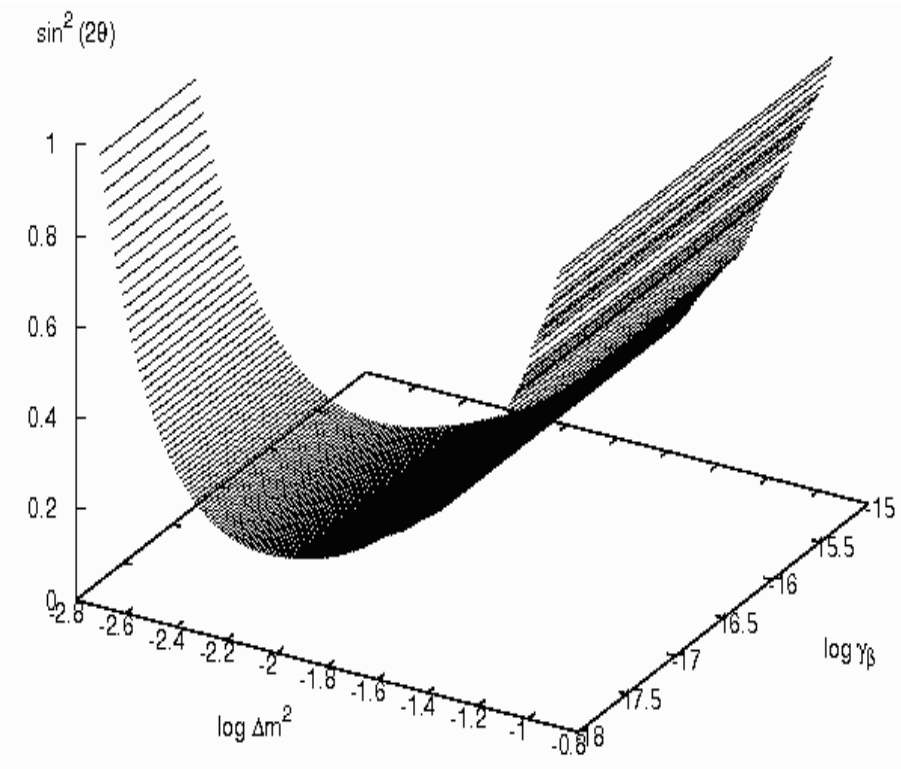

Figure 5.61: Sensitivity volume for model **QD8** at 90 percent confidence level for standard oscillations and quantum decoherence effects with no dependence on the neutrino energy.

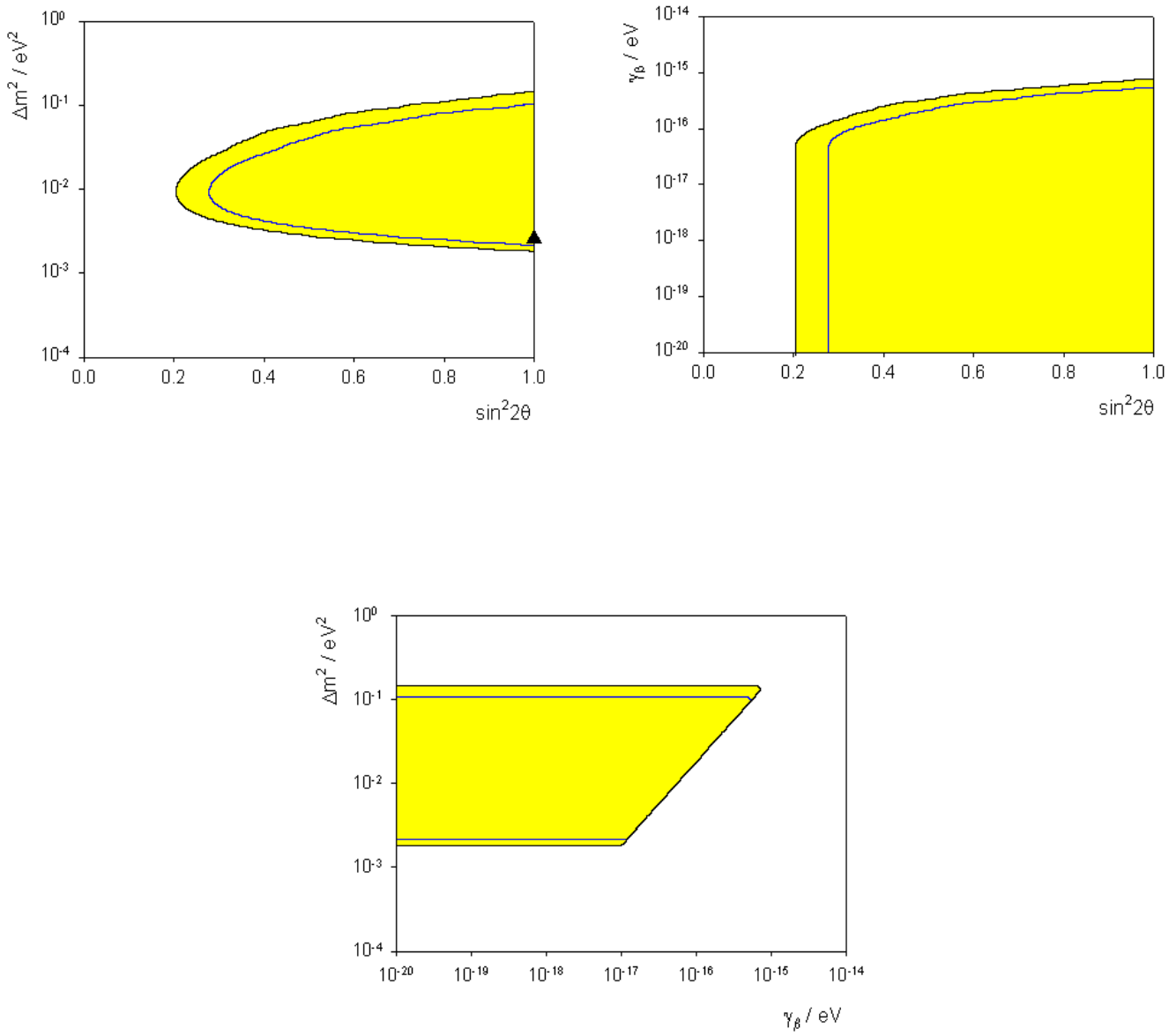

Figure 5.62: Sensitivity contours for model **QD8** at 90 and 99 percent confidence level including standard oscillations and quantum decoherence effects with no dependence on the neutrino energy.

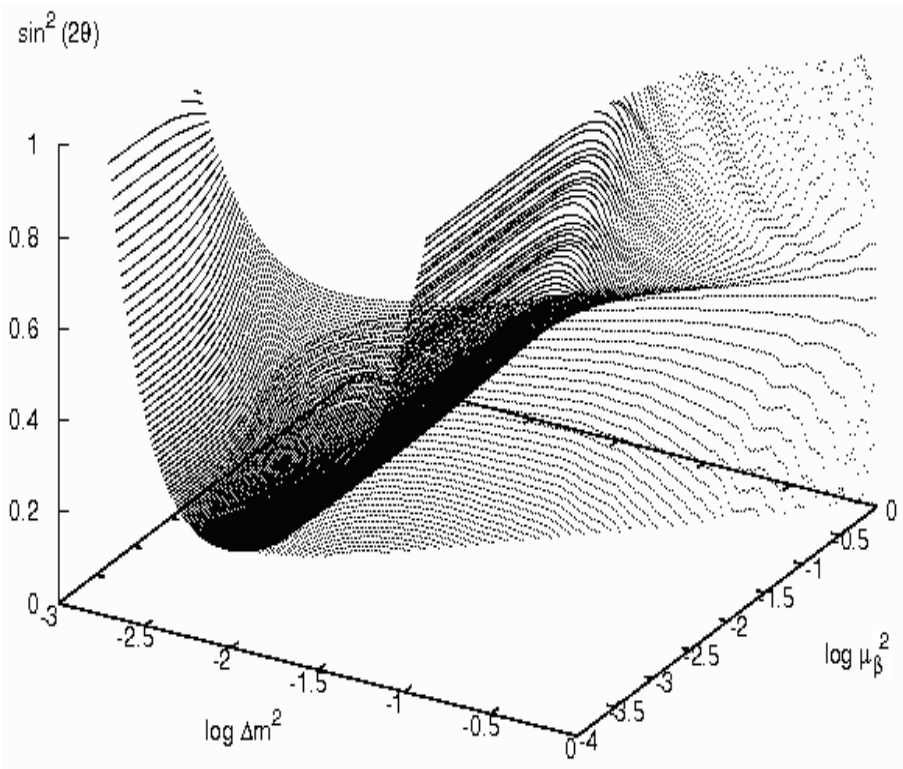

Figure 5.63: Sensitivity volume for model **QD8** at 90 percent confidence level for standard oscillations plus quantum decoherence effects inversely proportional to the neutrino energy.

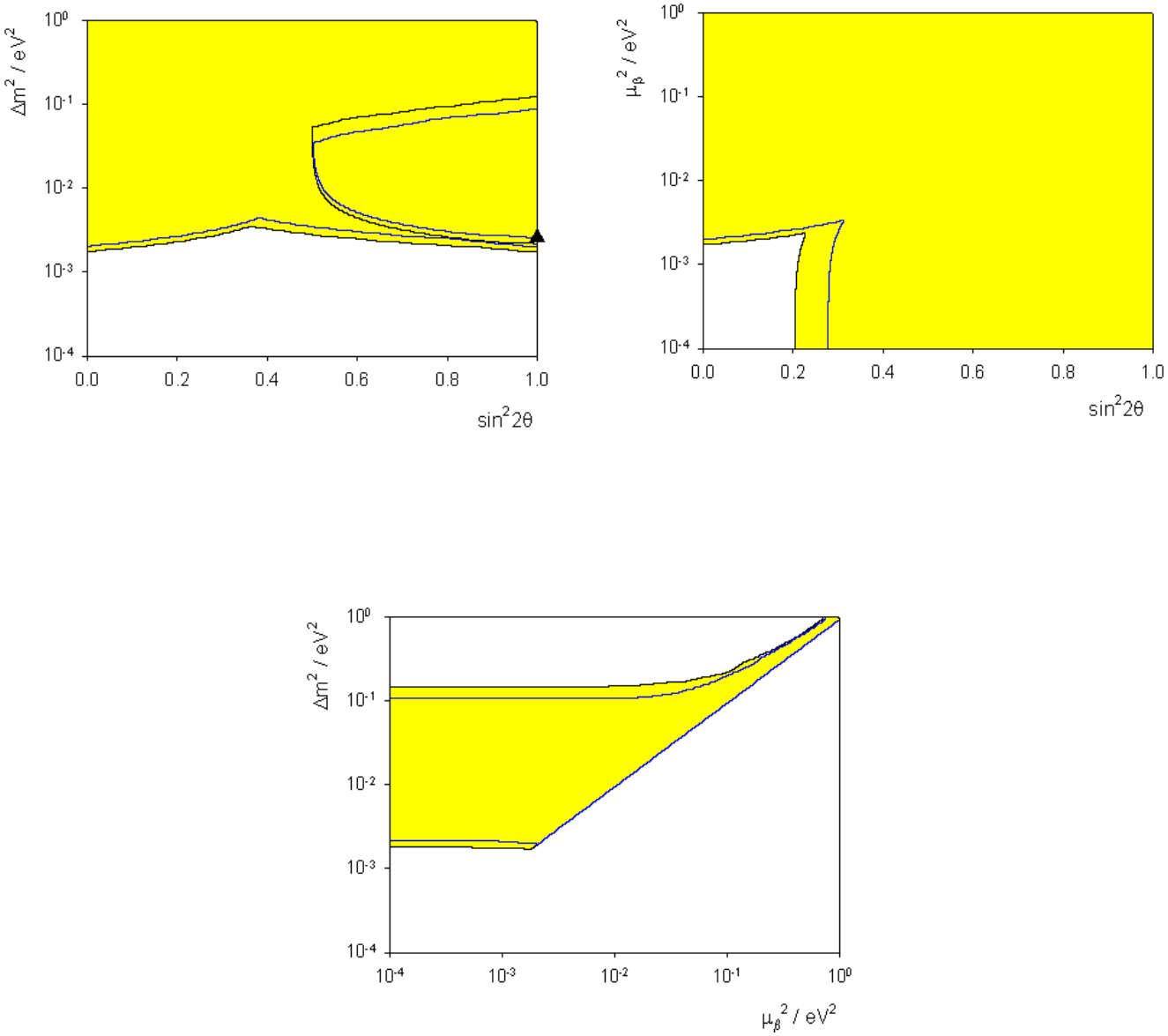

Figure 5.64: Sensitivity contours for model **QD8** at 90 and 99 percent confidence level including standard oscillations and quantum decoherence effects inversely proportional to the neutrino energy.

Decoherence parameters proportional to the neutrino energy squared

In this case, we set $\beta = \frac{\kappa_\beta E^2}{2}$. Restoring the constants, c and $\hbar$, the oscillation probability is given by (5.15) with

$$\omega = 1.27\Delta m^2 \frac{L}{E}, \qquad \beta = 2.53 \times 10^{27} \kappa_\beta E^2 L. \tag{5.47}$$

Here, κ_β is measured in eV^{-1}.

The three dimensional sensitivity volume and two dimensional sensitivity regions are shown in figures 5.65 and 5.66 respectively. Inspection of the surface in figure 5.65 shows that it is quantitatively the same as the surface in figure 5.61 and, hence, the sensitivity regions in figure 5.66 are qualitatively similar to those in figure 5.62. The first plot of figure 5.66 shows Δm^2 against $\sin^2 2\theta$ with the triangle denoting the current experimental point of best fit. This point clearly lies within the sensitivity region. The top right frame of the same figure shows the quantum decoherence parameter, κ_β, plotted as a function of the mixing angle. The sensitivity region lies within the contours and includes the value $\kappa_\beta = 0$. In this case, we are able to place an upper bound of $\kappa_\beta < 10^{-43}\ eV^{-1}$ on the parameter. The final frame in figure 5.66 shows the relationship between Δm^2 and κ_β.

Summary of Model QD8

The model contains a single quantum decoherence parameter, β. As we have only one extra parameter, we were able to let Δm^2 vary and in all cases, we found that the current experimental point of best fit is contained within the sensitivity regions generated in our simulations. For two of the three energy dependences, we were able to place an upper bound of the quantum decoherence parameter but were not able to do so when the parameter was inversely proportional to the neutrino energy. The upper bounds we found are directly comparable to the parameter, b, in models **QD3**, **QD4** and **QD7**.

5.2.10 Model QD9

Our final model contains the parameter d. This model is somewhat different to those we previously considered as the oscillation probability (5.16) now contains a contribution from the $\sin 4\theta$ term. In this model, we set all parameters to zero except

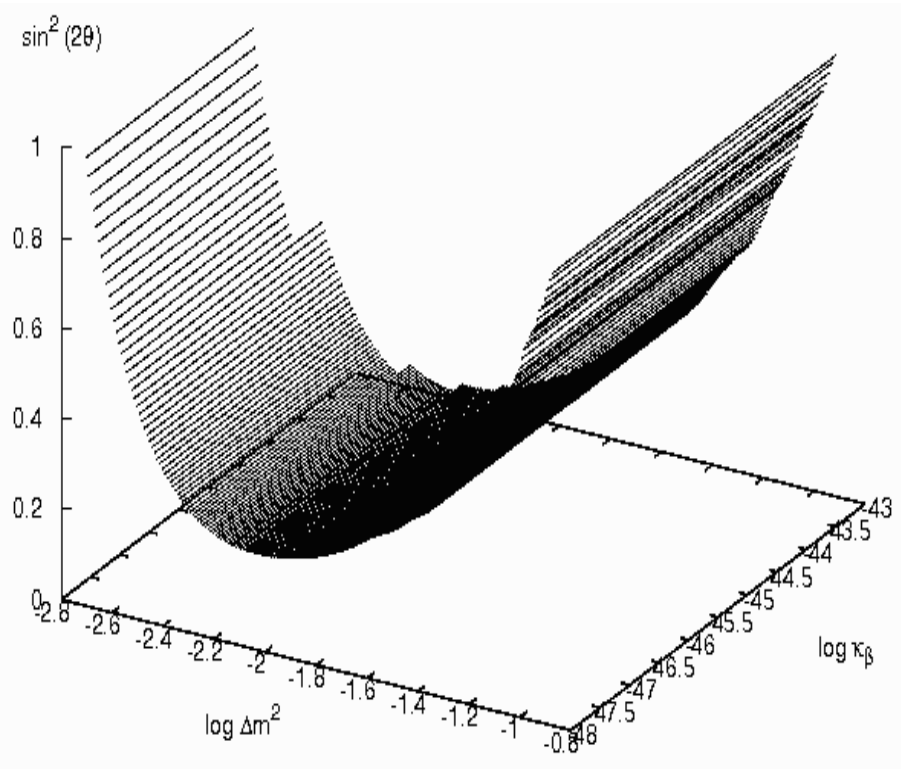

Figure 5.65: Sensitivity volume for model **QD8** at 90 percent confidence level for standard oscillations plus quantum decoherence effects proportional to the neutrino energy squared.

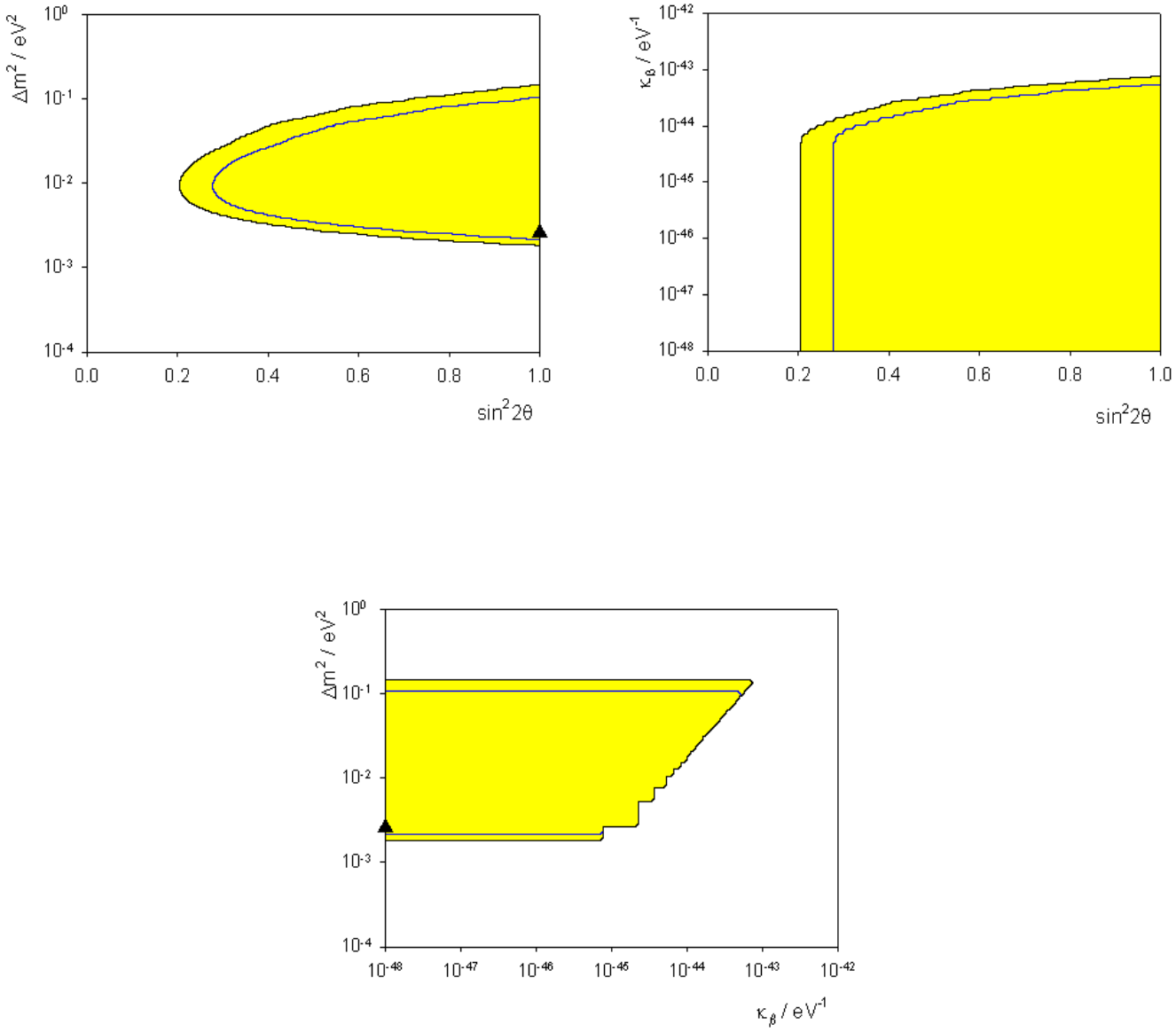

Figure 5.66: Sensitivity contours for model **QD8** at 90 and 99 percent confidence level including standard oscillations and quantum decoherence effects proportional to the neutrino energy squared.

d and Δm^2.

Decoherence parameters with no dependence on the neutrino energy

Firstly, we set $d = \frac{\gamma_d}{2}$. Restoring the constants c and $\hbar$, the oscillation probability (5.16) contains

$$\omega = 1.27\Delta m^2 \frac{L}{E}, \qquad d = 2.5 \times 10^9 \gamma_d L, \tag{5.48}$$

where γ_d is measured in eV.

The sensitivity volume and sensitivity regions are shown in figures 5.67 and 5.68 respectively. We note that both the sensitivity volume and contours in figures 5.67 and 5.68 are similar to those for the last model with the same energy dependence. The experimental point of best fit for Δm^2, denoted by the triangle in the first frame of figure 5.68, lies within the sensitivity region. The second plot of the same figure shows γ_d plotted against $\sin^2 2\theta$. Again, the sensitivity region lies within the contours and includes $\gamma_d = 0$. We are able to place an upper bound on this parameter of $\gamma_d < 10^{-15}\ eV$. The lower frame of this figure shows a plot of Δm^2 against γ_d.

Decoherence parameters inversely proportional to the neutrino energy

In this case, we set $d = \frac{\mu_d^2}{4E}$ and, replacing the constants c and $\hbar$, the oscillation probability (5.16) contains the quantities

$$\omega = 1.27\Delta m^2 \frac{L}{E}, \qquad d = 1.27\mu_d^2 \frac{L}{E}. \tag{5.49}$$

Here, μ_d^2 is measured in eV^2.

Figure 5.69 shows the sensitivity volume for this energy dependence with the related sensitivity regions shown in figure 5.70. The sensitivity regions in this case differ from those for the previous energy dependence. The top left frame shows Δm^2 against $\sin^2 2\theta$. The large region on the right of this plot is the standard region which includes the experimental point of best fit denoted by the triangle. However, we also find regions of parameter space allowed at small values of $\sin^2 2\theta$ and these are a direct consequence of the $\sin 4\theta$ term in the oscillation probability (5.16). The top right plot shows μ_d^2 against $\sin^2 2\theta$. The sensitivity region lies to the right of the large curves on the right hand side of the plot and also in the smaller regions close to $\sin^2 2\theta = 0$. Since experimentally, $\sin^2 2\theta \sim 1$, we are able to place an upper bound on μ_d^2 of around $10^{-1}\ eV^2$ and we also note that $\mu_d^2 = 0$ is contained

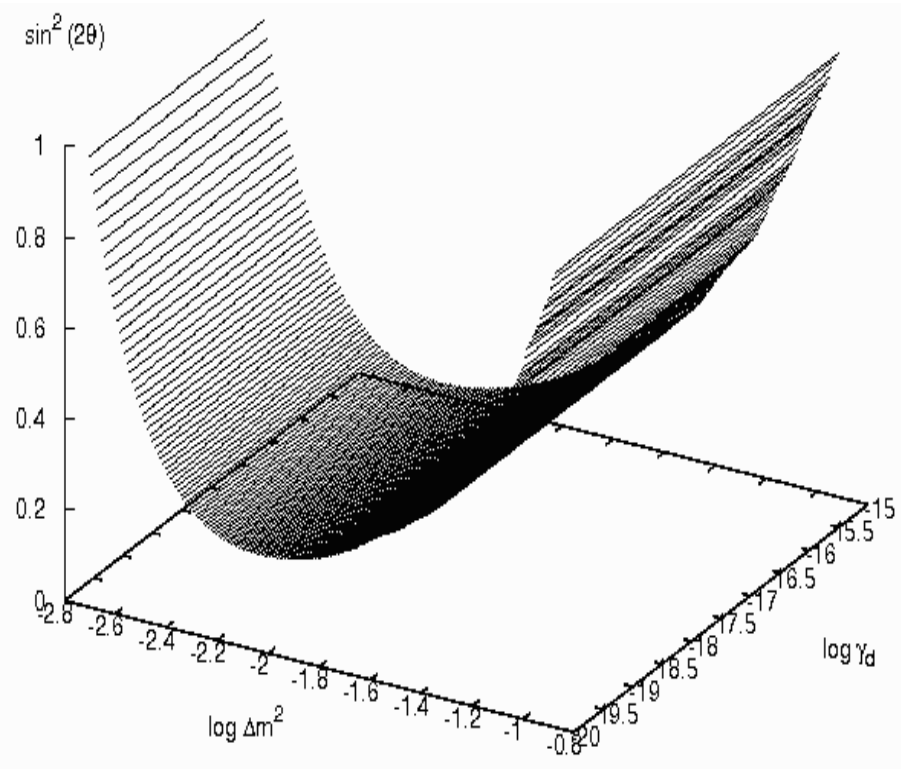

Figure 5.67: Sensitivity volume for model **QD9** at 90 percent confidence level for standard oscillations and quantum decoherence effects with no dependence on the neutrino energy.

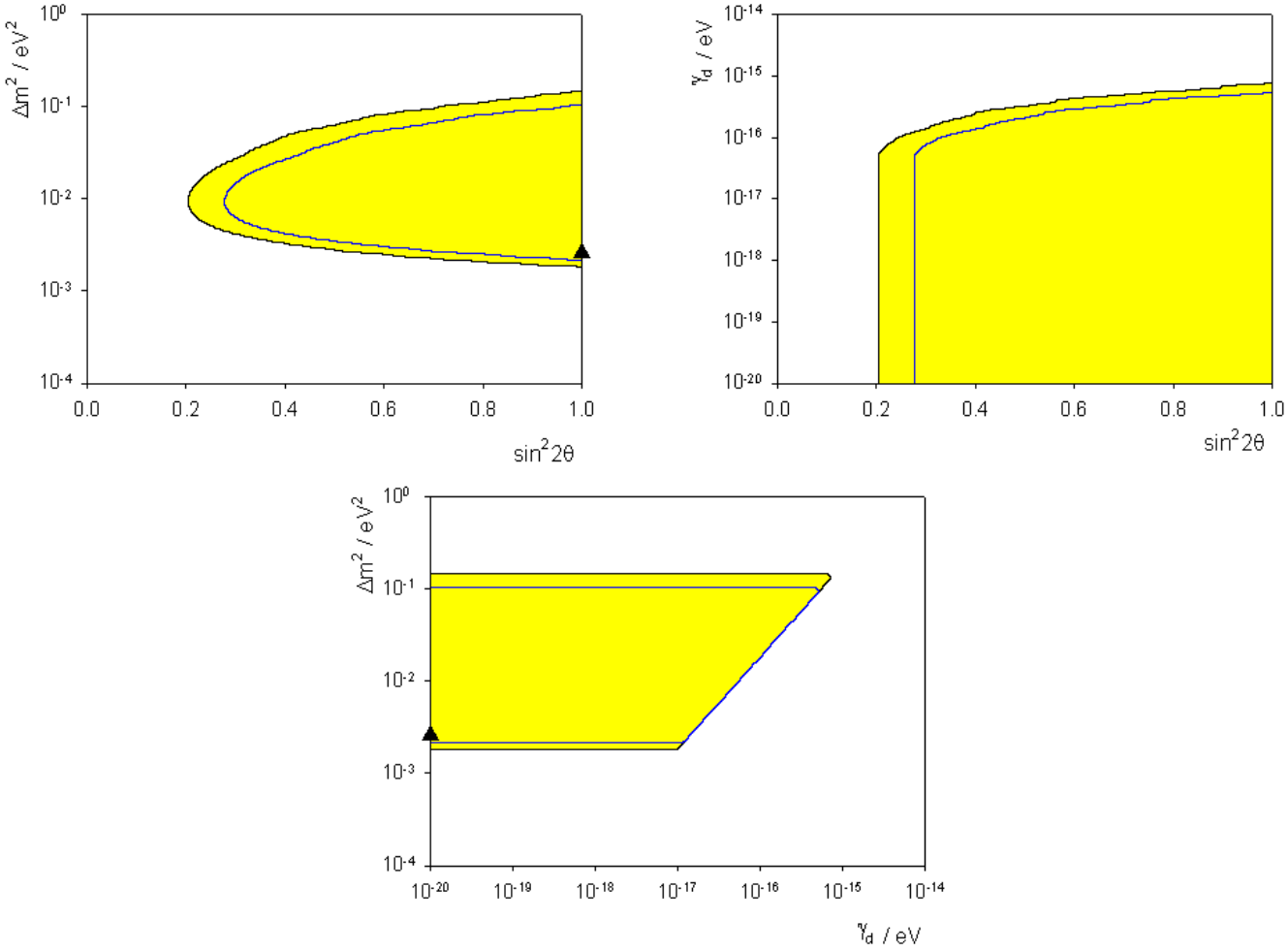

Figure 5.68: Sensitivity contours for model **QD9** at 90 and 99 percent confidence level including standard oscillations and quantum decoherence effects with no dependence on the neutrino energy.

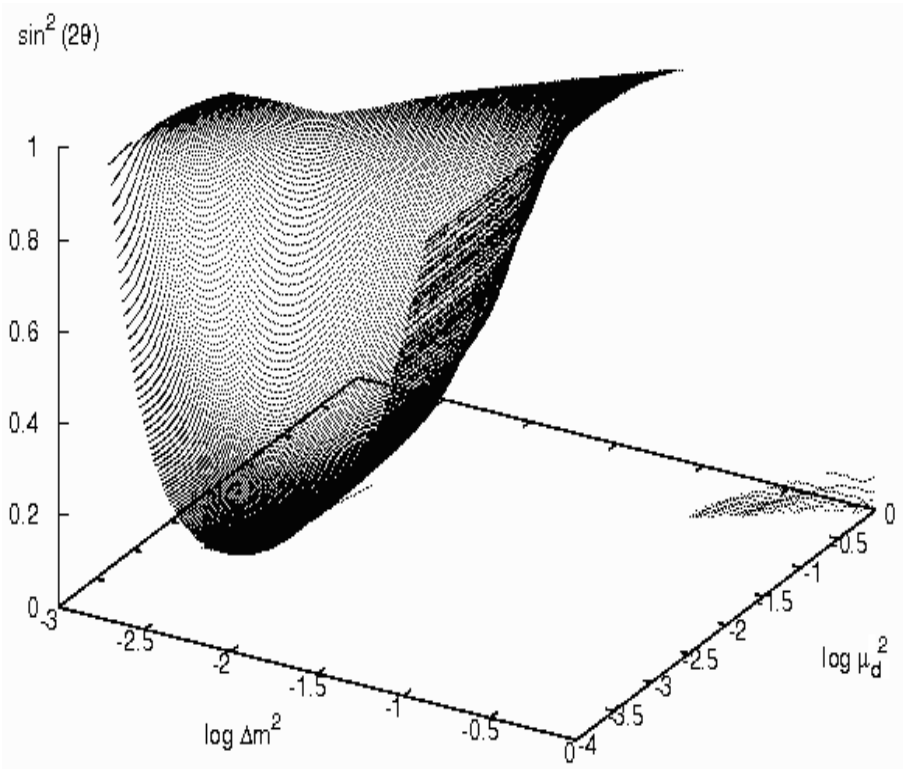

Figure 5.69: Sensitivity volume for model **QD9** at 90 percent confidence level for standard oscillations plus quantum decoherence effects inversely proportional to the neutrino energy.

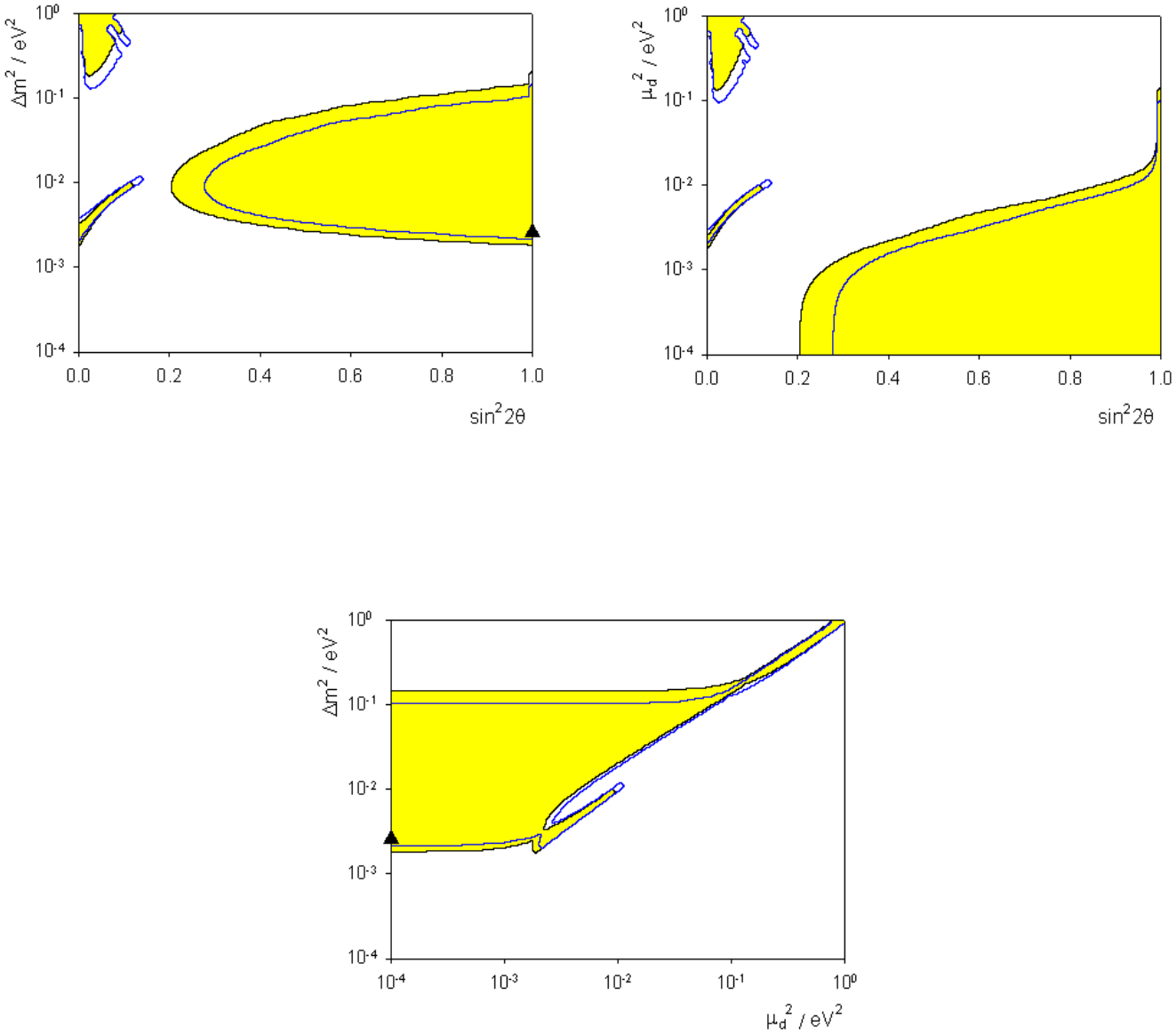

Figure 5.70: Sensitivity contours for model **QD9** at 90 and 99 percent confidence level including standard oscillations and quantum decoherence effects inversely proportional to the neutrino energy.

within the sensitivity region. The final diagram of figure 5.70 shows the standard oscillation parameter, Δm^2, against the quantum decoherence parameter, μ_d^2, with the sensitivity region lying inside the contours.

Decoherence parameters proportional to the neutrino energy squared

Finally, we set $d = \frac{\kappa_d E^2}{2}$. Replacing the constants c and $\hbar$, the oscillation probability is given in (5.16) with

$$\omega = 1.27\Delta m^2 \frac{L}{E}, \qquad d = 2.53 \times 10^{27} \kappa_d E^2 L, \tag{5.50}$$

where κ_d is measured in eV^{-1}.

The sensitivity volume and contours are shown in figures 5.71 and 5.72 respectively. The first plot of figure 5.72 shows Δm^2 against $\sin^2 2\theta$ with the sensitivity region lying inside the curves. The experimental point of best fit, denoted by a triangle, is clearly within the sensitivity region. The top right frame of figure 5.72 plots κ_d against $\sin^2 2\theta$. Again, the sensitivity region lies within the contours. This model is consistent with $\kappa_d \to 0$ and we are able to place an upper bound on this parameter of 10^{-43} eV^{-1}. The lower frame of 5.72 shows Δm^2 against κ_d with the sensitivity region lying within the contours.

Summary of Model QD9

Model **QD9** contains one non-zero quantum decoherence parameter, d. The sensitivity regions, when the decoherence parameters have no energy dependence and a dependence on the neutrino energy squared, are qualitatively the same as those in Model **QD8**. However, there are differences when the quantum decoherence parameter is inversely proportional to the neutrino energy. In this case, contributions from the $\sin 4\theta$ term in (5.16) can clearly be seen. In all cases, the experimental point of best fit for the standard neutrino parameters are contained within the sensitivity regions and we have been able to place upper bounds on the quantum decoherence parameters.

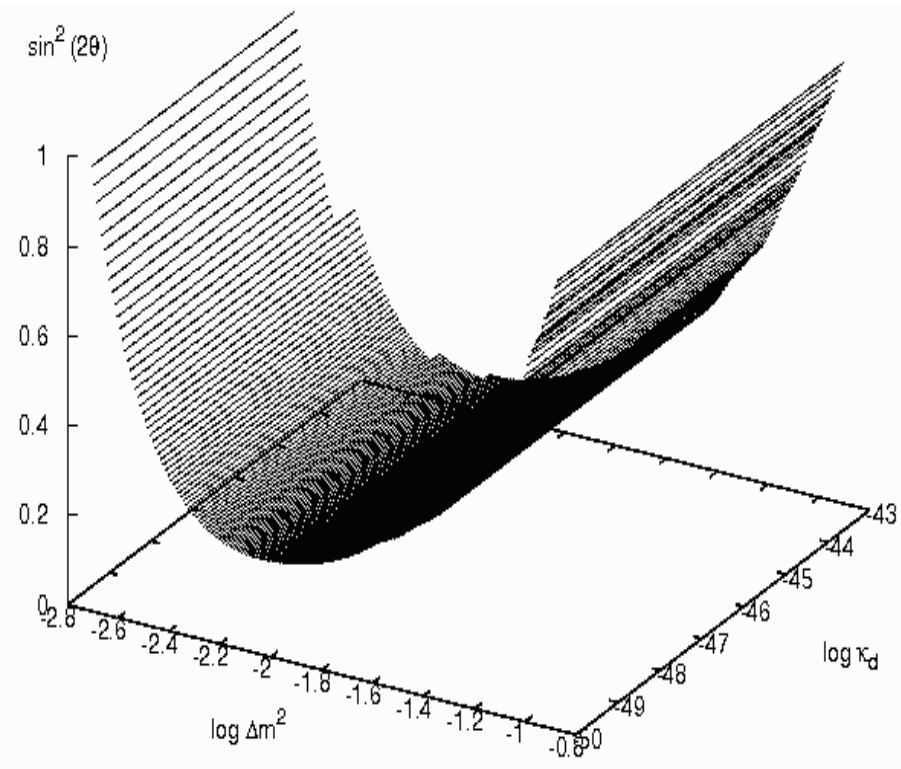

Figure 5.71: Sensitivity volume for model **QD9** at 90 percent confidence level for standard oscillations plus quantum decoherence effects proportional to the neutrino energy squared.

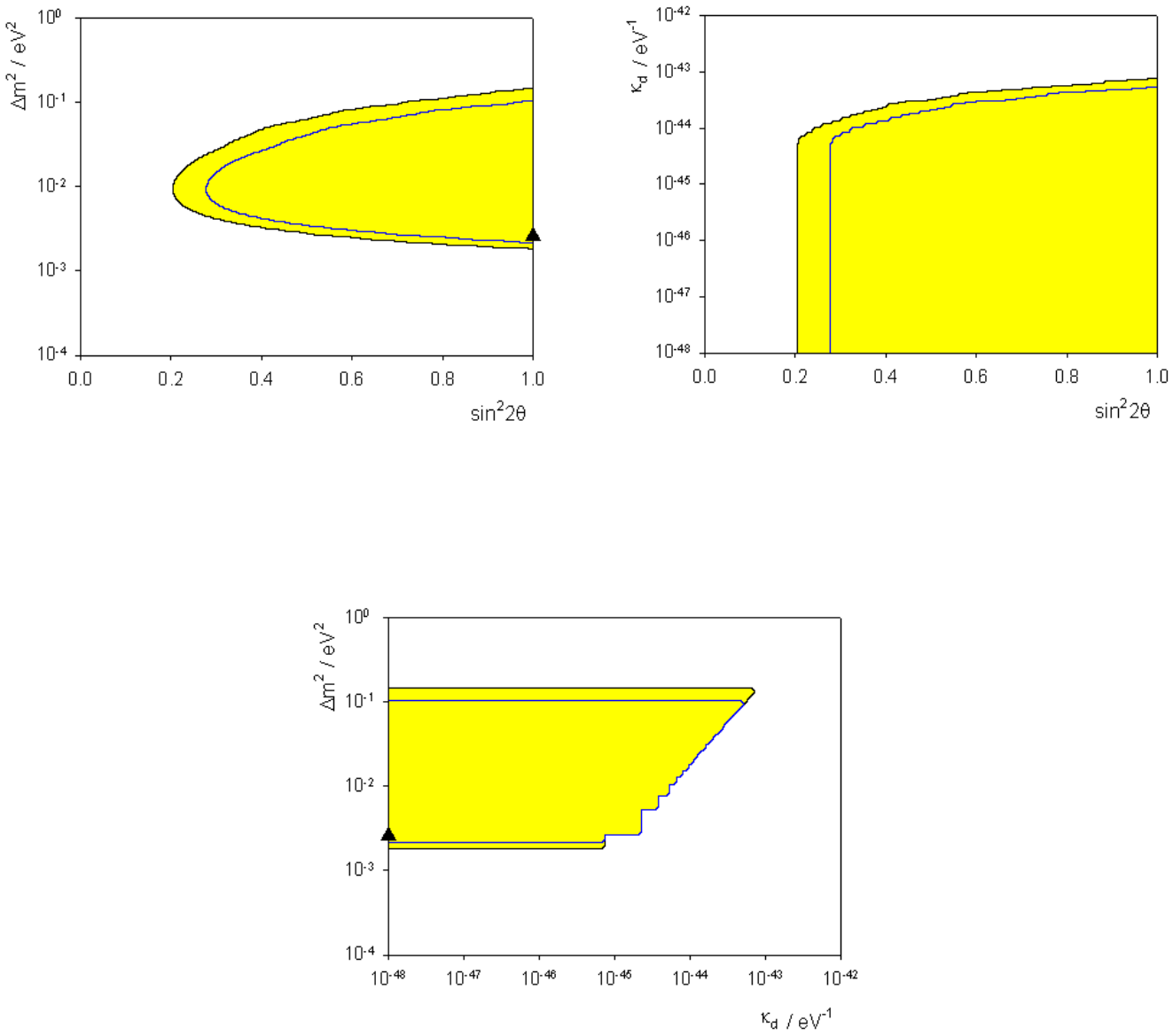

Figure 5.72: Sensitivity contours for model **QD9** at 90 and 99 percent confidence level including standard oscillations and quantum decoherence effects proportional to the neutrino energy squared.

model	a	b	d	α	β
$\gamma(GeV)$	9×10^{-23}	7×10^{-25}	7×10^{-25}	9×10^{-23}	7×10^{-25}
$\mu^2(GeV^2)$	2×10^{-19}	6×10^{-19}	6×10^{-19}	2×10^{-19}	-
$\kappa(GeV^{-1})$	4×10^{-26}	7×10^{-35}	7×10^{-35}	4×10^{-26}	7×10^{-35}

Table 5.1: Table showing the upper bounds of the quantum decoherence parameters for different dependences on the neutrino energy.

5.3 Comparing bounds on the decoherence parameters

In section 5.1, we modelled a two neutrino system which is affected by quantum decoherence, altering the standard model of neutrino oscillations by adding an extra matrix (4.20):

$$h' = -2 \begin{pmatrix} 0 & 0 & 0 & 0 \\ 0 & a & b & d \\ 0 & b & \alpha & \beta \\ 0 & d & \beta & \delta \end{pmatrix}, \tag{5.51}$$

where a, b, d, α, β and δ are quantum decoherence parameters. We have examined three different models which have varying energy dependences and are related to these quantum decoherence parameters by

$$\begin{aligned} 2x &= \gamma_x, \\ 2x &= \frac{\mu_x^2}{2E}, \end{aligned} \tag{5.52}$$

and

$$2x = \kappa_x E^2 \tag{5.53}$$

where $x = a$, b, d α, β or δ. Table 5.1 gives the upper bounds on the sensitivity regions for the various model parameters. We have been unable to put an upper bound on the parameter δ at $\sin^2 2\theta = 1$.

Upper bounds have been placed experimentally on the decoherence parameters by examining data from the Super-Kamiokande experiment [180]. It was found that the parameters had upper bounds of

$$\gamma = 3.5 \times 10^{-23} eV, \qquad \mu^2 = 2.44 \times 10^{-21} eV^2 \qquad \kappa = 9 \times 10^{-10} eV^{-1}. \tag{5.54}$$

Here, we see that our results are entirely comparable with those in [180] when the quantum decoherence parameters have no dependence upon the neutrino energy. When the parameters have an inverse dependence on the neutrino energy, our bounds are not as good as those from the Super-Kamiokande experiment. This is because neutrino telescopes detect higher energy neutrinos than those detected by Super-Kamiokande. Since this is the case, the bounds we find here are many orders of magnitude better than those from [180] when the quantum decoherence parameters are proportional to the square of the neutrino energy. We find, therefore, that low energy experiments, such as Super-Kamiokande, are better at bounding the μ^2 parameters whilst high energy neutrino telescopes are much better at bounding the effects proportional to the neutrino energy squared.

The neutrino system is not the only system which may be affected by interactions with the space-time foam and, assuming that quantum decoherence affects all particles in the same way, we may compare the results found here for neutrinos with those discussed below for different systems. Experiments such as CPLEAR [45] have examined this problem with neutral kaons, as kaons may oscillate into their anti-particle and it has been suggested that this oscillation may be modified by quantum decoherence. Considering this system, upper bounds on the quantum decoherence parameters were found [17, 121]:

$$\alpha < 4 \times 10^{-17} GeV, \quad |\beta| < 2.3 \times^{-19} GeV, \quad \delta < 3.7 \times 10^{-21} GeV. \tag{5.55}$$

We are not able to directly compare the values in table 5.1 with these from the neutral kaon system due to the energy dependence of some of our models. However, using equations (5.52) and (5.53) with the values from table 5.1, we find that the upper bounds for the quantum decoherence parameters which appear in the matrix in equation (5.51) are

$$a = \alpha = 4.75 \times 10^{-23} GeV, \quad b = d = \beta = 3.3 \times 10^{-25} GeV, \tag{5.56}$$

for the model in which the quantum decoherence parameters have no dependence on the neutrino energy,

$$a = \alpha = 1.85 \times 10^{-21} GeV, \quad b = d = \beta = 6.38 \times 10^{-21} GeV, \tag{5.57}$$

for the model in which the quantum decoherence parameters are inversely propor-

tional to the neutrino energy and

$$a = \alpha = 7.96 \times 10^{-25} GeV. \quad b = d = \beta = 1.32 \times 10^{-29} GeV. \tag{5.58}$$

for the model in which the quantum decoherence parameters are proportional to the neutrino energy squared. In order to calculate these values, we took $E = 24.3\ GeV$ for the μ^2 model and $E = 631\ GeV$ for the κ model. These energies correspond to the minimum and maximum energies in our simulations, respectively, and give us the most conservative bounds on a, b, d, α and β. We note that our most conservative bounds on the parameters α and β in equations (5.56)-(5.58) are much better than those from references [17] and [121]. A second analysis of this experiment took place in reference [65] with all six quantum decoherence parameters appearing in the additional matrix h'. The authors of reference [65] were able to put bounds all the parameters in this matrix and they found upper bounds of a, b and α to be of order $10^{-17} - 10^{-18}\ GeV$. Therefore, it seems that the ANTARES experiment will be able to improve the upper bounds of these parameters with respect to the CPLEAR experiment.

This problem has also been explored using neutron interferometry [164, 213, 223] experiments where a slow neutron beam is separated into two parts, which then travel along different paths and are recombined. This results in an interference pattern. The authors of reference [66] were able to put upper bounds on the parameters a and α using data from a neutron interferometry experiment and found

$$a < 1 \times 10^{-22}\, GeV \quad \text{and} \quad \alpha < 7.4 \times 10^{-22}\, GeV. \tag{5.59}$$

In this case, we see that our most conservative results are entirely consistent with these bounds.

5.4 Summary

In this chapter, we presented the results of our numerical simulations to show how ANTARES will be able to look for quantum decoherence effects and place bounds on the size of these effects. Our results will be equally applicable to other neutrino telescopes.

- We began by presenting the nine models which we considered in our numerical

simulations. For each model, we described the parameter content and whether simulations of neutrino oscillations arising purely from quantum decoherence was possible (section 5.1).

- We then presented the results of our simulations. We first showed how we were able to produce spectra describing the number of expected events and saw that quantum decoherence effects would reduce this number in each case, and that the shape of the spectra would also be altered. We then presented the regions of parameter space which ANTARES will be able to probe for each model. In most cases, we were able to use these simulations to place upper bounds on the model parameters (section 5.2).

- Finally, we showed how our results compare to those in the literature. We found that for models which depended inversely on the neutrino energy, the existing bounds in the literature are better than those found here. For the model which has no dependence upon the neutrino energy, our bounds are consistent with those in the literature but the main result is that quantum decoherence parameters which are proportional to the energy squared will be probed to much greater precision than before with high energy neutrino telescopes (section 5.3).

So, the main result of this chapter is that the one model with a theoretical link to quantum gravity, the model in which the quantum decoherence parameters are proportional to the neutrino energy squared, will be probed to precisions many orders of magnitudes lower than has been possible before.

In chapter 8, we examine how quantum decoherence will be probed with astrophysical neutrinos, detected by neutrino telescopes, and, as we shall see, the bounds on quantum decoherence expected from those sources will surpass even those found in this chapter.

Chapter 6

Lorentz invariance violation-theory

In this chapter, we present the theory underlying the possible phenomena of CPT invariance violation which arises due to the violation of Lorentz invariance. We describe how Lorentz invariance may be violated in theories of quantum gravity and then show how these effects may manifest themselves within the neutrino sector, at least for a two neutrino system. We consider how these effects would manifest themselves in a three neutrino system in chapter 8.

6.1 The violation of Lorentz invariance

As we saw in chapter 4, any violations of Lorentz invariance also lead to the violation of CPT. Here, we consider why some theories of quantum gravity predict the violation of Lorentz invariance (LV).

6.1.1 LV in quantum gravity

As we discussed in chapter 2, some theories of quantum gravity predict the existence of a fundamental length scale. This, in itself, may be enough to bring about LV. Imagine if we were able to somehow measure this fundamental length scale. We would measure it in our lab frame and probably find that it was of order the Planck length, $10^{-35}\ m$. If we now repeated the experiment in a different inertial frame, we would expect the length to be shorter, as predicted by the Lorentz transformation. However, we are considering a fundamental length scale and, therefore, we would

expect to measure the same length in all inertial frames. There is, therefore, an error in our naive thought experiment or Lorentz symmetry, at least at the Planck scale, is broken.

Therefore, there exist three possibilities for the fate of Lorentz invariance within theories of quantum gravity:

- It may be that our naive thought experiment is wrong, or that a fundamental length scale does not exist, and so Lorentz invariance remains intact at Planck scales;
- It may be that, at the Planck scale, Lorentz invariance is broken and physics takes on a preferred frame;
- It may be that Lorentz invariance as we know it is deformed, so, for example, the Lorentz transformations involves a second quantity which is not observer dependent. So, perhaps the Planck length is invariant in an identical way to the speed of light.

In the second and third option, this may mean that quantities we think of as being Lorentz invariant, such as the standard dispersion relation, $E^2 = p^2 + m^2$, may have to be modified to take into account this new phenomenon.

6.1.2 The theoretical status of LV

We have seen that if a fundamental length scale exists, then this may lead to LV. Here, we review the theoretical status of Lorentz invariance violation.

Lorentz invariance violation in string theory

String theory approaches the quantum gravity problem from a particle physics perspective. Although string theory does not discretize space-time, since it describes the background space-time entirely classically, the issues related to this are still far from being resolved. At this moment in time, since the background is classical, there are no indications that Lorentz invariance is broken within string theory. Of course, if it is found that the background space-time needs to be discretized, then this could lead to Lorentz invariance violating string theories. Having said that, two particular theories which are considered to be low energy limits of string theory, namely flat non-commutative space-times [184] and the Standard Model Extensions (SMEs) [171],

indicate the presence of LV. The non-commutative space-time approach assumes that space-time coordinates do not commute, leading to the breaking of Lorentz symmetry and various forms of the dispersion relation [187, 194]. The SMEs extend the Standard Model Lagrangian to include all LV [92] and CPT violating [91] operators which are of dimension 4 or less, in order to be renormalizable. Again, this phenomenological model modifies the dispersion relation.

Lorentz invariance violation in loop quantum gravity

In contrast to string theory, loop quantum gravity approaches the quantum gravity problem from a general relativity perspective. The theory is fully background independent, as is general relativity, which leads to the prediction of discrete space-times [220]. Initially, it was thought that loop quantum gravity would preserve Lorentz symmetry, however it is now thought that this theory could break [28–30, 135, 231] or deform [38, 129] Lorentz symmetry, thus leading to modified dispersion relations. The issue of whether Lorentz symmetry is preserved, broken or deformed is still unresolved in loop quantum gravity.

Doubly special relativity

On particular theory which has received much attention in the literature is that of doubly special relativity [37]. Here, special relativity is modified to include two observer independent quantities; the speed of light, c and the Planck length, l_p. This leads to modified dispersion relations of the form discussed in the next section.

In addition to the phenomenology arising from these modified dispersion relations, the theory leads to the possible resolution of two outstanding problems, namely the observation of TeV photons and of cosmic ray events above the GZK cutoff [40]. In the first case, photons created above energies of $\sim 10\ TeV$ should interact with CIRB photons, leading to electron-positron pair production and the disappearance of these high energy photons. However, the HEGRA telescope [13] has detected high energy photons up to $24\ TeV$ [21]. In the second case, ultra high energy cosmic rays interact with CMB photons and produce pions. The cosmic rays lose energy through this process until they pass below the GZK [144, 243] cutoff $\sim 10^{19}\ eV$. However, there is evidence that the cosmic ray spectrum extends beyond this energy [229]. In both these cases, by modifying special relativity, doubly special relativity alters the threshold energy at which the cutoff occur. The effects of LV may, therefore, already

have been observed.

6.2 Modified dispersion relations

From the discussions above, if we allow LV then this may lead to the modifications of the dispersion relation:

$$E^2 = p^2 + m^2 + f(p, E, E_p), \tag{6.1}$$

where E is the energy of the neutrino, p the neutrino momentum, m is the mass eigenstate of the neutrino and E_p is the Planck energy. The function f contains all the novel LV effects. For our analysis here, we find it useful to parameterize this function so the dispersion relation (6.1) becomes

$$E^2 = p^2 + m^2 + \eta p^2 \left(\frac{E}{E_p}\right)^{\alpha}, \tag{6.2}$$

where η and α are parameters of the Lorentz invariance violating theory.

Using (6.2) and assuming the parameter η has a dependence upon the mass eigenstate, then we find that the Hamiltonian in the mass basis, for a two neutrino system, may be written, approximately, as

$$H = \begin{pmatrix} \frac{m_1^2}{2E} + \frac{\eta_1 E^{\alpha+1}}{2} & 0 \\ 0 & \frac{m_2^2}{2E} + \frac{\eta_2 E^{\alpha+1}}{2} \end{pmatrix}. \tag{6.3}$$

The probability that a neutrino of flavour a oscillates to one of flavour b is then given by

$$P[\nu_a \to \nu_b] = \left| \sum_{i=1}^{2} U_{ai} e^{-H_{ii}} U_{bi}^{*} \right|^2, \tag{6.4}$$

where the U's are components of the neutrino mixing matrix:

$$U = \begin{pmatrix} \cos\theta & \sin\theta \\ -\sin\theta & \cos\theta \end{pmatrix}. \tag{6.5}$$

n	$\Delta\eta_n$ (eV^{1-n})
1	2.3×10^{-21}
2	2.3×10^{-30}
3	2.3×10^{-39}

Table 6.1: Table showing the values of $\Delta\eta$ for various energy dependences of the LV parameters.

The probability is therefore given by

$$P[\nu_a \to \nu_b] = \sin^2 2\theta \sin^2 \left[\frac{\Delta m^2 L}{4E} + \frac{\Delta\eta E^{\alpha+1} L}{4E_p^\alpha} \right]. \tag{6.6}$$

Replacing c and $\hbar$ and absorbing the Planck energy into the parameter $\Delta\eta$ gives

$$P[\nu_a \to \nu_b] = \sin^2 2\theta \sin^2 \left[1.27 \frac{\Delta m^2 L}{E} + 1.27 \times 10^{9(n+1)} \Delta\eta E^n L \right], \tag{6.7}$$

where we have set $n = \alpha + 1$. If we set $\Delta\eta = 0$, then we recover the standard oscillation probability (1.7). Furthermore, we assumed that the LV parameter η had a dependence upon the mass eigenstate. If this is not the case and the parameter η is universal to all mass eigenstates, then, even if the theory violates Lorentz invariance, the neutrino oscillation probability is invariant. Figures 6.1 and 6.2 show how these LV effects modify the neutrino oscillation probability. To construct these plots, we used the upper bounds found in the next chapter and shown in table 7.1 Comparing figures 6.1 and 6.2 with those for standard oscillations in figures 4.2 and 4.3, we see that for low energy neutrinos, the effects are negligible. However, for higher energy neutrinos, this is not the case. If we compare the plots of probability against path length for high energy neutrinos, we see that for standard oscillations, almost no oscillations occur, however, if we include the LV effects, the oscillation probability becomes significant at much shorter path lengths.

In the next chapter, we will model these effects numerically in the atmospheric neutrino system in order to place upper bounds on the model parameters. It would be useful therefore to have a guide to the approximate values of these parameters. In order to do this, we note from (6.7) that the LV effects become significant when

$$1.27 \frac{\Delta m^2}{E} \approx 1.27 \times 10^{9(n+1)} \Delta\eta E^n. \tag{6.8}$$

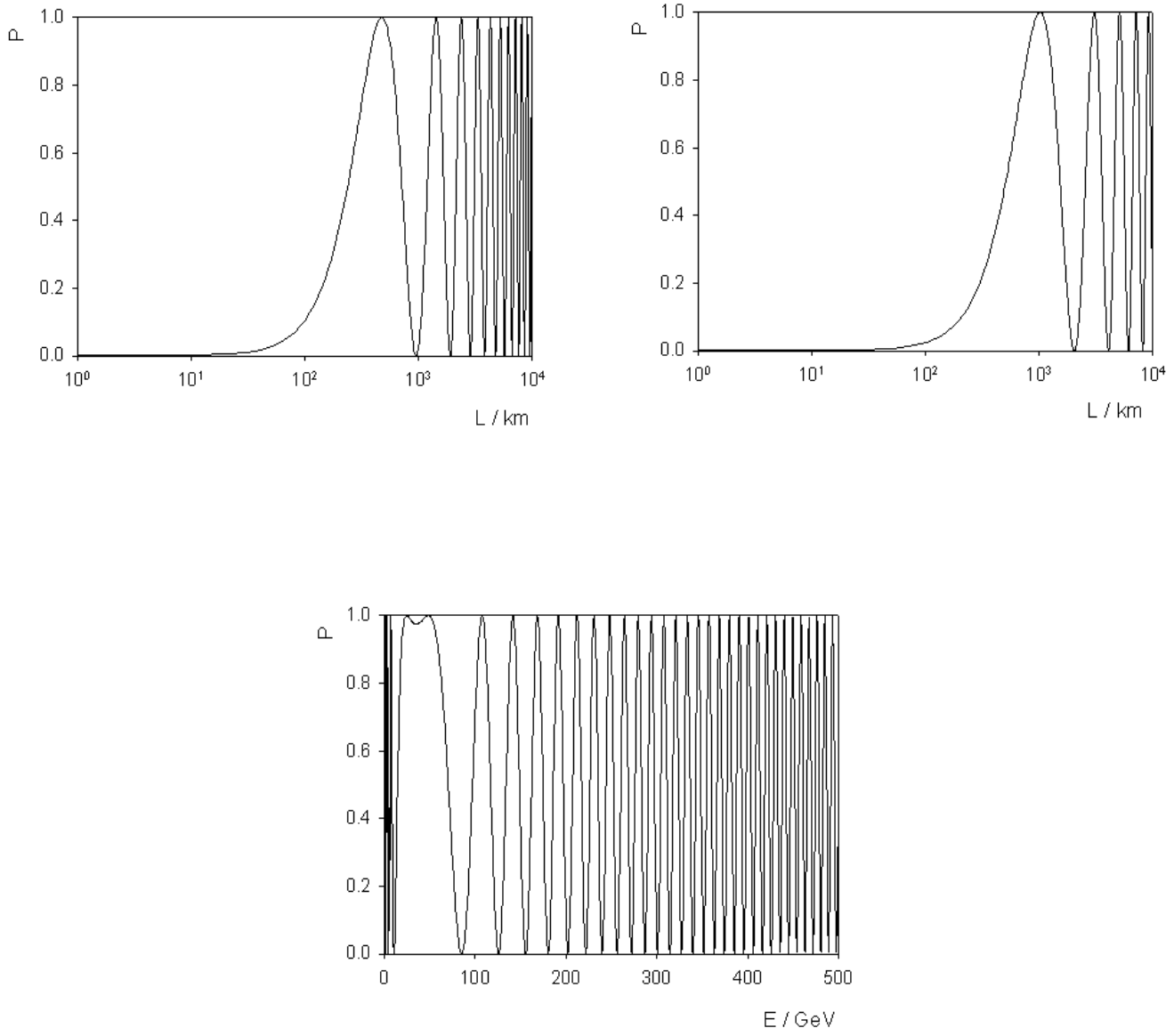

Figure 6.1: Neutrino oscillation probabilities for $n = 2$ ($\alpha = 1$). The top left plot shows the oscillation probability as a function of path length for low energy neutrinos, with $E = 1\ GeV$, for comparison. The top right plot shows the oscillation probability versus path length for neutrinos with an energy of 200 GeV whilst the lower plot shows the oscillation probability as a function of energy for $L = 10^4\ km$.

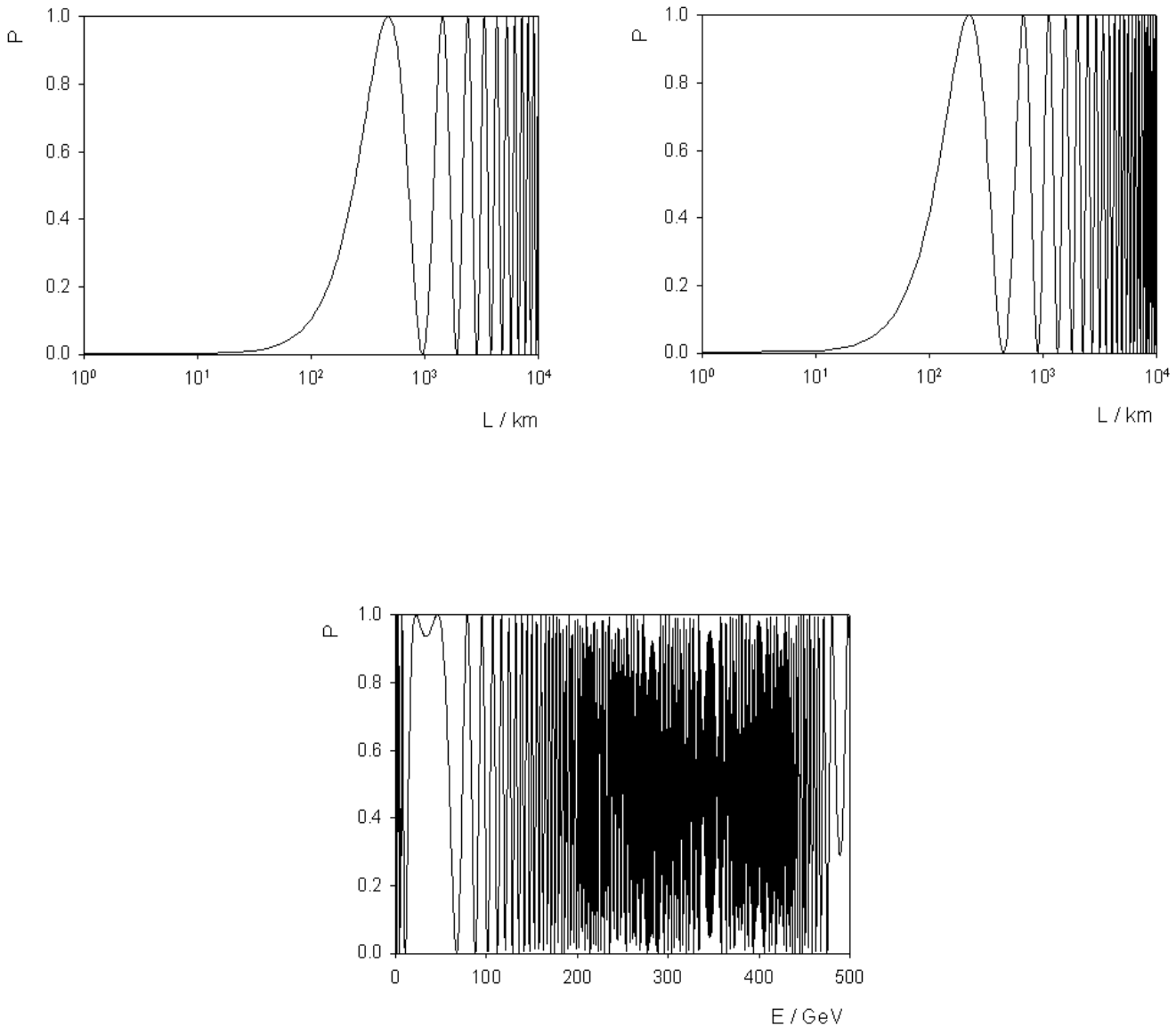

Figure 6.2: As figure 6.1 but with $n = 3$ ($\alpha = 2$).

Thus, the LV parameter is given approximately by

$$\Delta\eta \approx 1 \times 10^{-9(n+1)} \frac{\Delta m^2}{E^{n+1}}. \tag{6.9}$$

Using the value of Δm^2 from table 1.2 and $E = 1\ GeV$, the peak in the atmospheric neutrino flux, we are able to place bounds on this parameter. Table 6.1 shows the value of the LV parameter for various energy dependences (values of n).

6.3 LV models with off-diagonal elements in the Hamiltonian

As we outlined in section 6.1, the standard model extensions (SMEs) can be considered as a low energy phenomenological model of quantum gravity which includes LV and CPT violating operators. The effective SME Hamiltonian describing flavour neutrino propagation, to first order, is [172]

$$H^{eff}_{\alpha\beta} = |\overrightarrow{p}|\delta_{\alpha\beta} + \frac{1}{2|\overrightarrow{p}|}[\widetilde{m}^2 + 2(a^{\mu}_L p_\mu - (c_L)^{\mu\nu} p_\mu p_\nu)]_{\alpha\beta} \tag{6.10}$$

where $\widetilde{m}$ is related to the standard neutrino mass, the indices, α and β denote the flavour and a_L, c_L are the LV parameters. One of the main differences between this model and the LV effects described in section 6.2 is that, in this case, the Hamiltonian need not be diagonal. In reference [172], various assumptions are made to simplify the model but here, we shall adopt a general off diagonal formalism.

Firstly, we shall assume that the Hamiltonian in the mass basis takes the form

$$H_{eff} = \begin{pmatrix} \frac{m_1^2}{2E} & a_1 - ia_2 \\ a_1 + ia_2 & \frac{m_2^2}{2E} \end{pmatrix}, \tag{6.11}$$

where a_1 and a_2 are real LV parameters. In order to calculate the oscillation probability, we shall adopt the density matrix approach introduced in chapter 4 although, since we are dealing with standard quantum mechanics, the probability may also be derived in the standard way. Writing the Hamiltonian (6.11) in terms of the Pauli

matrices gives

$$h_{ij} = -2 \begin{pmatrix} 0 & -\frac{\Delta m^2}{4E} & -a_2 \\ \frac{\Delta m^2}{4E} & 0 & a_1 \\ a_2 & -a_1 & 0 \end{pmatrix}, \tag{6.12}$$

where we have omitted the zeroth row and column for simplicity as all these components are identically zero. The matrix (6.12) has eigenvalues, λ_i, given by $\{\pm i\Omega,\ 0\}$ and is diagonalized by the unitary matrix

$$U = \frac{1}{\sqrt{2a_1^2 + 2a_2^2}\Omega} \begin{pmatrix} \omega a_1 - i a_2 \Omega & \omega a_1 + i a_2 \Omega & -a_1\sqrt{2a_1^2 + a_2^2} \\ \omega a_2 + i a_1 \Omega & \omega a_2 - i a_1 \Omega & -a_2\sqrt{2a_1^2 + a_2^2} \\ a_1^2 + a_2^2 & a_1^2 + a_2^2 & \omega\sqrt{2a_1^2 + a_2^2} \end{pmatrix}, \tag{6.13}$$

where, $\Omega \quad \sqrt{\omega^2 + a_1^2 + a_2^2}$ with $\omega = \Delta m^2/4E$. The components of the density matrix are then given by

$$\rho_i(L) = \sum_{j,k} U_{ij} e^{\lambda_j L} U^{-1}_{jk} \rho_k(0), \tag{6.14}$$

where U_{ij} are the components of the matrix in (6.13) and $\rho(0)$ is the density matrix initially. Assuming we have a muon neutrino which oscillates into a tau neutrino, the probability of oscillation is

$$P = \mathrm{Tr}[\rho_\mu(L)\rho_\tau(0)] \tag{6.15}$$

where $\rho_\mu(0)$ and $\rho_\tau(0)$ are given in equations (4.24) and (4.26) respectively. Thus, the oscillation probability is

$$\begin{aligned} P[\nu_\mu \to \nu_\tau] \quad & \frac{1}{2}\left[\cos^2 2\theta \left(1 - \frac{\omega^2}{\Omega^2} - \frac{|a|^2}{\Omega^2}\cos(2\Omega L)\right)\right. \\ & + \sin^2 2\theta \left(1 - \frac{a_1^2}{\Omega^2} - \frac{(\omega^2 + a_2^2)}{\Omega^2}\cos(2\Omega L)\right) \\ & \left. + \frac{1}{2}\sin 4\theta \left(\frac{4\omega a_1}{\Omega^2}\sin^2(\Omega L)\right)\right], \end{aligned} \tag{6.16}$$

with $a = a_1 + i a_2$. In an analogous way to the diagonal case, the LV parameter may have an explicit dependence upon the neutrino energy and so we let $a_i \to a_i E^n$ where n is an extra parameter of the theory. The SMEs expect $n = 0, 1$, since the theory only allows operators of dimension 4 or less in order to be renormalizable [202]. We

shall not make this assumption, instead, we shall assume that any LV effects, whether they appear in the diagonal or off-diagonal elements of the Hamiltonian, result in dispersion relations similar to that in equation (6.2) and so we shall consider the cases $n = 1,\ 2$ and 3, thus considering cases where the operators of the theory have dimension 4, 5 and 6.

If we consider atmospheric neutrinos, then the mixing is maximal ($\sin^2 2\theta = 1$) and so, in the high energy limit, the probability of oscillation tends towards zero. Thus, we would expect the ratio of electron to muon neutrinos to take on an energy dependence if LV effects are present.

The second case we consider is that where the LV effects are flavour based, so we assume the Hamiltonian in the flavour basis to have the form

$$H_{eff}^{flav} = \begin{pmatrix} m_{ee}^2 & m_{e\mu}^2 \\ m_{e\mu}^2 & m_{\mu\mu}^2 \end{pmatrix}. \tag{6.17}$$

Transforming back to the mass basis, we find the form of the Hamiltonian to be

$$H_{eff}^{mass} = \begin{pmatrix} \frac{m_1^2}{2E} - a_1 \sin 2\theta & a_1 \cos 2\theta - i a_2 \\ a_1 \cos 2\theta + i a_2 & \frac{m_2^2}{2E} + a_1 \sin 2\theta \end{pmatrix}. \tag{6.18}$$

The probability of oscillation is therefore given by (6.16) with

$$\begin{aligned} \omega &\rightarrow \omega + a_1 \sin 2\theta, \\ a_1 &\rightarrow a_1 \cos 2\theta, \\ a_2 &\rightarrow a_2. \end{aligned} \tag{6.19}$$

If we take the high energy limit in this case and assume maximal mixing as in the case of atmospheric neutrinos, then the oscillation probability goes to unity. Thus, for extremely high energy atmospheric neutrinos, we would expect to see a significant deficit in the muon neutrino flux.

It is also interesting to note that if we let

$$\begin{aligned} m_1^2 &\rightarrow m_1^2 + A\cos^2\theta, \\ m_2^2 &\rightarrow m_1^2 + A\sin^2\theta, \\ a_1 &\rightarrow \frac{A}{2E}\sin\theta\cos\theta, \\ a_2 &\qquad 0. \end{aligned} \tag{6.20}$$

then we recover the Lorentz invariant matter effects probability as described in chapter 1.

6.4 Summary

In this chapter, we have considered how standard neutrino oscillation phenomenology may be modified by the presence of Lorentz invariance violating effects.

- We began by reviewing the link between theories of quantum gravity and the violation of Lorentz invariance (section 6.1).
- We then considered modified dispersion relations and how they lead to LV effects being present in the neutrino Hamiltonian. In this case, the Hamiltonian in the mass basis remained diagonal. We were able to derive the neutrino oscillation probability analytically for the two neutrino system and we will utilize our findings in the next chapter (section 6.2).
- Finally, we considered off-diagonal LV entries in the Hamiltonian, in both the mass and flavour bases. We again found that we are able to derive an oscillation probability when we consider just two neutrinos (section 6.3).

In the next chapter, we use the results derived here to numerically model how LV effects, which are simplest in the mass basis, would modify the atmospheric neutrino system. We consider the three neutrino system and LV effects in chapter 8.

Chapter 7

Lorentz invariance violation-simulations

In this chapter we present the results of our numerical simulations of Lorentz invariance violation (LV) in atmospheric neutrinos using the package *OSCFIT*. We show how the expected number of events is altered by the presence of LV effects and how neutrino telescopes will be able to place upper bounds on model parameters. We consider the models for two neutrinos introduced in chapter 6, where the LV effects appear firstly in the diagonal terms of the Hamiltonian and also those models which allow for off-diagonal entries.

7.1 LV models with a diagonal Hamiltonian

We firstly consider those models which result in the Hamiltonian in the mass basis being diagonal. As described in the chapter 6, these effects may lead to atmospheric neutrino oscillation probabilities of the form (6.7)

$$P[\nu_\mu \to \nu_\tau] = \sin^2 2\theta \sin^2 \left[1.27 \frac{\Delta m^2 L}{E} + 1.27 \times 10^{9(n+1)} \Delta\eta E^n L \right], \qquad (7.1)$$

where we have replaced the constants c and $\hbar$. We begin by considering how these effects may alter the observed spectra of atmospheric neutrinos.

7.1.1 Spectra including diagonal LV effects

As in chapter 5, we are able to examine how these novel effects alter the spectra in both $E/\cos\vartheta$ and L. We consider three models with differing energy dependences, namely

- Model **LV1** - with $n = 1$:
- Model **LV2** - with $n = 2$:
- Model **LV3** - with $n = 3$:

the first value being motivated by the SME's with the other two values arising from directly considering modifications to the dispersion relation of the form (6.1).

Model LV1

We begin by examining the spectra obtained when we consider the possibility that neutrino oscillations occur as a consequence of LV only ($\Delta m^2 = 0$) when the LV parameters are proportional to the neutrino energy. Figure 7.1 show the expected spectra of events as a function of $E/\cos\vartheta$ and $\cos\vartheta$. Again, E is the reconstructed neutrino energy whilst ϑ is the zenith angle, where $\cos\vartheta$ corresponds to the path length, L. In each case, the solid line corresponds to the Monte Carlo simulation with standard oscillations whereas the dotted and dashed lines are the MC simulations for LV only induced oscillations. The plot in the top left shows the spectra as a function of $E/\cos\vartheta$ whilst the bottom left shows the spectra as a function of $\cos\vartheta$. We have also plotted the ratio of the number of events compared to no oscillations. These plots are shown on the right of figure 7.1. The first thing we notice about the plots on the left of figure 7.1 is that, for the larger values of the LV parameter, there is a definite suppression in the number of observed events by a factor of approximately two. If, however, we consider the case that the LV parameter takes the smaller value, it is more difficult to distinguish oscillations that arise as a consequence of LV effects from those arising in the standard oscillation picture. If we consider the frames on the right of this figure, we note that there are some features which would allow us to differentiate between the two phenomenologies. In the top left frame, we note that at low energies, the LV model does not result in an oscillation minima whereas the standard oscillation model does. Secondly, although the difference is small, the bottom right frame shows a deviation from the standard picture at high

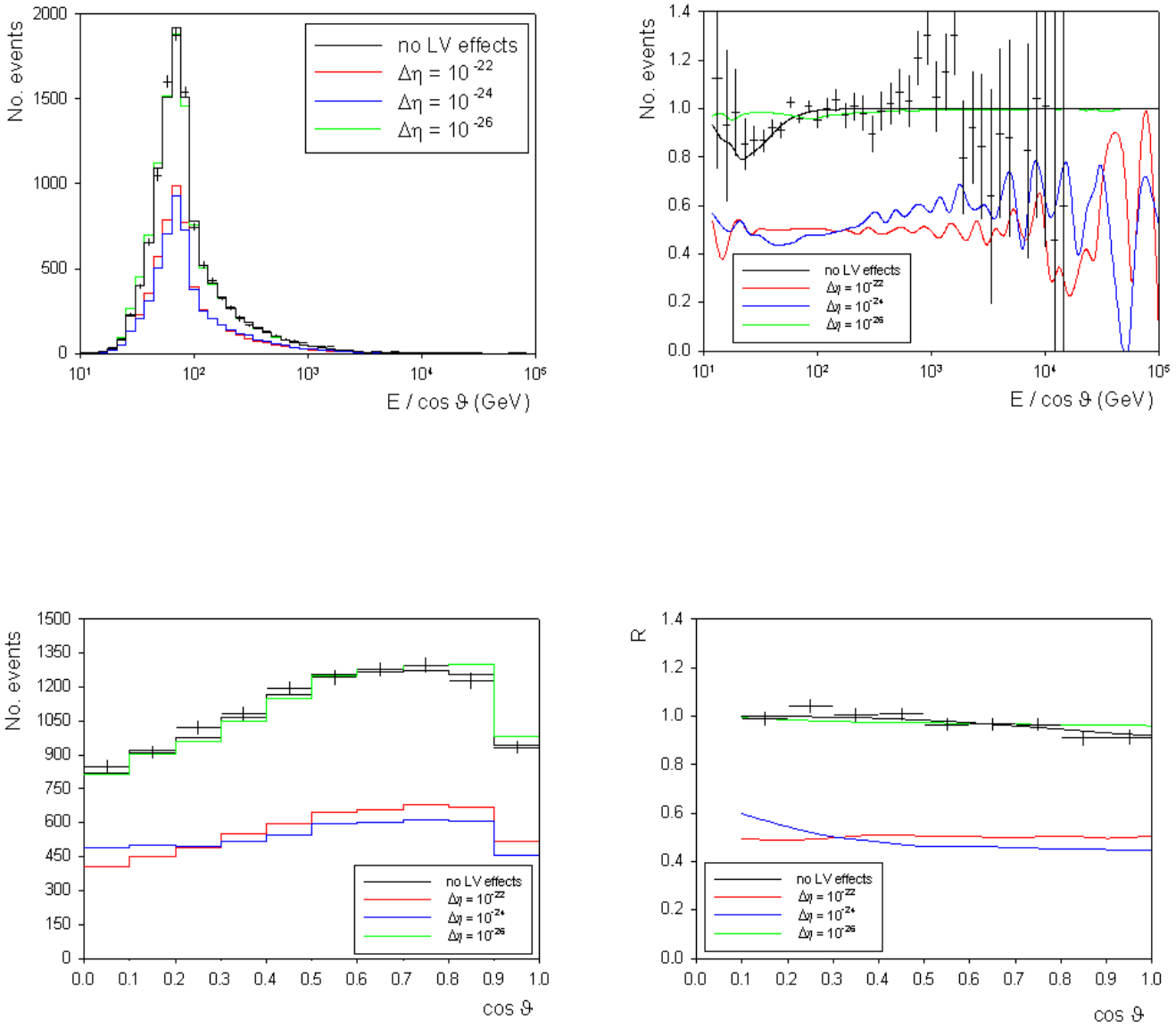

Figure 7.1: Spectra of events when the diagonal LV effects are proportional to the neutrino energy. The black line represents the MC simulation of standard oscillations with the coloured lines showing the spectra for oscillations from LV.

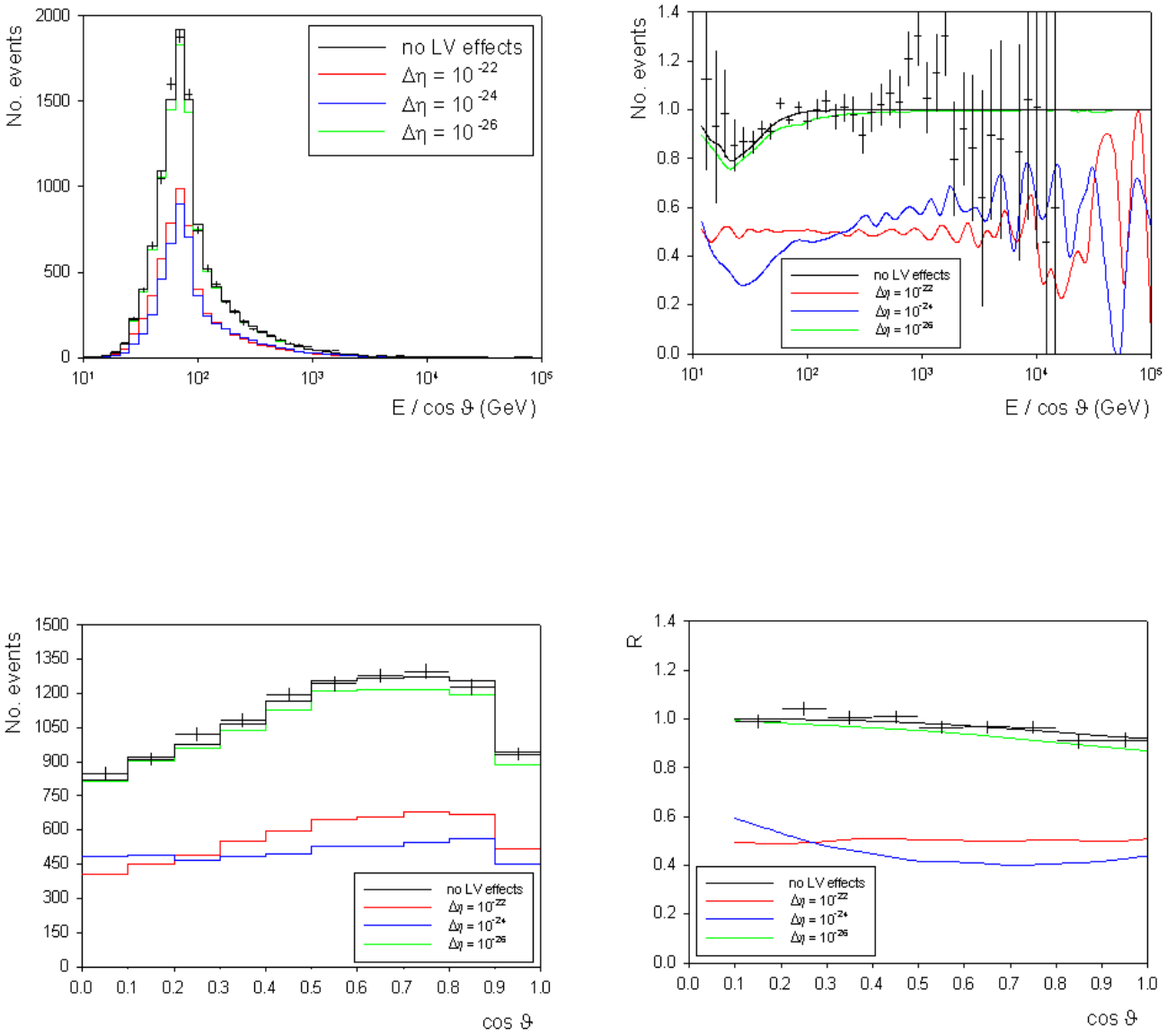

Figure 7.2: As figure 7.1 but the coloured lines show the spectra for standard oscillations plus LV.

values of the zenith angle corresponding to large path lengths. It may be possible, therefore to distinguish between the standard oscillation picture and this LV model by considering the spectra in $E/\cos\vartheta$ and $\cos\vartheta$.

Secondly, we consider the case of standard oscillations plus Lorentz violation. Figure 7.2 shows the spectra and ratio of number of events compared to no oscillations as functions of $E/\cos\vartheta$ and $\cos\vartheta$. Again, we note that large values of the LV parameters results in a large suppression of the number of expected events. Also, for very large values of the LV parameter, we see a considerable flattening in the ratio of the number of events compared with no oscillations. The situation is much trickier, however, for very small values of the LV parameter. In this case, the number of events expected is not suppressed and we also see an oscillation minimum in the top right frame of figure 7.2. Therefore, this makes it very difficult to distinguish between standard oscillations and those which are modified to include LV effects, if the LV parameter is of the order of 10^{-26} or smaller.

Model LV2

We now consider the spectra when the LV parameters are proportional to the square of the neutrino energy. Figure 7.3 shows the spectra and ratios of number of events to those expected if there were no oscillations for the case in which we consider oscillations as an effect of LV only. For large values of the LV parameters, we note that the spectra are very different from standard neutrino oscillations. Firstly, as in the case before, the number of events is significantly suppressed for very large values of the LV parameter. Secondly, the shape of the spectra in the lower right frame is much flatter than the case with no LV effects. For smaller values of the LV parameter, the number of events and the shape of the spectrum is not significantly different from the case with no LV effects. However, perhaps the most outstanding feature of the LV model appears in the ratio of the number events to the number expected with no oscillations, presented in the top right frame. For standard neutrino oscillations, we observe an oscillation minimum, however, for large values of the LV parameter, the ratio increases and so we see a peak. Even for smaller values of the LV parameter, the ratio is flat and so by considering the spectra it should be possible to distinguish between these two models.

If we consider the case where the LV effects modify standard oscillations, then, as in the case before, it becomes much more difficult to untangle any LV effects from

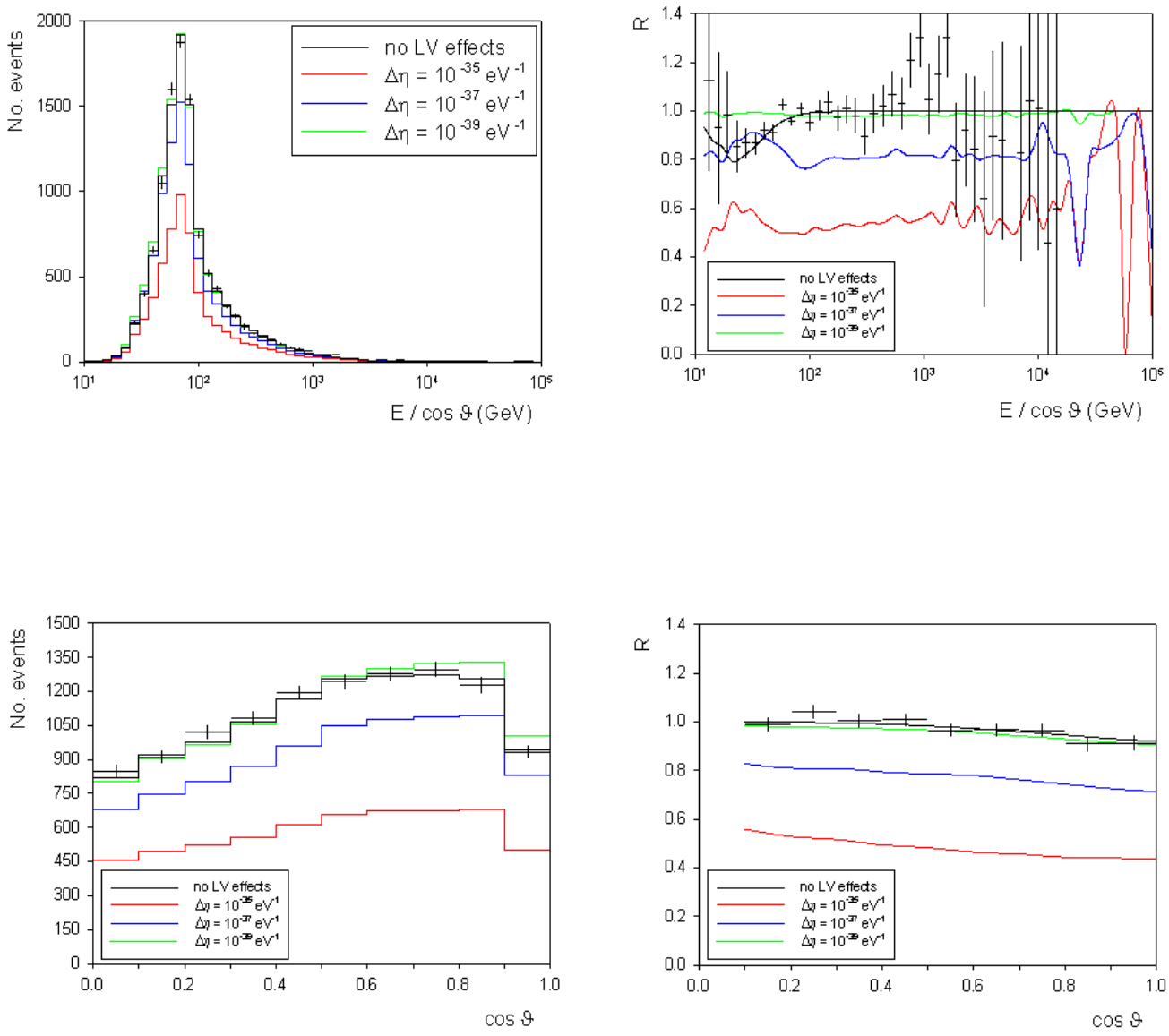

Figure 7.3: Spectra of events when the diagonal LV effects are proportional to the neutrino energy squared. The black line represents the MC simulation of standard oscillations with the coloured lines showing the spectra for oscillations from LV.

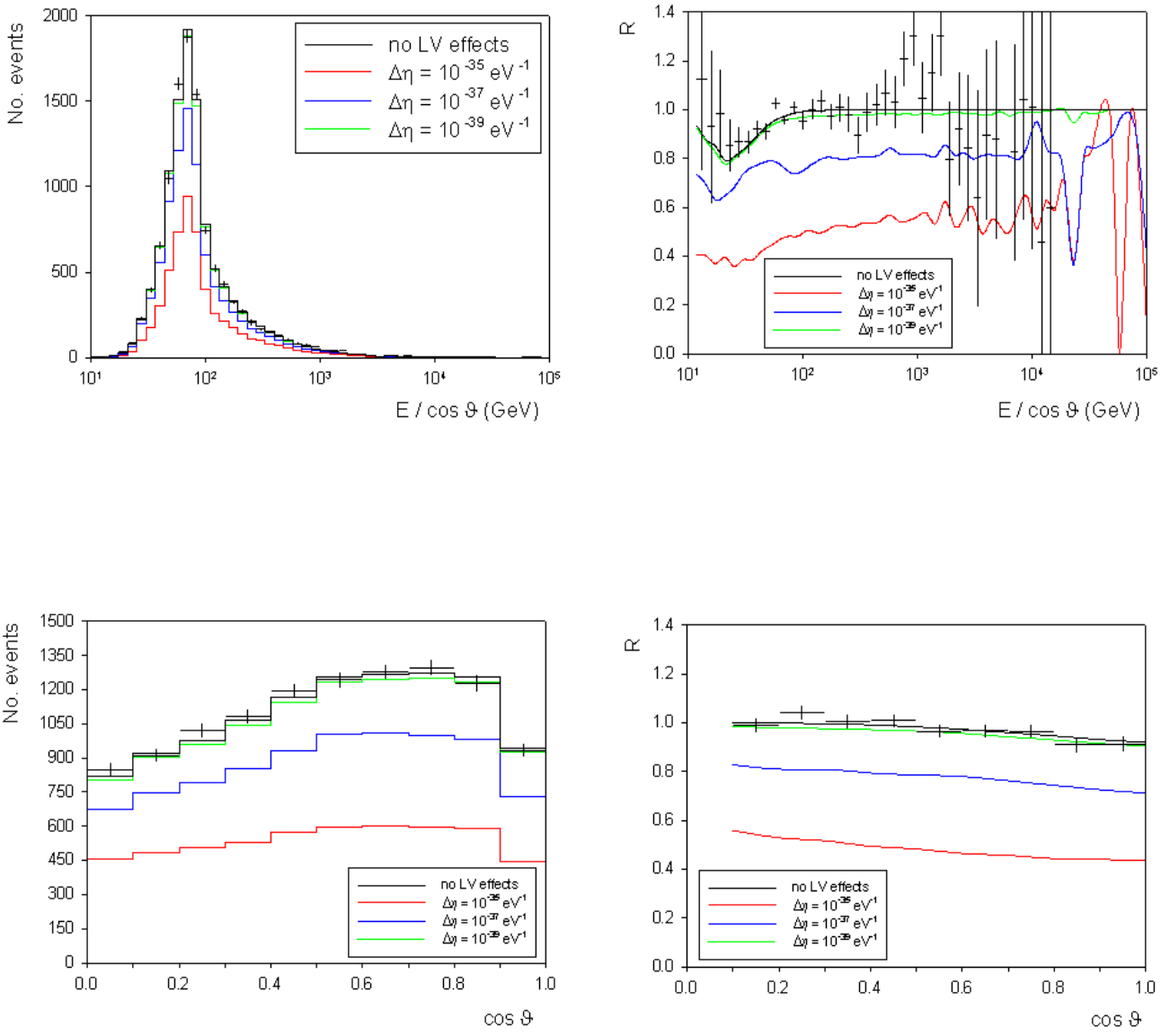

Figure 7.4: As figure 7.3 but the coloured lines show the spectra for standard oscillations plus LV.

those of standard oscillations. Figure 7.4 shows the spectra in this case. For large values of the LV parameter, the only distinguishing feature is that the number of events we expect to see is somewhat reduced and that the spectrum of events as a function of $\cos\vartheta$ is much flatter. If we consider the ratios of events, for large values of the LV parameter, the curve in the top left frame is much flatter than we would expect from standard oscillations. However, for smaller values of the LV parameter, it is extremely difficult to distinguish between the case of standard oscillations and that of standard oscillations which are modified by LV effects.

Model LV3

We end our discussion of the spectra of expected events by considering the model in which the LV parameters are proportional to the neutrino energy cubed. We first consider the case in which neutrino oscillations arise as a consequence of LV effects only. Figure 7.5 shows the spectra in this case. Again, we note that for large values of the LV parameter, we would expect a suppression in the number of events observed. If we consider the spectra as a function of the zenith angle only, as shown in the lower right frame of figure 7.5, then we would expect a much flatter spectrum than that for standard neutrino oscillations. If we consider the same frame but for smaller values of the LV parameter, at small values of the zenith angle, it is very difficult to untangle the case of LV effects only from standard oscillations. However, for larger values of the LV parameter, we would expect an increase in the number of events observed, thus giving us a potential method to disentangle these two models, since neutrino telescopes have very good angular resolution. If we consider the plots of the ratio of expected events to those with no neutrino oscillations, we see that for large values of the LV parameter, there is a significant difference in the ratio of the number of events. In addition, the shape of the curves differ from those of standard oscillations. In the top frame, we observe the oscillation minimum for the standard oscillation case but not for the LV case. In fact, for small values of the LV parameter, we note there is no difference between the LV model and the case of no neutrino oscillations. This is repeated in the lower right frame.

7.1.2 Sensitivity regions

In the previous section, we saw how LV effects can modify the number of events seen in the detector and how they would modify the shape of the spectra. We now

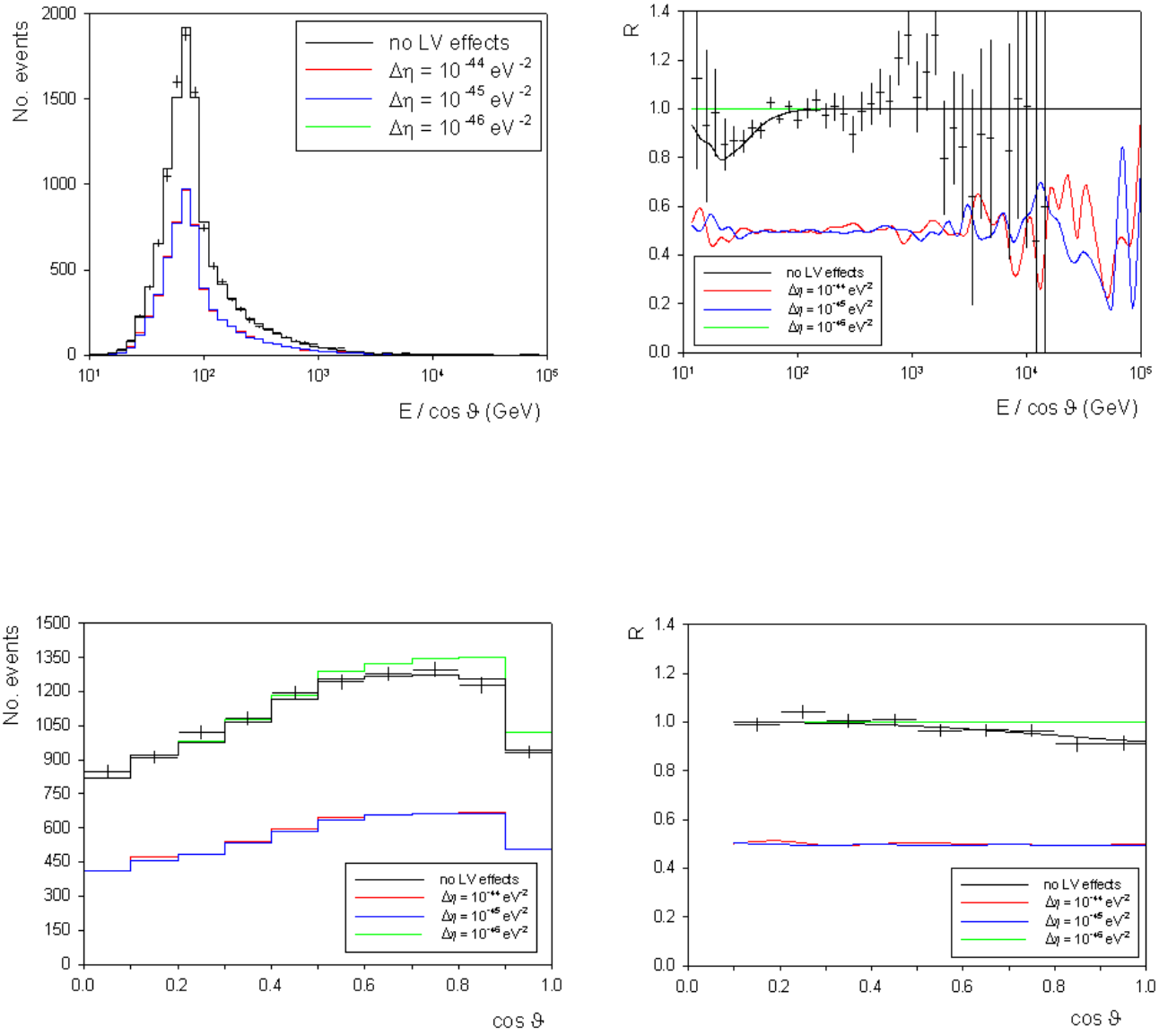

Figure 7.5: Spectra of events when the diagonal LV effects are proportional to the neutrino energy cubed. The black line represents the MC simulation of standard oscillations with the coloured lines showing the spectra for oscillations from LV.

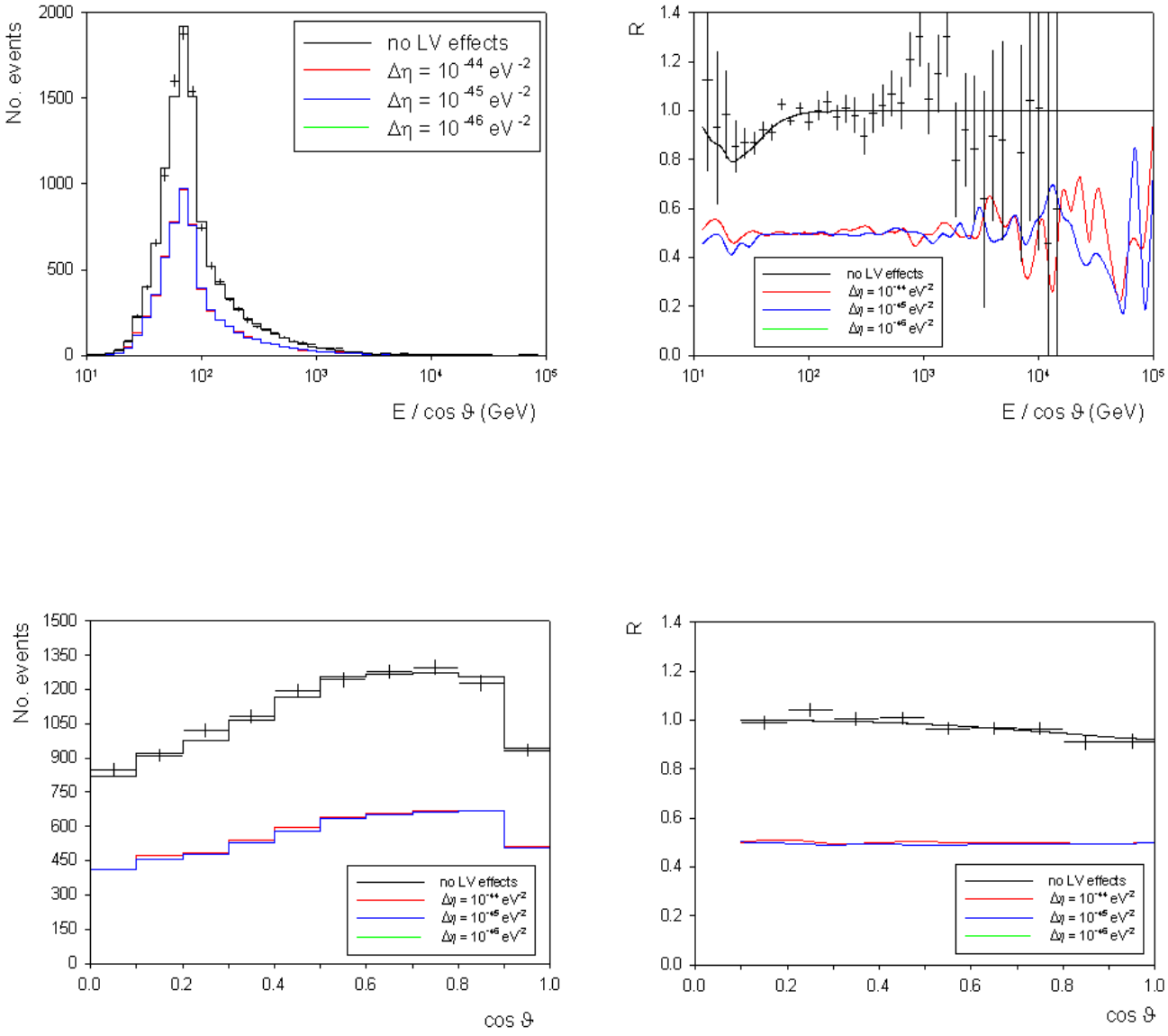

Figure 7.6: As figure 7.5 but the coloured lines show the spectra for standard oscillations plus LV.

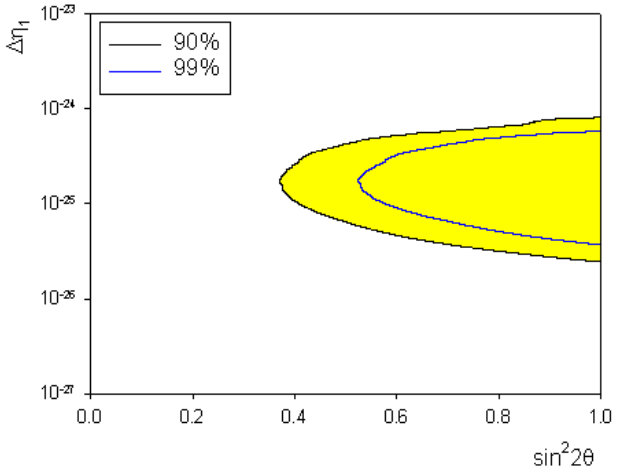

Figure 7.7: Sensitivity contours at 90 and 99% confidence levels for LV effects only (no standard oscillations) for model **LV1**.

turn to the discussion of the ANTARES sensitivity regions found from our numerical simulations. As in the case of quantum decoherence, we are particularly interested in finding upper bounds for the LV parameters.

Model LV1

We firstly consider the case in which $\Delta m^2 = 0$, so that there are no standard oscillations, only those which arise as a consequence of the LV effects. Figure 7.7 shows the sensitivity curves in this case. As before, it is clear that the smallest values of the LV parameter may be probed when $\sin^2 2\theta$ is close to one; the region of parameter space in which we are most interested. We are able to place an upper bound on $\Delta\eta_1$ of 8.2×10^{-25}.

We also considered the case of non-zero Δm^2. Figures 7.8 and 7.9 show the obtained sensitivity volume in parameter space and the sensitivity contours when they are projected onto the relevant coordinate plane, respectively. The region of interest lies above the surface in figure 7.8. As we see from the projections of this surface in figure 7.9, the experimental point of best fit of Δm^2 [140], denoted by the triangle, lies within the sensitivity region. However, the region extends down to very small values of Δm^2 and so we find that our results allow the previous case where neutrino oscillations arise as a consequence of LV effects only. The top right frame in figure 7.9 shows the sensitivity contour for the $\Delta\eta_1$ as a function of the mixing angle, θ. Again, zero is an allowed value for this parameter and so standard oscillations

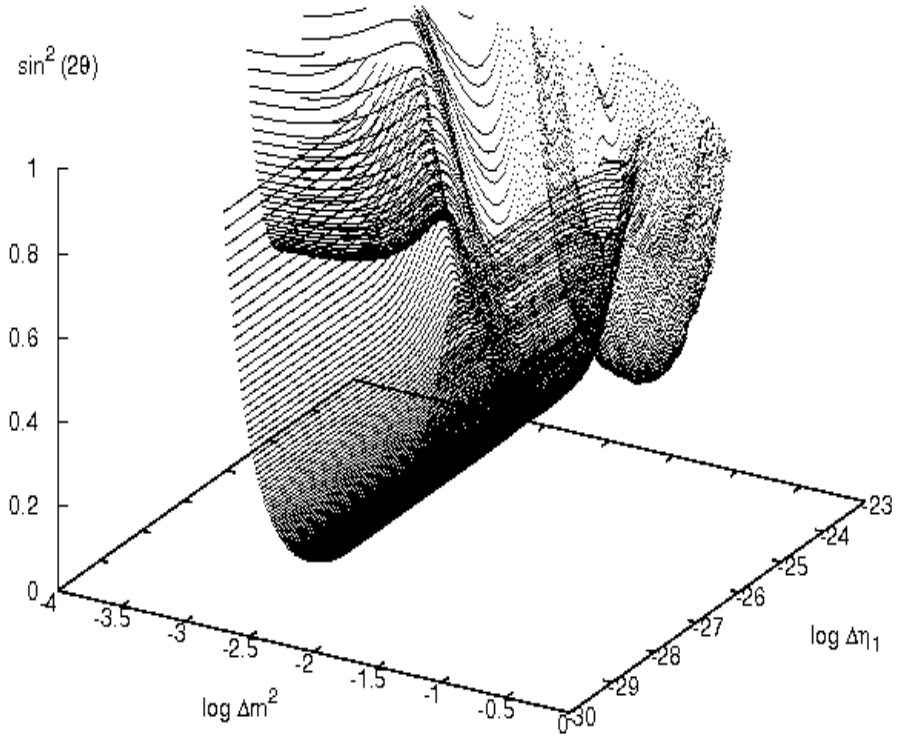

Figure 7.8: Sensitivity volume for model **LV1** at 90 percent confidence level for standard oscillations plus diagonal LV effects proportional to the neutrino energy.

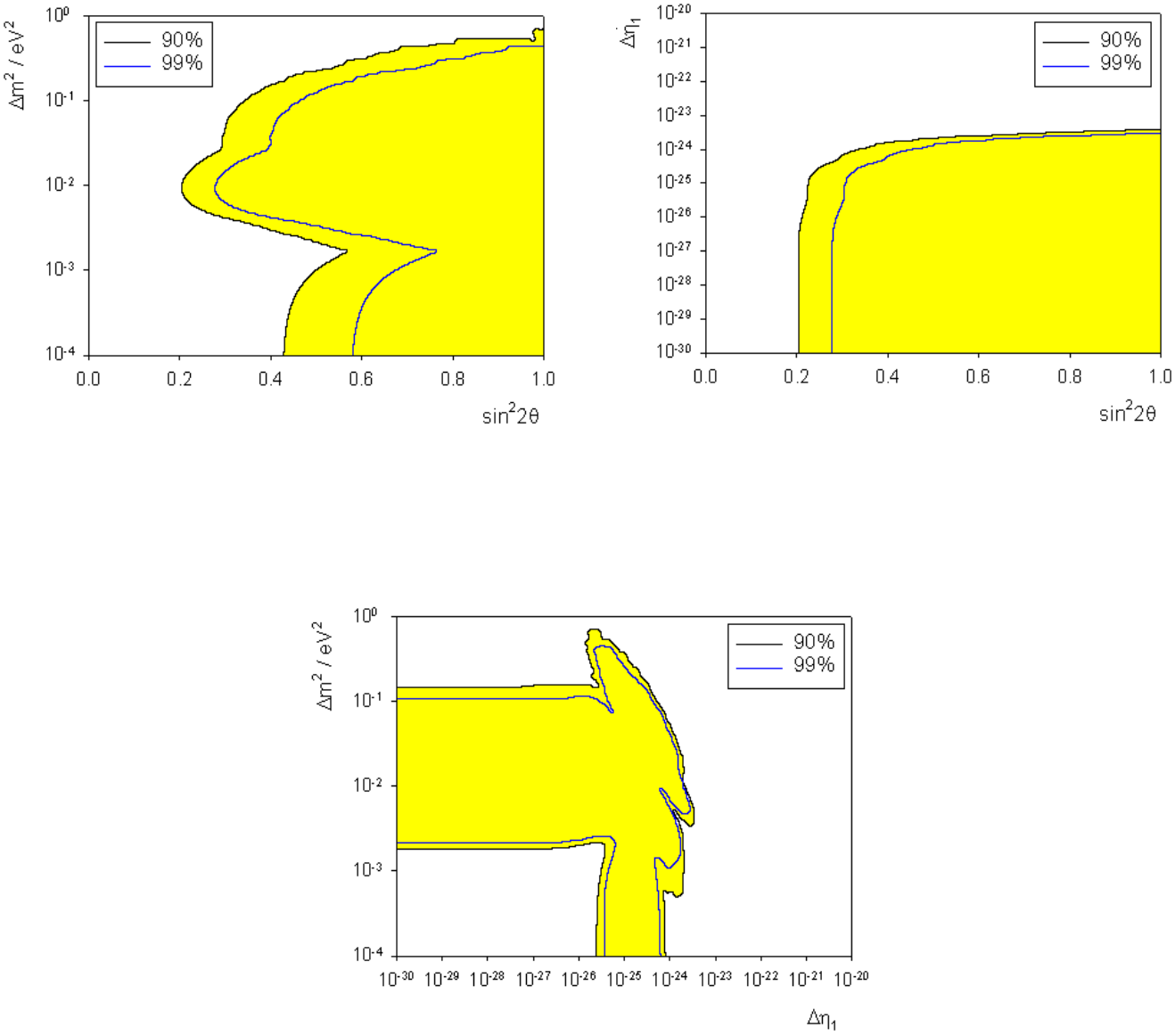

Figure 7.9: Sensitivity contours for model **LV1** at 90 and 99 percent confidence level for standard oscillations plus diagonal LV effects proportional to the neutrino energy.

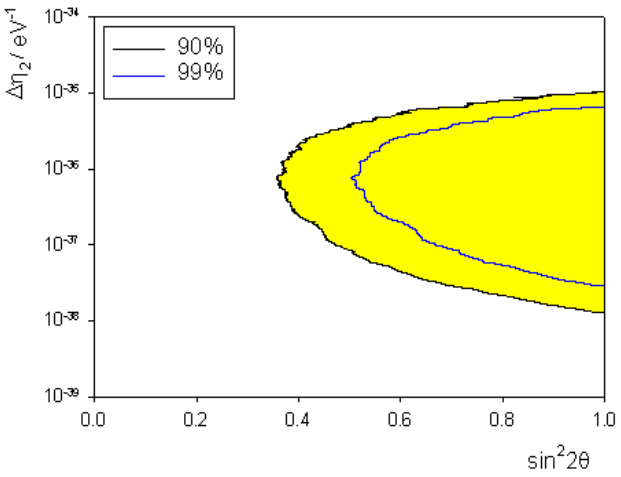

Figure 7.10: Sensitivity contours at 90 and 99% confidence levels for LV effects only (no standard oscillations) for model **LV2**.

with no LV effects are also allowed. We are able to place an upper bound on $\Delta\eta_1$ of $\Delta\eta_1 < 2.9 \times 10^{-24}$. The third frame in this figure shows the remaining sensitivity contours.

Model LV2

The sensitivity contour for the case of LV effects only with $n = 2$ is shown in figure 7.10. We are able to place an upper bound on the parameter $\Delta\eta_2$ of $1 \times 10^{-35}\ eV^{-1}$.

The sensitivity volume and contours for this model when Δm^2 is non-zero are shown in figures 7.11 and 7.12 respectively. We find that these figures are similar to those for model **LV1.** Once again, the region of parameter space that the ANTARES neutrino telescope is sensitive to lies above the surface in figure 7.11. We find that the experimental point of best fit, shown as a triangle in the top left frame of figure 7.12, lies inside the sensitivity contours and that $\Delta m^2 = 0$ is a consistent value, thus indicating that in this model, oscillations due to LV effects only are allowed. The top left frame of figure 7.12 shows the parameter $\Delta\eta_2$ as a function of the mixing angle. We are able to place an upper bound on this parameter of $3 \times 10^{-35}\ eV^{-1}$. The lower frame of figure 7.12 shows the standard oscillation parameter, Δm^2, against the parameter, $\Delta\eta_2$.

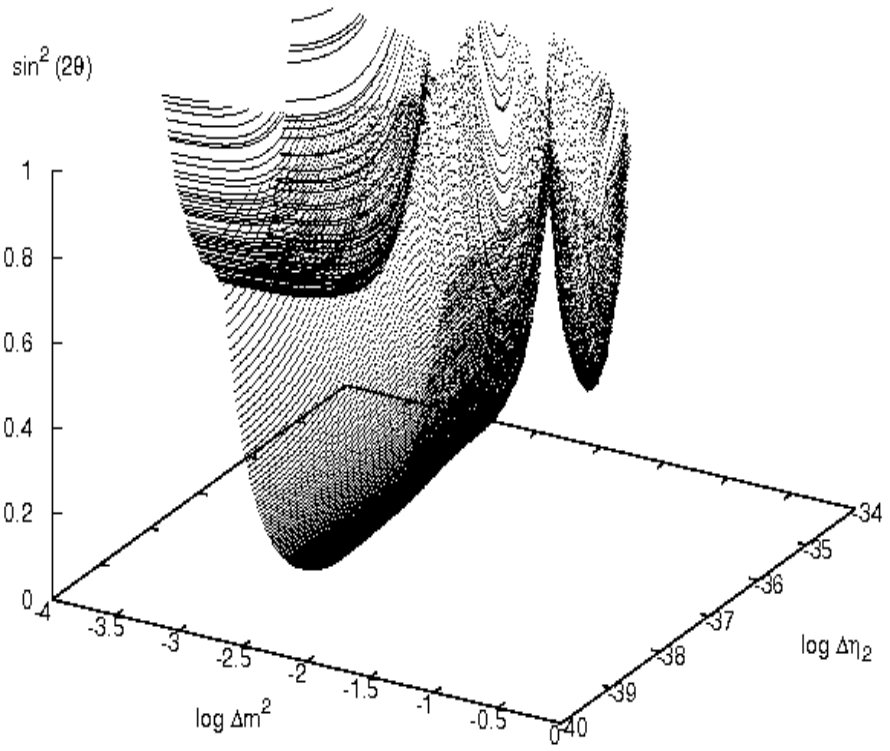

Figure 7.11: Sensitivity volume for model **LV2** at 90 percent confidence level for standard oscillations plus diagonal LV effects proportional to the neutrino energy squared.

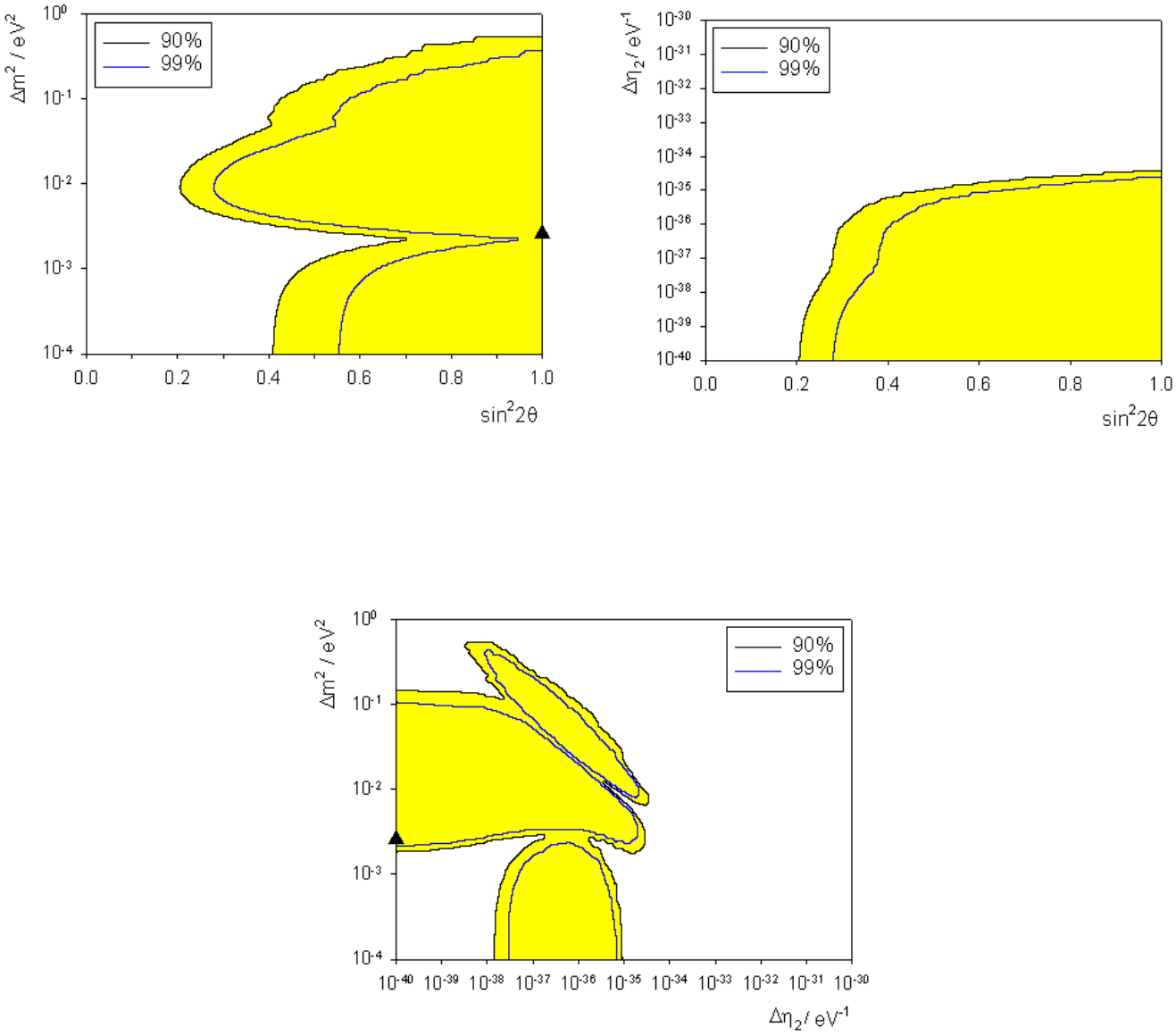

Figure 7.12: Sensitivity contours for model **LV2** at 90 and 99 percent confidence level for standard oscillations plus diagonal LV effects proportional to the neutrino energy squared.

n	$\Delta\eta$ (eV^{1-n}) $(\Delta m^2 = 0)$	$\Delta\eta(eV^{1-n})$ $(\Delta m^2 \neq 0)$
1	8.2×10^{-25}	2.9×10^{-24}
2	1.0×10^{-35}	2.9×10^{-35}
3	X	6.9×10^{-46}

Table 7.1: Table showing the upper bounds on $\Delta\eta$, the LV parameter in diagonal entries of the Hamiltonian, for various values of n. The X indicates that we were unable to place a bound on this parameter.

Model LV3

The final model we consider has $n = 3$. If we set $\Delta m^2 = 0$, then we find that we are unable to derive any meaningful results for this model.

However, if we have a non-zero Δm^2, we find we can obtain meaningful results. The sensitivity volume and the sensitivity contours are presented in figures 7.13 and 7.14 respectively. In this case, the sensitivity volume shown in figure 7.13 is very simple, being parabolic in shape with the region of interest lying above this surface. The projections of this surface, the sensitivity contours, are also much simpler than the previous two cases. The top left plot of figure 7.14 shows Δm^2 as a function of the mixing angle and we note that it is very similar to that obtained when we consider only standard neutrino oscillations. Again the experimental point of best fit is included in the sensitivity region but in this case, $\Delta m^2 = 0$ is not included, so this model does not seem to allow the possibility that neutrino oscillations arise as a solely LV effect. This is in direct agreement with the first part of our analysis as we were unable to find any meaningful results for this model when we considered LV effects only. The top right frame of figure 7.14 shows the LV parameter as a function of the mixing angle. We note that zero is an allowed value for this parameter indicating that standard neutrino oscillations are still allowed in this case. We are able to place an upper bound on this parameter of 6.9×10^{-46} eV^{-2}. The lower frame of figure 7.14 shows the relationship between the standard oscillation parameter Δm^2 and the LV parameter.

7.1.3 Summary

In this section, we have shown ANTARES will be able to place stringent bounds on LV parameters which appear in the diagonal entries of the Hamiltonian. Table

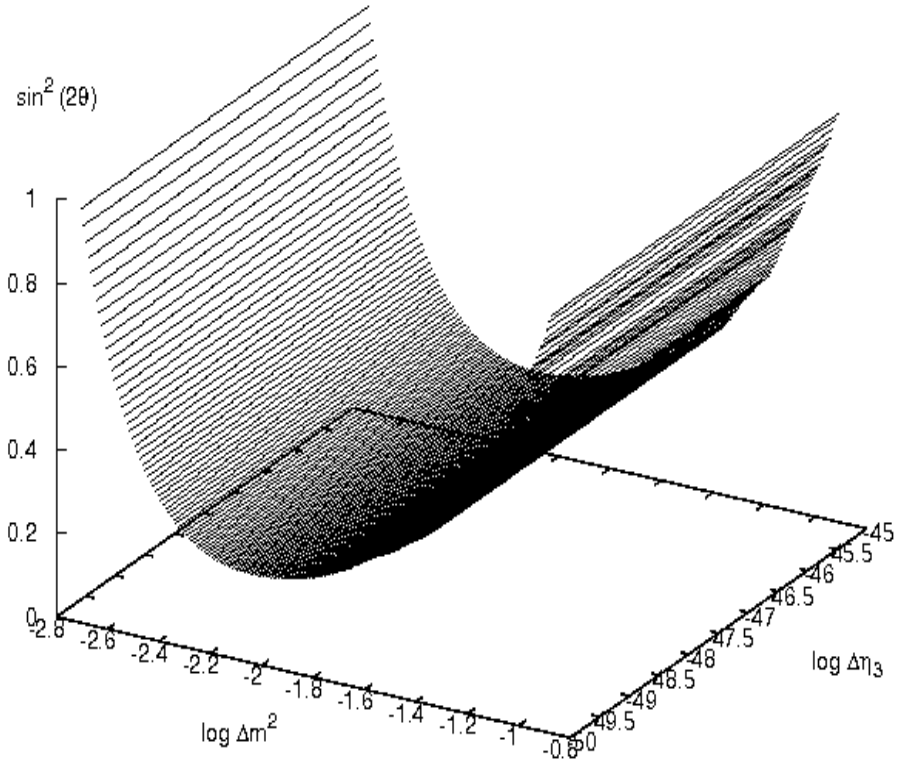

Figure 7.13: Sensitivity volume for model **LV3** at 90 percent confidence level for standard oscillations plus diagonal LV effects proportional to the neutrino energy cubed.

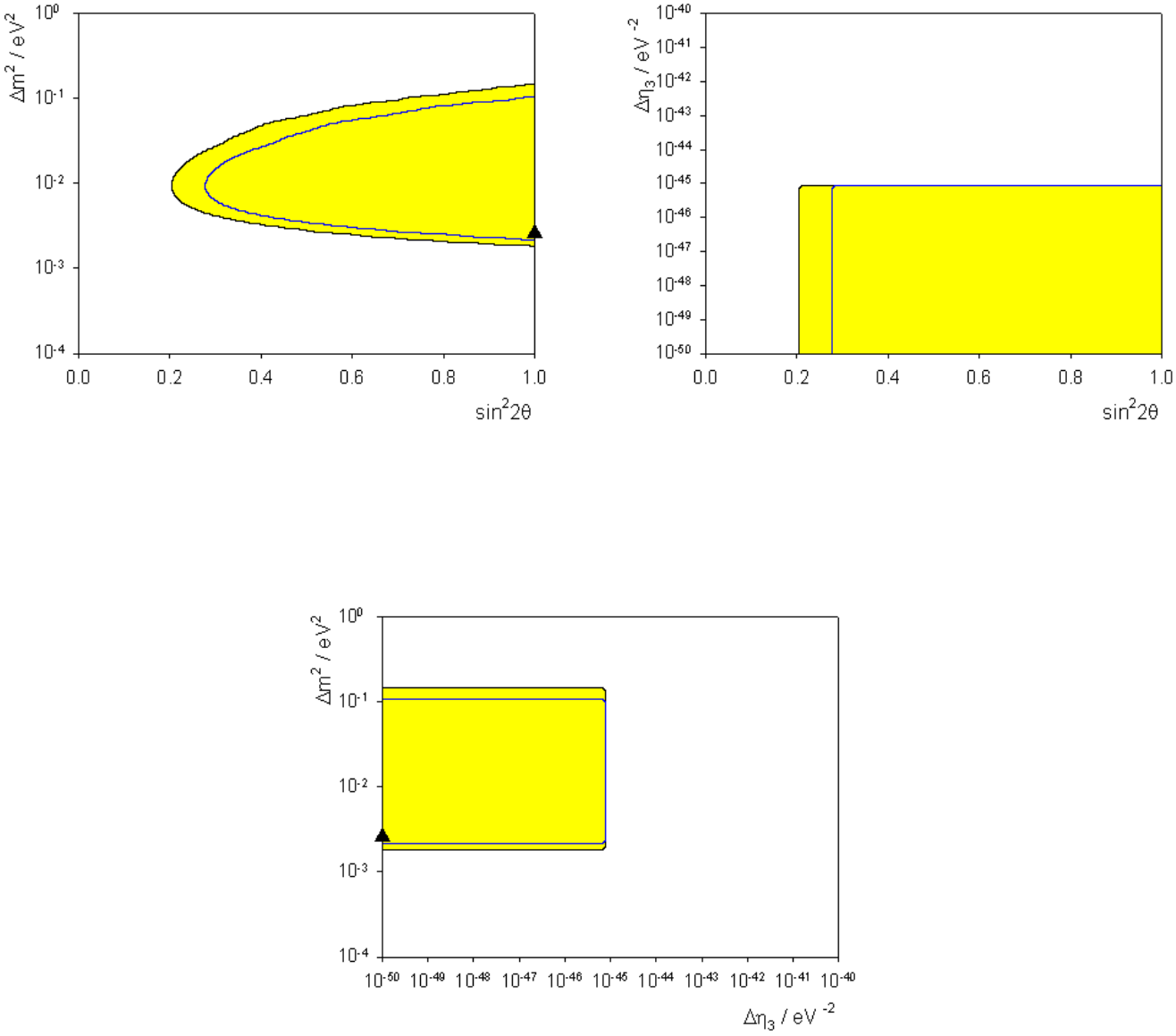

Figure 7.14: Sensitivity contours for model **LV3** at 90 and 99 percent confidence level for standard oscillations plus diagonal LV effects proportional to the neutrino energy cubed.

7.1 shows the upper bounds for this model for various energy dependences. We found that if the LV effects had a dependence on either the neutrino energy or the neutrino energy squared, then oscillations may be induced from these effects with no contributions from standard oscillations. However, for the case of $n = 3$, then we cannot measure the effects of LV only in atmospheric neutrinos. From a naturalness perspective, we would expect $\Delta\eta \sim 10^{-28(n-1)}$ for $n > 2$. We note that for the case $n = 2$, the bounds obtained from our simulations surpass the expected value of the LV parameter by seven orders of magnitude and so ANTARES may be able to observe these effects or rule out this model. For the case $n = 3$, however, the bound from our simulations is ten orders of magnitude larger than that expected and so we cannot rule out this model using atmospheric neutrinos. The situation is somewhat more complicated if $n = 1$ as this corresponds to $\alpha = 0$ in (6.2) and so we have no indication as to the value of $\Delta\eta$ except to say that it should be small.

7.2 LV models with off-diagonal entries in the Hamiltonian

In the last section we saw how LV parameters in the diagonal entries of the Hamiltonian in the mass basis could alter neutrino oscillation phenomenology. In this section, we examine the possibility that the LV parameters are present in the off-diagonal entries of the Hamiltonian in the mass basis. Allowing this modification means the neutrino oscillation probability takes the form (6.16)

$$\begin{aligned} P[\nu_\mu \to \nu_\tau] \quad & \frac{1}{2}\left[\cos^2 2\theta \left(1 - \frac{\omega^2}{\Omega^2} - \frac{|a|^2}{\Omega^2}\cos(2\Omega L)\right)\right. \\ & + \sin^2 2\theta \left(1 - \frac{a_1^2}{\Omega^2} - \frac{(\omega^2 + a_2^2)}{\Omega^2}\cos(2\Omega L)\right) \\ & \left. - \frac{1}{2}\sin 4\theta \left(-\frac{4\omega a_1}{\Omega^2}\sin^2(\Omega L)\right)\right], \end{aligned} \tag{7.2}$$

where, replacing c and $\hbar$, we use the notation $\omega = \Delta m^2/4E$ and $a_i = 1\times 10^{9(n+1)} E^n a_i$ with $i = 1$ or 2. Since the mixing angle is large for atmospheric neutrinos, then we expect that the $\cos^2 2\theta$ and $\sin 4\theta$ terms are small and so the spectra in this case will be very similar to that for the diagonal LV case. We go, therefore, directly to discussing the sensitivity regions.

From equation (7.2), we note that we have four parameters, the mixing angle, θ, the standard neutrino oscillation parameter, Δm^2 and two LV parameters, $a_1 = \mathrm{Re}(a)$, the real part of the LV parameter and $a_2 = \mathrm{Im}(a)$, the imaginary part of the LV parameter. From the discussion in chapter 3, we can realistically only model three of these parameters simultaneously. We consider, therefore, four models with various combinations of parameters:

- Model **LVA**: The first model we consider is where neutrino oscillations arise as a consequence of LV effects only, so we set $\Delta m^2 = 0$ and fit for the parameters $\mathrm{Re}(a)$, $\mathrm{Im}(a)$ and θ;

- Model **LVB**: In this model, we consider the case where standard oscillations are modified by LV effects but where the LV parameter is purely real, thus reducing the number of parameters to three, namely, Δm^2, $\mathrm{Re}(a)$ and θ,

- Model **LVC**: In this case, we again consider how LV effects may modify standard neutrino oscillations but, in contrast to model **LVB**, we consider the case where the LV parameter is purely imaginary. The three parameters we have in this case are Δm^2, $\mathrm{Im}(a)$ and θ,

- Model **LVD**: The final model we consider is the more general case of models **LVB** and **LVC**. In this case we fit for the parameters $\mathrm{Re}(a)$, $\mathrm{Im}(a)$ and θ and fix $\Delta m^2 = 2.6 \times 10^{-3}\ eV^2$ [140].

Before we present our results, we have just one more comment to make. Since the form of the neutrino oscillation probability is more complicated than any considered before, the sensitivity contours obtained by projecting the sensitivity volume onto the relevant coordinate planes are not as 'clean' as those presented in the previous chapters. We often find spurious points which do not form easily interpreted sensitivity regions. Therefore, when we present the results of our simulations in the following sections, we shall present the sensitivity volume and the projections at a 90% confidence level only. Although this is the case, we shall see that our sensitivity regions still contain the experimental point of best fit for Δm^2 and also that we are still able to place upper bounds on the LV parameters.

7.2.1 Model LVA

In this case, we consider neutrino oscillations which arise due to LV effects only. We have three parameters, two LV parameters, Re(a), Im(a), and the standard neutrino mixing angle, θ.

Model LVA with parameters proportional to the neutrino energy

We begin our discussion of the sensitivity regions for this model by considering the case when the LV effects are proportional to the neutrino energy. Figure 7.15 shows the sensitivity volume in this case. The sensitivity region lies below the parabolic curve but we also notice that there is a collection of points at larger values of Im(a). The resulting projections of this volume are presented in figure 7.16. The top frame in figure 7.16 shows the parameter Re(a) as a function of the mixing angle. We are able to see the parabolic curve, as shown in figure 7.15, for small values of the mixing angle but the contours are obscured by those points discussed above. However, we are still able to place an upper bound on this parameter of 2.9×10^{-25}. The top left frame in figure 7.16 shows the imaginary part of the LV parameter as a function of the mixing angle. Here, we see that the projection is much cleaner and that we are able to accurately define sensitivity contours. We are, therefore, able to place an upper bound on the parameter of 6.5×10^{-25}. The final frame in figure 7.16 shows the two LV parameters plotted against each other. Again we see that we are able to accurately define sensitivity contours.

Model LVA with parameters proportional to the neutrino energy squared

We now turn to examining the sensitivity regions when $n = 2$. The sensitivity volume in this case is shown in figure 7.17. The sensitivity volume lies below the parabolic shaped surface. We again note that we have a collection of points at large values of the imaginary part of the LV parameter. The sensitivity contours obtained when this volume is projected onto the corresponding coordinate planes are shown in figure 7.18. The figures in this case are very similar to the case when the LV effects are proportional to a single power of the neutrino energy. The top left frame shows the real part of the LV parameter as a function of the mixing angle, θ. As in the case we considered above, the sensitivity region lies within the parabolic curve at low values of $\sin^2 2\theta$ but we also have a collection of allowable points outside this contour with which we cannot easily define a sensitivity contour. However, we note

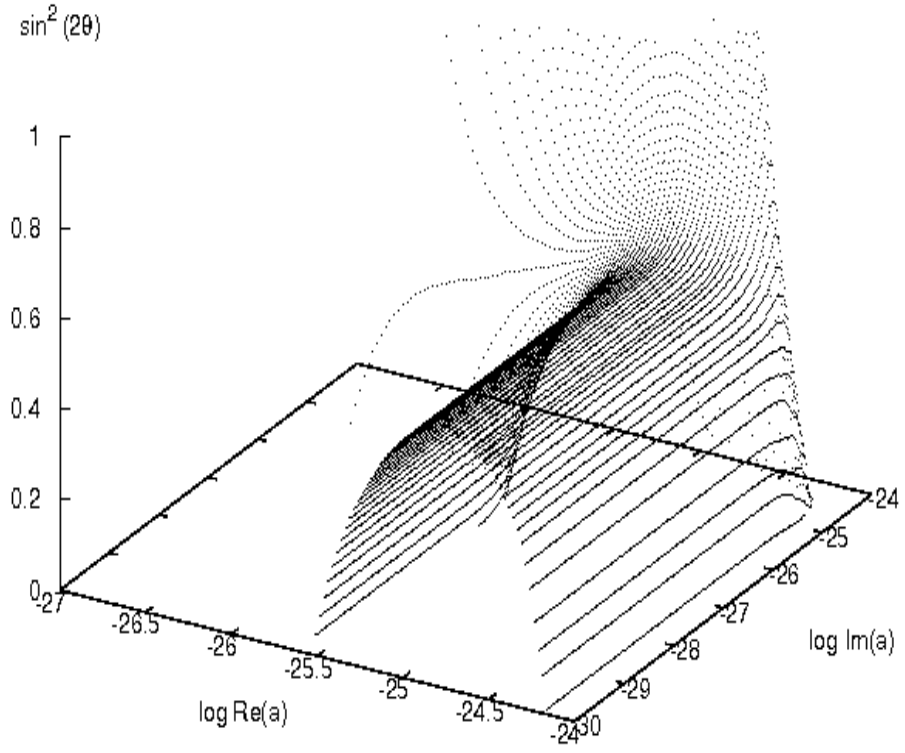

Figure 7.15: Sensitivity volume for model **LVA** at 90 percent confidence level for off-diagonal LV effects proportional to the neutrino energy.

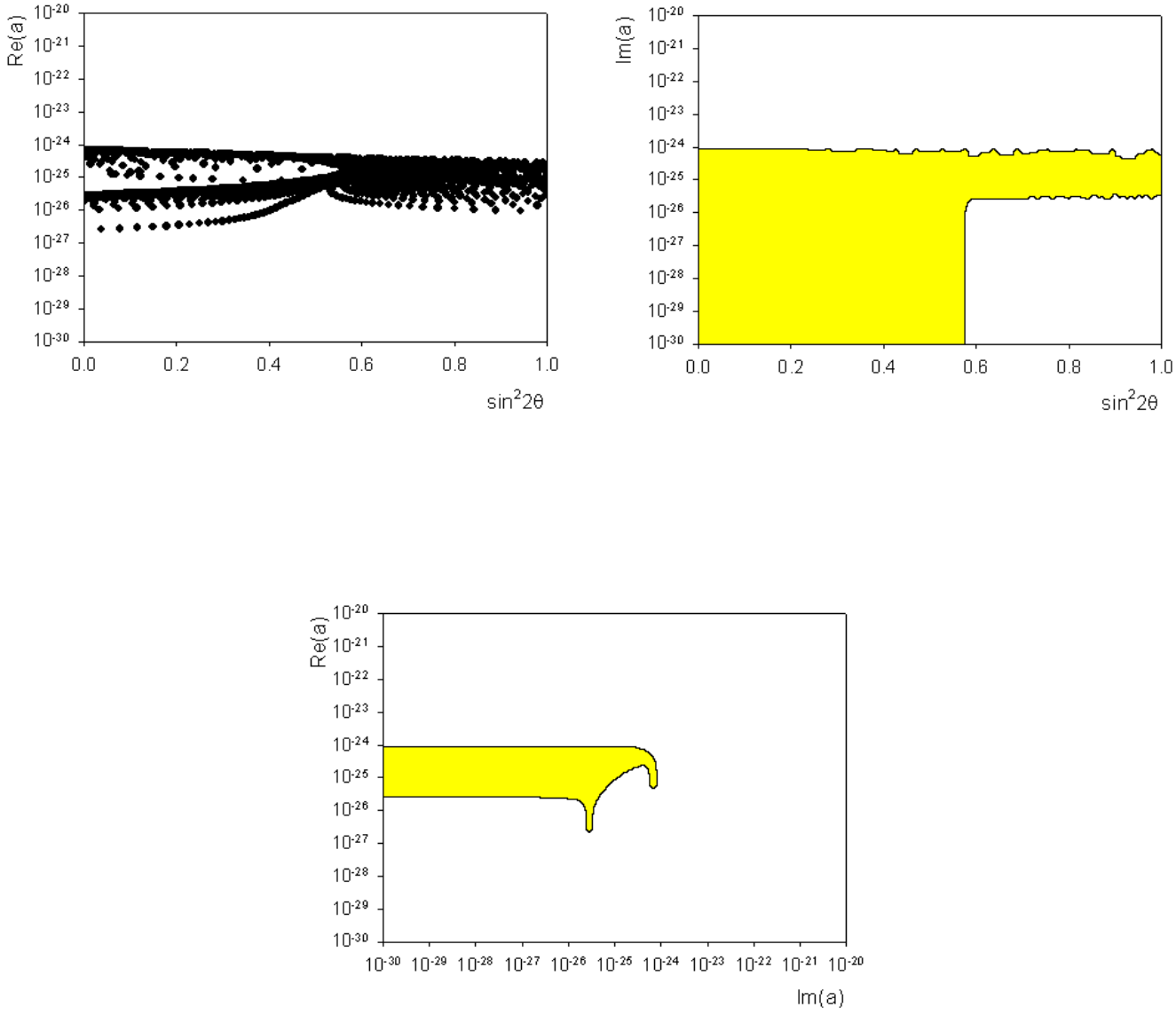

Figure 7.16: Sensitivity contours for model **LVA** at 90 percent confidence level for off-diagonal LV effects proportional to the neutrino energy.

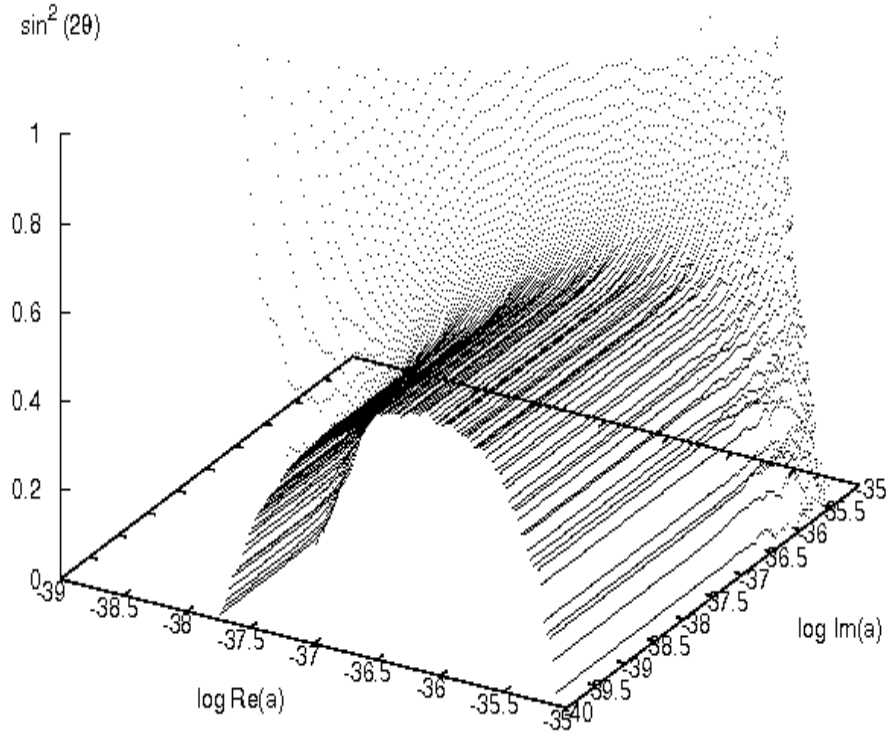

Figure 7.17: Sensitivity volume for model **LVA** at 90 percent confidence level for off-diagonal LV effects proportional to the neutrino energy squared.

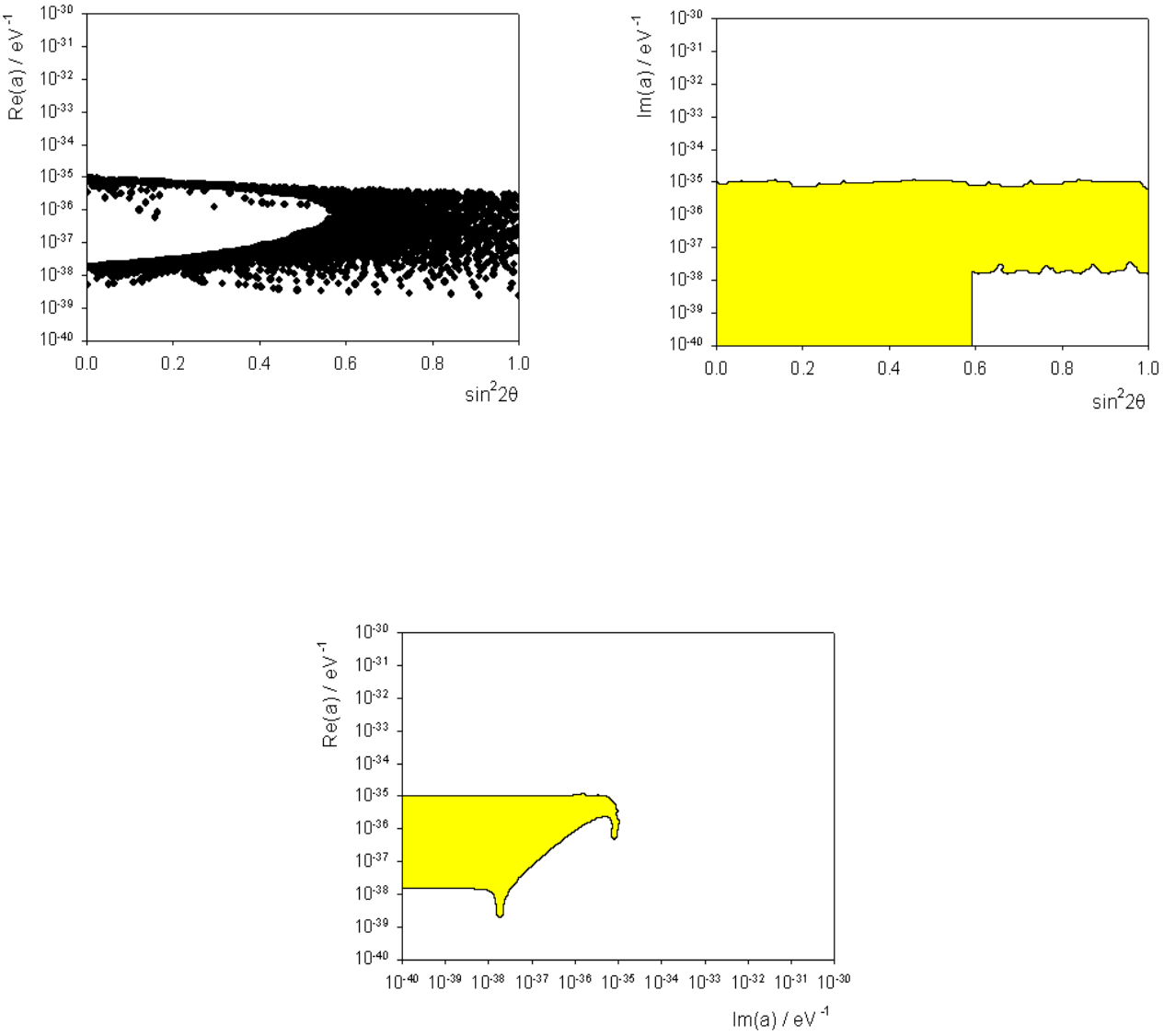

Figure 7.18: Sensitivity contours for model **LVA** at 90 percent confidence level for off-diagonal LV effects proportional to the neutrino energy squared.

that the parameter experiences a cutoff and so we are able to place an upper bound when $\sin^2 2\theta = 1$ of $3.1 \times 10^{-36}\ eV^{-1}$. The top right frame in figure 7.18 shows the imaginary part of the LV parameter. We are again able to define a clean sensitivity contour in this case and thus able to place an upper bound on this parameter of $8.2 \times 10^{-36}\ eV^{-1}$. The lower frame shows the relationship between the two LV parameters.

Model LVA with parameters proportional to the neutrino energy cubed

Finally, we consider model **LVA** when $n = 3$. For this model, with the LV parameters proportional to the neutrino energy cubed, we find that we cannot derive any meaningful results from our numerical simulations. This fits with the results we found when we considered simple LV effects in the last section as, for this energy dependence, we find that we cannot probe these effects.

7.2.2 Model LVB

We now turn our attention to the second model outlined above. In this case we consider modifications of standard oscillations where our LV parameters are considered to be purely real.

Model LVB with parameters proportional to the neutrino energy

If we assume that the LV effects are dependent upon a single power of the neutrino energy, then the sensitivity volume we obtain is shown in figure 7.19. The sensitivity region in this case, lies above the scoop shaped surface but we note that there is a collection of points at high Δm^2 and $\mathrm{Re}(a)$ which do not seem to form a surface. The projections of this volume are shown in figure 7.20. The top left frame shows the standard neutrino oscillation parameter Δm^2 as a function of the mixing angle, θ. We first note that we have been able to construct a sensitivity contour, this region being contained within the curve. However, as in the first model, we also obtain regions of points from which it is not possible to construct sensitivity contours. However, the important features to note are that the experimental point of best fit from table 1.2, as denoted by the triangle is contained with the sensitivity region and that this model allows the case whereby oscillations come about due to LV effects only since $\Delta m^2 = 0$ is included. The top right frame of figure 7.20 shows

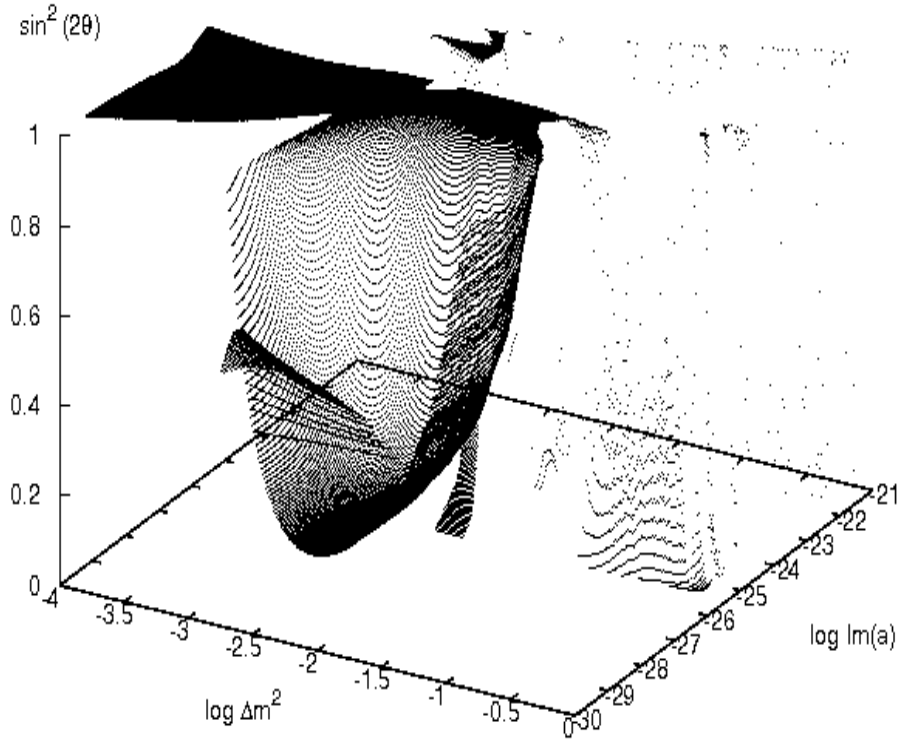

Figure 7.19: Sensitivity volume for model **LVB** at 90 percent confidence level for standard oscillations and real off-diagonal LV effects proportional to the neutrino energy.

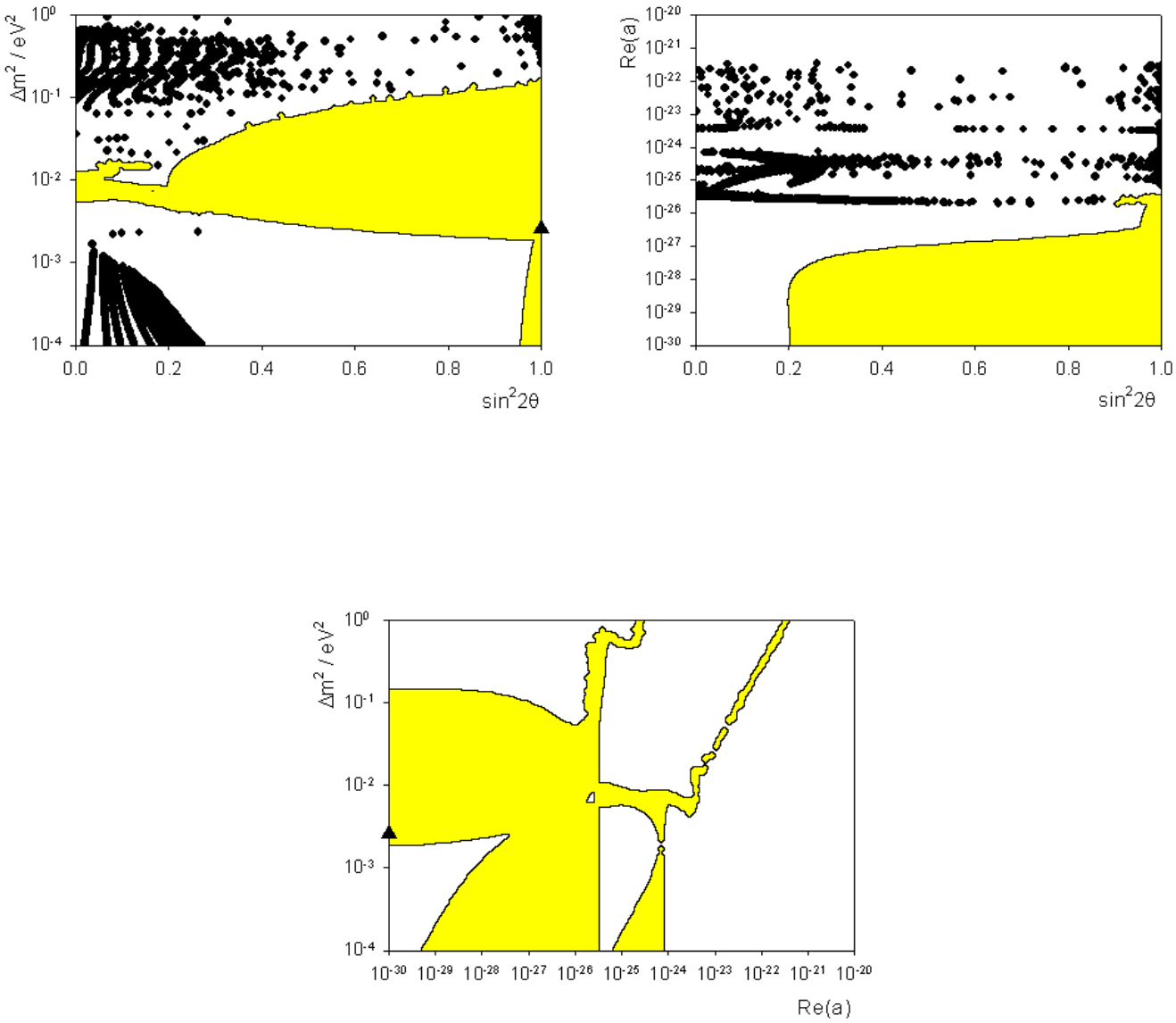

Figure 7.20: Sensitivity contours for model **LVB** at 90 percent confidence level for standard oscillations and real off-diagonal LV effects proportional to the neutrino energy.

the LV parameter Re(a) as a function of the mixing angle. In this case, we are able to construct a sensitivity region which includes the point Re(a) = 0 allowing the case of standard oscillations only. We also obtain points from which we are not able to construct meaningful sensitivity contours. However, these points experience a cutoff and so we are able to place an upper bound on this parameter of 3.1×10^{-22}. The bottom frame of figure 7.20 shows the two parameters plotted against each other. We are, again, able to construct sensitivity contours in this case, the region of interest lying within the contours.

Model LVB with parameters proportional to the neutrino energy squared

The sensitivity volume for model **LVB** when $n = 2$ is shown in figure 7.21. The volume is very similar to the case for $n = 1$, with the sensitivity region lying above the scoop shaped surface. We also obtain a region of points which do not seem to easily form a surface. The similarity between the previous case and this case is bourne out when we examine the sensitivity contours for this case, shown in figure 7.22. The top left frame shows Δm^2 as a function of the mixing angle θ. We again note that we are able to construct a sensitivity contour but that we also have a large number of spurious points from which we are not able to construct sensitivity contours. However, we note that the experimental point of best fit denoted by the triangle lies within the sensitivity region and that this model does allow oscillations which arise as a result of LV effects only since $\Delta m^2 = 0$ is contained within the sensitivity region. The top right frame shows the LV parameter as a function of the mixing angle. In the lower part of this plot, we are able to construct a sensitivity contour but there is a large region of allowed points above this contour. However, there is again a cut-off in these points and so we are able to place an upper bound on this parameter of $6.1 \times 10^{-33}\ eV^{-1}$. The lower frame of figure 7.22 shows the two parameters plotted against each other and in this case we are able to construct a sensitivity contour. We note that the experimental point of best fit for Δm^2 again lies within the sensitivity region.

Model LVB with parameters proportional to the neutrino energy cubed

We conclude our examination of model **LVB** by considering the case when the LV effects have a cubic dependence upon the neutrino energy cubed. In contrast to model **LVA**, we are able to find meaningful results. The sensitivity volume for this

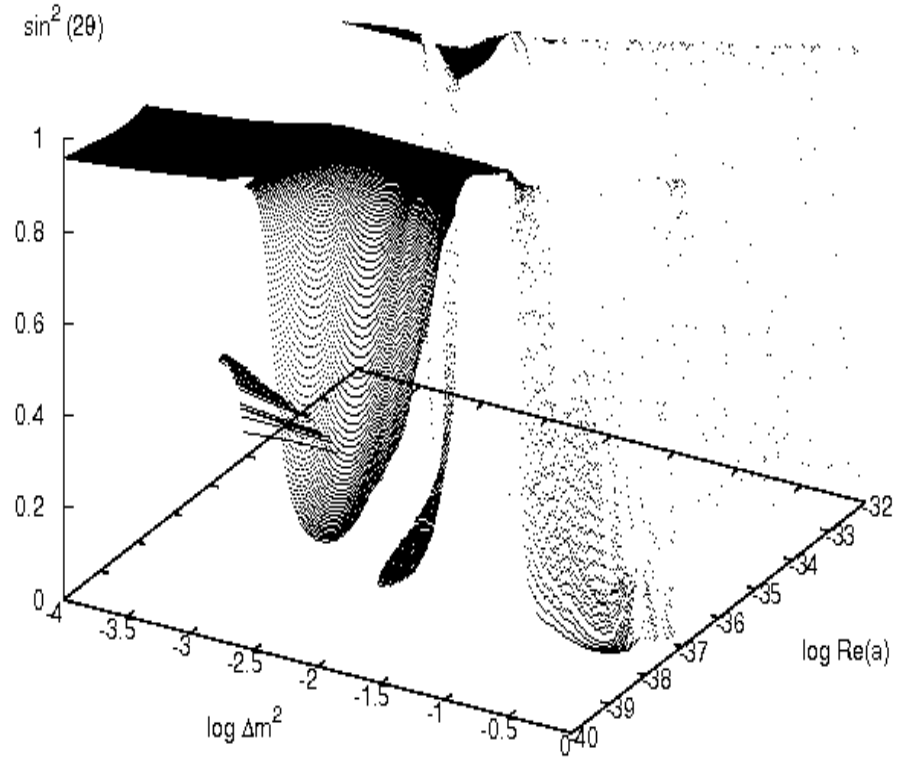

Figure 7.21: Sensitivity volume for model **LVB** at 90 percent confidence level for standard oscillations and real off-diagonal LV effects proportional to the neutrino energy squared.

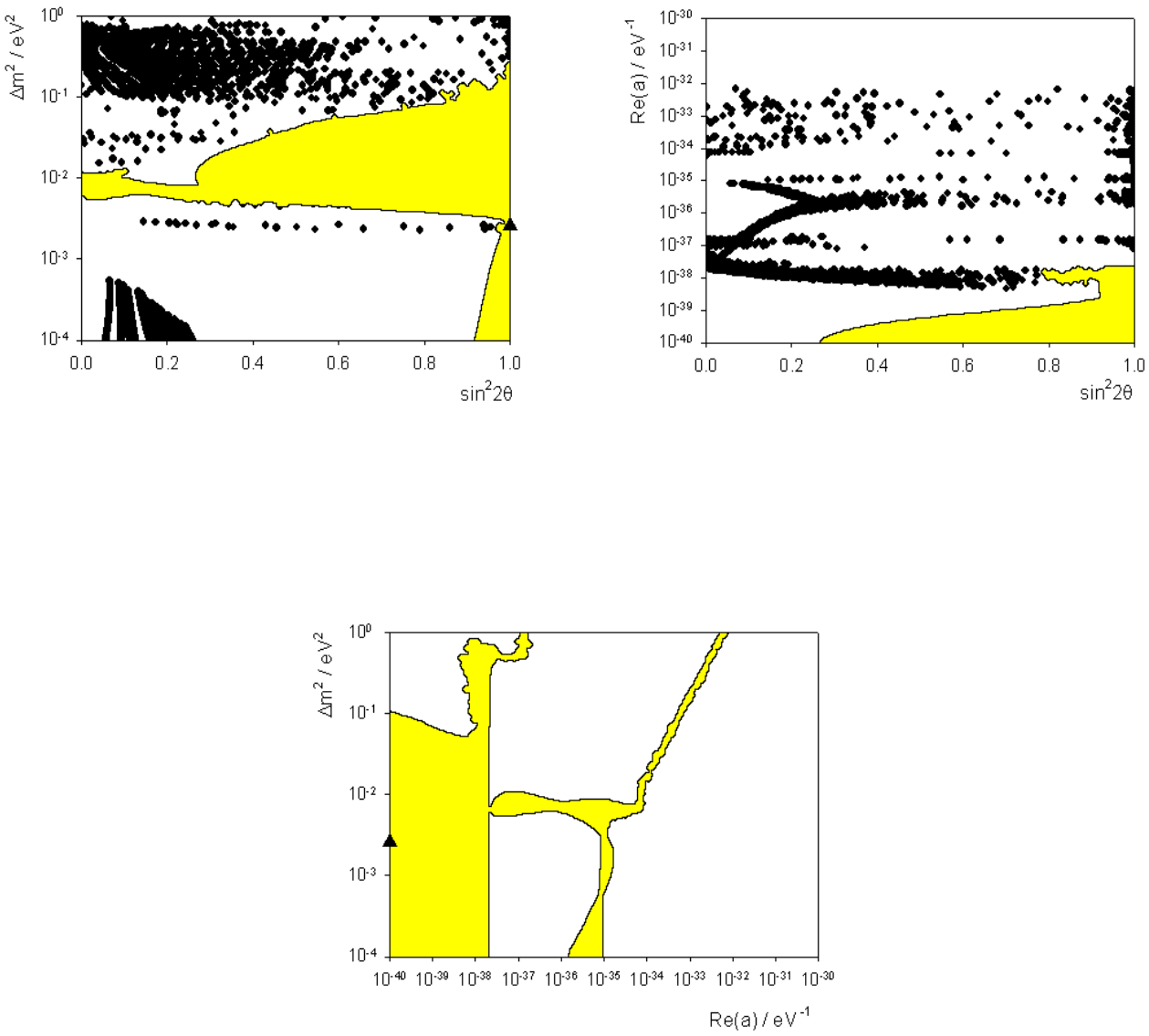

Figure 7.22: Sensitivity contours for model **LVB** at 90 percent confidence level for standard oscillations and real off-diagonal LV effects proportional to the neutrino energy squared.

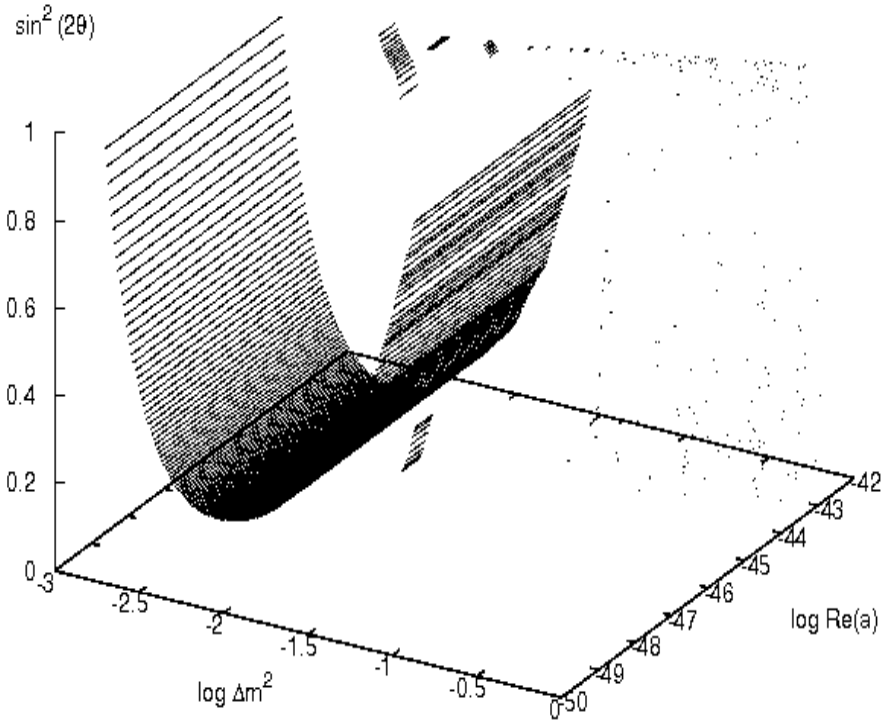

Figure 7.23: Sensitivity volume for model **LVB** at 90 percent confidence level for standard oscillations and real off-diagonal LV effects proportional to the neutrino energy cubed.

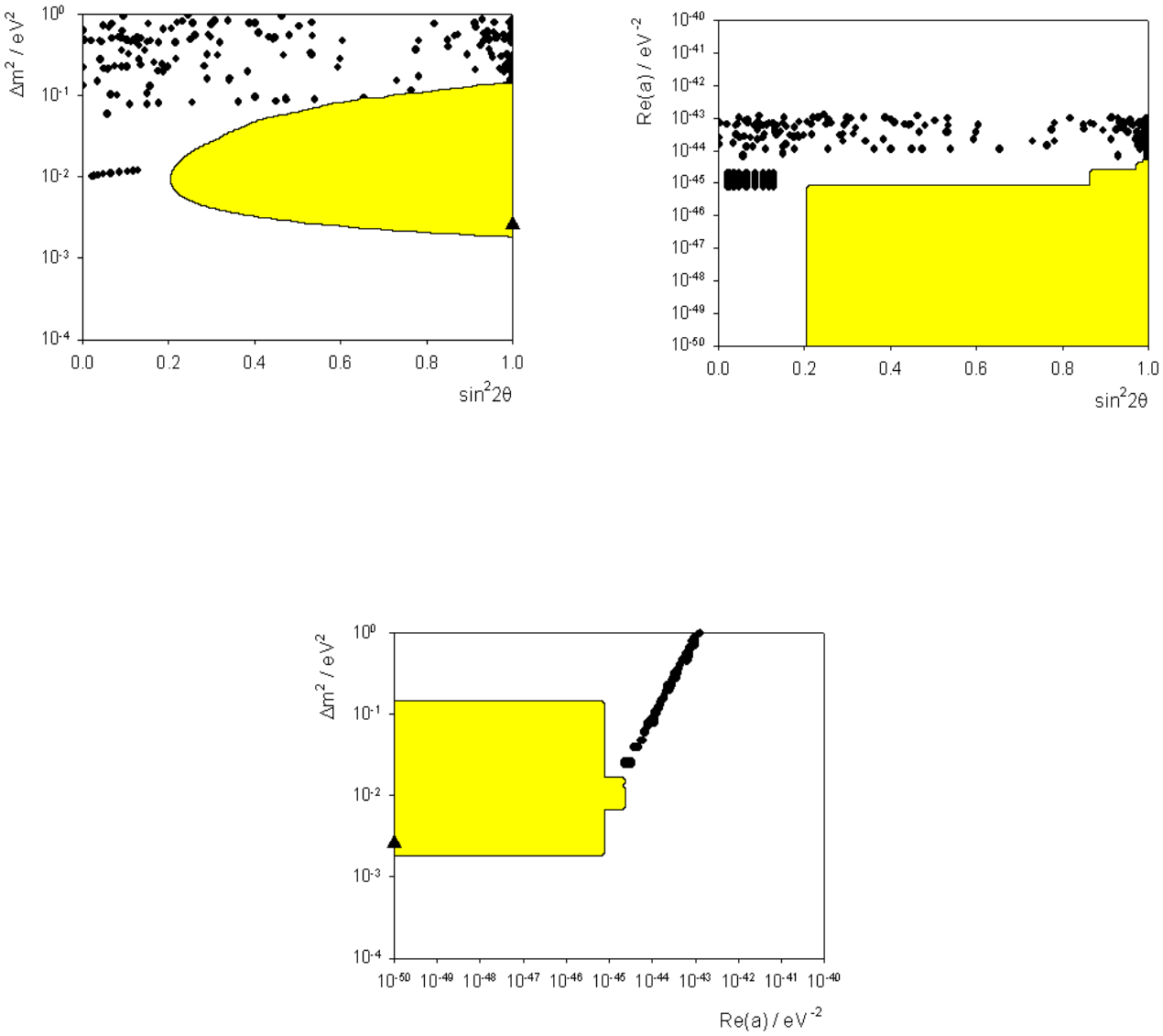

Figure 7.24: Sensitivity contours for model **LVB** at 90 percent confidence level for standard oscillations and real off-diagonal LV effects proportional to the neutrino energy cubed.

case is shown in figure 7.23. The first thing to note is that the sensitivity volume is much simpler than the cases with $n = 1$ and 2, with the sensitivity volume in this case lying above the parabolic shaped surface. However, we again obtain allowed points outside this region at larger values of the LV parameter. The projections of this volume onto the coordinate planes are shown in figure 7.24. The top left frame shows the standard neutrino oscillation parameter, Δm^2, plotted as a function of the mixing angle. We are able to construct a sensitivity contour which takes the same shape as that when we consider just standard neutrino oscillations. We also note that the experimental point of best fit, denoted by the triangle lies within this region. However, we also note that we have some spurious allowed points not included within this region. The top right plot shows the LV parameter as a function of the mixing angle. We are able to construct a meaningful sensitivity contour with the sensitivity region lying below this contour. This contour contains $\mathrm{Re}(a) = 0$ and so we see that this model is consistent with standard oscillations only. This frame also contains spurious points which experience a cut-off, enabling us to place an upper bound on the LV parameter of $9.7 \times 10^{-44}\ eV^{-2}$. The lower frame of figure 7.24 shows the standard oscillation parameter against the LV parameter. We are able to construct a sensitivity contour, the sensitivity region being enclosed within the square shaped contour. There are also points which lie outside this region, forming the diagonal line.

7.2.3 Model LVC

This model contains both standard oscillations and an LV parameter which is purely imaginary.

Model LVC with parameters proportional to the neutrino energy

In this case, with $n = 1$, we are able to construct a sensitivity volume, shown in figure 7.25. The region to which the ANTARES neutrino telescope will be sensitive lies above the parabolic shaped surface. However, we also obtain a less well defined sensitivity region at larger values of the LV parameter. The projections of this volume are shown in figure 7.26. The top left frame in figure 7.26 shows Δm^2 as a function of the mixing angle, θ. Here, we are not able to construct meaningful sensitivity contour as the points in the less well defined region wash out those forming the normal parabolic shaped contour. However, we note that the current experimental

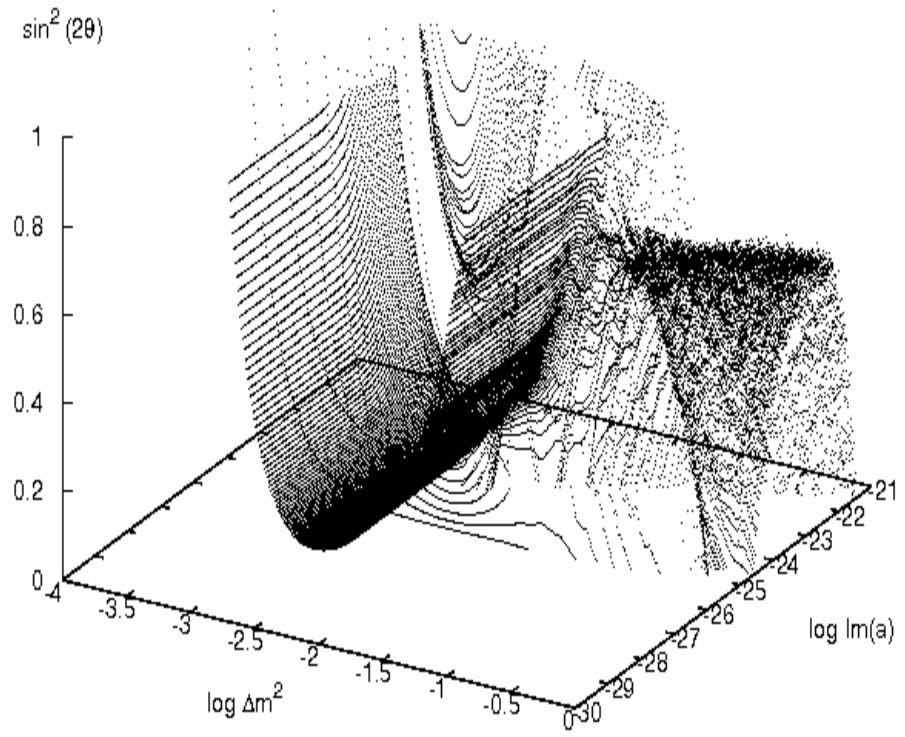

Figure 7.25: Sensitivity volume for model **LVC** at 90 percent confidence level for standard oscillations and imaginary off-diagonal LV effects proportional to the neutrino energy.

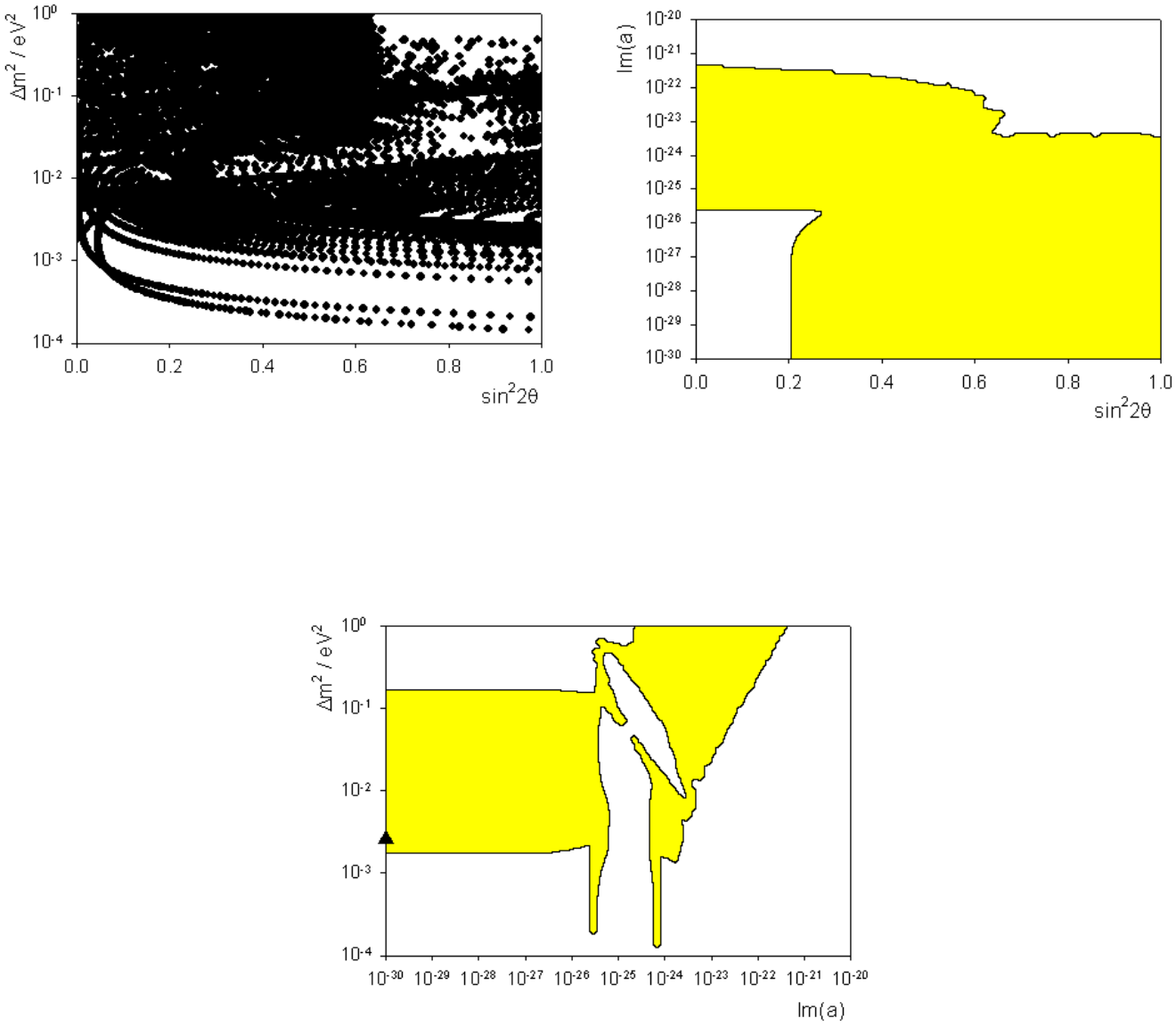

Figure 7.26: Sensitivity contours for model **LVC** at 90 percent confidence level for standard oscillations and imaginary off-diagonal LV effects proportional to the neutrino energy.

point of best fit is contained within the sensitivity region. In this case, it is very difficult to tell if this model is consistent with oscillations which arise from LV effects only, as we cannot be sure if the region extends down the parameter space to include $\Delta m^2 = 0$. However, if we examine the three dimensional sensitivity volume in figure 7.25, it seems as if $\Delta m^2 = 0$ is not included within the sensitivity region and so, therefore, we cannot measure neutrino oscillations which arise as a consequence of LV effects only. The top right frame shows the imaginary LV parameter Im(a) as a function of the mixing angle and we see that we are able to define a meaningful sensitivity contour. The sensitivity region is contained within the two curves. For $\sin^2 2\theta = 1$, we are able to place an upper bound on the LV parameter of 3.2×10^{-24}. The final, lower frame of figure 7.26 shows Δm^2 against Im(a). We are able to construct a sensitivity contour, the allowed region lying within the contours. The triangle, denoting the experimental point of best fit for Δm^2, is contained within this region.

Model LVC with parameters proportional to the neutrino energy squared

We now move on to examine the case when the LV parameters are proportional to the neutrino energy squared, so $n = 2$. The sensitivity volume we obtain is shown in figure 7.27. The sensitivity region is very similar to that for the case $n = 1$. In this case, the sensitivity region lies above the well defined parabolic surface but we again find a less well defined region, forming an inverted parabolic region, at higher values of the LV parameter. The projections of this volume are shown in figure 7.28. The top left frame shows the relationship between the standard oscillation parameter and the mixing angle. Again, we are not able to construct a well defined sensitivity contour but we note that the experimental point of best fit is included within the ill defined allowed region. The top right frame of figure 7.28 shows the imaginary LV parameter as a function of the mixing angle. In this case, we are able to define sensible sensitivity contours, the allowed region lying below the top curve. The point with $\sin^2 2\theta = 1$ and Im(a) $= 0$ is contained within this region and so we can probe standard neutrino oscillations only. We are able to place an upper bound on the LV parameter of 3.4×10^{-35} eV^{-1}. The lower plot of figure 7.28 shows the standard oscillation parameter, Δm^2, as a function of the LV parameter, Im(a). We are able to construct a sensitivity contour in this case, the allowed region lying within the two outer curves but excluding the central regions. We note that the experimental

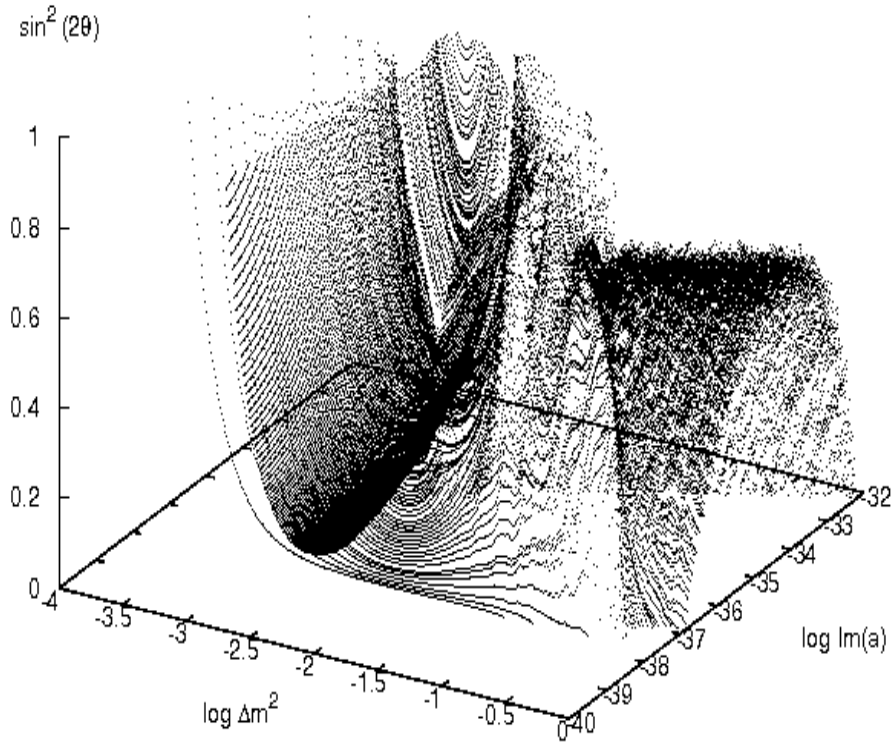

Figure 7.27: Sensitivity volume for model **LVC** at 90 percent confidence level for standard oscillations and imaginary off-diagonal LV effects proportional to the neutrino energy squared.

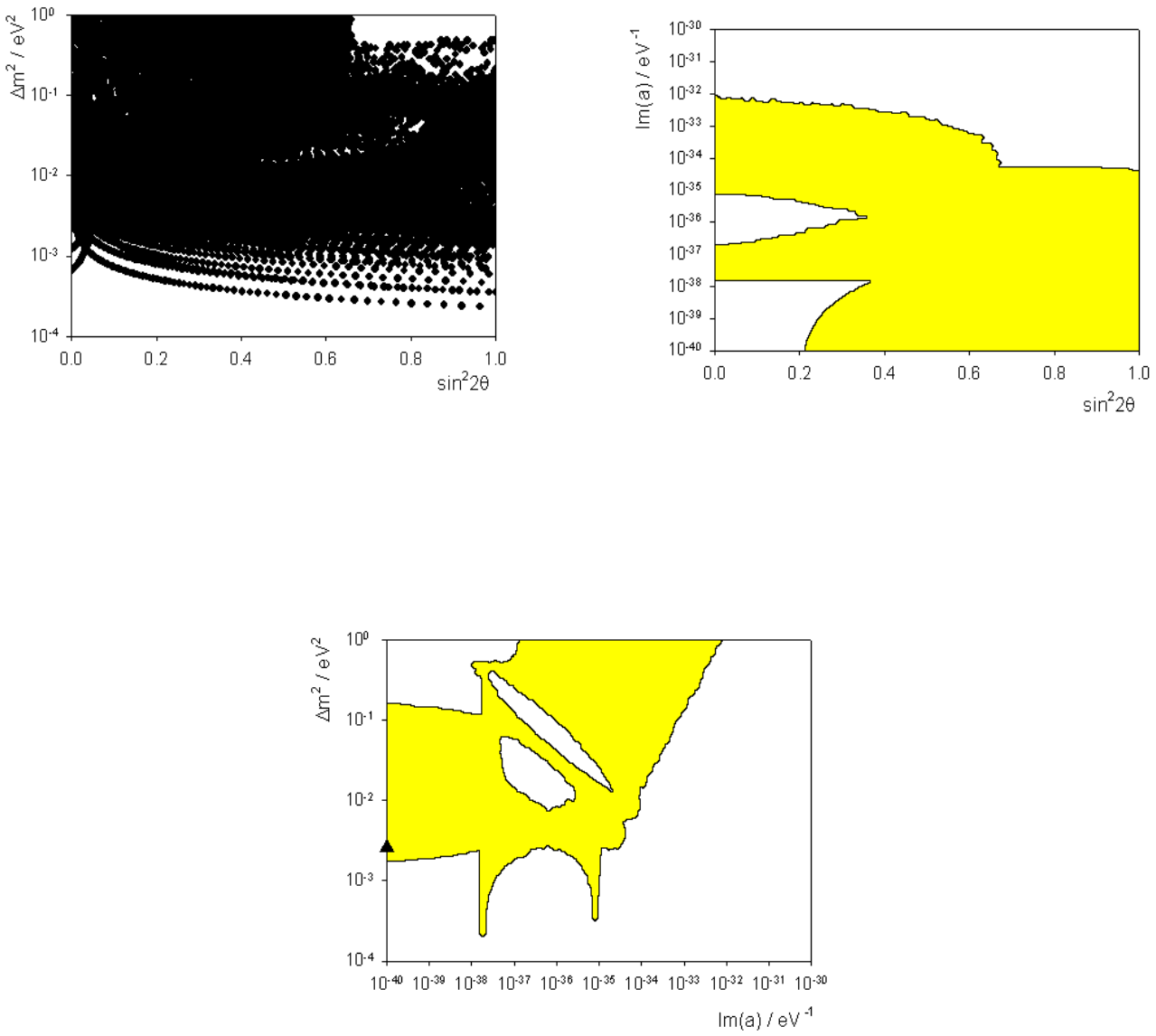

Figure 7.28: Sensitivity contours for model **LVC** at 90 percent confidence level for standard oscillations and imaginary off-diagonal LV effects proportional to the neutrino energy squared.

point of best fit for Δm^2 is contained within this region.

Model LVC with parameters proportional to the neutrino energy cubed

We conclude our discussion of model **LVC** by considering the case when the LV effects are proportional to the neutrino energy cubed. Figure 7.29 shows the sensitivity volume in this case. The region of interest lies above the parabolic shaped surface and also includes the collection of points located at the larger values of the LV parameter. The projections of this volume are shown in figure 7.30. In this case, we are able to construct meaningful sensitivity contours for all three projections. The top left frame, showing Δm^2 against the mixing angle, is a modification of the contour we would expect if we just considered standard oscillations. The sensitivity region lies within the curves. When we include LV effects, we obtain an additional region located for larger values of Δm^2 and low values of $\sin^2 2\theta$. We note that $\Delta m^2 = 0$ is not contained within the sensitivity contours and so we could not probe oscillations that arise due to LV effects only in this case. The experimental point of best fit, denoted by the triangle, is, however, contained within this region. The top right frame of figure 7.30 shows the LV parameter, $\mathrm{Im}(a)$, as a function of the mixing angle. In this case, the sensitivity region is below the upper curve and we are able to place an upper bound on this parameter at $\sin^2 2\theta = 1$ of $\mathrm{Im}(a) < 6.9 \times 10^{-46}\ eV^{-2}$. The lower frame of this figure shows the parameters Δm^2 and $\mathrm{Im}(a)$ plotted against each other. The sensitivity region lies between the curves with the experimental point of best fit for Δm^2 denoted by the triangle lying inside this region.

7.2.4 Model LVD

The final model we consider is a combination of the previous three. We include standard neutrino oscillations but fix $\Delta m^2 = 2.6 \times 10^{-3}\ eV^2$ [140] and fit for the parameters $\mathrm{Re}(a)$, $\mathrm{Im}(a)$ and θ.

Model LVD with parameters proportional to the neutrino energy

As in the models above, we begin our discussion by considering the case when $n = 1$, the LV effects being proportional to the neutrino energy. The sensitivity volume in this case is shown if figure 7.31. The sensitivity region lies above the surface at the top left of this figure and we again obtain allowed points which are not contained

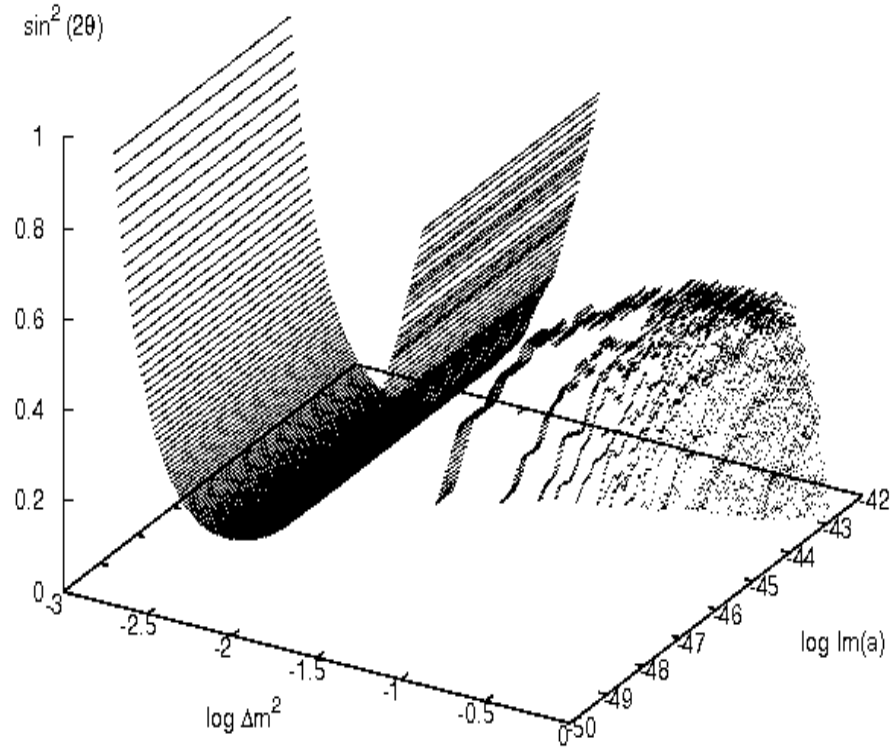

Figure 7.29: Sensitivity volume for model **LVC** at 90 percent confidence level for standard oscillations and imaginary off-diagonal LV effects proportional to the neutrino energy cubed.

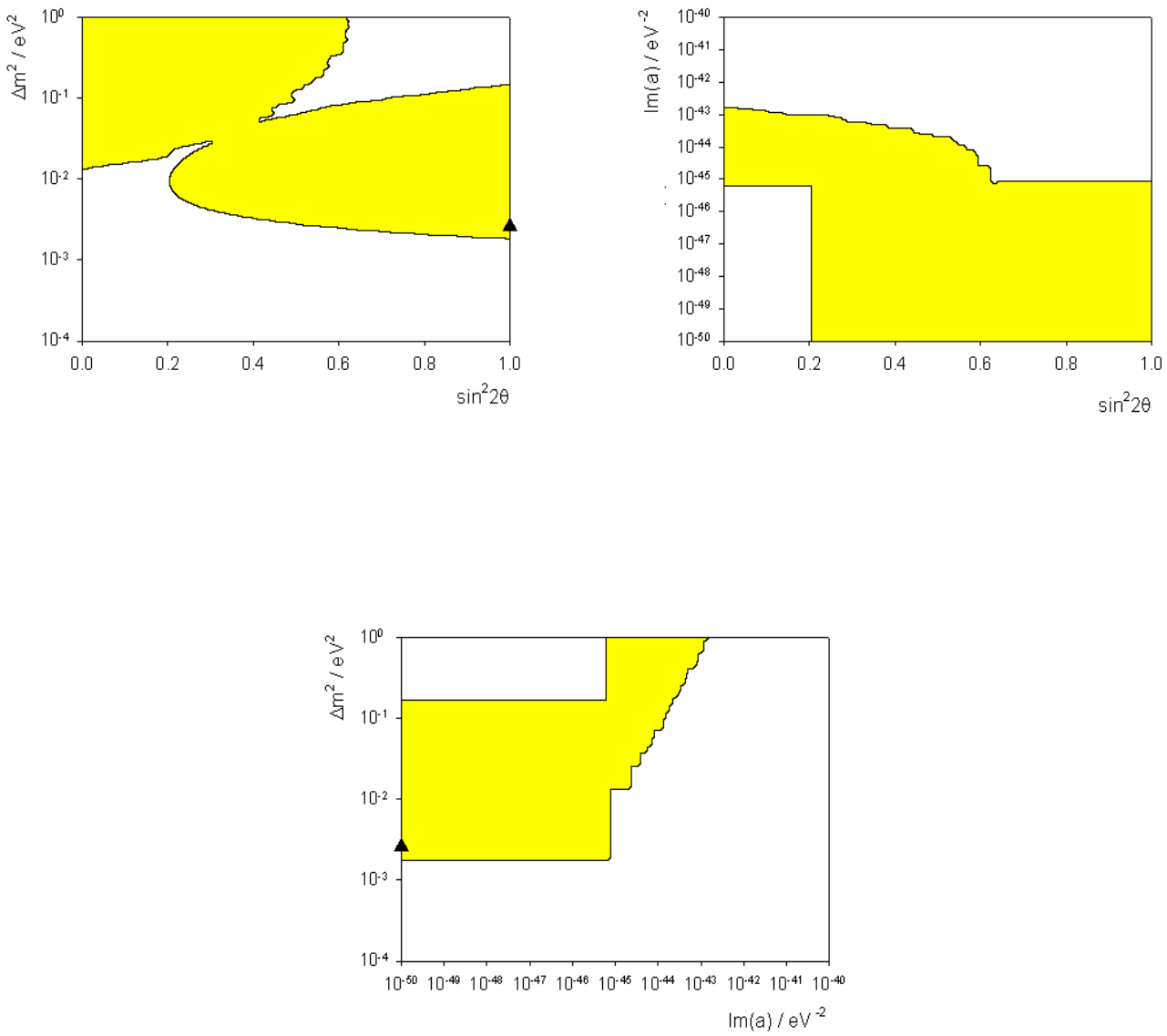

Figure 7.30: Sensitivity contours for model **LVC** at 90 percent confidence level for standard oscillations and imaginary off-diagonal LV effects proportional to the neutrino energy cubed.

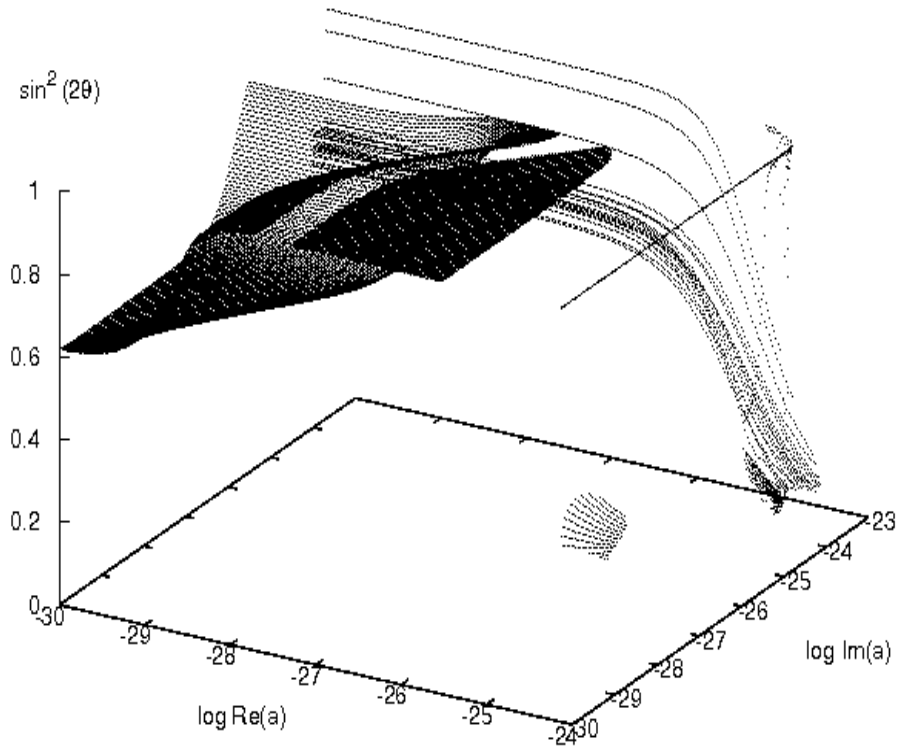

Figure 7.31: Sensitivity volume for model **LVD** at 90 percent confidence level for standard oscillations and both real and imaginary off-diagonal LV effects proportional to the neutrino energy.

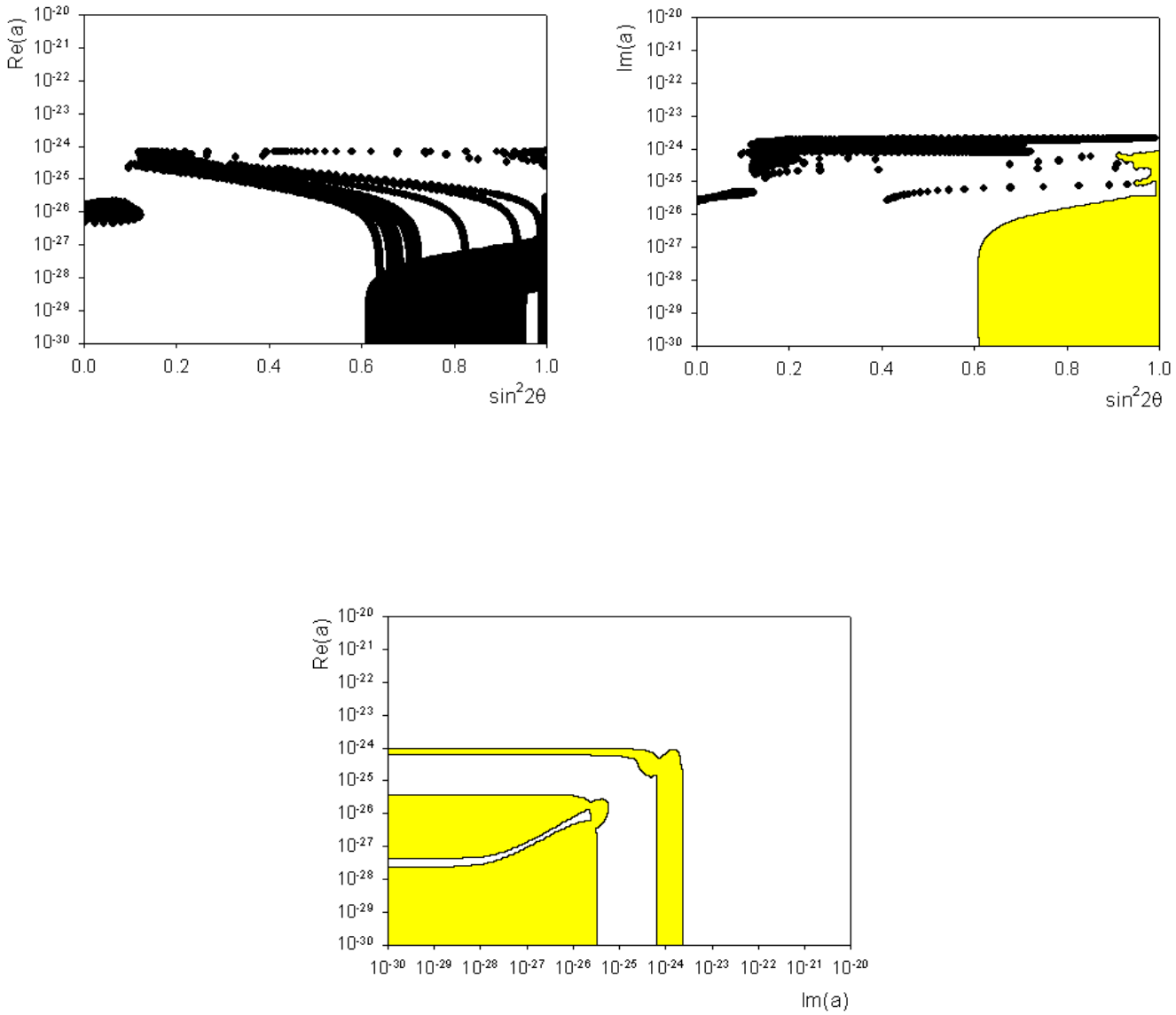

Figure 7.32: Sensitivity contours for model **LVD** at 90 percent confidence level for standard oscillations and both real and imaginary off-diagonal LV effects proportional to the neutrino energy.

within this region, particularly at larger values of the LV parameters. The three projections of this volume are shown in figure 7.32. The top left frame shows the real part of the LV parameter as a function of the mixing angle but we are unable to construct any simple sensitivity contours. However, we are able to place an upper bound on this parameter for this model of 7.3×10^{-25}. The top right frame shows the imaginary part of the LV parameter as a function of the mixing angle. In this case, we are able to define a sensitivity contour for the region with large $\sin^2 2\theta$ and small $\mathrm{Im}(a)$ but we still have some points outside this region from which we cannot easily construct a sensitivity contour. Since this parameter experiences a cut-off, we are able to place an upper bound of 2.1×10^{-24}. The lower frame of figure 7.32 shows the two LV parameters plotted against each other. In this case, we are able to construct sensitivity contours. The allowed regions here are contained within the large block at very small values of both parameters and also within the thin region which goes from around 10^{-24} on one axis to 10^{-24} on the other axis.

Model LVD with parameters proportional to the neutrino energy squared

We now turn to examine the case when the LV effects are proportional to the neutrino energy squared. The sensitivity volume in this case is shown in figure 7.33. The sensitivity volume is particularly difficult to interpret. There is a surface at high $\sin^2 2\theta$ and small values of the LV parameters above which there is a sensitivity region but we also obtain many points which do not form easily interpretable surfaces. The projections of this volume are shown in figure 7.34. The top right figure shows the real part of the LV parameter as a function of the mixing angle. We are able to construct a sensitivity contour, the allowed region lying below this curve. However, we still obtain a few points outside of this region. We are able, in this case, to place an upper bound of $9.7 \times 10^{-36}\ eV^{-1}$ on $\mathrm{Re}(a)$. The top right plot shows the imaginary part of the LV parameter against the mixing angle. Here, we cannot construct any meaningful sensitivity contours but are still able to place an upper bound of $2.9 \times 10^{-36}\ eV^{-1}$ on $\mathrm{Im}(a)$. The bottom frame of figure 7.34 shows the two LV parameters plotted against each other. The sensitivity regions in this case have been highlighted in yellow.

Model LVD with parameters proportional to the neutrino energy cubed

Finally, we finish by considering the case when $n = 3$. The interpretation of our

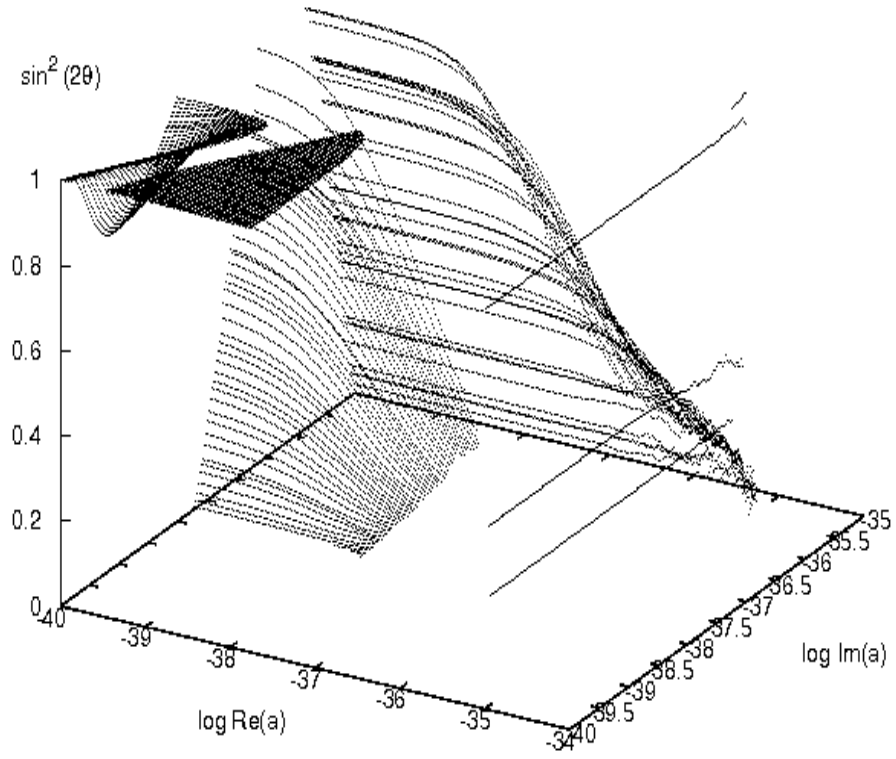

Figure 7.33: Sensitivity volume for model **LVD** at 90 percent confidence level for standard oscillations and both real and imaginary off-diagonal LV effects proportional to the neutrino energy squared.

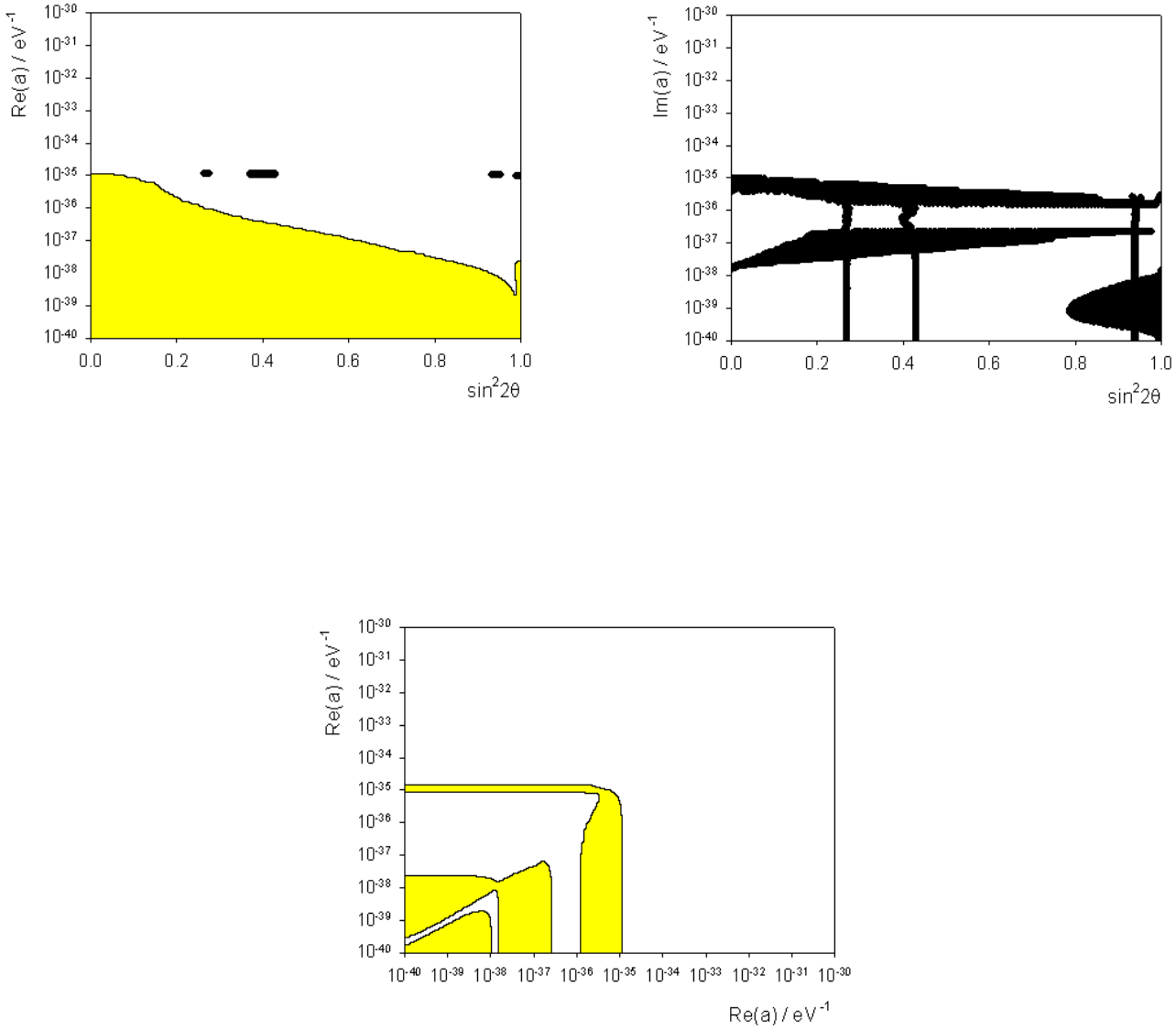

Figure 7.34: Sensitivity contours for model **LVD** at 90 percent confidence level for standard oscillations and both real and imaginary off-diagonal LV effects proportional to the neutrino energy squared.

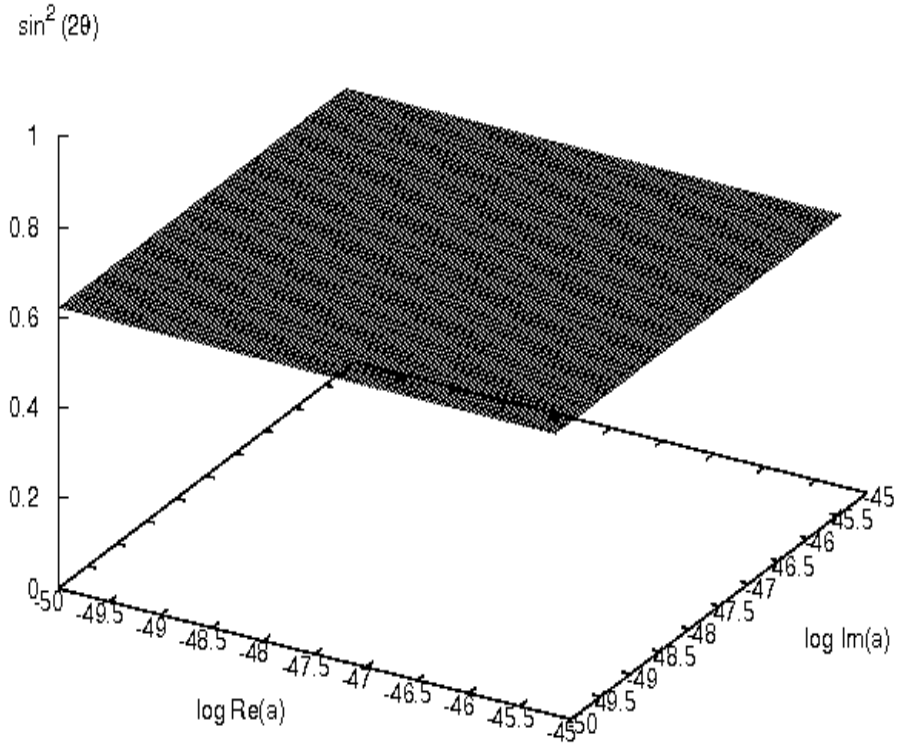

Figure 7.35: Sensitivity volume for model **LVD** at 90 percent confidence level for standard oscillations and both real and imaginary off-diagonal LV effects proportional to the neutrino energy cubed.

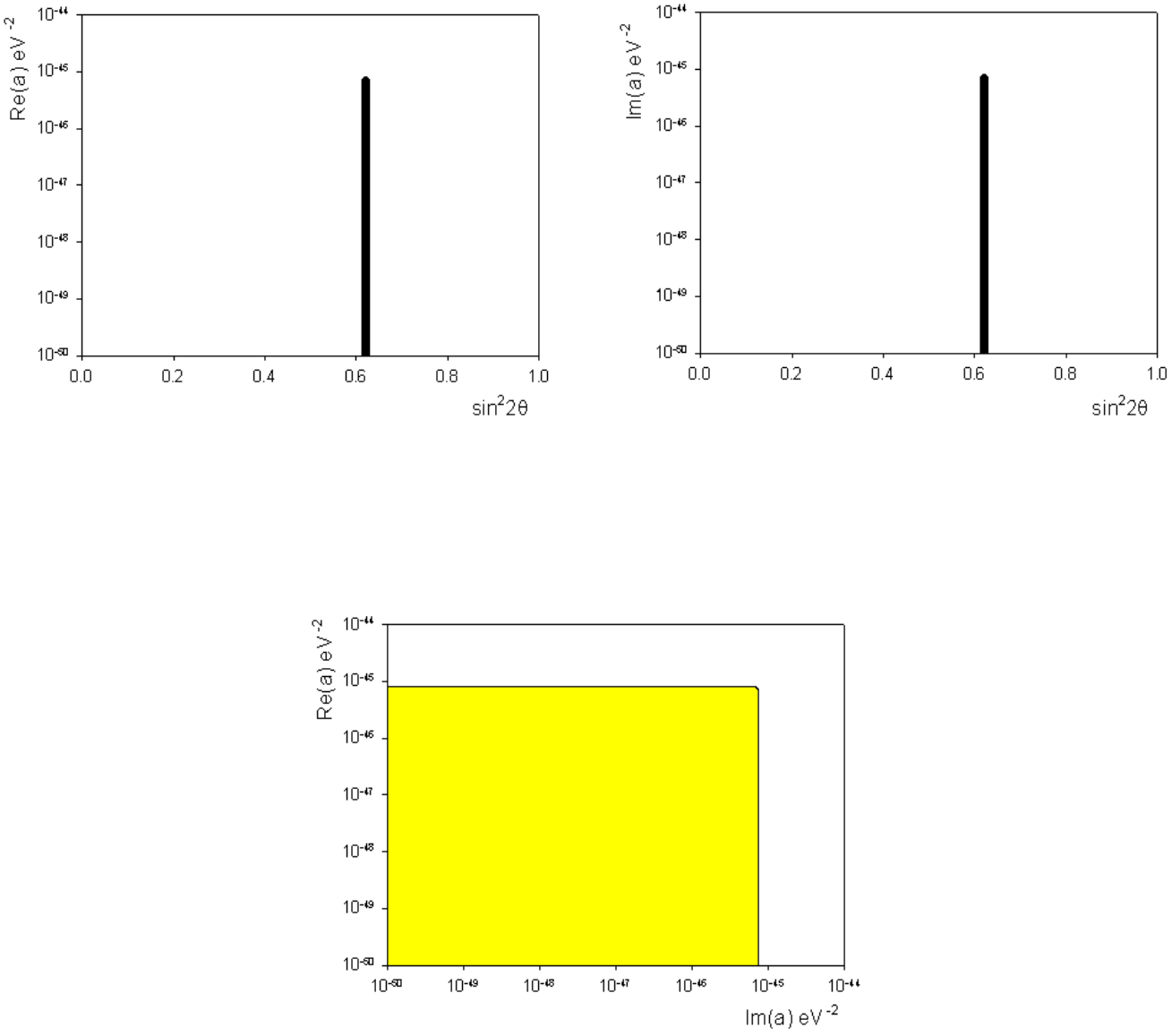

Figure 7.36: Sensitivity contours for model **LVD** at 90 percent confidence level for standard oscillations and both real and imaginary off-diagonal LV effects proportional to the neutrino energy cubed.

results in this case is particularly difficult. The three dimensional parameter space is shown in figure 7.35. For this energy dependence, we obtain a completely flat surface and there is no indication as to which side is contained in the sensitivity region. However, if we consider the volume obtained at the 99% confidence level, we note that surface lies at higher values of $\sin^2 2\theta$. Since we expect the sensitivity region at the 99% confidence level to be smaller than that for the 90% confidence level, we expect the sensitivity region to lie above the flat surface in figure 7.35. The projections of this volume are shown in figure 7.36. As we would expect, the plots of the real part of the LV parameter and imaginary part of the LV parameter as functions of the mixing angle are simply vertical lines. From the discussion above, we expect the sensitivity regions lie to the right of this line and therefore we are able to place an upper bound of $6.9 \times 10^{-46}\ eV^{-2}$ on both of these parameters. The bottom frame in figure 7.36 shows the real part of the LV parameter plotted against the imaginary part. The sensitivity region lies within the square contour.

7.2.5 Summary

In this section, we presented our simulations for the ANTARES telescope when we consider LV parameters which appear in the off-diagonal entries of the neutrino Hamiltonian. We considered four models with various combinations of parameters and showed how we may place upper bounds on these parameters. Furthermore, we considered LV effects which were proportional to the neutrino energy, E, and also E^2 and E^3. Table 7.2 shows a summary of the upper bounds found from the sensitivity contours. Assuming that, the off-diagonal LV effects can be parameterized in the same way as the extra term in (6.2), then we are able to examine how stringent our bounds are in the same way as we did for the case when the LV effects were contained in the diagonal entries of the Hamiltonian. For the case $n = 2$, we would expect from a naturalness point of view the parameter $\eta \sim 1$. Therefore, the term would be suppressed by one power of the Planck energy. This would indicate the LV parameter should be of the order of $10^{-28}\ eV^{-1}$. From table 7.2, we see that the largest bound for this parameter is five orders of magnitude smaller and the smallest upper bound we have from our simulations are eight orders of magnitude below what we would expect. Therefore, ANTARES should be able to observe these effects or rule this model out. The case for $n = 3$ is somewhat different as we would expect the LV parameters to be suppressed by the Planck energy squared and so be

model	parameter	$n=1$	$n=2$ (eV^{-1})	$n=3$ (eV^{-2})
1	$\mathrm{Re}(a)$	2.9×10^{-25}	3.1×10^{-36}	X
	$\mathrm{Im}(a)$	6.5×10^{-25}	8.2×10^{-36}	X
2	$\mathrm{Re}(a)$	3.1×10^{-22}	6.1×10^{-33}	9.7×10^{-44}
	$\mathrm{Im}(a)$	-	-	-
3	$\mathrm{Re}(a)$	-	-	-
	$\mathrm{Im}(a)$	3.2×10^{-24}	3.4×10^{-35}	6.9×10^{-46}
4	$\mathrm{Re}(a)$	7.3×10^{-25}	9.7×10^{-36}	6.9×10^{-46}
	$\mathrm{Im}(a)$	2.1×10^{-24}	2.9×10^{-36}	6.9×10^{-46}

Table 7.2: Table showing the upper bounds on the off-diagonal LV parameters, for various values of n. The X indicates that we were unable to place a bound on this parameter whilst the dashes denote that this parameter is not considered in this model.

of order $10^{-56}\ eV^{-2}$. The smallest value of the LV parameter we have in this case is 10 orders of magnitude larger than the expected value and our biggest upper bound is 12 orders of magnitude away. However, without a full theory of quantum gravity which allows these LV effects, our order of magnitude arguments may be naive and the LV parameters may be larger than we expect.

7.3 Summary

In this chapter, we have described how the ANTARES neutrino telescope will be able to place upper bounds on Lorentz violating parameters when we consider atmospheric neutrino oscillations. For simplicity, we considered a system of two neutrinos.

- We first considered the case when the LV parameters are contained within the diagonal entries of the neutrino Hamiltonian. We showed how these effects would modify the spectra of the number of observed events. We showed how the ANTARES experiment would be able to probe the parameter space of interest and place upper bounds on the diagonal LV effects (section 7.1).

- Secondly, we considered the case when the LV effects are present in the off-diagonal entries of the neutrino Hamiltonian. Again, we saw that the ANTARES experiment will be able to examine the relevant regions of parameter space and place upper bounds on these parameters(section 7.2).

Although these simulations are specific to the ANTARES experiment, we would expect other neutrino telescopes, such as AMANDA and IceCUBE, to obtain similar results.

Specifically, we saw that including LV effects modified the spectra of observed events in both $E/\cos\vartheta$ and $\cos\vartheta$. When we consider atmospheric neutrino oscillations which arise due to LV effects only, the spectra is significantly altered which would enable us to distinguish between this model and standard oscillations. We also saw that if LV effects modify standard oscillations, then, for large values of LV parameters, the cases of standard oscillations and standard oscillations plus LV effects could be distinguished due to the large differences in the expected number of events. In this case, however, separating the two models by the shape of the spectra alone is much more difficult.

We then considered how the ANTARES experiment will be able to place upper bounds on the LV effects when they are present in either the diagonal or off-diagonal terms of the neutrino Hamiltonian. In both cases, we were able to fit the experimental data to the oscillation probabilities to construct sensitivity regions within a three dimensional parameter space. Using these sensitivity volumes, we constructed two dimensional sensitivity contours which enabled us to find the upper bounds for these parameters. In the diagonal case, the interpretation of our results was relatively straightforward. However, when the LV parameters are contained within the off-diagonal entries of the neutrino Hamiltonian the interpretation of the sensitivity volumes is more difficult.

Finally, we considered, in each case, how the upper bounds we obtained for the LV parameters compared with the values we would expect from a naturalness point of view. We saw that if the LV effects are dependent upon the square of the neutrino energy, then the bounds appear to be particularly stringent, being several orders of magnitude smaller than those expected. For the case when the LV effects were proportional to the cube of the neutrino energy, then the situation was very different. In this case, the bounds on the LV effects were several orders of magnitude larger than those expected. The interpretation of the case when the case when the LV effects are proportional to the neutrino energy is also very difficult as we have no indication as to the natural value of this parameter from a quantum gravity point of view.

Chapter 8

Quantum decoherence and Lorentz invariance violating effects on astrophysical neutrinos

In this chapter, we show how quantum decoherence and Lorentz invariance violating effects may manifest themselves in the neutrino system, when the neutrinos originate from astrophysical sources. We begin by reviewing what we would expect to observe in the absence of new physics. We then show how the effects of both quantum decoherence and the violation of Lorentz invariance would affect this neutrino system.

8.1 Astrophysical neutrinos and standard oscillations

Throughout this chapter, the importance of neutrino flavour ratios will be paramount. As we discussed in chapter 1, there are two mechanisms for the creation of neutrinos around cosmic accelerators; pion decay, which produces neutrinos in the ratio

$$R_{\nu_e} : R_{\nu_\mu} : R_{\nu_\tau} = 1/3 : 2/3 : 0, \tag{8.1}$$

and neutron decay which produces neutrinos with the flavour ratio

$$R_{\nu_e} : R_{\nu_\mu} : R_{\nu_\tau} = 1 : 0 : 0. \tag{8.2}$$

Therefore, we may consider that we know the flavour content at the source of these neutrinos. We can, therefore, calculate the relative number of different types of neutrino we would expect to see at our detector due to neutrino oscillations.

The standard neutrino oscillation probability is given by (cf. (1.5)):

$$P(\nu_\alpha \to \nu_\beta) \quad - \quad \delta_{\alpha\beta} - 4\sum_{j>i} U_{\alpha j}U_{\beta j}U_{\alpha i}U_{\beta i}\sin^2[\Delta m^2_{ji}(L/4E)] \tag{8.3}$$

where $\Delta m^2_{ji} \equiv m^2_j - m^2_i$, the $U_{\alpha i}$'s are components of the unitary leptonic mixing matrix (1.6), with E the energy of the neutrino and L is the path length. Here, we have assumed for simplicity that the mixing matrix is real and so we do not consider effects due to CP violation. Since we are considering neutrinos which have travelled vast distances, we are able to simplify (8.3) further as the phase of the sine term will be averaged out. We therefore let $\sin^2[\Delta m^2_{ji}(L/4E)] \to \frac{1}{2}$ and so the probability is

$$P(\nu_\alpha \to \nu_\beta) \qquad \delta_{\alpha\beta} - 2\sum_{j>i} U_{\alpha j}U_{\beta j}U_{\alpha i}U_{\beta i}. \tag{8.4}$$

Using the most up to date mixing angles [142], from 2005, in table 1.2 with the mixing matrix in (1.6), we find the standard oscillation probabilities are

$$\begin{aligned} P[\nu_e \to \nu_e] \quad &- \quad 0.564, \\ P[\nu_e \to \nu_\mu] \quad & \quad 0.264, \\ P[\nu_e \to \nu_\tau] \quad &- \quad 0.180, \\ P[\nu_\mu \to \nu_\mu] \quad & \quad 0.365, \\ P[\nu_\mu \to \nu_\tau] \quad & \quad 0.367, \\ P[\nu_\tau \to \nu_\tau] \quad &- \quad 0.449. \end{aligned} \tag{8.5}$$

Using these probabilities, it is possible to find the expressions describing the flux of astrophysical neutrinos expected at the detector. Assuming that only electron and muon type neutrinos are created, an assumption justified in chapter 1, we may parameterize the initial flux of neutrinos at the source as

$$\begin{aligned} \Phi_e \quad &- \quad \varepsilon\Phi_{tot}, \\ \Phi_\mu \quad &- \quad (1-\varepsilon)\Phi_{tot}, \end{aligned} \tag{8.6}$$

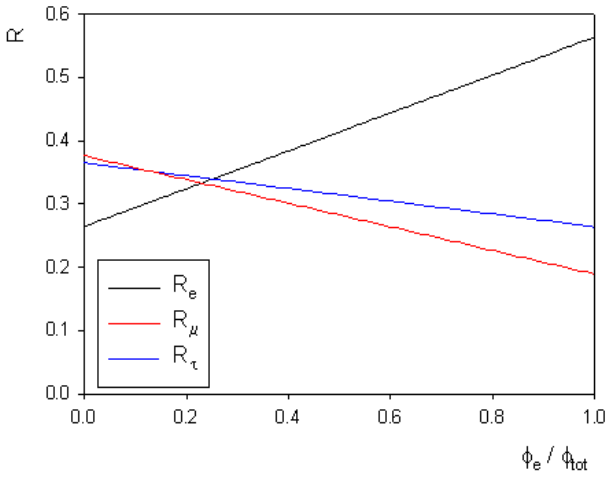

Figure 8.1: The astrophysical neutrino flux at the detector as a function of the parameter ε which embodies the ratio of flavours at the source, for standard neutrino oscillations (see [79]).

where $\varepsilon \in [0,1]$ and Φ_{tot} is the total flux. In terms of the neutrino probabilities (8.5), the neutrino flavour composition at the detector is

$$\begin{aligned} R_{\nu_e} &= (P[\nu_e \to \nu_e]\Phi_{\nu_e} + P[\nu_\mu \to \nu_e]\Phi_{\nu_\mu} + P[\nu_\tau \to \nu_e]\Phi_{\nu_\tau})/\Phi_{\text{tot}}, \\ R_{\nu_\mu} &= (P[\nu_e \to \nu_\mu]\Phi_{\nu_e} + P[\nu_\mu \to \nu_\mu]\Phi_{\nu_\mu} + P[\nu_\tau \to \nu_\mu]\Phi_{\nu_\tau})/\Phi_{\text{tot}}, \\ R_{\nu_\tau} &= (P[\nu_e \to \nu_\tau]\Phi_{\nu_e} + P[\nu_\mu \to \nu_\tau]\Phi_{\nu_\mu} + P[\nu_\tau \to \nu_\tau]\Phi_{\nu_\tau})/\Phi_{\text{tot}}, \end{aligned} \tag{8.7}$$

and so we find

$$\begin{aligned} R_{\nu_e} &= 0.264 + 0.300\varepsilon. \\ R_{\nu_\mu} &= 0.365 - 0.101\varepsilon. \\ R_{\nu_\tau} &= 0.367 - 0.187\varepsilon. \end{aligned} \tag{8.8}$$

The flavour ratios are shown diagrammatically in figure 8.1. The observed ratios expected at the detector from a pion decay source is found by setting $\varepsilon = 1/3$ in (8.8) and gives

$$R_{\nu_e} : R_{\nu_\mu} : R_{\nu_\tau} = 0.364 : 0.331 : 0.305. \tag{8.9}$$

whilst the ratios for a source of neutrinos from neutrino decay is found by setting $\eta = 1$ giving

$$R_{\nu_e} : R_{\nu_\mu} : R_{\nu_\tau} = 0.564 : 0.264 : 0.18. \tag{8.10}$$

Since we know the expected flux of astrophysical neutrinos we would see at the detector in the absence of any new physics, we are now in a position to examine how quantum decoherence and the violation of Lorentz invariance would affect the astrophysical neutrino system.

8.2 Quantum decoherence

We saw in chapter 4 how quantum decoherence effects would manifest themselves in the atmospheric neutrino system and there, we considered a system containing just two neutrinos. In the case of neutrinos which originate in astrophysical neutrinos, they travel large distances and so all three flavours of neutrino have time to mix. We need, therefore, to extend the analysis in chapter 4 from two to three neutrinos.

8.2.1 Quantum decoherence in a three neutrino system

To model quantum decoherence in a three neutrino system, we continue in an analogous way to the method in chapter 4, so we need to represent H and ρ in (4.11) in terms of a specific basis. We choose for this basis, the generators of SU(3), L_i, where $i = 1 \ldots 8$ and L_0, the identity matrix. Therefore, we write the Hamiltonian, the density matrix and the additional term, $\delta\not{H}$, in terms of these basis matrices as

$$\rho = \frac{1}{2}\rho_\mu L_\mu, \qquad H = \frac{1}{2}h_\nu L_\nu, \qquad \delta\not{H} = \frac{1}{2}h'_\kappa L_\kappa, \tag{8.11}$$

where the Greek indices run from 0 to 8. If we decompose the time derivative in terms of the same basis, then we find (cf. (4.18))

$$\dot{\rho}_\mu = \left(h_{\mu\nu} + h'_{\mu\nu}\right)\rho_\nu, \tag{8.12}$$

where both h and h' are now 9×9 matrices. We may in principle, therefore, introduce 28 decoherence parameters but this is impractical. To continue, we therefore adopt a

block diagonal form, in order that we may solve the resulting differential equations:

$$h' = -2\begin{pmatrix} 0 & 0 & 0 & 0 & 0 & 0 & 0 & 0 & 0 \\ 0 & A & B & 0 & 0 & 0 & 0 & 0 & 0 \\ 0 & B & \Lambda & 0 & 0 & 0 & 0 & 0 & 0 \\ 0 & 0 & 0 & \Psi & 0 & 0 & 0 & 0 & 0 \\ 0 & 0 & 0 & 0 & x & y & 0 & 0 & 0 \\ 0 & 0 & 0 & 0 & y & z & 0 & 0 & 0 \\ 0 & 0 & 0 & 0 & 0 & 0 & a & b & 0 \\ 0 & 0 & 0 & 0 & 0 & 0 & b & \alpha & 0 \\ 0 & 0 & 0 & 0 & 0 & 0 & 0 & 0 & \delta \end{pmatrix}. \tag{8.13}$$

This form of the matrix, h', was considered in reference [191] with a simple diagonal matrix being considered in [132]. It is perhaps somewhat surprising that, although we have three neutrinos, only two of the parameters, Ψ and δ, violate the conservation of energy within the neutrino sector. If we include standard oscillations, then the time evolution of the density matrix becomes

$$\dot{\boldsymbol{\rho}} = -2\mathcal{H}\boldsymbol{\rho}, \tag{8.14}$$

where $\boldsymbol{\rho} = (\rho_0, \rho_1 \ldots \rho_8)^T$ and

$$\mathcal{H} = \begin{pmatrix} 0 & 0 & 0 & 0 & 0 & 0 & 0 & 0 & 0 \\ 0 & A & B+\omega_{21} & 0 & 0 & 0 & 0 & 0 & 0 \\ 0 & B-\omega_{21} & \Lambda & 0 & 0 & 0 & 0 & 0 & 0 \\ 0 & 0 & 0 & \Psi & 0 & 0 & 0 & 0 & 0 \\ 0 & 0 & 0 & 0 & x & y+\omega_{31} & 0 & 0 & 0 \\ 0 & 0 & 0 & 0 & y-\omega_{31} & z & 0 & 0 & 0 \\ 0 & 0 & 0 & 0 & 0 & 0 & a & b+\omega_{32} & 0 \\ 0 & 0 & 0 & 0 & 0 & 0 & b-\omega_{32} & \alpha & 0 \\ 0 & 0 & 0 & 0 & 0 & 0 & 0 & 0 & \delta \end{pmatrix}. \tag{8.15}$$

Here, the quantities ω_{ji} are the standard neutrino oscillation parameters and are given by $\omega_{ji} = \frac{\Delta m^2_{ji}}{4E}$ where the indices i and j represent the mass eigenstate. Substituting (8.15) into (8.14), we obtain nine differential equations for the components

of the density matrix:

$$\begin{aligned}
\dot{\rho_0} &= 0; \\
\dot{\rho_1} &= -2A\rho_2 - (B+\omega_{21})\rho_2; \\
\dot{\rho_2} &= -2(B-\omega_{21})\rho_1 - 2A\rho_2; \\
\dot{\rho_3} &= -2\Psi\rho_3; \\
\dot{\rho_4} &= -2x\rho_4 - 2(y+\omega_{31})\rho_5; \\
\dot{\rho_5} &= -2(y-\omega_{31})\rho_4 - 2z\rho_5; \\
\dot{\rho_6} &= -2a\rho_6 - 2(b+\omega_{32})\rho_7; \\
\dot{\rho_7} &= -2(b-\omega_{32})\rho_6 - 2\alpha\rho_7; \\
\dot{\rho_8} &= -2\delta\rho_8.
\end{aligned} \tag{8.16}$$

Assuming the neutrino is initially of flavour a, then the components of the density matrix at $t = 0$ are

$$\begin{aligned}
\rho_0 &= \frac{2}{3}(U_{a1}^2 + U_{a2}^2 + U_{a3}^2); \\
\rho_1 &= 2U_{a1}U_{a2}; \\
\rho_2 &= 0; \\
\rho_3 &= U_{a1}^2 - U_{a2}^2; \\
\rho_4 &= 2U_{a1}U_{a3}; \\
\rho_5 &= 0; \\
\rho_6 &= 2U_{a2}U_{a3}; \\
\rho_7 &= 0; \\
\rho_8 &= \frac{1}{\sqrt{3}}(U_{a1}^2 + U_{a2}^2 - 2U_{a3}^2);
\end{aligned} \tag{8.17}$$

where the quantities U_{xi} are elements of the standard mixing matrix (1.6) and we have assumed that these components are real. Integrating (8.16) with the initial conditions given in (8.17) enables us to find the density matrix in terms of t. The probability of oscillation is given by

$$P|\nu_a \to \nu_b| = \mathrm{Tr}(\rho(t)\rho_b(0)) \tag{8.18}$$

where $\rho_b(0)$ is the density matrix for a neutrino of flavour $b \neq a$:

$$\rho_b(0) = \begin{pmatrix} U_{b1}^2 & U_{b1}U_{b2} & U_{b1}U_{b3} \\ U_{b1}U_{b2} & U_{b2}^2 & U_{b2}U_{b3} \\ U_{b1}U_{b3} & U_{b2}U_{b3} & U_{b3}^2 \end{pmatrix}. \tag{8.19}$$

The probability of oscillation from $\nu_a \to \nu_b$ with $a \neq b$ is therefore given by

$$\begin{aligned} P[\nu_a \to \nu_b] \;=\; & \frac{1}{3} + \frac{1}{2}(U_{a1}^2 - U_{a2}^2)(U_{b1}^2 - U_{b2}^2)e^{-2\Psi L} \\ & + \frac{1}{6}(U_{a1}^2 + U_{a2}^2 - 2U_{a3}^2)(U_{b1}^2 + U_{b2}^2 - 2U_{b3}^2)e^{-2\delta L} \\ & + 2U_{a1}U_{a2}U_{b1}U_{b2}e^{-(A+\Lambda)L}\left[\cos(2\Omega_{21}L) + \frac{(\Lambda - A)}{2\Omega_{21}}\sin(2\Omega_{21}L)\right] \\ & + 2U_{a1}U_{a3}U_{b1}U_{b3}e^{-(x+z)L}\left[\cos(2\Omega_{31}L) + \frac{(z - x)}{2\Omega_{31}}\sin(2\Omega_{31}L)\right] \\ & + 2U_{a2}U_{a3}U_{b2}U_{b3}e^{-(a+\alpha)L}\left[\cos(2\Omega_{32}L) + \frac{(\alpha - a)}{2\Omega_{32}}\sin(2\Omega_{32}L)\right]. \end{aligned} \tag{8.20}$$

where

$$\begin{aligned} \Omega_{21} &= \left[\left(\frac{\Delta m_{21}^2}{4E}\right)^2 - [\Lambda - A]^2\right]^{\frac{1}{2}}; \\ \Omega_{31} &= \left[\left(\frac{\Delta m_{31}^2}{4E}\right)^2 - [z - x]^2\right]^{\frac{1}{2}}; \\ \Omega_{32} &= \left[\left(\frac{\Delta m_{32}^2}{4E}\right)^2 - [\alpha - a]^2\right]^{\frac{1}{2}}. \end{aligned} \tag{8.21}$$

Note that complete positivity is not satisfied for this model. If we again consider neutrinos travelling large distances from astrophysical sources, then we may average the sine and cosine terms in (8.20). Assuming for simplicity $\Phi = \delta$, the probability then reduces to

$$\begin{aligned} P[\nu_a \to \nu_b] \;=\; & \frac{1}{3} + \frac{1}{6}e^{-2\delta L}\left[3(U_{a1}^2 - U_{a2}^2)(U_{b1}^2 - U_{b2}^2)\right. \\ & \left. + (U_{a1}^2 + U_{a2}^2 - 2U_{a3}^2)(U_{b1}^2 + U_{b2}^2 - 2U_{b3}^2)\right]. \end{aligned}$$

We can now derive equations describing the flavor composition at the detector. Using the up to date mixing angles from table 1.2, parameterizing the initial flux as in (8.6) and using equation (8.7), the flavour composition at the detector is

$$\begin{aligned} R_{\nu_e} &= \frac{1}{3} + e^{-2\delta L}[0.287\varepsilon - 0.065], \\ R_{\nu_\mu} &= \frac{1}{3} - e^{-2\delta L}[0.096\varepsilon - 0.03], \\ R_{\nu_\tau} &\quad \frac{1}{3} - e^{-2\delta L}[0.189\varepsilon - 0.034]. \end{aligned} \tag{8.22}$$

Therefore, as $L \to \infty$, the signature of quantum decoherence in astrophysical neutrinos is an equal number of each flavour of neutrino.

8.2.2 Detecting quantum decoherence in astrophysical neutrinos

In the last section, we saw that the inclusion of quantum decoherence into the three neutrino astrophysical picture would lead to an equal number of each flavour of neutrinos being detected. Unfortunately, as we saw in section 8.1, sources which produce neutrinos through pion decay generate almost this ratio after oscillations. Therefore, neutrinos which originate from these sources are not very helpful in probing these effects. However, since neutrinos from neutron decay oscillate to flavour ratios very much different from $R_{\nu_e} : R_{\nu_\mu} : R_{\nu_\tau} = 1/3 : 1/3 : 1/3$, they provide a useful probe with which to look for quantum decoherence effects.

Decoherence parameters with no energy dependence

In this case, the main signature of quantum decoherence would be an observation of equal number of all three flavours of neutrinos. The flavour ratios in (8.22) approach their asymptotic values of 1/3 for path lengths $L >> \delta^{-1}$. If we assume a source of electron neutrinos at a distance of 10 kiloparsecs, then we can probe values of $\delta \sim 10^{-21}\ m^{-1}$, or equivalently, $\delta \sim 10^{-37}\ GeV$. As we saw in chapter 5, the current bounds for the quantum decoherence parameter with no dependence on the neutrino energy, from Super-Kamiokande and K2K data is of the order $10^{-23}\ GeV$ [180].

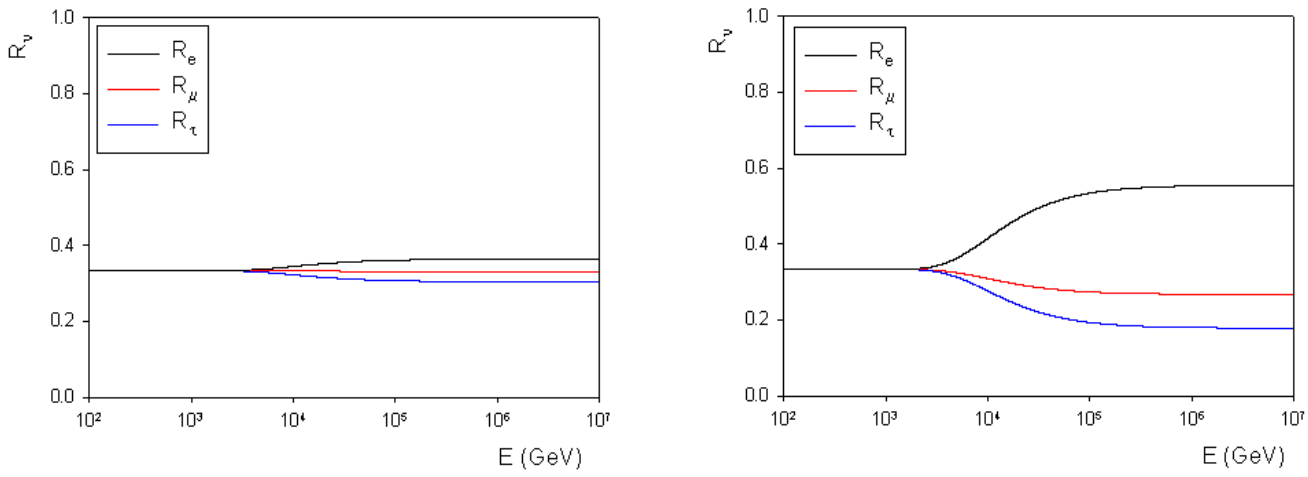

Figure 8.2: The flavour ratios at the detector as a function of energy including decoherence effects proportional to the inverse of the neutrino energy. In the frame on the left, the initial ratios are those values found from pion decay ($R_{\nu_\epsilon} : R_{\nu_\mu} : R_{\nu_\tau} = 1/3 : 2/3 : 0$) whilst those on the right are from neutron decay ($R_{\nu_e} : R_{\nu_\mu} : R_{\nu_\tau} = 1 : 0 : 0$). In both cases, we considered a model with $2\delta L = (E/10\ TeV)^2$.

Decoherence parameters inversely proportional to the neutrino energy

If we consider the case when the quantum decoherence parameters are proportional to the inverse of the neutrino energy, then for a 10 kiloparsec source of TeV neutrinos, we could probe $\mu^2 \sim 10^{-21}\ m^{-1}\ TeV$, where $\mu^2 = \delta E$. Therefore, we find an upper bound on this parameter of $\mu < 10^{-34}\ GeV^2$ at GeV energies.

In addition, the flavour ratios in (8.22) take on an energy dependence due to the decoherence parameter. Therefore, direct observation of quantum decoherence may be possible and from the value of the energy at the threshold of these effects, we may be able to place an accurate bound on the size of the model parameters. Figure 8.2 shows this diagrammatically with the threshold set so $2\delta L = 1$ at $E = 10\ TeV$. The left frame shows the case when the initial flux of neutrinos is from pion decay, here quantum decoherence has very little effect on the flavour ratios. The frame on the right shows the case when neutrinos originate from neutron decay. Here, quantum decoherence makes a marked difference in the ratios observed.

Decoherence parameters proportional to the neutrino energy squared

Considering the case when the quantum decoherence parameters are proportional to the neutrino energy squared, then for a source of TeV electron neutrinos at a distance of 10 kiloparsecs, we could test $\kappa < 10^{-21}\ m^{-1}\ TeV^{-2}$, where $\kappa = \delta/E^2$.

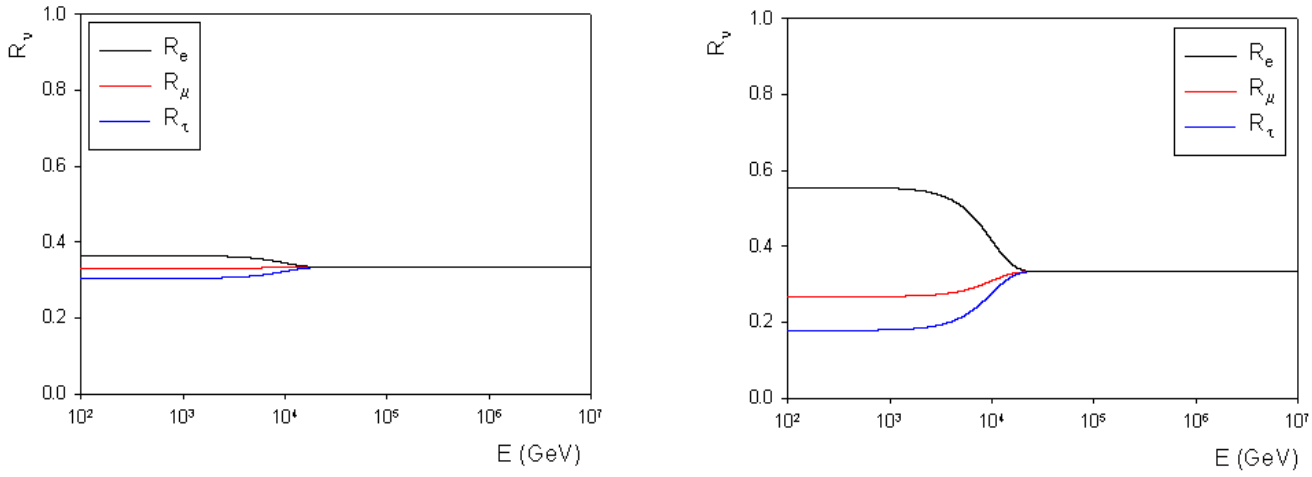

Figure 8.3: As figure 8.2 but for quantum decoherence parameters proportional to the neutrino energy squared.

In this case, therefore, we would be able to place a bound of $\kappa < 10^{-43}\ GeV^{-2}$, at GeV energies, on the quantum decoherence parameter. This is thirty-three orders of magnitude better than the current upper bound from Super-Kamiokande and K2K data [180].

Since the quantum decoherence parameter is dependent on the neutrino energy, the flavour ratios also take on an energy dependence. Figure 8.3 shows the flavour ratios as a function of energy in this case when we have set $2\delta L = 1$ at $E = 10\ TeV$. The situation is similar to that in the last subsection, since, for neutrinos which originate from pion decay, very little difference is seen with quantum decoherence effects whilst for neutrinos which come from neutron decay, a large difference in the observed flavour ratios is expected. However, the shape of the curves is somewhat different.

8.2.3 Summary

Using neutrinos which originate in astrophysical objects, we will be able to place very stringent bounds on quantum decoherence parameters. In fact, we saw that, even for the model in which the quantum decoherence parameter is inversely proportional to the neutrino energy, then we will be able to surpass the existing bounds by many orders of magnitude. In addition, for two of the models, the flavour ratios take on an energy dependence which may be observed.

8.3 Violation of Lorentz invariance

In chapters 6 and 7, we saw how the violations of Lorentz invariance could affect the neutrino system and how atmospheric neutrinos could be used to place bounds on the Lorentz invariance violating parameters. Here, we consider astrophysical neutrinos.

8.3.1 Three neutrino LV models with a diagonal Hamiltonian

In an analogous way to that in chapter 6, we may find oscillation probabilities which involve Lorentz invariance violation for three neutrinos where we consider the Hamiltonian of the system to be diagonal. In this case, the probability of oscillation is given by equation (1.5) with

$$\frac{\Delta m^2_{ij}}{E} \to \frac{\Delta m^2_{ij}}{E} + \Delta\eta_{ij} E^n, \tag{8.23}$$

where the subscripts i and j denote the mass eigenstates. The LV parameters, therefore, are found within the sine and cosine terms of the oscillation probability. As we discussed above, when the neutrinos travel over large distances, the phase information contained within these arguments is lost. Therefore, when the LV parameters lie within the diagonal entries of the Hamiltonian, we are unable to glean any information about them from astrophysical neutrinos.

An alternative to the method we consider here was considered in reference [89]. Rather than consider how LV may alter flavour ratios, the author of [89] considered how modifications to the dispersion relation would alter the neutrino oscillation length. By considering neutrinos from astrophysical sources detected by neutrino telescopes, the author of reference [89] was able to show that neutrinos could probe effects suppressed by up to seven powers of the Planck energy.

8.3.2 Three neutrino LV models with an off-diagonal Hamiltonian

In order to potentially observe LV effects within the astrophysical neutrino system, we turn to Hamiltonians with off-diagonal LV entries. To do this, we would like to continue in an analogous way to that in chapter 6, however, the situation becomes

very difficult as, in general, we have three mixing angles, three mass differences and three LV parameters. Therefore, we take three approaches to solving this problem:

- We begin by examining the how the LV effects alter the flavour ratios at threshold, that is, when the LV effects just start to be observable.
- We also consider how LV effects alter the flavour ratios in the high energy limit.
- Finally, we examine the intermediate energy range numerically.

We first do this when the Hamiltonian has its simplest form in the mass basis.

8.3.3 LV parameters in the mass basis

In order to examine how the LV effects manifest themselves, we begin by considering a first order approximation to the LV parameters when we consider the Hamiltonian to take the form

$$H = \begin{pmatrix} \frac{m_1^2}{2E} & h & h \\ h & \frac{m_2^2}{2E} & h \\ h & h & \frac{m_3^2}{2E} \end{pmatrix} \tag{8.24}$$

where h is an LV parameter.

Flavour ratios at threshold

In the standard oscillation case, the time evolution of the density matrix is given by

$$\frac{d\rho}{dt} = B\rho \tag{8.25}$$

where B is the matrix representing the Hamiltonian in the SU(3) basis. Perturbing the density matrix and the matrix B:

$$\begin{aligned} \rho &\rightarrow \rho_0 + \delta\rho_1 \\ B &\rightarrow B + \delta C, \end{aligned} \tag{8.26}$$

where the quantities ρ_0 and B are the unperturbed density matrix and Hamiltonian matrix in the SU(3) basis and the quantities multiplied by δ, namely ρ_1 and C, contain the LV effects. Here, δ is a small quantity, representing the perturbation.

Substituting (8.26) into (8.25) and equating coefficients gives

$$\dot{\rho}_1 = B\rho_1 + C\rho_0. \tag{8.27}$$

Defining the vectors $\mathbf{x}$, $\mathbf{y}$ as

$$\boldsymbol{\rho_0} = U\mathbf{x}, \qquad \boldsymbol{\rho_1} = W\mathbf{y}, \tag{8.28}$$

where the components of the ρ vectors are the components of the unperturbed density matrix ($\boldsymbol{\rho_0}$) and perturbed density matrix ($\boldsymbol{\rho_1}$) and W is the unitary matrix diagonalizing B, we may rewrite equation (8.27) as

$$\dot{\mathbf{y}} - W^{-1}BW\mathbf{y} = W^{-1}CW\mathbf{x}. \tag{8.29}$$

Since we know W, B, C and can evaluate $\mathbf{x}$, then solving this equation will give us the perturbation to the density matrix from which we may calculate oscillation probabilities. In reality, this calculation still results in complicated expressions for the probabilities. However, the expressions are greatly simplified if we assume very long path lengths. This is entirely reasonable since we need only consider the three neutrino system when considering neutrinos from astrophysical sources. Using the most up to date values of the mixing parameters from table 1.2, assuming a normal mass hierarchy and that the LV parameter, a, is real, we find the oscillation probabilities to be

$$\begin{aligned}
P[\nu_e \to \nu_e] &= 0.549 - 9.124 \times 10^{9n+12} aE^{n+1}, \\
P[\nu_e \to \nu_\mu] &= 0.269 + 3.142 \times 10^{9n+12} aE^{n+1}, \\
P[\nu_e \to \nu_\tau] &= 0.182 + 5.982 \times 10^{9n+12} aE^{n+1}, \\
P[\nu_\mu \to \nu_\mu] &= 0.364 - 2.549 \times 10^{9n+11} aE^{n+1}, \\
P[\nu_\mu \to \nu_\tau] &= 0.368 - 2.887 \times 10^{9n+12} aE^{n+1}, \\
P[\nu_\tau \to \nu_\tau] &= 0.450 - 3.095 \times 10^{9n+12} aE^{n+1},
\end{aligned} \tag{8.30}$$

where we set $h = \frac{aE^n}{4}$, have written out in full the explicit dependence of the LV parameter on the neutrino energy and replaced c and $\hbar$. Using these probabilities, it is possible to find expressions describing the flux of neutrinos originating in astrophysical sources. If we assume that only electron and muon neutrinos are created,

we parameterize the initial flux as in (8.6), and so are able to find the flavour composition at the detector in terms of the neutrino oscillation probabilities, as in (8.7). We therefore find the flavour ratios to be

$$\begin{aligned} R_{\nu_e} &= 0.269 + 0.280\varepsilon - aE^{n+1}[0.123\varepsilon - 0.314] \times 10^{9n+14}, \\ R_{\nu_\mu} &= 0.364 - 0.095\varepsilon + aE^{n+1}[0.340\varepsilon - 0.025] \times 10^{9n+13}, \\ R_{\nu_\tau} &= 0.368 - 0.186\varepsilon + aE^{n+1}[0.887\varepsilon - 0.289] \times 10^{9n+13}. \end{aligned} \tag{8.31}$$

Again, it is important to note that these expressions are valid only at the threshold where the LV effects begin to modify standard neutrino physics.

Flavour ratios in the high energy limit

In addition to examining threshold effects, it is also possible to examine the flavour ratios in the high energy limit. Since standard neutrino oscillations are inversely proportional to the neutrino energy, at high energies these effects may be neglected. In this case, we assume the Hamiltonian has the form

$$H_{highE} = \begin{pmatrix} 0 & h & h \\ h & 0 & h \\ h & h & 0 \end{pmatrix}, \tag{8.32}$$

where h is a LV parameter. When represented in the basis with the generators of SU(3) as the basis matrices, equation (8.32) takes the form

$$H_{highE}^{SU(3)} = \frac{1}{2} \begin{pmatrix} 0 & 0 & 0 & 0 & h & 0 & h & 0 \\ 0 & 0 & -2h & -h & 0 & h & 0 & 0 \\ 0 & 2h & 0 & 0 & h & 0 & -h & 0 \\ 0 & h & 0 & 0 & 0 & 0 & -h & 0 \\ -h & 0 & -h & 0 & 0 & h & 0 & -\sqrt{3}h \\ 0 & -h & 0 & 0 & -h & 0 & 0 & 0 \\ -h & 0 & h & h & 0 & 0 & 0 & -\sqrt{3}h \\ 0 & 0 & 0 & 0 & \sqrt{3}h & 0 & \sqrt{3}h & 0 \end{pmatrix}. \tag{8.33}$$

In order to find the components of the density matrix and hence the probability, we must solve the eight differential equations given by

$$\boldsymbol{D} = H^{SU(3)}_{HighE}.\mathbf{R} \tag{8.34}$$

where the components of the vectors $\mathbf{D}$ and $\mathbf{R}$ are given by

$$D_i = \frac{d\rho i}{dt}; \qquad R_i = \rho_i(t). \tag{8.35}$$

Using the initial conditions in equations (4.24) and (4.26), and averaging out the sine and cosine terms, we find the probability that a neutrino of flavour a oscillates into one of flavour b is

$$\begin{aligned} P[\nu_a \to \nu_b] \quad = \quad & \frac{1}{9}[3 + U_{a1}U_{a2}(14U_{b1}U_{b2} + 2U_{b1}U_{b3} + 2U_{b2}U_{b3} - 2U^2_{b1} - 2U^2_{b2} + 4U^2_{b3}) \\ & + U_{a1}U_{a3}(2U_{b1}U_{b2} + 14U_{b1}U_{b3} + 2U_{b2}U_{b3} - 2U^2_{b1} + 4U^2_{b2} - 2U^2_{b3}) \\ & + U_{a1}U_{a2}(2U_{b1}U_{b2} + 2U_{b1}U_{b3} + 14U_{b2}U_{b3} + 4U^2_{b1} - 2U^2_{b2} - 2U^2_{b3}) \\ & + U^2_{a1}(-2U_{b1}U_{b2} - 2U_{b1}U_{b3} + 4U_{b2}U_{b3} + 2U^2_{b1} - U^2_{b2} - U^2_{b3}) \\ & + U^2_{a2}(-2U_{b1}U_{b2} + 4U_{b1}U_{b3} - 2U_{b2}U_{b3} - U^2_{b1} + 2U^2_{b2} - U^2_{b3}) \\ & + U^2_{a3}(4U_{b1}U_{b2} - 2U_{b1}U_{b3} - 2U_{b2}U_{b3} - U^2_{b1} - U^2_{b2} + 2U^2_{b3})], \end{aligned} \tag{8.36}$$

where U_{ij} are the components of the standard mixing matrix (1.6). Using the up to date mixing angles from table 1.2, the high energy limit of the neutrino oscillation probabilities are

$$\begin{aligned} P[\nu_e \to \nu_e] \quad &= \quad 0.697, \\ P[\nu_e \to \nu_\mu] \quad &= \quad 0.273, \\ P[\nu_e \to \nu_\tau] \quad &= \quad 0.030, \\ P[\nu_\mu \to \nu_\mu] \quad &= \quad 0.721, \\ P[\nu_\mu \to \nu_\tau] \quad &= \quad 0.006, \\ P[\nu_\tau \to \nu_\tau] \quad &= \quad 0.964. \end{aligned} \tag{8.37}$$

The flavour ratios in the high energy limit are

$$\begin{aligned} R_e &= 0.273 + 0.424\varepsilon, \\ R_\mu &= 0.721 - 0.448\varepsilon, \\ R_\tau &= 0.006 + 0.024\varepsilon, \end{aligned} \tag{8.38}$$

where, as previously, ε denotes the flavour composition at the source. Thus, at very high energies, we would expect a large suppression of tau neutrinos.

Intermediate flavour ratios

We have found how the LV effects manifest themselves at threshold and at very high energies. However, comparing the flavour ratios of (8.31) with (8.38) we see that, for example, the electron neutrino component is initially reduced by the LV effects whereas at high energies it has increased above the standard values. In order to examine the behaviour of the neutrino flux between the threshold energy and the high energy limit, we turn to numerical calculations. If the LV effects originate in the mass basis, then assuming the LV parameters are all equal, the Hamiltonian takes the form in (8.24). Transforming to the flavour basis, using the most recent values for the mass differences and mixing angles from table 1.2 and replacing c and $\hbar$, the Hamiltonian takes the form

$$H_{num} = H_{stand} + H_{LV}. \tag{8.39}$$

where the standard neutrino oscillation part is

$$H_{stand} = \frac{1}{E}\begin{pmatrix} 7.29\times10^{-5} & 4.94\times10^{-4} & 4.30\times10^{-4} \\ 4.94\times10^{-4} & 1.36\times10^{-3} & 1.40\times10^{-3} \\ 4.30\times10^{-4} & 1.40\times10^{-3} & 1.38\times10^{-3} \end{pmatrix}, \tag{8.40}$$

and the Hamiltonian containing the LV parameters is

$$H_{LV} = hE^n \times 10^{9(n+1)} \begin{pmatrix} 0.183 & 0.141 & 0.047 \\ 0.141 & 0.063 & 0.021 \\ 0.047 & 0.021 & 0.120 \end{pmatrix}. \tag{8.41}$$

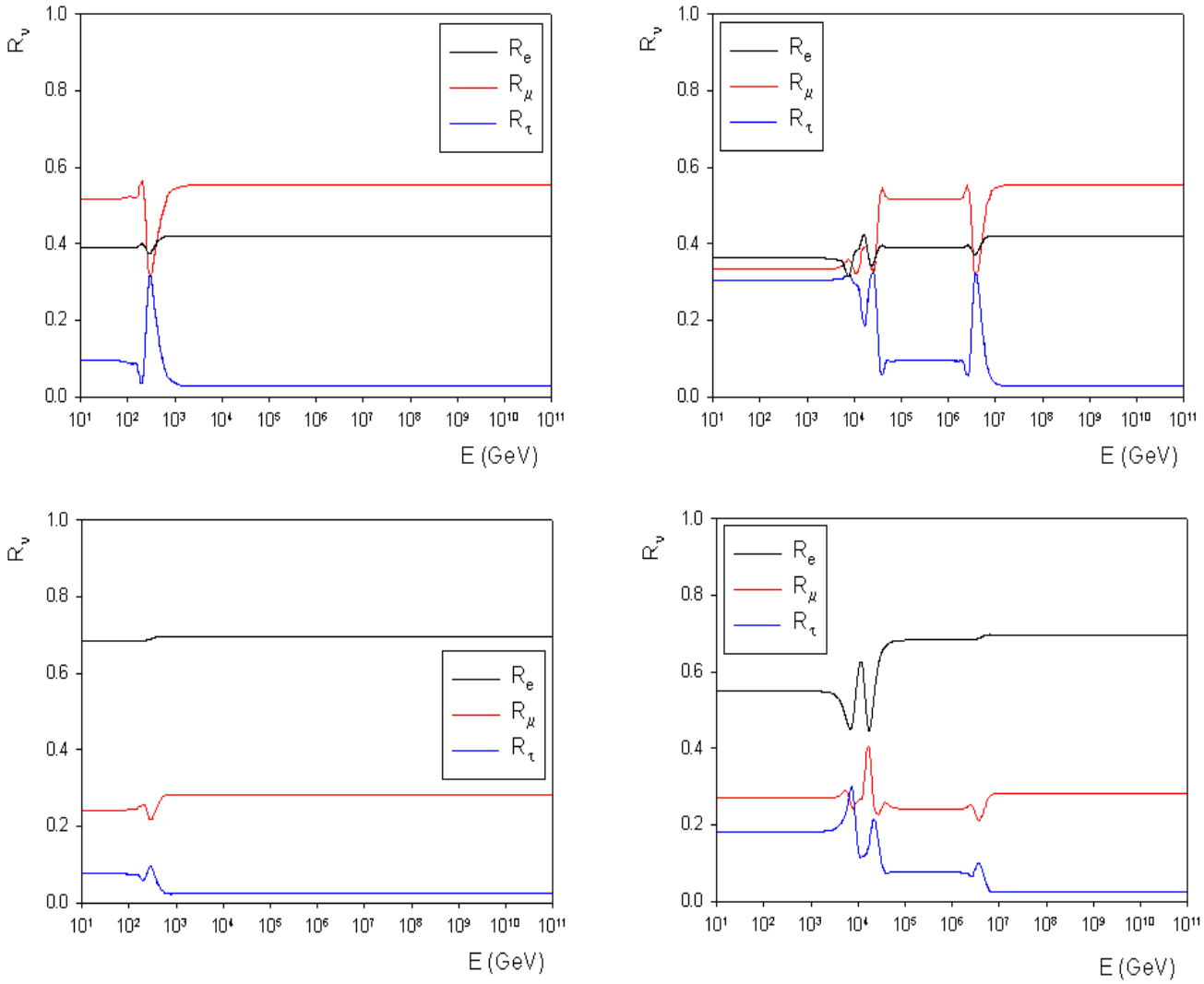

Figure 8.4: The estimated effects on the ratio of flavours observed after propagation when the LV effects originate in the mass basis. The top frames correspond to neutrinos produced by pion decay at the source whilst the lower plots correspond to (anti)-neutrinos produced from the decay of neutrons. The left and right plots correspond to models in which the LV parameters are proportional to E^2 and E^3 respectively.

Assuming a particular model of Lorentz invariance by picking a value for n and a value for the parameter h, we reduce H_{num} to a function of the neutrino energy only. If we loop over values of the energy, then for each case we may find the eigenvectors of H_{num} and hence the probability. In this way, we are able to numerically find the flavour ratios of astrophysical neutrinos at an Earth based detector including LV effects. Figure 8.4 shows these flavour ratios for $n = 2,\ 3$ where we have assumed the parameter h takes the value E_p^{n-1}. These numerical calculations show that the transition from standard neutrino oscillation phenomenology to the phenomenology of large LV effects takes place very suddenly. If modifications to the neutrino flavour ratios were observed which were similar to figure 8.4, then we would be able to place a bound on the LV parameter by measuring the threshold energy at which the transition between standard and LV phenomenology took place.

8.3.4 LV parameters in the flavour basis

In an analogous way to the approach taken above, we may also consider the situation when the Hamiltonian takes the form in equation (8.24) in the flavour basis rather than the mass basis. In this case, the situation is much more complicated as we first transform from the flavour basis to the mass basis and then apply the perturbation methodology we used in the previous section. However, we find that the expressions for the oscillation probabilities and flavour ratios are identical to those when the LV effects manifest themselves in the mass basis. That is, the oscillation probabilities are given by (8.30) with the flavour ratios being given in (8.31). In this case, however, the high energy limits do differ from the first case and are given by

$$\begin{aligned} P[\nu_e \to \nu_e] &= 0.556, \\ P[\nu_e \to \nu_\mu] &= 0.222, \\ P[\nu_e \to \nu_\tau] &= 0.222, \\ P[\nu_\mu \to \nu_\mu] &= 0.389, \\ P[\nu_\mu \to \nu_\tau] &= 0.389, \\ P[\nu_\tau \to \nu_\tau] &= 0.389, \end{aligned} \tag{8.42}$$

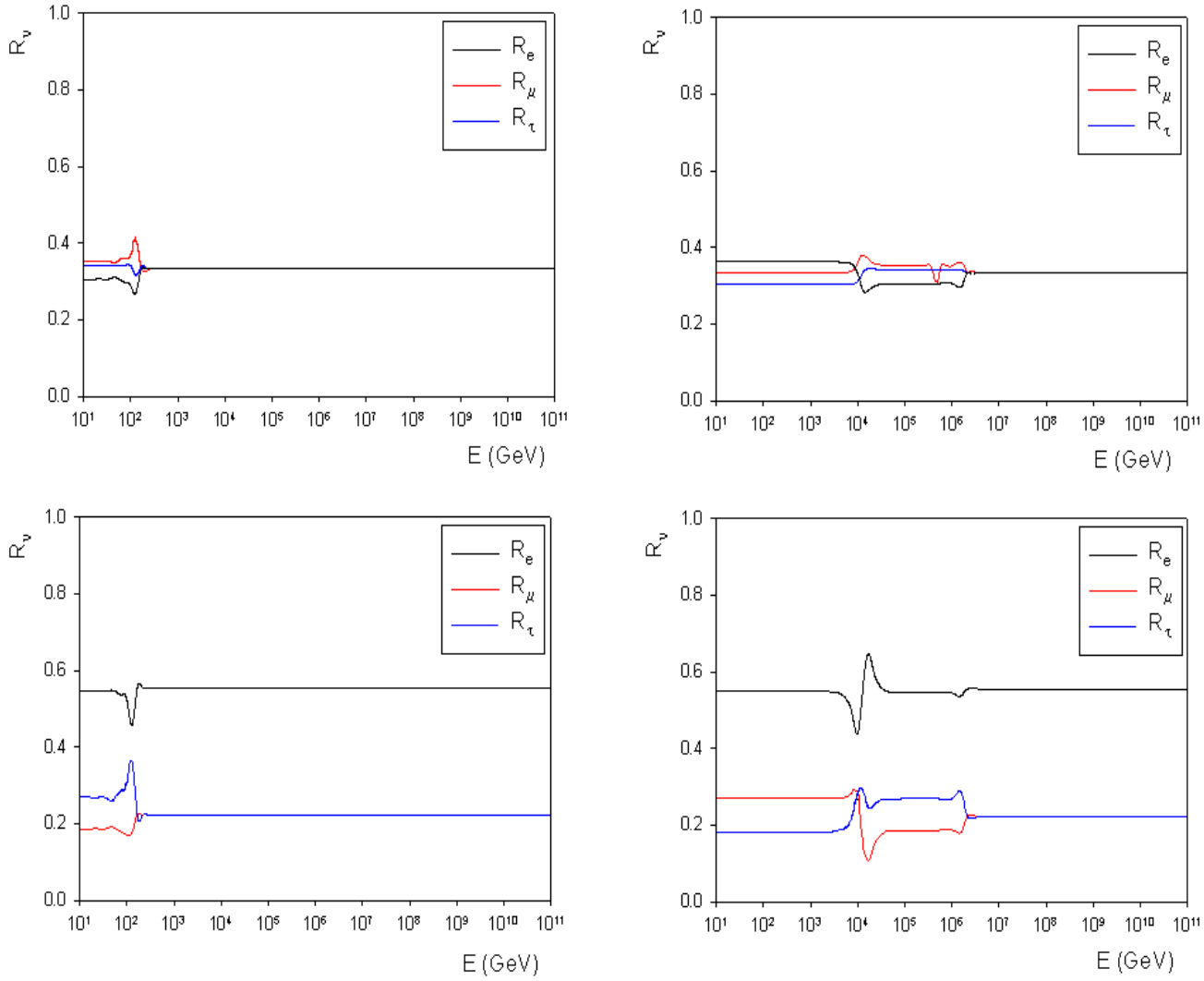

Figure 8.5: The estimated effects on the ratio of flavours observed after propagation when the LV effects originate in the flavour basis. The top frames correspond to neutrinos produced by pion decay at the source whilst the lower plots correspond to (anti)-neutrinos produced from the decay of neutrons. The left and right plots correspond to models in which the LV parameters are proportional to E^2 and E^3 respectively.

leading to flavour ratios in the high energy limit of the form

$$\begin{aligned} R_e &= 0.222 + 0.333\varepsilon, \\ R_\mu &= 0.389 - 0.167\varepsilon, \\ R_\tau &= 0.389 + 0.167\varepsilon. \end{aligned} \tag{8.43}$$

Figure 8.5 shows the results of numerical simulations of the flavour ratios for this model. It is interesting to note that the curves have approximately the same form as those presented in figure 8.4 with the exception of the high energy limiting behaviour. Whilst the model in which the LV effects manifest themselves in the mass basis is easily distinguishable from the standard case via the suppression of tau neutrinos, in this model, this is not the case and as such it is extremely difficult to observe the new physics.

8.4 Summary

In this chapter, we showed how neutrinos which originate in astrophysical objects may be utilized to examine both quantum decoherence and the violation of Lorentz invariance.

- We began by showing how we may calculate the flavour ratios expected at the detector when we take into account standard oscillations. We considered two particular cases; neutrinos which originate from pion decay and neutrinos which are created from the decay of neutrons (section 8.1).

- We then considered how the addition of quantum decoherence to standard oscillations would alter the expected flavour ratios. We found that neutrinos from pion decay cannot be used as probes of quantum decoherence as it is almost impossible to distinguish between quantum decoherence induced oscillations and standard oscillations. However, we found that by considering neutrinos from neutron decay, the two scenarios were distinguishable and we were able to place order of magnitude estimates onto the upper bounds we place on the quantum decoherence parameters. By considering a source of TeV (anti)-electron neutrinos at a distance of 10 kiloparsecs from the Earth, we found upper bounds of

- $\delta < 10^{-37}\ GeV$ for the model with no dependence on the neutrino energy;
- $\delta < 10^{-34}\ GeV^2$ for the model inversely proportional to the neutrino energy;
- $\delta < 10^{-43}\ GeV^{-1}$ for the model proportional to the neutrino energy squared (section 8.2).

- Finally, we considered how astrophysical neutrinos may be used to probe violations of Lorentz invariance. We found that the situation was difficult to model and approached it in three different ways. We considered LV effects at threshold and also the effect LV has on neutrino flavour ratios in the high energy limit. We also utilized numerical methods to extrapolate between these two regions (section 8.3).

Overall, it seems that astrophysical neutrinos will be able to probe for new physics to very high precision. This high precision is a result of the long path lengths the neutrinos have to travel and also the very high energies they have.

Conclusions

The search for a theory which describes gravity at quantum scales goes on. The traditional way to tackle this problem is to take a theoretical approach and many advances have been made in the last twenty years. Until recently, however, taking an experimental approach to quantum gravity was not considered as any effects were believed to be too small to be observed. This view point has changed.

In this thesis we have considered how two possible quantum gravity effects, quantum decoherence and the violation of Lorentz invariance, would alter the oscillation probability for neutrinos. We specifically consider those high energy neutrinos created within the Earth's atmosphere and in astrophysical objects, such as active galactic nuclei, which would be observed by neutrino telescopes such as ANTARES and IceCUBE.

In chapter 4, we saw how quantum decoherence could be a result of neutrinos interacting with a quantum gravitational environment and saw how this affected the system of atmospheric neutrinos. We used these results in chapter 5 to simulate the regions of parameter space the ANTARES neutrino telescope would be able to probe and also to place upper bounds on the quantum decoherence model parameters. We followed the same methodology in chapters 6 and 7 when we considered quantum gravity induced violations of Lorentz invariance. In both these cases, we saw that high energy neutrinos, observed by neutrino telescopes, would be able to place stringent bounds on the size of these novel effects.

In chapter 8, we extended our analysis to include all three flavours of neutrinos as we considered those neutrinos which originate in cosmic accelerators. We found that, because of the very high energies these neutrinos may have and because they travel vast distances, neutrino telescopes, such as IceCUBE, will, in the case of quantum decoherence, surpass existing bounds on model parameters by as much as 33 orders of magnitude. In the case of Lorentz invariance violation, we found the analysis was very involved and, therefore, could not place any bounds on the size of these

effects. We were, however, able to show how these effects would alter the number of neutrinos we would expect to see, providing us with the prospect of observing these effects, if they exist.

Overall, we found that neutrino telescopes have great potential to observe, or rule out, these effects and so, upon their completion, we will enter a very exciting time in quantum gravity phenomenology.

Bibliography

[1] http://amanda.uci.edu/.

[2] http://antares.in2p3.fr.

[3] http://astrosun2.astro.cornell.edu/academics/courses/astro201/equivalence_princ.htm.

[4] http://hep.bu.edu/ superk/atmnu/.

[5] http://icecube.wisc.edu/.

[6] http://lhc.web.cern.ch/lhc/.

[7] http://universe-review.ca/r01-07-quantumfoam.htm.

[8] http://www.astro.phys.s.chiba-u.ac.jp/ca2005.

[9] http://www.clf.rl.ac.uk/facilities/astraweb/astrageminihome.htm.

[10] http://www.cv.nrao.edu/ abridle/images.htm.

[11] http://www.hep.lu.se.

[12] http://www.ligo.caltech.edu/advligo/.

[13] http://www.mpi-hd.mpg.de/hfm/ct/ct.html.

[14] http://www.shef.ac.uk/physics/research/ pppa/research/acorne.htm.

[15] J. N. Abdurashitov *et al.*, SAGE, Measurement of the solar neutrino capture rate with gallium metal, Phys. Rev. **C60**, 055801 (1999), astro-ph/9907113.

[16] F. Acernese *et al.*, VIRGO, VIRGO status and commissioning results, Class. Quant. Grav. **22**, S185 (2005).

[17] R. Adler *et al.*, CPLEAR, Test of CPT symmetry and quantum mechanics with experimental data from CPLEAR, Phys. Lett. **B364**, 239 (1995), hep-ex/9511001.

[18] S. L. Adler, Comment on a proposed Super-Kamiokande test for quantum gravity induced decoherence effects, Phys. Rev. **D62**, 117901 (2000), hep-ph/0005220.

[19] G. Aggouras *et al.*, NESTOR, A measurement of the cosmic-ray muon flux with a module of the NESTOR neutrino telescope, Astropart. Phys. **23**, 377 (2005).

[20] A. Aguilar *et al.*, LSND, Evidence for neutrino oscillations from the observation of anti-ν_e appearance in a anti-ν_μ beam, Phys. Rev. **D64**, 112007 (2001), hep-ex/0104049.

[21] F. Aharonian *et al.*, The temporal characteristics of the TeV -emission from Mkn 501 in 1997, II. Results from HEGRA CT1 and CT2, Astron. Astrophys. **349**, 29 (1999), astro-ph/9903386.

[22] Q. R. Ahmad *et al.*, SNO, Direct evidence for neutrino flavor transformation from neutral-current interactions in the Sudbury Neutrino Observatory, Phys. Rev. Lett. **89**, 011301 (2002), nucl-ex/0204008.

[23] S. N. Ahmed *et al.*, SNO, Measurement of the total active B-8 solar neutrino flux at the Sudbury Neutrino Observatory with enhanced neutral current sensitivity, Phys. Rev. Lett. **92**, 181301 (2004), nucl-ex/0309004.

[24] S. H. Ahn *et al.*, K2K, Detection of accelerator produced neutrinos at a distance of 250-km, Phys. Lett. **B511**, 178 (2001), hep-ex/0103001.

[25] J. Ahrens *et al.*, ICECUBE, IceCube: The next generation neutrino telescope at the South Pole, Nucl. Phys. Proc. Suppl. **118**, 388 (2003), astro-ph/0209556.

[26] I. J. R. Aitchison, Supersymmetry and the mssm: An elementary introduction, (2005), hep-ph/0505105.

[27] E. N. Alekseev, L. N. Alekseeva, I. V. Krivosheina, and V. I. Volchenko, Detection of the neutrino signal from SN1987a in the LMC using the INR Baksan underground scintillation telescope, Phys. Lett. **B205**, 209 (1988).

[28] J. Alfaro, H. A. Morales-Tecotl, and L. F. Urrutia, Quantum gravity corrections to neutrino propagation, Phys. Rev. Lett. **84**, 2318 (2000), gr-qc/9909079.

[29] J. Alfaro, H. A. Morales-Tecotl, and L. F. Urrutia, Loop quantum gravity and light propagation, Phys. Rev. **D65**, 103509 (2002), hep-th/0108061.

[30] J. Alfaro, H. A. Morales-Tecotl, and L. F. Urrutia, Quantum gravity and spin-1/2 particles effective dynamics, Phys. Rev. **D66**, 124006 (2002), hep-th/0208192.

[31] E. Aliu *et al.*, K2K, Evidence for muon neutrino oscillation in an accelerator-based experiment, Phys. Rev. Lett. **94**, 081802 (2005), hep-ex/0411038.

[32] W. W. M. Allison *et al.*, SOUDAN-2, The Soudan 2 detector: The design and construction of the tracking calorimeter modules, Nucl. Instrum. Meth. **A376**, 36 (1996).

[33] W. W. M. Allison *et al.*, SOUDAN-2, Measurement of the atmospheric neutrino flavour composition in Soudan-2, Phys. Lett. **B391**, 491 (1997), hep-ex/9611007.

[34] G. Amelino-Camelia, C. Lammerzahl, A. Macias, and H. Muller, The search for quantum gravity signals, AIP Conf. Proc. **758**, 30 (2005), gr-qc/0501053.

[35] G. Amelino-Camelia, On the fate of Lorentz symmetry in loop quantum gravity and noncommutative spacetimes, (2002), gr-qc/0205125.

[36] G. Amelino-Camelia, Quantum-gravity phenomenology: Status and prospects, Mod. Phys. Lett. **A17**, 899 (2002), gr-qc/0204051.

[37] G. Amelino-Camelia, Relativity in space-times with short-distance structure governed by an observer-independent (Planckian) length scale, Int. J. Mod. Phys. **D11**, 35 (2002), gr-qc/0012051.

[38] G. Amelino-Camelia, The three perspectives on the quantum-gravity problem and their implications for the fate of Lorentz symmetry, (2003), gr-qc/0309054.

[39] G. Amelino-Camelia, A perspective on quantum gravity phenomenology, (2004), gr-qc/0402009.

[40] G. Amelino-Camelia and T. Piran, Cosmic rays and TeV photons as probes of quantum properties of space-time, Phys. Lett. **B497**, 265 (2001), hep-ph/0006210.

[41] L. A. Anchordoqui, H. Goldberg, F. Halzen, and T. J. Weiler, Galactic point sources of TeV antineutrinos, Phys. Lett. **B593**, 42 (2004), astro-ph/0311002.

[42] M. Ando, TAMA, Current status of TAMA, Class. Quant. Grav. **19**, 1409 (2002).

[43] E. Andres *et al.*, Observation of high-energy neutrinos using Cherenkov detectors embedded deep in Antarctic ice, Nature **410**, 441 (2001).

[44] E. Andres *et al.*, AMANDA, Results from the AMANDA high energy neutrino detector, Nucl. Phys. Proc. Suppl. **91**, 423 (2001), astro-ph/0009242.

[45] A. Angelopoulos *et al.*, CPLEAR, Physics at CPLEAR, Phys. Rept. **374**, 165 (2003).

[46] K. Aoki, E. D'Hoker, and D. H. Phong, Unitarity of closed superstring perturbation theory, Nucl. Phys. **B342**, 149 (1990).

[47] M. Apollonio *et al.*, CHOOZ, Initial results from the CHOOZ long baseline reactor neutrino oscillation experiment, Phys. Lett. **B420**, 397 (1998), hep-ex/9711002.

[48] T. Araki *et al.*, KamLAND, Measurement of neutrino oscillation with KamLAND: Evidence of spectral distortion, Phys. Rev. Lett. **94**, 081801 (2005), hep-ex/0406035.

[49] Y. Ashie *et al.*, Super-Kamiokande, Evidence for an oscillatory signature in atmospheric neutrino oscillation, Phys. Rev. Lett. **93**, 101801 (2004), hep-ex/0404034.

[50] A. Ashtekar, J. C. Baez, and K. Krasnov, Quantum geometry of isolated horizons and black hole entropy, Adv. Theor. Math. Phys. **4**, 1 (2000), gr-qc/0005126.

[51] A. Ashtekar, Quantum geometry and gravity: Recent advances, gr-qc/0112038, In proceedings of General relativity and gravitation, edited by N. Bishop and S. Maharaj (World Scientific, 2002).

[52] A. Ashtekar, Gravity and the quantum, New J. Phys. **7**, 198 (2005), gr-qc/0410054.

[53] C. Athanassopoulos *et al.*, LSND, The Liquid Scintillator Neutrino Detector and LAMPF Neutrino Source, Nucl. Instrum. Meth. **A388**, 149 (1997), nucl-ex/9605002.

[54] A. Atoyan and C. D. Dermer, High-energy neutrinos from photomeson processes in blazars, Phys. Rev. Lett. **87**, 221102 (2001), astro-ph/0108053.

[55] J. C. Baez, I. E. Segal, and Z. Zhou, Introduction to algebraic and constructive quantum field theory, (Princeton Uniersity Press, 1992).

[56] J. C. Baez, Spin network states in gauge theory, Adv. Math. **117**, 253 (1996), gr-qc/9411007.

[57] J. C. Baez, Spin foam models, Class. Quant. Grav. **15**, 1827 (1998), gr-qc/9709052.

[58] J. N. Bahcall, M. H. Pinsonneault, and S. Basu, Solar models: Current epoch and time dependences, neutrinos, and helioseismological properties, Astrophys. J. **555**, 990 (2001), astro-ph/0010346.

[59] C. Barbot, M. Drees, F. Halzen, and D. Hooper, Neutrinos associated with cosmic rays of top-down origin, Phys. Lett. **B555**, 22 (2003), hep-ph/0205230.

[60] G. Barenboim and N. E. Mavromatos, CPT violating decoherence and LSND: A possible window to Planck scale physics, JHEP **01**, 034 (2005), hep-ph/0404014.

[61] M. Barreira, M. Carfora, and C. Rovelli, Physics with nonperturbative quantum gravity: Radiation from a quantum black hole, Gen. Rel. Grav. **28**, 1293 (1996), gr-qc/9603064.

[62] R. Becker-Szendy *et al.*, The electron-neutrino and muon-neutrino content of the atmospheric flux, Phys. Rev. **D46**, 3720 (1992).

[63] J. A. Bellido, R. W. Clay, B. R. Dawson, and M. Johnston-Hollitt, Southern hemisphere observations of a 10^{18} eV cosmic ray source near the direction of the galactic centre, Astropart. Phys. **15**, 167 (2001), astro-ph/0009039.

[64] I. A. Belolaptikov *et al.*, BAIKAL, The BAIKAL underwater neutrino telescope: Design, performance, and first results, Astropart. Phys. **7**, 263 (1997).

[65] F. Benatti and R. Floreanini, Experimental limits on complete positivity from the K anti-K system, Phys. Lett. **B401**, 337 (1997), hep-ph/9704283.

[66] F. Benatti and R. Floreanini, Complete positivity and neutron interferometry, Phys. Lett. **B451**, 422 (1999), quant-ph/9902026.

[67] F. Benatti and R. Floreanini, Open system approach to neutrino oscillations, JHEP **02**, 032 (2000), hep-ph/0002221.

[68] C. L. Bennett *et al.*, First year Wilkinson Microwave Anisotropy Probe (WMAP) observations: preliminary maps and basic results, Astrophys. J. Suppl. **148**, 1 (2003), astro-ph/0302207.

[69] P. Bhattacharjee, C. T. Hill, and D. N. Schramm, Grand unified theories, topological defects and ultrahigh- energy cosmic rays, Phys. Rev. Lett. **69**, 567 (1992).

[70] D. J. Bird *et al.*, HIRES, Study of broad scale anisotropy of cosmic ray arrival directions from 2×10^{17} eV to 10^{20} eV from Fly's Eye data, Astrophys. J. **511**, 739 (1998), astro-ph/0104452.

[71] G. Blewitt *et al.*, Experimental limits on the nucleon lifetime for two and three-body decay modes, Phys. Rev. Lett. **54**, 22 (1985).

[72] J. Blumer, AUGER, Cosmic rays at the highest energies and the Pierre Auger Observatory, J. Phys. **G29**, 867 (2003).

[73] P. C. Bosetti, DUMAND, Dumand status report, Nucl. Phys. Proc. Suppl. **48**, 466 (1996).

[74] M. C. Bouwhuis, Ph.d. thesis: Detection of neutrinos from gamma-ray bursts.

[75] P. Brax and C. van de Bruck, Cosmology and brane worlds: A review, Class. Quant. Grav. **20**, R201 (2003), hep-th/0303095.

[76] J. C. Breckenridge *et al.*, Macroscopic and microscopic entropy of near-extremal spinning black holes, Phys. Lett. **B381**, 423 (1996), hep-th/9603078.

[77] L. M. Brown, Renormalization: From Lorentz to Landau (and beyond), (Springer, 1993).

[78] L. M. Brown, The idea of the neutrino, Physics Today **31**, 23 (1978).

[79] J. Brunner, Effect of 3-flavor neutrino oscillations on cosmic neutrino fluxes, ANTARES internal note:ANTARES-Phys/2000-9.

[80] J. Brunner, Measurement of neutrino oscillations with neutrino telescope, In proceedings of 15th International Conference on Particles and Nuclei (PANIC 99). Edited by G. Faldt, B. Hoistad, S. Kullander (Nucl. Phys. Vol **A663/A664**, 2000).

[81] J. Brunner, Measurement of oscillation parameters using χ^2 differences, ANTARES internal note:ANTARES-Soft/2001-010.

[82] J. Brunner, A minimum bias oscillation analysis, ANTARES internal note:ANTARES-Phys/2001-004.

[83] E. V. Bugaev and K. V. Konishchev, Extragalactic neutrino background from pbhs evaporation, (2001), astro-ph/0103265.

[84] J. Busenitz, KamLAND, The KamLAND experiment: Introduction and first results, AIP Conf. Proc. **672**, 154 (2003).

[85] J. C. L. Cowan *et al.*, Detection of the free neutrino: A confirmation, Science **124**, 103 (1956).

[86] K. S. Capelle, J. W. Cronin, G. Parente, and E. Zas, On the detection of ultra high energy neutrinos with the Auger Observatory, Astropart. Phys. **8**, 321 (1998), astro-ph/9801313.

[87] B. J. Carr and M. J. Rees, The anthropic principle and the structure of the physical world, Nature **278**, 605 (1979).

[88] C.-H. Chang *et al.*, Possible effects of quantum mechanics violation induced by certain quantum gravity on neutrino oscillations, Phys. Rev. **D60**, 033006 (1999), hep-ph/9809371.

[89] J. Christian, Testing quantum gravity via cosmogenic neutrino oscillations, Phys. Rev. **D71**, 024012 (2005), gr-qc/0409077.

[90] B. T. Cleveland *et al.*, Measurement of the solar electron neutrino flux with the Homestake chlorine detector, Astrophys. J. **496**, 505 (1998).

[91] D. Colladay and V. A. Kostelecky, CPT violation and the standard model, Phys. Rev. **D55**, 6760 (1997), hep-ph/9703464.

[92] D. Colladay and V. A. Kostelecky, Lorentz-violating extension of the standard model, Phys. Rev. **D58**, 116002 (1998), hep-ph/9809521.

[93] J. C. Collins, Renormalization. An introduction to renormalization, the renormalization group, and the operator product expansion, (Cambridge University Press, 1984).

[94] F. Combley and E. Picasso, The muon (g-2) precession experiments: past, present and future, Phys. Rept. **14**, 1 (1974).

[95] F. H. Combley, (g-2) factors for muon and electron and the consequences for QED, Rept. Prog. Phys. **42**, 1889 (1979).

[96] A. Connes, Noncommutative geometry. In proceedings of nonperturbative quantum field theory, Cargese (1987).

[97] J. W. Cronin, S. P. Swordy, and T. K. Gaisser, Cosmic rays at the energy frontier, Sci. Am. **276**, 32 (1997).

[98] M. Czachor, Nambu-type generalization of the Dirac equation, Phys. Lett **A225**, 1 (1997), quant-ph/9601015.

[99] G. Danby *et al.*, Observation of high-energy neutrino reactions and the existence of two kinds of neutrinos, Phys. Rev. Lett. **9**, 36 (1962).

[100] C. D. Dermer and A. Atoyan, High-energy neutrino production through photopion processes in blazars, (2001), astro-ph/0107200, In proceedings of 27th international cosmic ray conference (ICRC), Germany.

[101] C. D. Dermer and A. Atoyan, High-energy neutrinos from gamma ray bursts, Phys. Rev. Lett. **91**, 071102 (2003), astro-ph/0301030.

[102] A. Dhar, Noncritical string theory, Current Science **81**, 1598 (2001).

[103] E. D'Hoker, Equivalence of Liouville theory and 2-D quantum gravity, Mod. Phys. Lett. **A6**, 745 (1991).

[104] E. D'Hoker and P. S. Kurzepa, 2-D quantum gravity and Liouville theory, Mod. Phys. Lett. **A5**, 1411 (1990).

[105] E. D'Hoker and D. H. Phong, Two-loop superstrings. i: Main formulas, Phys. Lett. **B529**, 241 (2002), hep-th/0110247.

[106] C. Distefano, D. Guetta, E. Waxman, and A. Levinson, Neutrino flux predictions for known galactic microquasars, Astrophys. J. **575**, 378 (2002), astro-ph/0202200.

[107] J. Distler and H. Kawai, Conformal field theory and 2-d quantum gravity or who's afraid of Joseph Liouville?, Nucl. Phys. **B321**, 509 (1989).

[108] F. Dowker, Causal sets and the deep structure of spacetime, (2005), gr-qc/0508109, In 100 years of relativity space-time structure: Einstein and beyond. Edited by A. Ashtekar.

[109] G. Duffy, C. Harris, P. Kanti, and E. Winstanley, Brane decay of a (4+n)-dimensional rotating black hole: Spin-0 particles, JHEP **09**, 049 (2005), hep-th/0507274.

[110] F. W. Dyson, A. S. Eddington, and C. Davidson, A determination of the deflection of light by the sun's gravitational field, from observations made at the total eclipse of may 29, 1919, Phil. Trans. Roy. Soc. Lond. **A220**, 291 (1920).

[111] K. Eguchi *et al.*, KamLAND, First results from KamLAND: Evidence for reactor anti- neutrino disappearance, Phys. Rev. Lett. **90**, 021802 (2003), hep-ex/0212021.

[112] S. Eidelman *et al.*, Particle Data Group, Review of particle physics, Phys. Lett. **B592**, 1 (2004), (Partially updated July 2005).

[113] A. Einstein, On a heuristic viewpoint concerning the production and transformation of light, Ann. Phys. **17**, 132 (1905).

[114] A. Einstein, On the electrodynamics of moving bodies, Ann. Phys. **17**, 891 (1905).

[115] A. Einstein, On the motion of small particles suspended in liquids at rest required by the molecular-kinetic theory of heat, Ann. Phys. **17**, 549 (1905).

[116] A. Einstein, On the influence of gravitation on the propagation of light, Ann. Phys. **35**, 898 (1911).

[117] A. Einstein, Explanation of the perihelion motion of mercury from the general theory of relativity, Sitzungsber. Preuss. Akad. Wiss. Berlin (Math. Phys.) **1915**, 831 (1915).

[118] A. Einstein, The foundation of the general theory of relativity, Ann. Phys. **49**, 769 (1916).

[119] A. Einstein and N. Rosen, On gravitational waves, J. Franklin. Inst. **223**, 43 (1937).

[120] J. R. Ellis, J. S. Hagelin, D. V. Nanopoulos, and M. Srednicki, Search for violations of quantum mechanics, Nucl. Phys. **B241**, 381 (1984).

[121] J. R. Ellis, N. E. Mavromatos, and D. V. Nanopoulos, Testing quantum mechanics in the neutral Kaon system, Phys. Lett. **B293**, 142 (1992), hep-ph/9207268.

[122] J. R. Ellis, N. E. Mavromatos, and D. V. Nanopoulos, Quantum decoherence in a D-foam background, Mod. Phys. Lett. **A12**, 1759 (1997), hep-th/9704169.

[123] J. R. Ellis, N. E. Mavromatos, and D. V. Nanopoulos, A microscopic Liouville arrow of time, (1998), hep-th/9805120.

[124] J. R. Ellis, N. E. Mavromatos, D. V. Nanopoulos, and E. Winstanley, Quantum decoherence in a four-dimensional black hole background, Mod. Phys. Lett. **A12**, 243 (1997), gr-qc/9602011.

[125] L. R. Evans, Status of the Large Hadron Collider (LHC), Eur. Phys. J. **C34**, s11 (2004).

[126] R. P. Feynman and Hibbs, Quantum mechanics and path integrals, (McGraw-Hill, 1965).

[127] G. L. Fogli, E. Lisi, A. Marrone, and D. Montanino, Status of atmospheric $\nu_\mu \to \nu_\tau$ oscillations and decoherence after the first K2K spectral data, Phys. Rev. **D67**, 093006 (2003), hep-ph/0303064.

[128] G. W. Ford and R. F. O'Connell, Is there Unruh radiation?. (2005), quant-ph/0509151.

[129] L. Freidel, J. Kowalski-Glikman, and L. Smolin, 2+1 gravity and doubly special relativity, Phys. Rev. **D69**, 044001 (2004), hep-th/0307085.

[130] Y. Fukuda *et al.*, Super-Kamiokande, Evidence for oscillation of atmospheric neutrinos, Phys. Rev. Lett. **81**, 1562 (1998), hep-ex/9807003.

[131] Y. Fukuda *et al.*, Super-Kamiokande, Measurement of a small atmospheric ν_μ ν_e ratio, Phys. Lett. **B433**, 9 (1998), hep-ex/9803006.

[132] A. M. Gago, E. M. Santos, W. J. C. Teves, and R. Zukanovich Funchal, A study on quantum decoherence phenomena with three generations of neutrinos, (2002), hep-ph/0208166.

[133] T. K. Gaisser, T. Stanev, M. Honda, and P. Lipari, Primary spectrum to 1-TeV and beyond. In proceedings of 27th international cosmic ray conference (ICRC), Germany.

[134] R. Gambini, R. A. Porto, and J. Pullin, Decoherence from discrete quantum gravity, Class. Quant. Grav. **21**, L51 (2004), gr-qc/0305098.

[135] R. Gambini and J. Pullin, Nonstandard optics from quantum spacetime, Phys. Rev. **D59**, 124021 (1999), gr-qc/9809038.

[136] E. Gava, B. Greene, J. Louis, K. S. Narain, and S. Randjbar-Daemi (editors), String theory, gauge theory and quantum gravity. Proceedings of conference on Duality Symmetries in String Theory, Italy, 1997.

[137] G. Giacomelli and R. Giacomelli, The LEP legacy. (2005), hep-ex/0503050. In proceedings of 7th school of non-accelerator astroparticle physics. Edited by R. A. Carrigan, G. Giacomelli and N. Paver (World Scientific, 2005).

[138] A. Goldschmidt, ICECUBE, Scientific goals of the IceCube neutrino detector at the South Pole, Nucl. Phys. Proc. Suppl. **110**, 516 (2002).

[139] P. Gondolo, G. Gelmini, and S. Sarkar, Cosmic neutrinos from unstable relic particles, Nucl. Phys. **B392**, 111 (1993), hep-ph/9209236.

[140] M. C. Gonzalez-Garcia and C. Pena-Garay, Three-neutrino mixing after the first results from K2K and KamLAND, Phys. Rev. **D68**, 093003 (2003), hep-ph/0306001.

[141] V. Gorini, A. Kossakowski, and E. C. G. Sudarshan, Completely positive dynamical semigroups of N level systems, J. Math. Phys. **17**, 821 (1976).

[142] S. Goswami, A. Bandyopadhyay, and S. Choubey, Global analysis of neutrino oscillation, Nucl. Phys. Proc. Suppl. **143**, 121 (2005), hep-ph/0409224.

[143] O. W. Greenberg, CPT violation implies violation of Lorentz invariance, Phys. Rev. Lett. **89**, 231602 (2002), hep-ph/0201258.

[144] K. Greisen, End to the cosmic ray spectrum?, Phys. Rev. Lett. **16**, 748 (1966).

[145] D. Guetta, D. Hooper, J. Alvarez-Muniz, F. Halzen, and E. Reuveni, Neutrinos from individual gamma-ray bursts in the BATSE catalogue, Astropart. Phys. **20**, 429 (2004), astro-ph/0302524.

[146] F. Halzen and A. D. Martin, Quarks and leptons: an introductory course in modern particle physics, (Wiley, 1984).

[147] F. Halzen and D. Hooper, High-energy neutrino astronomy: The cosmic ray connection, Rept. Prog. Phys. **65**, 1025 (2002), astro-ph/0204527.

[148] F. Halzen and D. Hooper, High energy neutrinos from the TeV blazar 1ES 1959+650, Astropart. Phys. **23**, 537 (2005), astro-ph/0502449.

[149] F. Halzen, B. Keszthelyi, and E. Zas, Neutrinos from primordial black holes, Phys. Rev. **D52**, 3239 (1995), hep-ph/9502268.

[150] W. Hampel *et al.*, GALLEX, GALLEX solar neutrino observations: Results for GALLEX IV, Phys. Lett. **B447**, 127 (1999).

[151] S. W. Hawking, Black hole explosions, Nature **248**, 30 (1974).

[152] S. W. Hawking, Particle creation by black holes, Commun. Math. Phys. **43**, 199 (1975).

[153] S. W. Hawking, The unpredictability of quantum gravity, Commun. Math. Phys. **87**, 395 (1982).

[154] S. W. Hawking, Information loss in black holes, (2005), hep-th/0507171.

[155] N. Hayashida *et al.*, AGASA, The anisotropy of cosmic ray arrival directions around 10^{18} ev, Astropart. Phys. **10**, 303 (1999), astro-ph/9807045.

[156] K. S. Hirata *et al.*, Observation in the kamiokande-ii detector of the neutrino burst from supernova SN1987a, Phys. Rev. **D38**, 448 (1988).

[157] K. S. Hirata *et al.*, Kamiokande-II, Observation of a small atmospheric ν_μ / ν_e ratio in Kamiokande, Phys. Lett. **B280**, 146 (1992).

[158] J. Holder *et al.*, Detection of TeV gamma rays from the BL Lacertae object 1ES 1959+650 with the Whipple 10-meter telescope, Astrophys. J. **583**, L9 (2003).

[159] D. Hooper, D. Morgan, and E. Winstanley, Lorentz and cpt invariance violation in high-energy neutrinos, Phys. Rev. **D72**, 065009 (2005), hep-ph/0506091.

[160] D. Hooper, D. Morgan, and E. Winstanley, Probing quantum decoherence with high-energy neutrinos, Phys. Lett. **B609**, 206 (2005), hep-ph/0410094.

[161] G. T. Horowitz, Spacetime in string theory, New J. Phys. **7**, 201 (2005), gr-qc/0410049.

[162] G. T. Horowitz and J. Maldacena, The black hole final state, JHEP **02**, 008 (2004), hep-th/0310281.

[163] T. Ishida, T2k phase-i, Nucl. Phys. Proc. Suppl. **149**, 154 (2005).

[164] H. Kaiser and H. Rauch, De Broglie wave optics: neutrons, atoms and molecules, Optics of waves and particles, (Walter de Gruyter Verlag, 1999).

[165] M. Kaku, Quantum field theory: A modern introduction, (Oxford University Press, 1993).

[166] K. Kaneyuki, K2K, Recent results from K2K, Nucl. Phys. Proc. Suppl. **145**, 124 (2005).

[167] E. Katsavounidis, LIGO, LIGO detectors and data analyses: Current status and future prospects, In proceedings for 28th International Cosmic Ray Conferences (ICRC 2003), Japan. Edited by T. Kajita, Y. Asaoka, A. Kawachi, Y. Matsubara and M. Sasaki (Universal Academy Press, 2003).

[168] C. Kiefer, Quantum gravity: General introduction and recent developments, (2005), gr-qc/0508120.

[169] H. V. Klapdor-Kleingrothaus, H. Pas, and U. Sarkar, Effects of quantum space time foam in the neutrino sector, Eur. Phys. J. **A8**, 577 (2000), hep-ph/0004123.

[170] E. V. Korolkova, ANTARES, The status of the ANTARES experiment, Nucl. Phys. Proc. Suppl. **136**, 69 (2004), astro-ph/0408239.

[171] V. A. Kostelecky, Lorentz and CPT violation extension of the standard model, (1999), hep-ph/9912528, In proceedings of Beyond the desert 1999: Accelerator, non-accelerator and space approaches into the next millenium. Edited by H. V. Klapdor-Kleingrothaus and I. V. Kirvosheina (IOP, 2000).

[172] V. A. Kostelecky and M. Mewes, Lorentz and CPT violation in neutrinos, Phys. Rev. **D69**, 016005 (2004), hep-ph/0309025.

[173] V. A. Kostelecky and S. Samuel, Spontaneous breaking of Lorentz symmetry in string theory, Phys. Rev. **D39**, 683 (1989).

[174] K. V. Krasnov, Quantum geometry and thermal radiation from black holes, Class. Quant. Grav. **16**, 563 (1999), gr-qc/9710006.

[175] I. Kravchenko *et al.*, Limits on the ultra-high energy electron neutrino flux from the RICE experiment, Astropart. Phys. **20**, 195 (2003), astro-ph/0206371.

[176] D. Langlois, Brane cosmology: An introduction, Prog. Theor. Phys. Suppl. **148**, 181 (2003), hep-th/0209261.

[177] R. B. Laughlin, Emergent relativity, Int. J. Mod. Phys. **A18**, 831 (2003), gr-qc/0302028.

[178] A. Levinson and E. Waxman, Probing microquasars with TeV neutrinos, Phys. Rev. Lett. **87**, 171101 (2001), hep-ph/0106102.

[179] G. Lindblad, On the generators of quantum dynamical semigroups, Commun. Math. Phys. **48**, 119 (1976).

[180] E. Lisi, A. Marrone, and D. Montanino, Probing possible decoherence effects in atmospheric neutrino oscillations. Phys. Rev. Lett. **85**, 1166 (2000), hep-ph/0002053.

[181] Y. Liu, L.-z. Hu, and M.-L. Ge, The effect of quantum mechanics violation on neutrino oscillation, Phys. Rev. **D56**, 6648 (1997).

[182] J. A. Lobo, Lisa, (2004), gr-qc/0404079, 27th Spanish relativity meeting.

[183] F.-C. Ma and H.-M. Hu, Testing quantum mechanics in neutrino oscillation, (1998), hep-ph/9805391.

[184] J. Madore, S. Schraml, P. Schupp, and J. Wess, Gauge theory on noncommutative spaces, Eur. Phys. J. **C16**, 161 (2000), hep-th/0001203.

[185] J. M. Maldacena, Eternal black holes in anti-de sitter, JHEP **04**, 021 (2003), hep-th/0106112.

[186] F. Mandl and G. Shaw, Quantum field theory, (Wiley, 1984).

[187] A. Matusis, L. Susskind, and N. Toumbas, The IR/UV connection in the noncommutative gauge theories, JHEP **12**, 002 (2000), hep-th/0002075.

[188] N. E. Mavromatos, Neutrinos and the phenomenology of CPT violation, (2004), hep-ph/0402005, In proceedings of the 2nd international workshop on neutrino oscillations, Venice. Edited by M. Baldo Ceolin. (Papergraf, 2003).

[189] N. E. Mavromatos and J. L. Miramontes, Regularizing the functional integral in 2-D quantum gravity, Mod. Phys. Lett. **A4**, 1847 (1989).

[190] N. E. Mavromatos, On CPT symmetry: Cosmological, quantum-gravitational and other possible violations and their phenomenology, (2003), hep-ph/0309221, In proceedings of Beyond the desert 2003. Edited by H. V. Klapdor-Kleingrothaus (Springer, 2004). SLACcitation =.

[191] N. E. Mavromatos, CPT violation and decoherence in quantum gravity, (2004), gr-qc/0407005.

[192] D. E. McClelland, R. J. Sandeman, and D. G. Blair, AIGO: A southern hemisphere second generation gravitational wave observatory, In proceedings of 7th Marcel Grossmann Meeting on General Relativity. Edited by R. T. Jantzen, G. Mac Keiser and R. Ruffin (World Scientific, 1996).

[193] P. Meszaros and E. Waxman, TeV neutrinos from bursting and choked fireballs, Phys. Rev. Lett. **87**, 171102 (2001), astro-ph/0103275.

[194] S. Minwalla, M. Van Raamsdonk, and N. Seiberg, Noncommutative perturbative dynamics, JHEP **02**, 020 (2000), hep-th/9912072.

[195] T. Mohaupt, Introduction to string theory, Lect. Notes Phys. **631**, 173 (2003), hep-th/0207249.

[196] D. Morgan and E. Winstanley, Probing quantum decoherence with atmospheric neutrino oscillations: energy non-conserving models, ANTARES internal note:ANTARES-Phys/2004-003 (2004).

[197] D. Morgan and E. Winstanley, Probing quantum decoherence with atmospheric neutrino oscillations: general model, ANTARES internal note:ANTARES-Phys/2004-001 (2004).

[198] D. Morgan and E. Winstanley, Probing quantum decoherence with atmospheric neutrino oscillations: simple model, ANTARES internal note:ANTARES-Phys/2003-007 (2003).

[199] D. Morgan, E. Winstanley, J. Brunner, and L. F. Thompson, Probing the violation of lorentz invariance in atmospheric neutrino oscillations with a neutrino telescope, To appear.

[200] D. Morgan, E. Winstanley, J. Brunner, and L. F. Thompson, Probing quantum decoherence in atmospheric neutrino oscillations with a neutrino telescope, (2004), astro-ph/0412618.

[201] A. Mucke and R. J. Protheroe, Neutrino emission from HBLs and LBLs, (2001), astro-ph/0105543.

[202] R. C. Myers and M. Pospelov, Experimental challenges for quantum gravity, Phys. Rev. Lett. **90**, 211601 (2003), hep-ph/0301124.

[203] K. Okada, DONUT, Results from DONUT, Nucl. Phys. Proc. Suppl. **100**, 256 (2001).

[204] R. Penrose and M. A. H. MacCallum, Twistor theory: An approach to the quantization of fields and space-time, Phys. Rept. **6**, 241 (1972).

[205] S. Perlmutter *et al.*, Supernova Cosmology Project, Discovery of a supernova explosion at half the age of the universe and its cosmological implications, Nature **391**, 51 (1998), astro-ph/9712212.

[206] M. E. Peskin and D. V. Schroeder, An introduction to quantum field theory, (Addison-Wesley, 1995).

[207] A. Petrolini, EUSO, The Extreme Universe Space Observatory (EUSO) instrument, Nucl. Phys. Proc. Suppl. **113**, 329 (2002).

[208] B. Pontecorvo, Mesonium and antimesonium, Sov. Phys. JETP **6**, 429 (1957).

[209] B. Pontecorvo, Inverse beta processes and nonconservation of lepton charge, Sov. Phys. JETP **7**, 172 (1958).

[210] B. Pontecorvo, Neutrino experiments and the question of leptonic-charge conservation, Sov. Phys. JETP **26**, 984 (1968).

[211] W. H. Press *et al.*, Numerical recipes: The art of scientific computing: Fortran example book, (Cambridge University Press, 1993).

[212] R. J. Protheroe, High energy neutrinos from blazars, (1996), astro-ph/9607165.

[213] H. Rauch and S. A. Werner, Neutron interferometry, (Oxford University Press, 2000).

[214] H. L. Ray, MiniBooNE, Current status of the MiniBooNE experiment, (2004), hep-ex/0411022, In proceedings: Int. J. Mod. Phys. **A20** 2895, (2005).

[215] S. Refsdal, The gravitational lens effect, Mon. Not. Roy. Astron. Soc. **128**, 295 (1964).

[216] E. Resconi, Latest results from AMANDA;. In proceedings of The highest energy physics, USA (2005).

[217] L. K. Resvanis *et al.*, NESTOR, NESTOR: A Neutrino particle astrophysics underwater laboratory for the Mediterranean, Nucl. Phys. Proc. Suppl. **35**, 294 (1994).

[218] A. G. Riess *et al.*, Supernova Search Team, Observational evidence from supernovae for an accelerating universe and a cosmological constant, Astron. J. **116**, 1009 (1998), astro-ph/9805201.

[219] C. Rovelli, Loop quantum gravity, Living Rev. Rel. **1**, 1 (1998), gr-qc/9710008.

[220] C. Rovelli and L. Smolin, Discreteness of area and volume in quantum gravity, Nucl. Phys. **B442**, 593 (1995), gr-qc/9411005.

[221] J. H. Schwarz, Introduction to superstring theory, (2000), hep-ex/0008017, In proceedings of Techniques and concepts of high-energy physics, U.S.A.. Edited by H. B. Prosper and M. Danilov (NATO, 2000).

[222] K. Schwarzschild, On the gravitational field of a mass point according to einstein's theory, Sitzungsber. Preuss. Akad. Wiss. Berlin (Math. Phys.) **1916**, 189 (1916), physics/9905030.

[223] V. F. Sears, Neutron optics, (Oxford University Press, 1989).

[224] G. Sigl, S. Lee, P. Bhattacharjee, and S. Yoshida, Probing grand unified theories with cosmic ray, gamma-ray and neutrino astrophysics, Phys. Rev. **D59**, 043504 (1999), hep-ph/9809242.

[225] C. B. Smith, MINOS, Status of the MINOS experiment, Int. J. Mod. Phys. **A20**, 3059 (2005).

[226] L. Smolin, How far are we from the quantum theory of gravity?, (2003), hep-th/0303185.

[227] F. W. Stecker *et al.*, Observing the ultrahigh energy universe with OWL eyes, Nucl. Phys. Proc. Suppl. **136C**, 433 (2004), astro-ph/0408162.

[228] R. F. Streater and A. S. Wightman, PCT, spin and statistics, and all that, (Addison-Wesley,1989).

[229] M. Takeda *et al.*, Extension of the cosmic-ray energy spectrum beyond the predicted Greisen-Zatsepin-Kuzmin cutoff, Phys. Rev. Lett. **81**, 1163 (1998), astro-ph/9807193.

[230] J. H. Taylor, L. A. Fowler, and J. M. Weisberg, Measurements of General Relativistic Effects in the Binary Pulsar PSR1913+16, Nature **277**, 437 (1979).

[231] T. Thiemann, Introduction to modern canonical quantum general relativity, (2001), gr-qc/0110034.

[232] W. G. Unruh, Notes on black hole evaporation, Phys. Rev. **D14**, 870 (1976).

[233] J. C. Van Der Velde *et al.*, IMB, Neutrinos from SN1987a in the IMB detector, Nucl. Instrum. Meth. **A264**, 28 (1988).

[234] G. E. Volovik, Superfluid analogies of cosmological phenomena, Phys. Rept. **351**, 195 (2001), gr-qc/0005091.

[235] R. M. Wald, Quantum gravity and time reversibility, Phys. Rev. **D21**, 2742 (1980).

[236] E. Waxman and J. N. Bahcall, High energy neutrinos from cosmological gamma-ray burst fireballs, Phys. Rev. Lett. **78**, 2292 (1997), astro-ph/9701231.

[237] E. Waxman and J. N. Bahcall, Neutrino afterglow from gamma ray bursts: approx. 10^{18} eV, Astrophys. J. **541**, 707 (2000), hep-ph/9909286.

[238] S. Weinberg, The quantum theory of fields. vol. 1: Foundations. (Cambridge University Press, 1995).

[239] R. Wischnewski *et al.*, The AMANDA Neutrino Detector, Nucl. Phys. Proc. Suppl. **75A**, 412 (1999).

[240] E. Witten, M theory and quantum mechanics, Nucl. Phys. Proc. Suppl. **62**, 463 (1998).

[241] E. Witten, The cosmological constant from the viewpoint of string theory, (2000), hep-ph/0002297, In proceedings of Sources and detection of dark matter and dark energy in the Universe, U.S.A.. Edited by D. B. Cline (Springer, 2001).

[242] D. G. York *et al.*, SDSS, The Sloan Digital Sky Survey: technical summary, Astron. J. **120**, 1579 (2000), astro-ph/0006396.

[243] G. T. Zatsepin and V. A. Kuzmin, Upper limit of the spectrum of cosmic rays, JETP Lett. **4**, 78 (1966).

[244] K. Zuber, Neutrino physics, (IOP publishing, 2004).